

Inaugural dissertation
for
obtaining the doctoral degree
of the
Combined Faculty of Mathematics, Engineering and Natural Sciences
of the
Ruprecht-Karls-University
Heidelberg

Presented by

M.Sc. Klara Franziska Rehder

Born in: Berlin, Germany

Oral examination: 05.09.2024

Deciphering the role of heterozygous 3q28 deletion in the pathogenesis
of schizophrenia in iPSC-derived human cortical neurons

Referees: Prof. Dr. Valery Grinevich
Prof. Dr. med. Philipp Koch

Table of Contents

Table of Contents	I
List of Figures.....	V
List of Tables	VII
List of Abbreviations	IX
1. Abstract.....	1
2. Zusammenfassung.....	3
3. Introduction	5
3.1 Schizophrenia	5
3.1.1 General aspects of schizophrenia	5
3.1.2 Pathogenesis of schizophrenia.....	6
3.2 Genetic landscape on 3q28 gene locus	9
3.2.1 Central nervous system (CNS) immunity.....	10
3.2.2 Interleukin-1 beta and its multifaced signaling pathway	12
3.2.3 Interleukin-1 receptor accessory protein and Interleukin-1 receptor accessory protein like 1.....	16
3.2.4 Osteocrin and its dual role in the periphery and the brain.....	18
3.3 Stem cell technology	21
3.3.1 Human induced pluripotent stem cells (hiPSC) – potentials and limitations	21
3.3.2 Generation of cortical neurons derived from hiPSCs	25
3.3.3 Insights from human induced pluripotent stem cell-derived model systems into schizophrenia pathology.....	27
4. Aims of this study	29
5. Materials	30
5.1 Cell culture.....	30
5.1.1 Cell lines	30
5.1.2 Cell culture solutions, small molecules and media.....	30
5.1.3 Buffer and media compositions for cell culture	33
5.2 Molecular biology	38
5.2.1 Bacterial culture	38
5.2.2 Enzymes	38
5.2.3 Plasmids	39
5.2.4 Primers, oligonucleotides and PCR components.....	39
5.2.5 Kits.....	42
5.2.6 Antibodies and fluorescent probes	42
5.2.7 Buffers and solutions.....	44

Table of Contents

5.2.8	Reagents and chemicals	46
5.3	Consumables	48
5.4	Technical Equipment	49
5.5	Software	51
6.	Methods	52
6.1	Cell culture	52
6.1.1	Cultivation of hiPSCs	52
6.1.2	Generation of neural progenitors	52
6.1.3	Generation of cortical neurons	53
6.1.4	Treatment of cortical neurons	54
6.1.5	Co-culture with mouse derived astrocytes for electrophysiological measurements	55
6.1.6	Cryopreservation of cells	55
6.1.7	Defrosting of hiPSCs and neural progenitors	55
6.1.8	Organoid generation	55
6.2	Generation of isogenic <i>OSTN</i> mutant lines via CRISPR/Cas9	56
6.2.1	Generation of an <i>OSTN</i> -targeting CRISPR/Cas9 plasmid	56
6.2.2	Transformation of competent <i>E. coli</i>	58
6.2.3	Plasmid DNA isolation from <i>E. coli</i>	58
6.2.4	Nucleofection of hiPSCs and clone validation	58
6.3	Live cell analyses	60
6.3.1	Calcium imaging	60
6.3.2	Electrophysiology	61
6.4	Molecular Biology	61
6.4.1	Harvesting samples	61
6.4.2	DNA isolation	62
6.4.3	RNA isolation	62
6.4.4	Determination of DNA and RNA concentrations	63
6.4.5	Complementary DNA (cDNA) synthesis	63
6.4.6	Quantitative PCR (qPCR)	64
6.4.7	Reverse transcriptase PCR (RT-PCR)	64
6.4.8	Agarose gel electrophoresis, gel extraction and sanger sequencing	66
6.4.9	Measurement of RNA integrity	67
6.4.10	Bulk RNA sequencing (RNAseq)	67
6.5	Biochemistry	68
6.5.1	Protein isolation	68
6.5.2	Determination of protein concentration	68
6.5.3	SDS-PAGE and western blot	68

Table of Contents

6.5.4	Immunofluorescence staining.....	69
6.6	Microscopy - image acquisition	70
6.7	Analyses	70
6.7.1	Early outgrowth assay.....	70
6.7.2	Sholl analysis	71
6.7.3	Analysis of synaptic proteins	71
6.7.4	Statistical analysis.....	71
6.7.5	Visualization.....	71
7.	Results.....	72
7.1	hiPSC quality control revealed a chromosomal aberration in the SCZ patient	72
7.2	Generation of isogenic <i>OSTN</i> mutant hiPS cell line	73
7.3	Generation and Characterization of hiPSC-derived cortical neurons.....	74
7.3.1	Generation and validation of hiPSC-derived cortical neurons	74
7.3.2	Neuronal cultures show low expression of <i>OSTN</i>	77
7.3.3	RNAseq gene ontology (GO) term analysis uncovered research foci	79
7.4	Heterozygous 3q28 deletion impacts neuronal morphology	84
7.4.1	Impact of heterozygous 3q28 deletion on morphology-related genes	84
7.4.2	Increased neurite length in young neurons with heterozygous 3q28 deletion	86
7.4.3	SCZ neurons display higher ramification and an increased size compared to Ctrl cells (d55-60)	87
7.4.4	Investigation of <i>OSTN</i> impact on neuronal morphology as a	89
	3q28-located gene	
7.4.5	Neuronal cultures respond to IL-1 β pathway activation	91
7.4.6	Influence of <i>OSTN</i> and IL-1 β pathways on Ctrl and SCZ neuronal	91
	morphology	
7.4.7	Influence of <i>OSTN</i> and IL-1 β pathways on WT and <i>OSTN</i> _2+/-	95
	neuronal morphology	
7.5	Heterozygous 3q28 deletion affects synapses	99
7.5.1	Mature SCZ neurons display increased synapse density	99
7.5.2	Mutation of <i>OSTN</i> impacts synapse density	102
7.5.3	Influence of <i>OSTN</i> and IL-1 β pathway modulation on synapses.....	106
7.6	Impacts of heterozygous 3q28 deletion on neuronal function.....	110
7.6.1	Calcium imaging uncovers slight variation in neuronal activity.....	111
7.6.2	Electrophysiological measurements reveal changes in sEPSC frequencies	119
7.7	Organoids as a measure to investigate more complex systems	122
8.	Discussion.....	124
8.1	Generation of hiPSC-derived cortical neurons as a model for schizophrenia	124
8.2	Impacts of <i>OSTN</i> and IL-1 β pathways on neuronal morphology.....	127
8.3	Influence of <i>OSTN</i> and IL-1 β pathways on synapses.....	131

Table of Contents

8.4	Consequences of heterozygous 3q28 deletion on neuronal function.....	133
9.	Summary and outlook	137
10.	References	139
11.	Appendix.....	160
	Appendix I for introduction section 3.2	160
	Appendix II for results section 7.4.4 and 7.4.7.....	161
12.	Contributions.....	164
13.	Acknowledgements.....	165

List of Figures

Figure 1: Flowchart of symptom categories in schizophrenia.....	6
Figure 2: Schematic karyogramm.....	10
Figure 3: Schematic depiction of IL-1 signaling pathway.....	13
Figure 4: Effects of IL-1 β on neurons.....	15
Figure 5: Schematic overview of NP pathway and predicted mode of action of OSTN.....	19
Figure 6: Schematic overview of OSTN expression sites and effects on different tissues.....	20
Figure 7: Hypothesized mode of action of OSTN in the brain.....	21
Figure 8: Schematic depiction of working sequence of obtaining hiPSCs and the experimental opportunities	22
Figure 9: Embryonal brain development and the necessary morphogen gradients.....	26
Figure 10: Quality control of hiPSCs representative for Ctrl and SCZ.....	72
Figure 11: Generation of <i>OSTN</i> mutant hiPS cell line with CRISPR/Cas9.....	73
Figure 12: Overview of differentiation protocol from hiPSCs to cortical neurons.....	74
Figure 13: Characterization of NPCs and neuronal cultures.....	76
Figure 14: <i>OSTN</i> expression in neuronal cultures.....	78
Figure 15: GO term enrichment of d42 Ctrl and SCZ neurons.....	80
Figure 16: GO term enrichment of d42 WT, <i>OSTN</i> _1+/- and <i>OSTN</i> -/- neurons.....	82
Figure 17: Differentially expressed genes related to neuronal morphology of d42 neurons.....	84
Figure 18: Early outgrowth assay of Ctrl and SCZ neurons.....	87
Figure 19: Sholl analysis of Ctrl and SCZ neurons (d55-60).....	88
Figure 20: Sholl analysis of WT and <i>OSTN</i> mutant neurons (d55-60).....	90
Figure 21: IL-1 β responsiveness of neurons.....	91
Figure 22: Modulation of <i>OSTN</i> and IL-1 β pathways impacts morphology in Ctrl and SCZ neurons.....	93
Figure 23: Modulation of <i>OSTN</i> and IL-1 β pathways impacts morphology in WT and <i>OSTN</i> _2+/- neurons.....	97
Figure 24: SCZ neurons display an increase in synapse density at late time points.....	100
Figure 25: Heterozygous 3q28 deletion elicits differential expression of genes encoding for synaptic receptors and adhesion molecules.....	101

List of Figures

Figure 26: Expression of synapse and SNARE complex related genes in WT, <i>OSTN_1</i> ^{+/-} and <i>OSTN</i> ^{-/-}	102
Figure 27: <i>OSTN</i> mutation does not significantly change expression of genes encoding for synaptic receptors and adhesion molecules.....	103
Figure 28: Mutation of <i>OSTN</i> gene reduces synapse density in mature neurons (d105).....	105
Figure 29: Modulation of <i>OSTN</i> and IL-1 β pathways impacts synapsin particle density mainly in Ctrl neurons (d55-60).....	106
Figure 30: Modulation of <i>OSTN</i> and IL-1 β pathways impacts synapsin particle density in WT and <i>OSTN_2</i> ^{+/-} neurons (d55-60).....	108
Figure 31: Modulation of <i>OSTN</i> and IL-1 β pathways impacts synaptic particle density mainly in d105 SCZ neurons.....	109
Figure 32: Heterozygous 3q28 deletion affects AIS length and position.....	110
Figure 33: Ctrl and SCZ neurons (d45) do not show significant differences in Ca ²⁺ transient frequency under baseline conditions.....	112
Figure 34: Ctrl and SCZ neurons (d45) show significant differences in number of active cells and synchronicity under stimulating conditions.....	113
Figure 35: Ca ²⁺ imaging of d45 <i>OSTN</i> mutant neuronal cultures reveals mostly subtle influence of <i>OSTN</i> mutation on neuronal activity.....	115
Figure 36: Ca ²⁺ imaging of d45 Ctrl and SCZ neuronal cultures with modulation of <i>OSTN</i> and IL-1 β pathways.....	117
Figure 37: Expression patterns of activity related genes in d42 neuronal cultures.....	118
Figure 38: Ca ²⁺ imaging of d70 Ctrl and SCZ neuronal cultures.....	119
Figure 39: D56/57 SCZ neurons co-cultured on astrocytes display reduced sEPSC frequency.....	120
Figure 40: D56/57 <i>OSTN</i> mutant neurons co-cultured on astrocytes display increased sEPSC frequency.....	121
Figure 41: IF on cryosections of d37 Ctrl and SCZ organoids.....	123
Figure S1: Sholl graphs of single WT neuron batches demonstrate large batch variance.....	161
Figure S2: Sholl analysis of WT and <i>OSTN</i> mutant neurons (d55-60), before WT batch 3 inclusion.....	162
Figure S3: Modulation of <i>OSTN</i> and IL-1 β pathways barely impacts synaptic particle density in d105 WT neurons.....	163

List of Tables

Table 1: List of cell lines.....	30
Table 2: Base media.....	30
Table 3: Commercial ready-to use cell culture solutions.....	31
Table 4: Growth factors, small molecules and other chemicals for cell culture.....	31
Table 5: Composition of cell culture cultivation and freezing media.....	33
Table 6: Composition of buffers, supplements and solutions.....	37
Table 7: Media for bacteria cultivation and transformation.....	38
Table 8: Enzymes for molecular biology and cloning.....	38
Table 9: Plasmids used for cloning and <i>OSTN</i> mutant cell lines.....	39
Table 10: Primers for RT-PCR and qPCR.....	40
Table 11: Oligonucleotides and gRNA for cloning.....	41
Table 12: Substances for PCR reaction mix.....	41
Table 13: Substances for qPCR reaction mix.....	41
Table 14: Commercial kits.....	42
Table 15: Primary antibodies.....	42
Table 16: Secondary antibodies.....	43
Table 17: Fluorescent probes.....	44
Table 18: Self-made buffers and solutions.....	44
Table 19: Commercial buffers and solutions.....	46
Table 20: Molecular biology reagents.....	46
Table 21: Chemicals	46
Table 22: Consumables	48
Table 23: Notable laboratory equipment.....	49
Table 24: Computer Software.....	51
Table 25: Protocols for backbone digestion and gRNA phosphorylation reaction mixes.....	57
Table 26: Program for backbone digestion and gRNA phosphorylation.....	57
Table 27: Composition for ligation reaction mix.....	57
Table 28: Cycling program for cDNA synthesis with iScript™ cDNA Synthesis Kit.....	63
Table 29: qPCR cycling program.....	64
Table 30: RT-PCR cycling program (Taq DNA Polymerase, Biozym).....	65
Table 31: Composition of LongAmp® Taq Polymerase reaction mix.....	65
Table 32: LongAmp® cycling program.....	66
Table 33: Program mycoplasma PCR.....	66
Table S1: List of genes located on 3q28.....	160

List of Abbreviations

%	percent
(v/v)	volume percent
(w/v)	weight percent
°C	degree celsius
μ	micro
2D	2 dimensional
3D	3 dimensional
AAV	adeno-associated virus
ACSF	artificial cerebrospinal fluid
AIS	axon initial segment
AMPA	α-amino-3-hydroxy-5-methyl-4-isoxazolepropionic acid receptor
ANK3	ankyrin 3
ANKG	ankyrin G
ANP	atrial natriuretic peptide
AP	action potential
A-P	anterior-posterior
AP-1	activator protein 1
ARC	activity regulated cytoskeleton associated protein
ARSB	arylsulfatase B
ASCL1	achaete-scute homolog 1
ASD	autism spectrum disorder
ATF	activating transcription factor
BBB	blood-brain barrier
BCA	bicinchoninic acid
BDNF	brain-derived neurotrophic factor
BNP	brain natriuretic peptide
bp	base pair
BSA	bovine serum albumin
ca.	circa
Ca ²⁺	calcium
CaMKIIa	calcium/calmodulin-dependent protein kinase IIa
cAMP	cyclic adenosine monophosphate
Cas9	CRISPR-associated protein 9
CASP1	caspase 1
CBLN2	cerebellin 2 precursor
CDH2	cadherin 2
CDK4/6	cyclin dependent kinase 4/6

cDNA	complementary DNA
cGMP	cyclic guanosine monophosphate
CNP	c natriuretic peptide
CNS	central nervous system
CNTNAP2	contactin associated protein 2
CO ₂	Carbon dioxide
COBL	cordon-bleu WH2 repeat protein
COX2	cyclooxygenase 2
CREB	cAMP response element-binding protein
CRISPR	Clustered Regularly Interspaced Short Palindromic Repeats
CSF	cerebrospinal fluid
CTIP2	COUP-TF-interacting protein 2
Ctrl	control
d	day
DAPI	4',6-diamidino-2-phenylindole
DAPT	N-[N-(3,5-Difluorophenacetyl)-L-alanyl]-S-phenylglycine t-butyl ester
ddH ₂ O	double distilled water
DEG	differentially expressed gene
DEPC	diethylpyrocarbonate
DISC1	disrupted in schizophrenia 1
DLX1, 2	distal-less homeobox 1, 2
DMEM	Dulbecco's Modified Eagle Medium
DNA	deoxyribonucleic acid
DNase	deoxyribonuclease
DRAXIN	Dorsal inhibitory axon guidance protein
DSCAM	DS cell adhesion molecule
DSCAML1	DSCAM like 1
D-V	dorso-ventral
e.g.	exempli gratia (for example)
E8	essential 8
eAP	evoked action potential
EB	embryoid body
EDTA	ethylenediaminetetraacetic acid

List of Abbreviations

EPHB1	ephrin type-B receptor 1	IKK	inhibitor of nuclear factor kappa-B kinase
ErbB4	Erb-B2 receptor tyrosine kinase 4	IL	interleukin
ERK	extracellular signal-regulated kinases	IL-1R	interleukin-1 receptor
et al.	<i>et alia</i> (and others)	IL-1Ra	interleukin-1 receptor antagonist
etc.	<i>et cetera</i> (and so on)	IL1RAP	interleukin-1 receptor accessory protein
FDR	first-degree relatives	IL1RAPL1	ILRAP like 1
FEP	first episode of psychosis	iNOS	inducible nitric oxide synthase
FGF	fibroblast growth factor	IRAK	interleukin-1 receptor-activated protein kinase
fMRI	functional magnetic resonance imaging	IκB	inhibitor of nuclear factor kappa-B
FOXP1	forkhead box G1	JDP	Jun dimerization protein
FOXO1	forkhead box protein O1	JNK	c-Jun N-terminal kinase
fps	Frames per second	KCC2	potassium-chloride cotransporter 2
g	gram	kDa	kilodalton
GABA	γ-aminobutyric acid	KEGG	Kyoto Encyclopedia of Genes
GAD	Glutamate Decarboxylase	KIAA0319	dyslexia-associated protein KIAA0319
GC	guanylyl cyclase	KLF4	krüppel like factor-4
gDNA	genomic DNA	l	liter
GFAP	glial fibrillary acidic protein	LAAP	L-Ascorbic acid 2- phosphate
GO	gene ontology	LTD	long-term depression
GRIA	glutamate Ionotropic Receptor AMPA Type Subunit	LTP	long-term potentiation
GRIN	glutamate Ionotropic Receptor NMDA Type Subunit	LZTS3	leucine zipper tumor suppressor family member 3
GRM	glutamate metabotropic receptor	M	molar
gRNA	guide RNA	MAP2	microtubule associated protein 2
GTP	guanosine triphosphate	MAPK	mitogen-activated kinase
GWAS	genome-wide association studies	MCP1	monocyte chemoattractant protein 1
h	hour	MECP2	methyl CpG binding protein 2
HC	hippocampus	MEF2	myocyte enhancer factor 2
HGP	human genome project	MFG	middle frontal gyrus
hiPSC	human induced pluripotent stem cells	min	minute
Hz	hertz	miRNA	micro RNA
i. e.	id est	MKK	mitogen-activated kinase kinases
ICD-10	International Statistical Classification of Diseases and Related Health Problems	mM	millimolar
ID	intellectual disability	MRE	MEF2 responsive element
IF	immunofluorescence	ms	millisecond
IFN	interferon	MTG	middle temporal gyrus

List of Abbreviations

mTOR	mammalian target of rapamycin	pH	potential of hydrogen
mV	millivolt	PKG	protein kinase G
MYD88	myeloid differentiation primary response 88	PLP	proteolipid
n	nano	PRODH	proline dehydrogenase
ND media	neuronal differentiation media	PRSS12	serine protease 12
NES	nestin	PSD95	postsynaptic density protein 95
NETO2	neuropilin and tolloid like 2	PTPRD	protein tyrosine phosphatase receptor type D
NEUN	neuronal nuclei	pVIM	phospho-vimentin
NFH	neurofilament heavy chain	qPCR	quantitative polymerase chain reaction
NFL	neurofilament light polypeptide	REST	RE1-silencing transcription factor
NFM	neurofilament medium chain	rhOSTN	recombinant human OSTN
NFκB	nuclear factor kappa-B	RNA	ribonucleic acid
NGF	nerve growth factor	RNase	ribonuclease
NGN1	neurogenin 1	RNAseq	bulk RNA sequencing
NKCC1	neuronal Na-K-Cl cotransporter 1	ROBO	roundabout guidance receptor
NMDAR	N-methyl-d-aspartate receptor	ROI	area of interest
NP	natriuretic peptide	ROS	reactive oxygen species
NPC	neural progenitor cells	RT	room temperature
NPR	natriuretic peptide receptor	RT-PCR	reverse transcriptase PCR
NR2B	NMDAR subunit 2B	Runx2	runt-related transcription factor 2
NRG1	neuregulin 1	s	second
NRP2	neuropilin 2	S100B	S100 calcium binding protein B
ns	not significant	SAG	smoothened agonist
NT3	neurotrophin 3	SATB2	special AT-rich sequence-binding protein 2
OCT3/4	octamer-binding transcription factor-3/4	SCZ	schizophrenia
ON	Overnight	SDS-PAGE	sodium dodecyl sulfate–polyacrylamid gel electrophoresis
OSTN	osteocrin	SEMA	semaphorin
Osx	osterix	sEPSC	spontaneous excitatory postsynaptic current
OTX2	orthodenticle homeobox 2	SHANK2	SH3 and multiple ankyrin repeat domains 2
pA	picoampere	SHH	sonic hedgehog
PBMC	Peripheral blood mononuclear cell	SHISA6	shisa family member 6
PBS	Phosphate-buffered saline	sIL-1R2	soluble IL-R2
PCDH17	protocadherin 17	siRNAs	small interfering RNA
PCDHGB1	PCDH Gamma Subfamily B 1	sISC	spontaneous inhibitory synaptic current
PCR	polymerase chain reaction		
PEI	Polyethylenimin		
PET	positron emission tomography		
PFA	paraformaldehyde		
PFC	prefrontal cortex		
PGE2	prostaglandin E2		

List of Abbreviations

SLIT1	slit guidance ligand 1	TAB1/2	TAK1-binding proteins 1/2
SNAP25	synaptosomal-associated protein of 25 kDa	TAK1	transforming growth factor β -activated kinase 1
SNARE	soluble N-ethylmaleimide-sensitive-factor attachment receptor	TBR1	T-box brain 1
SNP	Single nucleotide polymorphism	TGF	transforming growth factor
SOX2	sex-determining region Y-box2	TIR	toll-IL-1 receptor
SPL	superior parietal lobe	TNF	tumor necrosis factor
SSEA4	stage specific embryo antigen 4	TOLLIP	toll interacting protein
ssODN	single-stranded oligodeoxynucleotide	TRAF6	TNF receptor associated factor 6
SSTR2	somatostatin receptor 2	TRKB, C	tyrosine receptor kinase B, C
SV2	synaptic vesicle glycoprotein 2	t-SNARE	target membrane SNARE
SYN	synapsin	TTX	tetrodotoxin
SYNPO	synaptopodin	TUBB3	tubulin beta 3
SYP	synaptophysin	U	unit
SYT	synaptotagmin	UNC5A	unc-5 netrin receptor A
		VGLUT	vesicular glutamate transporter
		vs.	versus
		WT	wild type
		x g	times gravity

1. Abstract

About one percent of the world's population is suffering from schizophrenia (SCZ), which is a multifactorial neuropsychiatric disorder with high heritability. SCZ is characterized by symptoms such as hallucinations, lack of motivation and memory deficits. On the molecular level, an imbalance of neurotransmitters and changes in the content of synaptic proteins and receptors have been suggested to critically contribute to its pathogenesis. Nonetheless, the underlying molecular causalities of SCZ remain elusive. In this project, out of a small cohort of healthy first-degree relatives and patients suffering from SCZ, one patient was identified to have a heterozygous deletion of chromosome 3q28. After careful consideration of the genetic landscape of this gene locus, I determined two candidate genes encoded on this gene locus: osteocrin (*OSTN*) and interleukin-1 receptor accessory protein (*IL1RAP*). While the interleukin-1 β (IL-1 β) pathway has been previously associated with SCZ, a link between *OSTN* and SCZ has not been described yet. A recent report revealed that *OSTN* has been evolutionary repurposed to be expressed in the central nervous system (CNS) exclusively of some anthropoid primates including humans. Interestingly, both, *OSTN* and IL-1 β signaling are described to affect neuronal morphology, by reducing neuronal complexity. In this thesis, an *in vitro* model of highly pure human induced pluripotent stem cell (hiPSC)-derived cortical neurons was used to study SCZ pathomechanisms in context of a heterozygous 3q28 deletion. Due to its novelty and limited information on *OSTN* in the brain, I additionally generated an isogenic system where I introduced an *OSTN* mutation in a healthy control cell line. This is an attempt to reduce genetic complexity and determine contributions of this candidate gene, while the IL-1 β pathway was modulated pharmacologically. Transcriptomic analysis of SCZ neurons uncovered that heterozygous 3q28 deletion has a major impact on the expression of genes related to synapses, adhesion molecules and neuronal growth. Morphological characterization of SCZ neurons at d55-60, disclosed a significant increase in neuronal ramification. Moreover, the findings in *OSTN* mutant neurons confirmed an impact of *OSTN* on neuronal morphology. Additionally, alterations in density of mature synapses were observed in both systems. These changes were accompanied by altered synaptic activity detected by electrophysiological measurements. Further, modulation of *OSTN* and IL-1 β pathway respectively revealed effects on neuronal ramification.

In sum, the presented data strongly suggests a link of the heterozygous 3q28 deletion to neuronal morphology and function in SCZ patients' neurons. My work endorses hiPSCs as an invaluable model to characterize complex disorders and human-specific aspects, which can help identifying genes that might qualify as molecular targets for therapy in the future.

2. Zusammenfassung

Etwa ein Prozent der Weltbevölkerung leidet an Schizophrenie (SCZ), einer komplexen neuropsychiatrischen Erkrankung mit hoher Erblichkeit. SCZ ist durch Symptome wie Halluzinationen, Antriebslosigkeit und Gedächtnisstörungen gekennzeichnet. Auf molekularer Ebene werden ein Ungleichgewicht der Neurotransmitter und veränderte Mengen synaptischer Proteine und Rezeptoren als maßgebliche Beiträge zur Pathogenese vermutet. Dennoch sind die zugrunde liegenden molekularen Ursachen der SCZ noch weitgehend unbekannt. In diesem Projekt wurde aus einer kleinen Kohorte gesunder Verwandter ersten Grades und Patienten mit SCZ ein Patient mit einer heterozygoten Deletion des Chromosoms 3q28 identifiziert. Nach eingehender Analyse der genetischen Landschaft dieses Genlocus, identifizierte ich zwei Kandidatengene: Osteocrin (*OSTN*) und Interleukin-1-Rezeptor-Accessory-Protein (*IL1RAP*). Während der IL-1 β -Signalweg bereits mit SCZ in Verbindung gebracht wurde, ist eine Verbindung zwischen *OSTN* und SCZ bisher nicht beschrieben. Eine aktuelle Studie zeigte, dass *OSTN* evolutionär so umfunktionierte, dass es ausschließlich im zentralen Nervensystem (ZNS) einiger Anthropoiden, einschließlich des Menschen, exprimiert wird. Interessanterweise wurde bereits beschrieben, dass sowohl *OSTN* als auch Aktivität des IL-1 β -Signalwegs die neuronale Morphologie beeinflussen, indem sie die neuronale Komplexität reduzieren. In dieser Arbeit wurde ein in vitro Modell hochreiner, aus humanen induzierten pluripotenten Stammzellen (hiPSCs) abgeleiteter kortikaler Neurone verwendet, um SCZ-Pathomechanismen im Zusammenhang mit einer heterozygoten 3q28-Deletion zu untersuchen. Aufgrund der Neuartigkeit und begrenzten Informationen zu *OSTN* im Gehirn, entwickelte ich zusätzlich ein isogenes System, in welches ich eine *OSTN*-Mutation in eine gesunde Kontrollzelllinie eingebracht habe. Dies ist ein Ansatz, die genetische Komplexität zu reduzieren und den Einfluss dieses Kandidatengens zu bestimmen, während der IL-1 β -Signalweg pharmakologisch moduliert wurde. Transkriptomanalysen der SCZ-Neurone zeigten, dass die heterozygote 3q28-Deletion einen erheblichen Einfluss auf die Expression von Genen im Zusammenhang mit Synapsen, Adhäsionsmolekülen und neuronalem Wachstum hat. Die morphologische Charakterisierung der SCZ-Neurone an den Tagen 55-60 zeigte eine signifikante Zunahme der neuronalen Verzweigung. Darüber hinaus bestätigten die Ergebnisse in *OSTN*-Mutanten-Neuronen einen Einfluss von *OSTN* auf die neuronale Morphologie. Zudem wurden Veränderungen in der Dichte reifer Synapsen in beiden Systemen beobachtet. Diese Veränderungen gingen mit veränderter synaptischer Aktivität einher, die durch elektrophysiologische Messungen nachgewiesen wurde. Weiterhin zeigte die Modulation der *OSTN*- und IL-1 β -Signalwege jeweils Effekte auf die neuronale Verzweigung. Zusammenfassend deuten die präsentierten Daten darauf hin, dass die heterozygote 3q28-Deletion mit Veränderungen der neuronalen Morphologie und Funktion in

Zusammenfassung

SCZ-Patienten-Neuronen in Zusammenhang steht. Meine Arbeit bestätigt hiPSCs als wertvolles Modell zur Charakterisierung komplexer Erkrankungen und humanspezifischer Aspekte, was dazu beitragen kann, Gene zu identifizieren, die sich möglicherweise als molekulare Ziele für zukünftige Therapien qualifizieren.

3. Introduction

3.1 Schizophrenia

3.1.1 General aspects of schizophrenia

With a life-time prevalence of up to 1% of the world-wide population, SCZ is a major concern medically as well as economically (1). SCZ has a relatively early onset, with the majority of the cases manifesting during early adulthood. Although SCZ shows a rather high degree of heritability (up to 80%) (2), it is now evident that environmental factors play a crucial role in its pathophysiology. In particular, pre-natal challenges such as a maternal infection, fetal hypoxia, premature birth and low birth weight might alter the physiological neurodevelopmental trajectory, thus increasing the risk of developing SCZ later in life (3,4).

The onset of the disorder usually coincides with additional environmental stressors like traumatic experiences (5–7), infections and sexual abuse (8) amongst others (9,10) that are unmasking the increased susceptibility due to prenatal stress. Upon their manifestation, SCZ symptoms are divided into three major categories: positive and negative symptoms and cognitive impairments (Figure 1) and typically occur first during childhood or adolescence after the aforementioned stress exposure, while the prefrontal cortex (PFC) is still developing. Positive symptoms include hallucinations and delusions, negative symptoms include a lack of motivation and as well as deficits in affect and cognitive impairments are characterized by memory and language deficits (3). The diagnosis of SCZ is not an easy task due to the variety of symptoms and the similarity to other psychiatric disorders. Moreover, it may take some time to identify SCZ since the symptomatic phase is usually preceded by a prodromal (sub-diagnostic symptoms) phase and is not identified until the first episode of psychosis (FEP) occurs (11). In contrast to the negative and cognitive symptoms, the positive symptoms tend to fluctuate over the progression of the disorder (12). Due to the heterogeneous response to currently available medications, it remains challenging to find satisfactory drug combinations that help each individual patient, decreasing the compliance of the patients to the therapy. Moreover, the drugs used to treat SCZ all address the symptoms and not the underlying cause, since the pathomechanisms of SCZ are not fully understood. Treatments usually have strong side effects (3) and discontinuation of drug treatment is associated with a high relapse rate which has a lasting impact on patients' quality of life (13,14). Considering that, it is a necessity to further elucidate the underlying mechanisms of SCZ and identify new therapeutic targets.

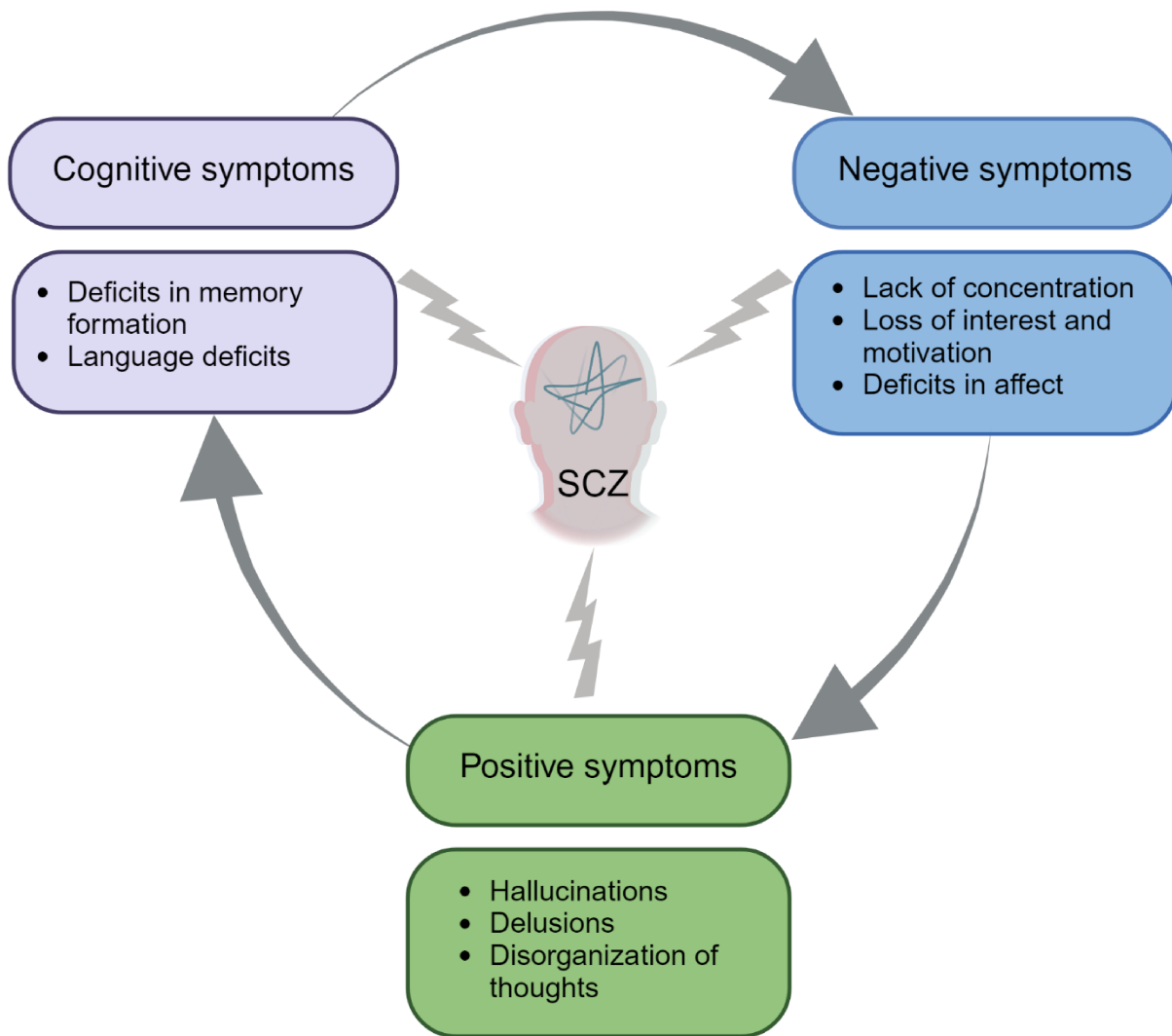


Figure 1: Flowchart of symptom categories in schizophrenia

Short examples of the three symptomatic categories observed in SCZ patients which are used to diagnose the disorder. The three major symptom categories are positive, negative, and cognitive symptoms that can occur in varying combinations. Created with BioRender.com

3.1.2 Pathogenesis of schizophrenia

Through non-invasive imaging procedures like functional magnetic resonance imaging (fMRI) or positron emission tomography (PET) it is possible to uncover alterations in functionality and neuroanatomy in the brain. Clinical studies using these techniques were able to show functional and anatomical abnormalities in the brains of SCZ patients. It is reported that SCZ brains show enlarged lateral ventricles and reduced cortical volume (15). It was shown that certain brain regions display functional alterations compared to healthy brains. Part of these brain regions are amongst others the hippocampus (HC), middle temporal gyrus (MTG), middle frontal gyrus (MFG), superior parietal lobe (SPL), ventromedial prefrontal cortex and thalamus (16–18). The medial temporal and prefrontal lobe brain regions are involved in declarative and working memory, which correlates to the cognitive symptoms of SCZ. In addition to these

observations, alterations in white and gray matter of SCZ brains were discovered. A reduction of gray matter reflects a decrease in dendritic complexity and synaptic density rather than reduced number of neurons and likely affects inter-neuronal communications (19). Such a reduction of gray matter is described for healthy adolescents in the PFC suggesting a normal developmental process such as synaptic pruning, however in SCZ the extent of gray matter reduction is larger. A similar situation can be found in the white matter of SCZ brains. In SCZ patients, white matter is reduced and the structural integrity is affected in white matter tracts as e.g. the HC, cingulate bundle or superior longitudinal fasciculus which impairs inter-regional communication. The affected tracts are associated with working and long-term memory manifesting cognitive impairments in SCZ. Both matter abnormalities are present already in FEP patients implying causality rather than a secondary phenomenon (17).

On molecular level, researchers have been approaching SCZ by different hypotheses of which many involve alterations in receptor function and transmitter release like dopamine and glutamate, suggesting the involvement of neurotransmitter imbalances. The dopamine hypothesis has been investigated for decades and has evolved over time. First, it was suggested that SCZ is caused by a hyperdopaminergia, later was specified to a subcortical hyper- and a prefrontal hypodopaminergia and finally the involvement of other neurotransmitters was taken into consideration as well (20). All in all, the dopamine hypothesis suggests explanations for each symptom category. However, many anti-psychotics target dopamine receptors but alleviate mainly the positive symptoms. On the other hand, the glutamate hypothesis resulted from the observation that N-methyl-d-aspartate receptor (NMDAR) antagonist treatment (such as phencyclidine and ketamine) induced SCZ-like symptoms (21). Since the NMDARs are key players of long-term potentiation (LTP) and memory formation (22) the hypothesis refers primarily to the cognitive symptoms of SCZ. Moreover, alterations in the glutamatergic system in postmortem analyses could be determined in different brain regions such as HC (23,24), thalamus (25), temporal cortex (26–28), dorsal PFC (29–32) and anterior cingulate cortex (32–35) to name a few. Despite their heterogeneity, all these findings pointed toward alterations in receptor composition and glutamate synthesis (21). Moreover, it is hypothesized that stress-induced serotonergic overdrive in the cerebral cortex contributes to SCZ pathology also by potentially disrupting glutamate signaling (36). Another reason to assume an involvement of serotonin in SCZ pathology is the mechanism of some antipsychotic drugs that block or activate serotonin receptors and thus alleviate symptoms (37). The inhibitory γ -aminobutyric acid (GABA) neurotransmitter system seems to contribute to SCZ phenotypes as well, since it has been observed that GABA receptor levels in HC are reduced, leading to a reduction or loss of GABA signaling (38). The alterations occurring in the GABA transmission system seem to happen in pre- and postsynaptic components but there is no scientific consensus about GABA amounts in SCZ yet since

research results for different brain regions are inconsistent (39). Considering the transmitter hypotheses, a general transmitter imbalance in SCZ can be suggested, however the identification of common mechanisms is essential for understanding and treating a disorder effectively. Interestingly, a common mechanism concerning neurotransmitter balances could involve vesicle fusion which is mediated via the soluble N-ethylmaleimide-sensitive-factor attachment receptor (SNARE) complex facilitating transmitter release in different neuronal cell types. It has been shown that SNARE complex formation is altered in SCZ. Synaptosomal-associated protein of 25 kDa (SNAP25) is a member of the SNARE complex located at the target membrane (t-SNARE) (40). SNAP25 previously has been associated with SCZ where its levels in the HC of patients were reduced (41). In neurons there is another protein involved in the vesicle fusion process called Munc18-1 which is associated with syntaxin (another t-SNARE) (42) and occurs in a SCZ mouse model (43); however, its function remains to be elucidated.

Recently, neuroinflammation and the interplay between the immune system and neurons has been identified as a crucial player in the pathogenesis of SCZ. Interestingly, microglia, the resident macrophagic population of the brain, are not only relevant to a proper immune answer, but also in the synaptic pruning process that naturally occurs during brain development (44). This process is regulated by the complement system factor C4, a part of the innate immune system. C4 labels synapses for degradation and in SCZ variations can occur leading to increased C4 expression and hence to excessive synapse elimination (45–49). A crucial role of an inflammatory response is the production of cytokines which are signaling molecules such as interleukins (ILs), interferons (IFN) or tumor necrosis factors (TNF). They are produced by different cells in the brain like microglia, astrocytes, neurons, and T cells, and influence a variety of processes which, if dysregulated, can contribute to the pathogenesis of SCZ (50,51).

Despite the existence of several hypotheses, the underlying cause of SCZ is far to be unraveled. As mentioned before, SCZ is likely to be multifactorial, meaning that there is a close interplay of environmental circumstances and a genetic predisposition. However, the identification of a clear genetic component still requires a lot of research to get any conclusive information because, thus far, there have been several genes associated to SCZ (e.g. by genome-wide association studies (GWAS)) that can be considered susceptibility genes. Nonetheless, it is unclear if there is any common gene or gene cluster alteration which is mandatory for the manifestation of SCZ. In this sense, mutations of many genes have been reported by clinical studies, but the combinations of affected genes vary strongly between SCZ patients.

Although there is no clear common genetic base underlying SCZ, several susceptibility genes have been identified such as disrupted-in-schizophrenia 1 (*DISC1*). A mutation of *DISC1* in

SCZ patients was first described in a Scottish family (52–54). This protein is involved in many processes essential for neuronal function like transport of synaptic vesicle precursors, mitochondria motility, calcium regulation and synaptic transmission (55). It has been observed that a *DISC1* mutation leads to a differential expression of synaptic proteins such as synapsin (SYN) 1 and synaptophysin (SYP) leading to altered function of the compartment (56). Furthermore, Ankyrin 3 (*ANK3*) has also been identified as a risk gene associated with SCZ (57). *ANK3* encodes for Ankyrin G (ANKG) a characteristic protein located in the axon initial segment (AIS), which is an important structure between the soma and the axon of a neuron and a key element in action potential initiation and regulation of neuronal excitability (58,59). Besides these two examples, other susceptibility genes have been identified for example dysbindin (60–62), neuregulin-1 (*NRG1*) (63), and proline dehydrogenase (*PRODH*) (64) indicating the large variety of genetic influences that might be involved in the causality of SCZ.

3.2 Genetic landscape on 3q28 gene locus

The human genome is encoded as deoxyribonucleic acid (DNA) and can be categorized in the nuclear genome and the mitochondrial genome. The human nuclear genome consists of 23 chromosome pairs contained in cell nuclei and encodes the vast majority of the genes compared to the mitochondrial genome. Over two decades ago, the human genome was started to be deciphered in context of the “Human Genome Project” (HGP) and to date, the entirety of the human genome is sequenced and researchers identified just under 20,000 protein-coding genes and their location (65).

Genes are mapped to a specific location on a specific chromosome (Figure 2). Thus, to name a location of a gene, chromosomes are numbered consecutively (chromosome 1-22, the so-called autosomes) and sex chromosomes are designated by X or Y, which is the first information in the locus' name. Next is the information about the arm of the chromosome which is either the short arm indicated by “p”, or the long arm indicated by “q”. Lastly, the cytogenic region or band on the indicated arm is given as a number and sub-bands can be indicated with a following decimal number.

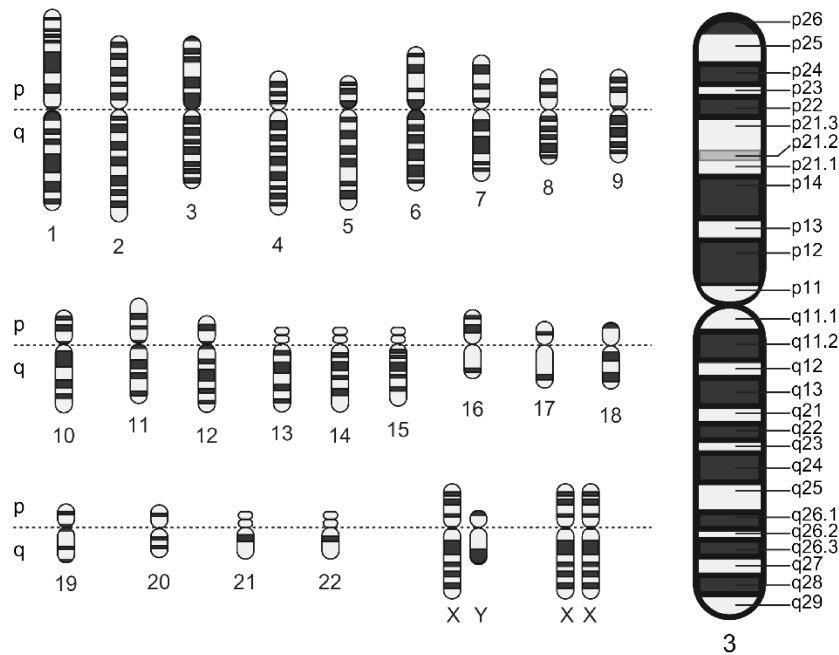


Figure 2: Schematic karyogram

23 chromosomes representative for the human chromosomal pairs are depicted schematically with the proper nomenclature; consecutive numbers or X/Y to identify the chromosome plus indication of short (p) or long (q) arms. On the right side a scheme of chromosome 3 can be seen with labeled cytogetic bands and exemplary sub-bands, indicated by decimal numbers. Created with BioRender.com

In summary, 3q28 is a locus on the long arm of chromosome 3 band number 28. On this specific locus about 40 genes are encoded (Table S1 in Appendix), some of which are relevant for CNS functions and development and others play a more important role in the periphery. Knowing which genes are located on each cytogetic band is of great convenience for deducing candidate genes to investigate once chromosomal aberrations were identified. In terms of relevance for neuronal development and function, two genes on locus 3q28 are especially interesting for this project, namely interleukin-1 receptor accessory protein (*IL1RAP*) and osteocrin (*OSTN*). Their function will be presented in more detail in the following sections.

3.2.1 Central nervous system (CNS) immunity

The brain used to be described as an immune-privileged organ that is separated from the peripheral immune system. However, in the last decades, it has been demonstrated that the brain is capable to elicit an immune response that -if dysregulated- could disrupt the homeostasis of the CNS, thus contributing to neurodegenerative disorders or altering the correct development of the brain. Consequently, nowadays the brain is regarded as a specially immune-controlled organ rather than an immune-privileged one (66). The brain is guarded from systemic insults by the blood-brain barrier (BBB) which prevents infiltration by peripheral immune cells, toxins, and pathogens. Further, the BBB is also involved in the tight regulation

of brain homeostasis by controlling movements of ions and cells between the blood and the brain (67). This fortification of the CNS is a highly useful security measure but admittedly can for instance complicate drug delivery to the brain (67). However strict this compartmentalization may be, there is bidirectional communication between the CNS and the periphery. The cerebrospinal fluid (CSF) and the meninges are in direct contact with the lymphatic system (68–70) and the skull bone marrow as a site of immune cell production (71,72). Moreover, messengers of the immune system like cytokines or interleukins (ILs) can cross the BBB, transmit information, and influence CNS-relevant processes. Indeed, cytokine signaling can lead to a temporal increase of the BBB permeability and induce the recruitment of peripheral immune cells into the brain to elicit a proper immune response (73–75). Furthermore, microglia as well as astrocytes and neurons can produce cytokines in the brain which can then in turn relay information to the periphery (75–79). Generally, cytokines are divided into two major groups: proinflammatory cytokines that facilitate further activation of immune cells and production of more cytokines, and anti-inflammatory cytokines that inhibit or interrupt the activation of immune cells. However, cytokines and other mediators of the immune response are far more than a defense mechanism against pathogens but are involved in the physiological and in the developmental processes of the healthy brain. In this sense, CD4⁺ T cells have been shown to be necessary for maintaining cellular plasticity for the neurogenesis in the HC or that a T cell deficiency leads to cognitive (e.g. spatial memory) and behavioral impairments and reduced brain-derived neurotrophic factor (BDNF) production in animal models (80–83). T cells also take on regulatory functions by producing anti-inflammatory cytokines hence showing neuroprotective effects (84). Further, IL-17, a strong proinflammatory cytokine, enhances glial BDNF production, influences plasticity of glutamatergic synapses and α -amino-3-hydroxy-5-methyl-4-isoxazole propionic acid receptor (AMPA)/NMDAR ratio and short-term memory, and was shown to play a role in the regulation of anxiety-like behavior (85,86). IL-6, in parallel to its proinflammatory activity, can inhibit LTP and short-term potentiation and acts as neurotrophic factor in dopaminergic neurons, induces neuronal differentiation, influences GABAergic signaling and neuronal excitability in the amygdala, regulates expression of proteins related to synaptic function and is involved in sleep regulation and theta activity (87–91). Another proinflammatory cytokine, interferon γ (IFN γ), was also shown to be involved in social behavior and neuronal connectivity by activating GABAergic neurons which delays seizure onset, reduces seizure severity and prevents aberrant hyperexcitability/hyperconnectivity in the PFC (92). Likewise, anti-inflammatory cytokines play important roles other than limiting the immune response. IL-13 stimulates astrocytes to increase their glial fibrillary acidic protein (GFAP) levels and produce BDNF and is shown to be essential for the working memory and reference memory (93). IL-4 as well induces BDNF production in the HC thereby supporting spatial memory formation and lack of IL-4 has

negative impacts on cognition. Moreover, IL-4 is an important regulator of microglia activity by switching their phenotype to the protective M2 state which leads e.g. to enhanced neurite outgrowth after an injury (94–96).

3.2.2 Interleukin-1 beta and its multifaced signaling pathway

Another well-studied cytokine is IL-1 β that, likewise other mediators of the inflammatory response, albeit being mostly known as a proinflammatory cytokine, has a variety of effects on the brain that will be summarized in this paragraph

IL-1 β is probably one of the most studied cytokines and is involved in various physiological processes. First, there are functions involved in the immune response, such as the initiation of sickness behavior and -usually in combination with IL-6- the induction of a fever (97,98). IL-1 β signaling promotes the amplification of the inflammatory signals within the body, through the production of ROS (99) and inducible nitric oxide synthase (iNOS), expression of more proinflammatory factors such as IL-1 β itself, IL-6 and TNF α (100,101). Furthermore, IL-1 β signaling increases prostaglandin E2 (PGE2) levels (101), activates microglia (102), promotes glial scar formation (101) and migration of immune cells (73). It can prime dendritic cells (73) and is involved in T cell activation (103).

The IL-1 family consists of 11 proteins encoded by 11 genes (104–106) and members of this family predominantly control proinflammatory responses. The most commonly known members are likely IL-1 α and IL-1 β which share a very high similarity in their functions. These two cytokines are produced as pro-proteins that are then cleaved by calpain, granzyme B for IL-1 α (107,108) or caspase-1 (CASP1), formerly known as IL-1 β -converting enzyme, for IL-1 β (109–111) into the mature forms that can be secreted (112,113). Once secreted, IL-1 α and IL-1 β bind either IL-1 receptor 1 or 2 (IL-1R1, IL-1R2 respectively). Binding of IL-1 β to IL-1R1 leads to a conformational change of the IL-1R1 protein and marks the beginning of its signaling cascade (Figure 3). The conformational change initiates the recruitment of IL-1 receptor accessory protein (IL-1RAP) and IL-1 β , IL-1R1 and IL-1RAP form a trimeric complex. Now this complex recruits myeloid differentiation primary response 88 (MYD88) and interleukin-1 receptor-activated protein kinase (IRAK) 4 (114,115). The autophosphorylation of IRAK4 enables the phosphorylation of IRAK1 and IRAK2 (116). Then TNF receptor associated factor 6 (TRAF6) is recruited and oligomerizes with IRAK1 and IRAK2 forming a complex which then dissociates from the receptor. This complex associates with transforming growth factor β (TGF β)-activated kinase 1 (TAK1) and TAK1-binding proteins 1 and 2 (TAB1/2) and TRAF6 gets ubiquitinated and TAK1 is phosphorylated.

Introduction

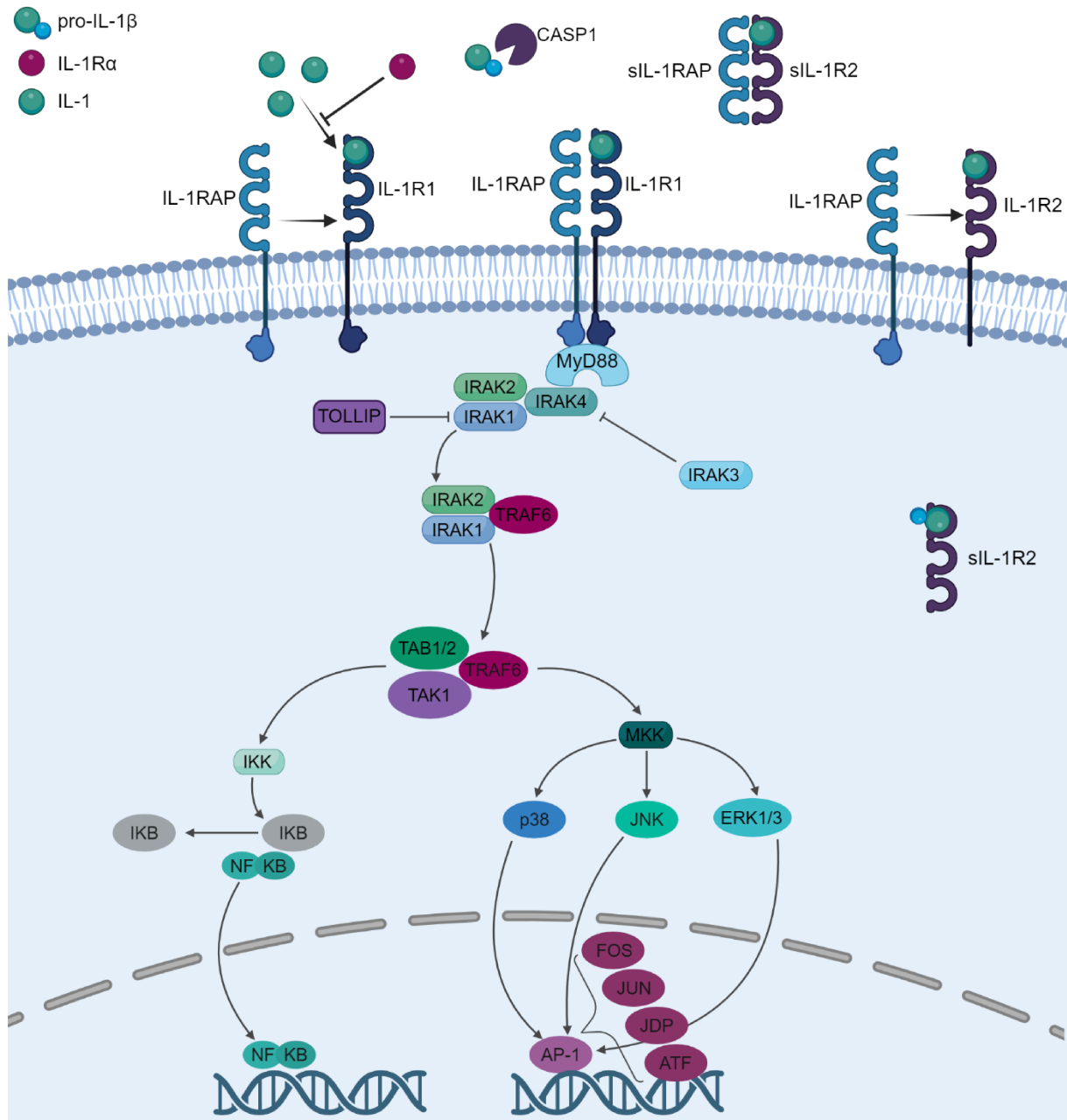


Figure 3: Schematic depiction of IL-1 signaling pathway

IL-1 signaling starts with the cleavage of e.g. pro-IL-1 β to IL-1 β by CASP1 and subsequent binding of IL-1 β to its receptors, while all forms of receptor type 2 are decoy receptors and do not initiate further signaling. If IL-1R1 is bound, IL-1RAP is recruited and the signaling cascade is started by recruitment of MYD88 followed by the activation of IRAK4, IRAK1 and IRAK2. IRAK1 and 2 form a complex with TRAF6 which recruits TAK1 and TAB1/2. From here on either disinhibition of NF κ B by IKK activation and I κ B degradation or AP-1 activation via MKK mediated activation of JNK, ERK1/3 or MAPK p38 can initiate IL-1-responsive gene transcription. Created with BioRender.com

From here on, two main paths can conduct the signaling. On the one hand, phosphorylated TAK1 can activate inhibitor of nuclear factor kappa-B kinase (IKK) which in turn phosphorylates the inhibitor of nuclear factor kappa-B (I κ B) and leads to its degradation. Subsequently, previously bound nuclear factor kappa-B (NF κ B) is now able to migrate into the nucleus and start transcription. The second signaling path proceeds by TAK1 mediated activation of mitogen-activated kinase kinases (MKK) which activate mitogen-activated kinase (MAPK) p38,

c-Jun N-terminal kinases (JNK) and extracellular signal-regulated kinases (ERK). These kinases activate members of the activator protein-1 (AP-1) family which are transcription factors such as C-FOS, C-JUN, activating transcription factor (ATF) 2 and Jun dimerization protein (JDP), thereby initiating expression of IL-1 responsive genes encoding for IL-1 (positive feedback loop), IL-6, IL-8, I κ B α , monocyte chemoattractant protein 1 (MCP1) or cyclooxygenase 2 (COX2) (114,115).

IL-1 signaling can be regulated on several levels. The first instance is an endogenous IL-1R antagonist (IL-1Ra) which binds the IL-1R1 in a competitive manner but does not start the signaling cascade. Another regulatory instance is an alternative IL-1 receptor. The IL-1R2 is a decoy receptor which lacks the Toll-IL-1 receptor (TIR) domain (117) and hence fails to initiate a downstream response to its binding (118–121). This receptor exists in a membrane-bound and soluble (sIL-1R2) form which is also true for the co-receptor IL-1RAP (sIL-1RAP) (122,123). If IL-1 binds the membrane-bound IL-1R2, IL-1RAP is recruited and a complex is formed without initiating further signaling but it reduces the amounts of IL-1 and IL-1RAP available to bind to IL-1R1. An intracellular version of the sIL-1R2 is able to bind even pro-IL-1 β thereby preventing the generation of mature IL-1 β by CASP1 reducing the probability of IL-1R1 activation (124,125). Additionally, if extracellular sIL-1R2 associates with sIL1RAP the binding affinity of the sIL-1R2 for IL-1 increases significantly without increasing its binding affinity to IL-1Ra (126). In general, IL-1R2 binds IL-1Ra with a significantly lower affinity compared to IL-1R1 (121,125). Other regulators of the IL-1 pathway are IRAK3 which inhibits the dissociation of IRAK1 and IRAK2 from the receptor complex and prevents the assembly with TRAF6 (127–130), toll interacting protein (TOLLIP) that inhibits the phosphorylation of IRAK1 and supports the degradation of internalized IL-1R (131–133) or a truncated form of MYD88 (134).

Other than the immunological context, IL-1 β contributes to a large number of processes outside the “classic” inflammation context but in the immune cell-independent healthy or pathophysiological setting, ranging from developmental influences to its involvement in daily processes in the brain.

During the development of the brain IL-1 β increases the expression of WNT5A which acts as a repulsive agent in axon guidance. Furthermore, IL-1 β stimulates the migration of cultured cortical neurons and increases the expression of neurotrophin 3 (NT3) and neurogenin 1 (NGN1) which promote neurite outgrowth (135,136). Every signaling molecule underlies a tight balance especially during development. However, if this balance is disturbed it can have wide-ranging consequences. IL-1 β levels can be increased by e.g. a maternal infection, which can contribute to a delayed switch of excitatory GABA to inhibitory GABA signaling (Figure 4A). This delayed switch increases the vulnerability for seizures in the adult brain. The GABA switch

is directed by a tightly controlled expression of potassium-chloride cotransporter 2 (KCC2) and neuronal Na-K-Cl cotransporter 1 (NKCC1), changing from high expression of NKCC1 and low expression of KCC2 to low expression of NKCC1 and high expression of KCC2. IL-1 β increases the expression of two KCC2 gene expression modulators, neuronal repressor gene RE1-silencing transcription factor (REST) and transcriptional repressor methyl CpG binding protein 2 (MECP2), and that way has an impact on KCC2 levels (137,138).

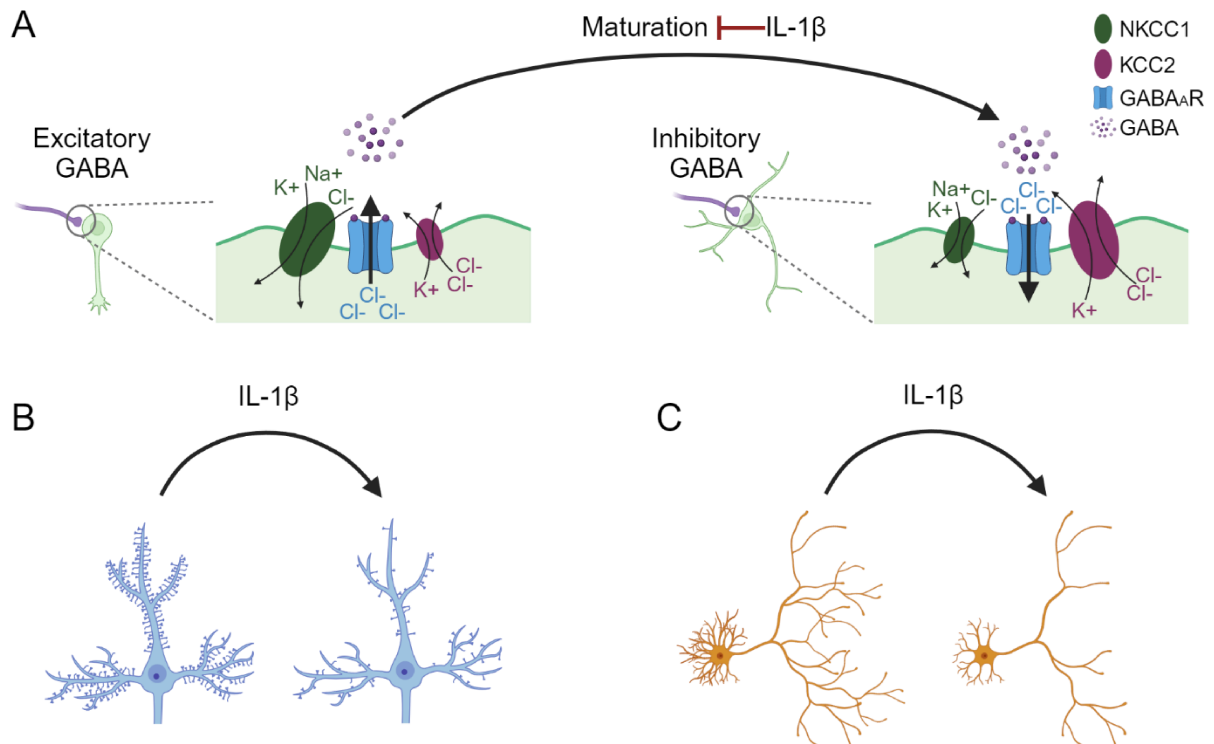


Figure 4: Effects of IL-1 β on neurons

Three major effects of IL-1 β on neurons in the brain have been described. Exposure of neurons to IL-1 β during **A**) early brain development can delay the GABA switch from initially excitatory GABA signaling to inhibitory GABA signaling in mature neurons. Further, IL-1 β exposure leads **B**) to a reduction of spines and **C**) to a reduced ramification of neurons. Created with BioRender.com

Processes that occur constantly in the brain like learning and memory formation, spine and synapse formation, modulation of transmission and neuronal ramification, are also impacted by IL-1 β . Depending on the amount of the agonist, the cytokine exerts different influences on different targets. Therefore, a low dose of IL-1 β can promote pro-survival effects and be beneficial for memory formation, however any deviation from physiological levels can disturb the system (139,140). For example, a low dose of IL-1 β has been described to inhibit voltage-gated Ca²⁺-currents, reduce intracellular Ca²⁺ in synaptosomes and reduce transmitter release while a high dose on the other hand reduces AMPARs on the surface and increases glutamate and GABA release which affects depolarization of neurons. Another effect of low doses was shown to be an increase of NMDAR-mediated Ca²⁺ levels by activating tyrosine kinase and NMDAR subunit 2B (NR2B) overall impacting the receptor landscape and subunit composition (141,142). Hence, increased IL-1 β signaling can modulate the glutamate response and lead

to a hyperactivation of NMDARs and AMPARs and an overall hyperexcitability (143,144). Furthermore, high IL-1 β reduces glutamate uptake by astrocytes, impairing the clearance of this potentially excitotoxic neurotransmitter (145). Increased IL-1 β signaling can potentiate its own signaling by increasing expression and insertion of IL-1R1 and IL-1RAP, laterally translocating IL-1R1 at the postsynapse or stabilizing existing IL-1R1 and therefore increase IL-1 β sensitivity (143). These processes can impact cortical synapse function and structure and induce loss of mature spines and synapses (Figure 4B), by an increase in the frequency of spontaneous excitatory post-synaptic currents (sEPSCs) and subsequent risk of excitotoxicity (144–146). A pathway linked to spine loss was shown to be the mammalian target of rapamycin (mTOR) pathway and elevated levels of MECP2 which were shown to be reduced by IL-1Ra (147). Another major effect of IL-1 β signaling is the adjustment of neuronal morphology (Figure 4C). Prolonged IL-1 β signaling impairs expression of proteins like BDNF, nerve growth factor (NGF), activity-regulated cytoskeleton-associated protein (ARC), cAMP-response element binding protein (CREB), cofilin, neurofilament light polypeptide (NFL), neurofilament medium chain (NFM), neurofilament heavy chain (NFH) and proteolipid (PLP) that are involved in neuronal morphology and synaptic plasticity (147–149). Overall, all these IL-1 β mediated effects on the brain result in inhibition of LTP formation, impairment of memory consolidation, impairment of long-term, short-term, and spatial memory, deficiency in contextual fear conditioning and spatial navigation learning (97,102,149–154). IL-1 β signaling can influence sleep regulation, mood control and social behavior (negative symptoms) and if active in the cerebellum induces motor deficits (98,145,155). Lastly, SCZ has been associated with and show elevated plasma and CSF levels of IL-1 β (98,155,156). This hints towards at least temporary neuroinflammation in SCZ, that could lead to an imbalance of the various functions and effects IL-1 β has on the brain, which likely contributes to the disease onset.

3.2.3 Interleukin-1 receptor accessory protein and Interleukin-1 receptor accessory protein like 1

An essential component of the IL-1 signaling pathway is the interleukin-1 receptor accessory protein (IL-1RAP) which is encoded by one of the two candidate genes on locus 3q28 chosen for this thesis. IL-1RAP is a co-receptor for the IL-1R1 that is essential for successful IL-1 signaling initiation (more detailed pathway description in previous section) (77,157). IL-1RAP occurs in a membrane-bound (here referred to just as IL-1RAP) and two soluble (sIL-1RAP) isoforms: sIL-1RAP and sIL-1RAP β (158) and the soluble forms seem to take on mainly regulatory functions in the IL-1 signaling pathway (122,123). Moreover, there is IL-1RAPb, a fourth isoform that is exclusively present in the CNS which has C-terminal alterations in the toll-interleukin-1 receptor (TIR) domain (159). Beyond its role in the canonical IL-1 signaling,

IL-1RAP fulfills further purposes that are linked to neuronal development and synaptogenesis. It has been shown that a nonsense mutation found in a Chinese family with SCZ, leads to inhibition of neuronal growth (axonal and dendritic) and IL-1 β -induced JNK activation during early development (160). In contrast to IL-1RAP, IL-1RAPb is not induced by IL-1 β and promotes pro-survival functions. During aging, IL-1 β levels increase and thus increase the expression of IL-1RAP which potentiates the IL-1 β responsiveness which in turn leads to suppression of LTP formation and memory impairments (161). IL-1RAP and IL-1RAPb are involved in the process of synaptogenesis where they function rather as trans-synaptic cell-adhesion molecules than co-receptors. To be able to exert the synaptogenic function an interaction with protein tyrosine phosphatase (PTP) δ has to take place. Through this interaction, post-synaptic differentiation is induced and IL-1RAP mediates accumulation of bassoon (pre-synapse) and IL-1RAPb stimulates bassoon puncta accumulation as well as dendritic spinogenesis regulating synapse formation bidirectionally (162).

At the postsynaptic compartment, another cell adhesion molecule IL-1RAP like 1 (IL-1RAPL1) has been identified which is very similar and fulfills similar functions as IL-1RAP but is encoded on the X chromosome. Mutations in this gene are associated with autism spectrum disorders (ASD) and intellectual disability (ID). IL-1RAPL1 interacts with PTP δ and is involved in synapse formation, differentiation and stabilization, and neuronal ramification (163,164). Furthermore, IL-1RAPL1 interacts with and regulates localization of postsynaptic density protein 95 (PSD95), positively regulates spine density, influences the activity of voltage-gated Ca²⁺-channels and has therefore an influence on behavior and memory formation (165,166). During cerebellar development IL-1RAPL1 controls the inhibitory network and plays a role in establishing an excitatory/inhibitory balance (167).

In conclusion, the effects on the brain exerted by IL-1 β signaling are very diverse and strongly dependent on the brain area, type of target cell, duration and concentration of IL-1 β exposure resulting in a very intricately regulated system.

3.2.4 Osteocrin and its dual role in the periphery and the brain

In the early 2000s, a novel bone-derived, secreted protein was discovered by Thomas and colleagues and, due to its origin, was named osteocrin (OSTN) (168). In 2004, musclin was identified as a skeletal muscle-derived secretory factor by Nishizawa et al. (169), which turned out to be the same protein as OSTN, hence the alternative names reflecting their tissues of discovery. First, *OSTN* was described to be expressed mainly in bones, specifically in osteoblasts in the growth plate and chondrocytes (168,170,171), but also in skeletal muscle, heart, testes and kidneys albeit at lower levels (168,169). OSTN is a small peptide with an estimated size of 11.4 kDa in its mature form but the protein exhibits two dibasic cleavage sites where posttranslational modifications can take place (168,169). *OSTN* is expressed in an age-related pattern and is especially high during prenatal development and in the early postnatal phase (168,172). At later stages of development, in the periphery, specific stimuli lead to an activation of *OSTN* expression such as mechanical strain like exercise (173,174), food intake (169,175) or possible influences of hormones such as insulin, vitamin D₃ and estrogens (168,169,171). On DNA level, regulators of *OSTN* expression are forkhead box protein O1 (FOXO1) (173–175), runt-related transcription factor 2 (RUNX2) and osterix (OSX) (176) which function as *OSTN* repressors in the periphery.

OSTN is a peptide that is secreted (168,169,174) auto- or paracrinally and has a high binding specificity for the natriuretic peptide receptor C (NPRC) (170,177). The NPRC is responsible for the clearance of natriuretic peptides (NPs) (178) such as atrial natriuretic peptide (ANP), C-type natriuretic peptide (CNP) or brain natriuretic peptide (BNP). NPs bind NPRC and are internalized into the cell and get degraded (Figure 5) (179). However, it has been suggested that NPRC is not only a clearance receptor but is coupled to an inhibitory G-protein which can inhibit adenylyl cyclase and thus limit cAMP in the cell (180–185). The high binding affinity of OSTN to NPRC leads to a competitive supersession of NPs at the NPRC which technically inhibits NP clearance and thus leads to an enrichment in NPs. In turn, NPs can bind natriuretic peptide receptor A or B (NPRA or NPRB) (Figure 5) which are coupled to a guanylyl cyclase (GC) that transforms guanosine triphosphate (GTP) into cyclic guanosine monophosphate (cGMP) (186–188). Increased levels of cGMP activate protein kinase G (PKG), a serine-threonine kinase (189), which potentially phosphorylates transcription factor CREB. Finally, phosphorylated CREB initiates transcription in the nucleus.

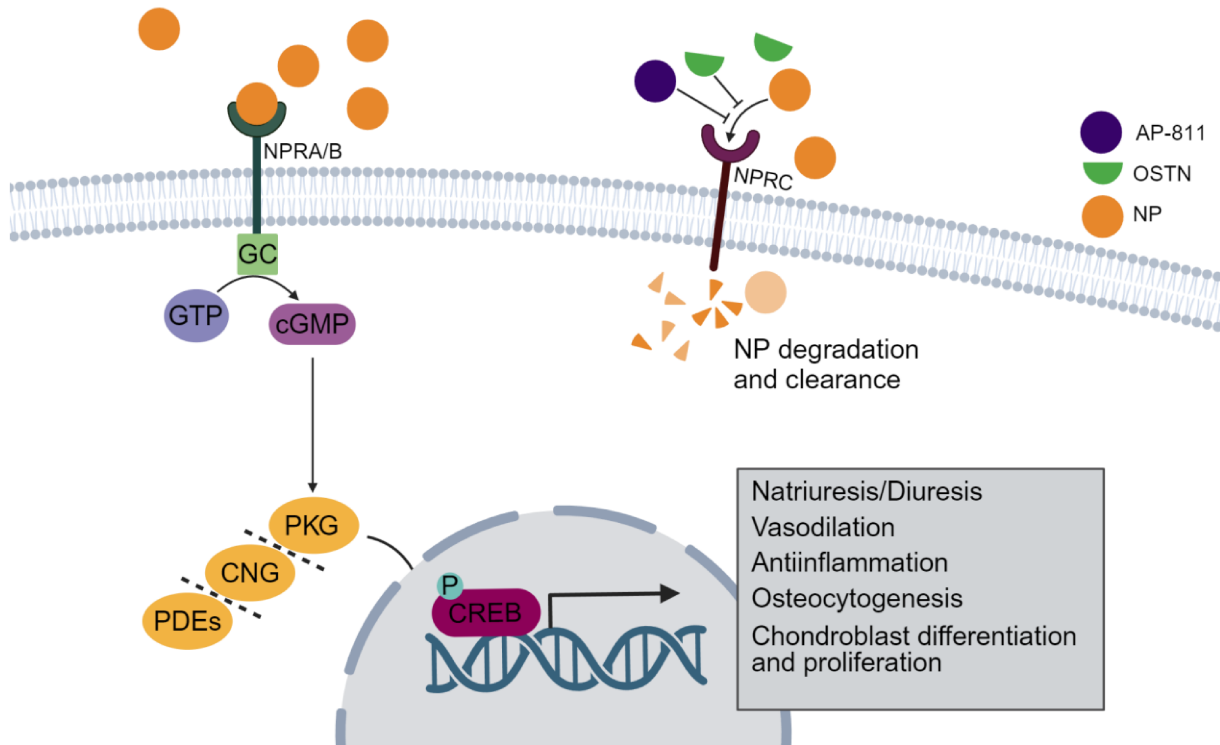


Figure 5: Schematic overview of NP pathway and predicted mode of action of OSTN

OSTN is described to have a high affinity for NPRC which is a clearance receptor for natriuretic peptides (NP). Without OSTN, NP bind natriuretic peptide receptor C (NPRC) and are internalized and degraded and cleared and the receptor gets recycled. OSTN binds NPRC in a competitive manner, blocking NP clearance and thus increasing the amount of available NP which in turn can bind to natriuretic peptide receptor A or B (NPR A/B). NPR A/B are guanylyl cyclase (GC) coupled receptors that transforms GTP into cGMP upon ligand-binding. CGMP production activates PKG that potentially phosphorylates CREB which activates transcription. Downstream effects of the NP pathway are amongst others, osteocytogenesis, chondroblast proliferation and differentiation. Another (artificial) NPRC inhibitor is AP-811 which should likewise compete with NPs and OSTN for the receptor. Created with BioRender.com

To date, it seems the effects exerted by OSTN are due to enrichment of NPs by blocking NPRC although it is suspected that there might be another receptor for OSTN which remains to be elucidated (190). Hence, the effects that can be observed upon *OSTN* expression are diverse (Figure 6) spanning various tissues. Looking at the initially researched tissues like skeletal muscle, *OSTN* is induced upon exercise and improves muscle endurance and increases mitochondrial protein content (174), in bones it is expressed especially in the growth plate driving bone growth, terminal differentiation of osteoblasts and regulating cartilage formation (168,170,171,177,190,191). Furthermore, OSTN was shown to mediate anti-inflammatory effects in tissues like heart, liver and kidney by inhibiting i.e. IL-1 β and TNF α synthesis, reducing leukocyte infiltration, trigger a rise of anti-inflammatory cytokine IL-10, reducing production of ROS by preventing the downregulation of superoxide dismutase (192–194) and have cardio- and renoprotective effects (192,193,195,196). Further general effects of NPs (not investigated in context of OSTN) are the regulation of systemic fluid homeostasis (natriuresis, diuresis) (197,198), vasodilation and blood pressure (199).

Introduction

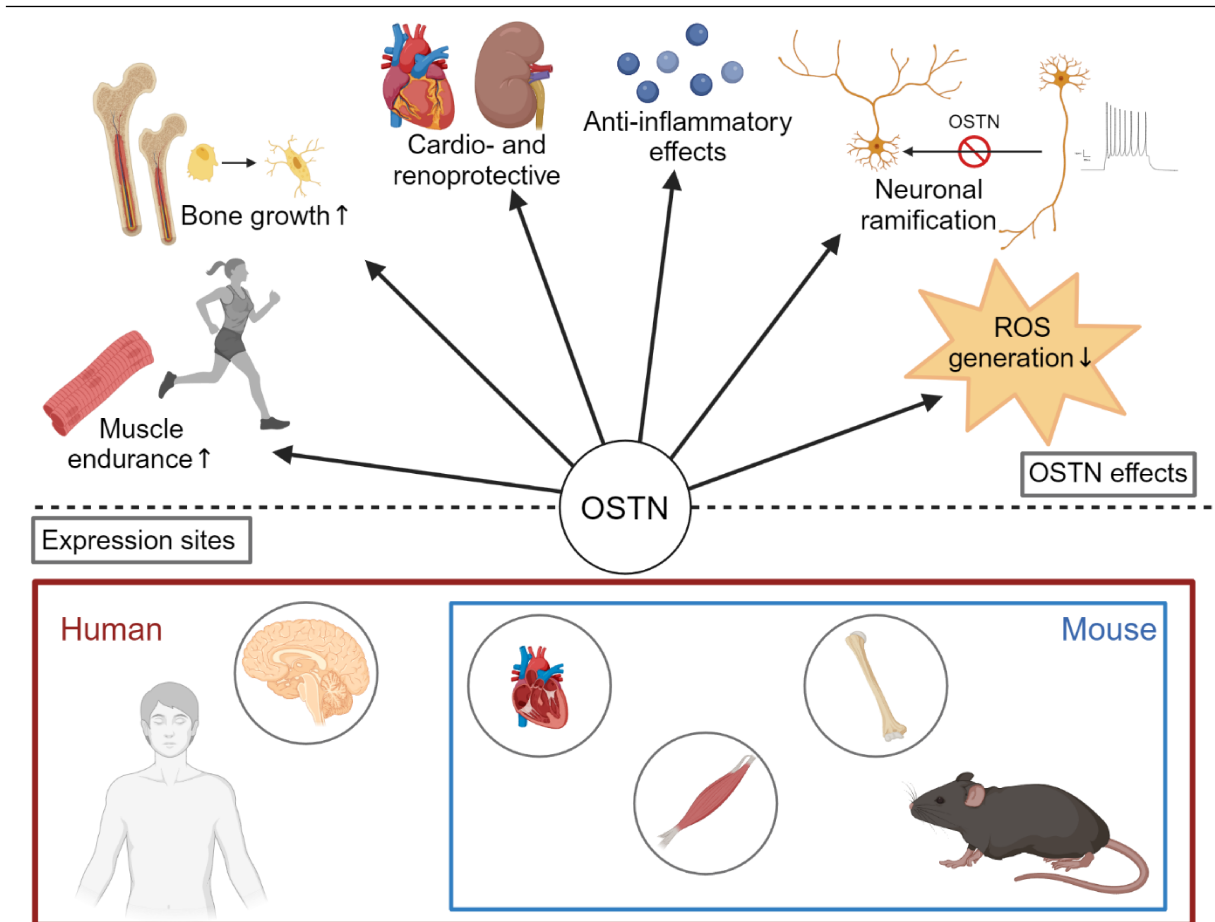


Figure 6: Schematic overview of OSTN expression sites and effects on different tissues

It has been shown that OSTN is mainly expressed in bones, skeletal muscle and heart muscle in a large variety of species but only in human and some anthropoid apes, OSTN has been repurposed and is expressed in the brain as well. The effects driven by OSTN expression vary between the tissues. The initially uncovered functions of OSTN are an improvement of muscle endurance and its role in bone growth, osteoblast and chondrocyte proliferation and differentiation. It is further described that OSTN has cardio- and renoprotective effects, exerts anti-inflammatory effects and has the capacity to reduce ROS production. Lastly, the human-specific expression of OSTN in the brain has a limiting effect on neurite ramification. Created with BioRender.com

As indicated in Figure 6, another tissue expressing *OSTN* is the brain, however this is exclusive for humans and apes. Other generally used model species such as mice and rats show no expression of *Ostn* in the brain, which suggests an exclusive repurposing of OSTN in the human brain. In 2016, Ataman and colleagues showed *OSTN* expression in primates' visual cortex and human-derived neuronal cell cultures (hiPSC-derived and primary human fetal brain cultures). They identified neuronal activity as the initiator of *OSTN* expression and attempted to clarify as to why the repurposing is exclusive for humans and primates (172). The human *OSTN* gene has three enhancer regions which are specific for the myocyte enhancer factor 2 (MEF2). Of these MEF2 responsive elements (MRE), only one is present in the mouse *Ostn* gene, which may be the reason why neuronal activity only induces *OSTN* expression in humans or apes. Furthermore, OSTN seems to be present mainly in the neocortex, specifically in special AT-rich sequence-binding protein 2 (SATB2)⁺, vesicular glutamate transporter 1

(VGLUT1)⁺ and COUP-TF-interacting protein 2 (CTIP2)⁻ neurons and although during early development *OSTN* expression is at a higher level before synaptic connections are fully established, in a more mature system *OSTN* production is driven by neuronal activity. The effect of the secreted *OSTN* on neurons is a limitation of neuron growth (Figure 7), which can be observed with smaller soma sizes and lower ramification of neurites upon *OSTN* expression (172). NPRC, the *OSTN* receptor in the periphery, is also widely expressed in the brain (200,201), however it is still unclear if another receptor is involved in the *OSTN* signaling as well. Thus far it is assumed that the effects of *OSTN* are mediated by its binding to NPRC and a consecutive increase of NPs in the brain. Research in rat hippocampus has shown an influence of CNP on neuroplasticity, namely NMDARs, GABA_A-mediated inhibition and on LTP and long-term depression (LTD) by increasing the frequency-dependent threshold for LTP formation (202). ANP and BNP are shown to have neuroprotective effects in the cortex (203,204) and in the retina of rats by reducing NMDA-mediated excitotoxicity (205). To this day, there are no further insights about *OSTN* in the brain and its effects. Also, up until now, *OSTN*, or 3q28 deletion, has not been associated with SCZ.

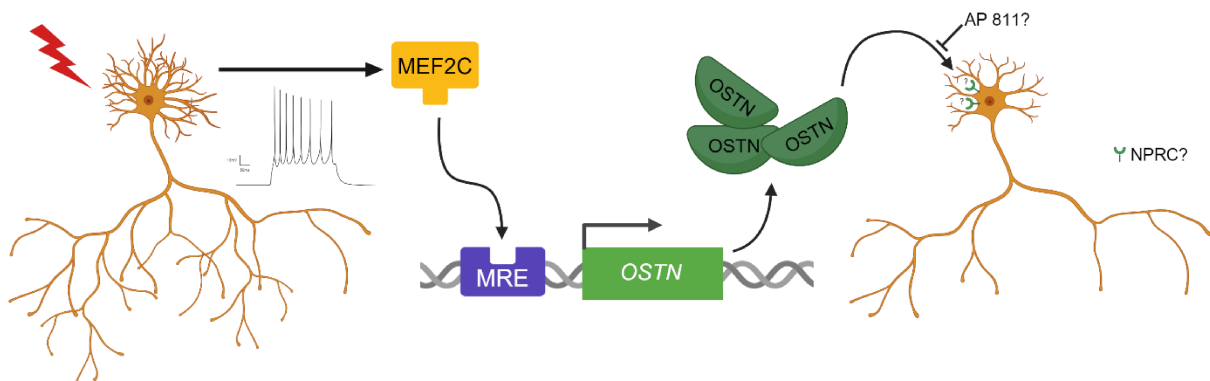


Figure 7: Hypothesized mode of action of *OSTN* in the brain

Upon high neuronal activity MEF2C binds to the MREs and initiates expression of *OSTN*. After protein synthesis, *OSTN* is secreted in an auto- or paracrine manner and binds NPRC or another unknown receptor. Binding of NPRC leads to a limitation of neurons' complexity, likely by an increase in NPs after inhibiting NP clearance. Created with BioRender.com

3.3 Stem cell technology

3.3.1 Human induced pluripotent stem cells (hiPSC) – potentials and limitations

Almost two decades ago, Shinya Yamanaka and colleagues developed a method to reprogram somatic cells into pluripotent stem cells. This discovery marked a major breakthrough in the field of stem cell research, opening a wide range of opportunities with less ethical controversy compared to the previous research focused on embryonic stem cells. The Yamanaka laboratory developed a protocol to turn skin fibroblasts into pluripotent stem cells by introducing

the so-called Yamanaka factors. These factors are the four transcription factors octamer-binding transcription factor-3/4 (OCT3/4), sex-determining region Y-box2 (SOX2), krüppel like factor-4 (KLF4) and C-MYC which were delivered by a retroviral system (206). The resulting pluripotent cells are defined by self-renewal and their capacity to bring forth cell types from all three germ layers (Figure 8). Yamanaka and colleagues first established the protocol with mouse fibroblasts and about a year later with human skin fibroblasts (207). Other than fibroblasts, also peripheral blood mononuclear cells (PBMCs) are used for reprogramming due to easy accessibility and minimal discomfort for the donors.

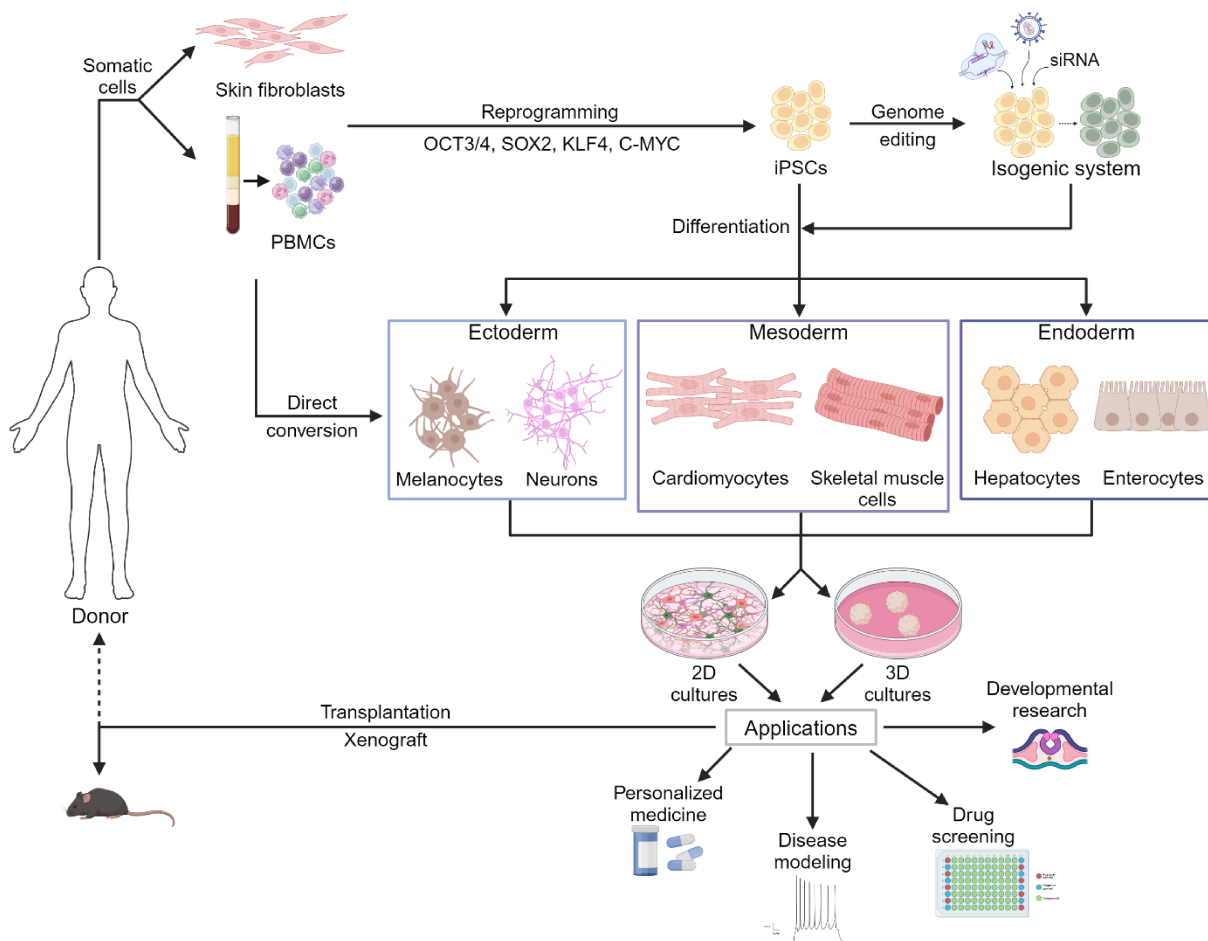


Figure 8: Schematic depiction of working sequence of obtaining hiPSCs and the experimental opportunities

First either healthy individuals or patients are recruited as donors, then somatic cells are obtained by either a skin punch or, more common today, by drawing a blood sample. From these cell donations either skin fibroblasts or peripheral blood mononuclear cells (PBMCs) are isolated and cultured in vitro. Cells are now reprogrammed by introducing the Yamanaka factors. HiPSCs can now be genetically modified with gene editing tools or be directly differentiated into all three germ layers in 2D or 3D cultures which can then be used for different research applications. Created with BioRender.com

Furthermore, non-integrating vectors such as sendai virus are now preferred to retroviral systems. Transduction of somatic cells with sendai viral vectors offers the advantage of a reprogramming process without the integration of the viral nucleic acids into the cell's genome, thus preventing any disruptions of the original genome (208). This renders the obtained hiPSCs

and their derivatives more reliable and safer for many research applications. Following the reprogramming process, the resulting hiPSCs usually undergo several quality control steps. Firstly, cells are tested for remnants of viral genome by polymerase chain reaction (PCR). Further, cells are tested for their pluripotency by immunofluorescence (IF) staining for pluripotency marker expression such as OCT3/4, SOX2, NANOG, stage specific embryo antigen 4 (SSEA4) or TRA1-60; and their differentiation capacity to determine if cell types of all three germ layers can be generated. Lastly, single-nucleotide polymorphism (SNP) karyotyping provides information about the chromosomal integrity of the cells (208). Hence if aberrations on chromosomes occur, the somatic donor cells are checked to determine if it is a donor-specific aberration or was introduced by the reprogramming process. This can also provide insight into interesting genetic research targets to investigate further.

In general, hiPSCs provide researchers with a human *in vitro* model system applicable in various research branches due to its capacity to differentiate into every cell type (Figure 8). Over time protocols have been developed to obtain numerous cell types of all germ layers such as hepatocytes, enterocytes, various types of neurons, skeletal muscle cells or cardiomyocytes, by application of specific factors and small molecules (209–216). The availability of a self-renewing pool of patient-specific cells and the diversity of derived cell types, diminish the limitations of accessibility, variety, and expansion of primary human cell cultures. Therefore, hiPSCs have become invaluable for *in vitro* disease modeling and pre-clinical drug screening (217–220). Further, hiPSCs show great potential in the field of developmental biology, transplantation research and regenerative medicine (209,215,221–228).

While animal models are giving valuable insight into disease pathomechanisms and potential therapeutic targets, there are always inter-species differences that can lead to vastly different results in animal models compared to clinical trials. The use of a human *in vitro* model has the potential to improve the understanding of e.g. compound-induced effects pre-clinically, to yield higher success rates in clinical trials, hence lessen the gap between animal models and clinical research (229,230). Additionally, a large part of genetic sequences relevant for gene expression are conserved across species, however there is a portion of such sequences that are not conserved. That leads to a species-specific gene expression in terms of tissue-specific expression or even existence of certain genes (231). Issues such as human-specific gene-expression can also be tackled by hiPSC-derived models. Thus, transferability of research results and understanding of underlying mechanisms should greatly improve in the future.

Furthermore, hiPSCs keep the genetic identity of the donor which especially enables research on complex genetic disorders on a personalized level. Especially for disorders with a high variability in symptoms and effective treatments across the population, hiPSCs are tools to

achieve better accuracy in treatment choices facilitating personalized medicine. To this date, several gene editing tools have been developed to change gene expression permanently or temporarily, such as the clustered regularly interspaced palindromic repeats/CRISPR-associated protein 9 (CRISPR/Cas9) or the use of small interfering (si)RNAs (232,233). Genetic manipulation of hiPSCs generates an isogenic system to investigate specific genetic alterations in a human *in vitro* system with various possible cell types.

Over the last years, many protocols have been developed to generate various cell types such as motor neurons, cortical, GABAergic, serotonergic, or dopaminergic neurons as well as several glia cell types like astrocytes, microglia, and oligodendrocytes (213,234–243). To increase the complexity of the model systems researchers designed protocols for co-cultures of different cell types that recreate a more physiological situation (244,245). To up the complexity even more, 3D models like organoids (i.e. cardiac, brain, intestinal organoids) have been engineered that are an even more accurate recapitulation of tissues comprising different cell types and a certain degree of self-organization, especially of early stages of tissue development which is especially interesting in developmental research (246–248). Both 2D and 3D systems are already used for experimental transplantation/xenografts as prospects for personalized cell therapy that should significantly reduce immunoreaction to transplants (215,221,223–227,249).

However, as any model, hiPSC-derived models have their limitations that one must be aware of. On the one hand, *in vitro* models are still limited in complexity as they lack organ systems that metabolize or detoxify, thus do not provide a holistic view as a whole organism would. Further, during the reprogramming process the cells lose the epigenetic memory which was accumulated donor-individually by the somatic cells over time (250). This loss of epigenetic memory poses a challenge when investigating i.e. neurodegenerative disorders or aging processes. Another approach to bypass this issue is the direct conversion of somatic cells into other cell types, skipping the pluripotency stage and mostly preserve the epigenetic memory of the cells (251). Hence, the direct conversion is especially suitable to investigate aging and degenerative disorders (252).

3.3.2 Generation of cortical neurons derived from hiPSCs

After reprogramming of somatic cells into hiPSCs, to maintain the cells' pluripotency and prevent spontaneous differentiation, it is necessary to maintain the stemness of the cell culture with defined culturing media. A simplified medium -named Essential 8 or E8- was developed by Chen et al. in 2011. The base media is DMEM/F12 supplemented with sodium bicarbonate for better pH buffering, L-ascorbic acid that promotes proliferation and selenium which is necessary for culture expansion. In addition, transferrin improves survival especially under hypoxic conditions, insulin and fibroblast growth factor 2 (FGF2) promote proliferation and cell survival and lastly transforming growth factor β (TGF β) activates canonical SMAD signaling and supports a stable long-term culture (253).

Proceeding from this pluripotent state hiPSCs can be differentiated into nearly any cell type. For each cell type, differentiation protocols have been developed over the years slightly varying from each other in differentiation speed and efficiency. To differentiate hiPSCs into neurons, protocols usually start with a neural induction phase in order to generate neural progenitor cells (NPCs). Those cells are already patterned toward neuroectoderm and still expandable. This first step of neural induction is obtained by blocking the iPSC differentiation into meso- and endoderm and therefore pushing the cells towards an ectodermal fate. To achieve this, it is sufficient to block SMAD-dependent TGF (via SB-431542 or A83-01) and BMP (using Noggin or LDN-193189) signaling (214). This dual SMAD inhibition approach was developed to overcome disadvantages like heterogeneity and poor yield of progenitors that arose from the use of embryoid body differentiation, selection processes or poorly defined differentiation factors (e.g. co-cultures with differentiation inducing cells) (214,254,255). Nowadays, this approach is widely used and depending on the striven for cellular subtypes additional patterning steps are necessary.

Regional patterning in the neural tube is pivotal for the neural fate (Figure 9). To manipulate the dorsal-ventral (D-V) axis the sonic hedgehog (SHH) pathway can be targeted via activators such as smoothened agonist (SAG) or purmorphamine or inhibitors, like cyclopamine (235,256). As an example, the activation of SHH pathway leads to the ventralization of the differentiation patterning necessary to generate GABAergic neurons (240).

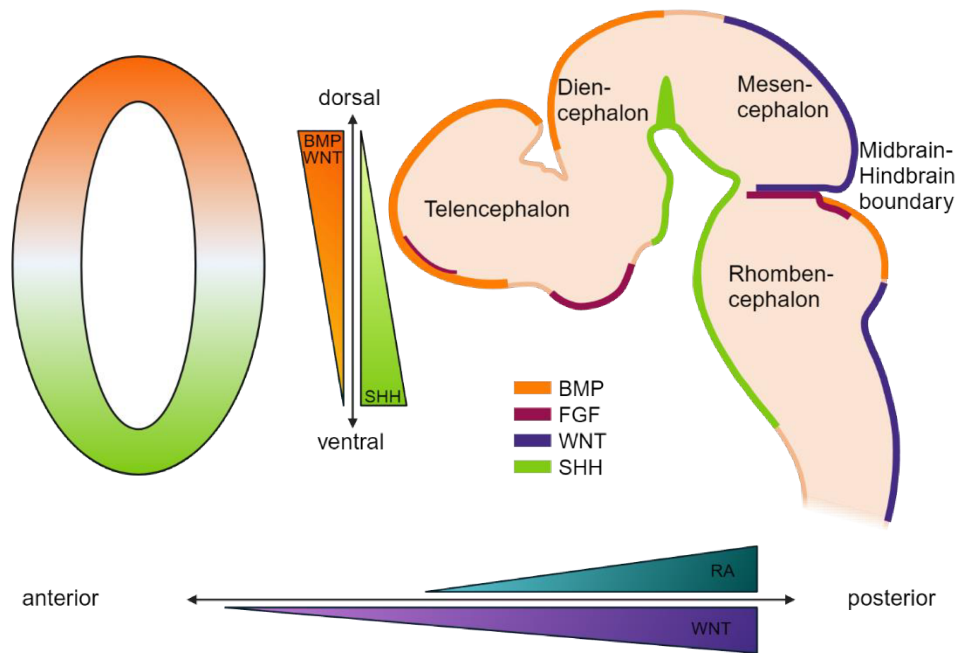


Figure 9: Embryonic brain development and the necessary morphogen gradients

On the left side a schematic coronal section through the neural tube shows a very early developmental stage with its morphogen gradients. In the dorsal part are high concentrations of BMP/WNT which decline towards the ventral section and in the ventral part there is strong SHH signaling which is declining towards the dorsal section. The anterior-posterior axis is mainly defined by a gradient of WNT signaling and partly retinoic acid (RA), which both increase concentrations towards the posterior section. These gradients, for dorsal-ventral and anterior-posterior, are valid throughout brain development, however once different brain areas start to develop the morphogen distribution becomes more complex with increasing complexity of the brain as can be seen on the right side. Created with BioRender.com

The adjustment of the anterior-posterior (A-P) axis can be achieved by influencing the WNT pathway. For instance, a commonly used agonist for WNT activation is CHIR99021, while XAV-939 is used as WNT inhibitor. Other approaches to modulate the A-P axis are the use of retinoic acid (RA) or the modulation of FGF signaling (257–259). In this sense, a patterning towards mid- and hindbrain identities (posteriorization) is required for the generation of serotonergic and dopaminergic neurons (242,243). Consequentially, to generate cortical neurons the progenitors should be patterned towards the prefrontal cortex. Thus, ventralization and posteriorization should be prevented (260). Subsequent of the NPC stage, are the terminal differentiation and maturation phase for which there are various protocols available of differing complexity and duration, ranging from spontaneous differentiation to complex factor application (261–263).

3.3.3 Insights from human induced pluripotent stem cell-derived model systems into schizophrenia pathology

Animal models have been very helpful for decades and have strongly contributed to basic and medical research, developing effective medical drugs, vaccines and more. Many SCZ susceptibility genes have been investigated in animal research to generate model organisms with SCZ-like symptoms. Therefore, several animal models have been developed such as *Disc1* mutant mice (264), reelin knockout mice (265), neuregulin-1 (*Nrg1*) and erb-b2 receptor tyrosine kinase 4 (*ErbB4*) knockout mice (266–269) which exhibit SCZ-like phenotypes. However, animal models do not allow to recapitulate the polygenic and heterogeneous background of SCZ patients and thus to fully shed light on the complexity of the disease and to decipher common causes or molecular phenotypes that underlie SCZ.

To overcome this limit, human induced pluripotent stem cells (hiPSCs) reflect exactly the genetic profile of the donor which enables patient-specific research. Somatic cells such as fibroblasts or peripheral blood mononuclear cells can be reprogrammed into hiPSCs which have the potential to differentiate into every cell type of the human body. In the field of psychiatric research, hiPSCs can be differentiated into different neuronal cell types as well as glial cells to identify and investigate specific SCZ phenotypes on a patient-specific cellular level. The use of hiPSCs provides a way to narrow the gap between animal models and clinical research and combine knowledge of the different research fields. With this approach, researchers were able to unravel molecular phenotypes on different levels, such as gene expression, synapses, mitochondria function or micro ribonucleic acids (miRNA) amongst others. The data were generated in either neuronal 2D cultures, co-cultures, in NPC cultures or 3D cultures (brain organoids) to reflect early developmental stages.

Findings from NPCs strongly correspond to the neurodevelopmental and metabolic components of SCZ. Hence, experiments on NPCs showed alterations in transcriptomics related to neuronal differentiation, WNT signaling, synaptic function and axonal guidance, increased cell proliferation, mitochondrial numbers and shapes were altered and additionally reduced Ca^{2+} reactivity upon glutamate stimulation (270). Furthermore, mitochondrial dysfunction was also detected in a study performed on NPCs (271) and related to that, high levels of oxidative stress, elevated basal respiration as well as altered cell migration, altered gene expression related to cytoskeletal remodeling and protein alterations related to cell morphology (272,273). Moreover, high variability in the activation levels of heat shock factor 1 in SCZ forebrain NPCs (274), impairments in apical polarity and adherens junctions in neural stem cells (275) were uncovered.

In studies of SCZ neuronal cultures, researchers discovered processes related to neurodevelopment or synapses, like neuronal connectivity, synaptic transmission and spinogenesis to be affected. For example, the rate of presynaptic vesicle release was observed to be decreased (56) and pathways like WNT and cyclic adenosine monophosphate (cAMP) signaling were dysregulated (276). Most of these synaptic phenotypes could be observed even in different types of neurons such as hippocampal neurons (277), forebrain neurons (56) or a culture generated by a pan-differentiation (276). Investigations of glutamatergic, and GABAergic neurons detected shortening of dendrites, limitation in neuronal outgrowth, decreased capacity of cortical differentiation and a reduction of excitatory and inhibitory synapses and reduced neuronal activity (278–280). Additionally, forebrain neurons were shown to have altered gene expression related to synaptic transmission and, here, showed higher spontaneous network activity (281), while in cortical neurons it could be demonstrated that the frequency of spontaneous inhibitory synaptic currents (sISC) and membrane resistance was increased (282). Another study too demonstrated, a deficit in neuronal differentiation and maturation in dopaminergic and glutamatergic neurons, as well as impairment in mitochondrial functions (283). Moreover, in the last years, miRNAs gained of importance and several studies on SCZ showed altered expressions of different miRNAs in glutamatergic and GABAergic neurons, astrocytes and forebrain or hippocampal NPCs (284–287).

Furthermore, the generation of 3D models can give insights into the neurodevelopmental and organizational processes at the basis of SCZ. Several studies could show a decreased NPC proliferation and hastened neuronal differentiation (288–290) or lowered NPC survival and thus lowered yields of neurons in SCZ organoids (291). One of these studies described a displacement of proliferating cells and neurons into cortical plate-like region and progenitor zones respectively (289). It was also observed that ventricle-like structures are decreased in size but increased in number in the SCZ organoids (290). In another study it was shown that neurons express multiple cortical layer markers at the same time and fail to form properly organized cortical layers (292). Lastly two of these studies could even show altered differentiation in glutamatergic and GABAergic neurons (288,290).

The partial heterogeneity of research results reflects the complexity of SCZ as a polygenic disorder and corroborates the necessity to use model systems like hiPSCs that properly reflect the complicated genetic backgrounds in SCZ to uncover pathomechanisms and pave the way for new medications. There are several more studies investigating SCZ in hiPSC-derived models of different neuronal subtypes and also investigating non-neuronal cells like astrocytes, microglia or oligodendrocytes. For further information, please refer to the references on the topic (293–297).

4. Aims of this study

SCZ is a highly complex polygenic disorder that is strongly influenced by environmental factors, which complicates the identification of its underlying common molecular alterations. Although several susceptibility genes have been linked to SCZ, a high number of patients do not display mutations in these genes but nonetheless suffer from the disorder. Human iPSCs as a model bring along the vital advantage of reflecting the exact genetic background of the donor which predestinates them to model polygenic disorders.

The present project aims to identify cellular and molecular phenotypes associated with SCZ by the means of hiPSC-derived cortical neurons to unravel new insights into the pathogenesis of this psychiatric disorder. First, a pair of candidate hiPS cell lines were chosen out of a small cohort of SCZ patients and the respective first-degree relatives cell lines. The choice was based on a chromosomal abnormality, a heterozygous 3q28 deletion, in one SCZ line which was identified by SNP karyotyping.

Once the cell lines were chosen, the first aim was to identify candidate genes on gene locus 3q28 and uncover potentially associated phenotypes. To this aim I selected osteocrin (*OSTN*) and IL-1 receptor accessory protein (*IL1RAP*) and analyzed the cells according to the defined categories: transcriptomic analysis with bulk RNA sequencing (RNAseq), morphological characterization, synaptic analysis and functionality assays.

The second part of the project was focused on the exploration and validation of the phenotypes in a different genetic background, by generating an isogenic system in a different control cell line. By using CRISPR/Cas9 systems the aim was to introduce a disruptive mutation in *OSTN*, one of the candidate genes in this project, and investigate how these cells compare to the SCZ patient-derived cell line.

The final aim of my work was to combine the genetic background with pharmacological modulation of OSTN and IL-1 β pathways to further investigate the molecular interaction between these pathways and evaluate its role in the cellular phenotypes.

5. Materials

5.1 Cell culture

5.1.1 Cell lines

In this thesis hiPSC derived from healthy individuals, first-degree relatives (FDR) and patients diagnosed with SCZ (F20 diagnosis according to ICD-10) were used. Either fibroblasts or PBMCs were taken from the donors and further reprogrammed into hiPSCs using a sendai virus reprogramming kit. The acquisition of donors and the reprogramming of these cell lines was performed by Dr. Sandra Horschitz Horschitz (Hector Institute for Translational Brain Research, Central Institute of Mental Health, Mannheim, Germany) before the start of this thesis. However, the modification of wild type (WT) with two different CRISPR systems into an OSTN mutants was part of this thesis.

Table 1: List of cell lines

Cell line	Donor	Source cell type	Reprogramming method	Source
Ctrl	Male, age 26, healthy FDR	PBMCs	Sendai virus	Mannheim, Germany
SCZ	Female, age 49, SCZ	PBMCs	Sendai virus	Mannheim, Germany
WT	Female, age 19, healthy	Dermal fibroblasts	Sendai virus	Mannheim, Germany
OSTN_1+/-	WT	N/A	N/A	Mannheim, Germany
OSTN_2+/-	WT	N/A	N/A	Mannheim, Germany
OSTN-/-	WT	N/A	N/A	Mannheim, Germany

All cell lines were checked with SNP karyotyping for chromosomal changes after reprogramming. Furthermore, pluripotency was ensured by immunofluorescence staining for pluripotency markers.

5.1.2 Cell culture solutions, small molecules and media

Table 2: Base media

Medium	Cat. Number	Manufacturer
Advanced DMEM/F12	12634010	Thermo Fisher Scientific (Waltham, USA)
Advanced MEM	12492013	Thermo Fisher Scientific (Waltham, USA)

Materials

DMEM with GlutaMAX™	10566016	Thermo Fisher Scientific (Waltham, USA)
DMEM/F12 with glutamine	11320033	Thermo Fisher Scientific (Waltham, USA)
DMEM/F12 with glutamine and HEPES	11330057	Thermo Fisher Scientific (Waltham, USA)
Neurobasal™	21103049	Thermo Fisher Scientific (Waltham, USA)

Table 3: Commercial ready-to use cell culture solutions

Compound	Concentration	Cat. number	Manufacturer
B-27 supplement	50x	17504044	Thermo Fisher Scientific (Waltham, USA)
BSA solution	7.5 %	15260037	Thermo Fisher Scientific (Waltham, USA)
DPBS	1x	14190144	Thermo Fisher Scientific (Waltham, USA)
DPBS + MgCl ₂ and CaCl ₂	1x	D8662	Sigma-Aldrich (St. Louis, USA)
EDTA pH 8.0 UltraPure™	0.5 M	15575020	Thermo Fisher Scientific (Waltham, USA)
FBS	100 %	10270106	Thermo Fisher Scientific (Waltham, USA)
Geltrex™	15 mg/ml	A1413302	Thermo Fisher Scientific (Waltham, USA)
GlutaMAX supplement	100x	35050038	Thermo Fisher Scientific (Waltham, USA)
KnockOut™ Serum Replacement	100 %	10828028	Thermo Fisher Scientific (Waltham, USA)
MEM-NEAA	100x	11140035	Thermo Fisher Scientific (Waltham, USA)
Penicillin/Streptomycin	100x	15140122	Thermo Fisher Scientific (Waltham, USA)
TrypLE™ Express	1x	12605028	Thermo Fisher Scientific (Waltham, USA)

Table 4: Growth factors, small molecules and other chemicals for cell culture

Compound	Solvent	Cat. number	Manufacturer
A83-01	DMSO	Cay9001799-25	Biomol GmbH (Hamburg, Germany)
AP-811	H ₂ O	5498	Tocris Bioscience (Bristol, UK)
BMP4	0.1% BSA in H ₂ O	130-111-165	Miltenyi Biotec (Bergisch Gladbach, Germany)
Boric acid	H ₂ O	15583	Thermo Fisher Scientific (Waltham, USA)
Bryostatins 1	Ethanol	203811	EMD Millipore (Burlington, USA)

Materials

CaCl ₂	H ₂ O	HN04.1	Carl Roth (Karlsruhe, Germany)
CHIR99021	DMSO	SM13-50	Cell Guidance Systems (Cambridge, UK)
D(+)-Glucose	H ₂ O	HN06.2	Carl Roth (Karlsruhe, Germany)
DAPT	DMSO	SM15-50	Cell Guidance Systems (Cambridge, UK)
DMSO	N/A	D5879	Sigma-Aldrich (St. Louis, USA)
EGF	H ₂ O	GFH26	Cell Guidance Systems (Cambridge, UK)
Ethanol	N/A	32205	Sigma-Aldrich (St. Louis, USA)
FGF-2 (147)	H ₂ O	GFH28	Cell Guidance Systems (Cambridge, UK)
FGF-2 (154)	0.1% BSA in H ₂ O	GFH146	Cell Guidance Systems (Cambridge, UK)
Forskolin	DMSO	SM18-100	Cell Guidance Systems (Cambridge, UK)
GABA	H ₂ O	A5835-337	Sigma-Aldrich (St. Louis, USA)
Gabazine	H ₂ O	S106	Sigma-Aldrich (St. Louis, USA)
Herparin sodium salt	PBS	H3149	Sigma-Aldrich (St. Louis, USA)
HEPES	H ₂ O	9105.4	Carl Roth (Karlsruhe, Germany)
IL-1 β	H ₂ O	GFH167	Cell Guidance Systems (Cambridge, UK)
IL-1Ra	0.1% BSA in H ₂ O	SRP3084	Sigma-Aldrich (St. Louis, USA)
Insulin	10 mM NaOH	91077C	Sigma-Aldrich (St. Louis, USA)
KCl	H ₂ O	A3582	AppliChem (Darmstadt, Germany)
Laminin	N/A	23017015	Thermo Fisher Scientific (Waltham, USA)
L-Ascorbic acid	H ₂ O	A4544	Sigma-Aldrich (St. Louis, USA)
L-Ascorbic acid 2-phosphate (LAAP)	H ₂ O	A8960	Sigma-Aldrich (St. Louis, USA)
LDN193189	DMSO	72148	StemCell Technologies
LM22A	H ₂ O	SML0848	Sigma-Aldrich (St. Louis, USA)
LM22B	DMSO	6037	Tocris Bioscience (Minneapolis, USA)
MgCl ₂	H ₂ O	105833	Merck Millipore (Darmstadt, Germany)
Myo-Inositol	H ₂ O	I5125	Sigma-Aldrich (St. Louis, USA)
NaCl	H ₂ O	31434	Sigma-Aldrich (St. Louis, USA)

Materials

PD-0332991	DMSO	1116	Selleck Chemicals (Houston, USA)
Pluronic F-127	DPBS	P2443	Sigma-Aldrich (St. Louis, USA)
Polyethyleneimine (PEI)	H ₂ O	P3143	Sigma-Aldrich (St. Louis, USA)
Polyvinylalcohol	DPBS	P8136	Sigma-Aldrich (St. Louis, USA)
Progesterone	Ethanol	P8783	Sigma-Aldrich (St. Louis, USA)
Puromycin	H ₂ O	540222	EMD Millipore (Burlington, USA)
Putrescine	H ₂ O	51799	Sigma-Aldrich (St. Louis, USA)
(rh)OSTN	PBS	9669-ON-050	R&D Systems (Minneapolis, USA)
SB431542	H ₂ O	SM33	Cell Guidance Systems (Cambridge, UK)
Sodium selenite	H ₂ O	A8960	Sigma-Aldrich (St. Louis, USA)
TGF- β 1	H ₂ O	GFH39	Cell Guidance Systems (Cambridge, UK)
Transferrin	H ₂ O	T3705	Sigma-Aldrich (St. Louis, USA)
TTX	H ₂ O	BN0518	Biotrend (Köln, Germany)
XAV939	DMSO	SM38	Cell Guidance Systems (Cambridge, UK)
Y-27632	H ₂ O	SM02	Cell Guidance Systems (Cambridge, UK)

5.1.3 Buffer and media compositions for cell culture

Table 5: Composition of cell culture cultivation and freezing media

Medium	Component	Concentration
Astrocyte medium	DMEM/F-12 Pen/Strep N-2 Glucose B27 EGF FGF-2 (147)	1 % (v/v) 1 % (v/v) 0.4 % (v/v) 0.1 % (v/v) 100 ng/ μ l 10 ng/ml
Astrocyte differentiation medium	DMEM/F-12 Pen/Strep N-2 Glucose B27 BMP4	1 % (v/v) 1 % (v/v) 0.4 % (v/v) 0.1 % (v/v) 10 ng/ml
iPSC medium	DMEM/F-12, HEPES Pen/Strep	1 % (v/v)

Materials

	LAAP Sodium selenite Insulin Transferrin FGF-2 (154) TGF- β 1	64 μ g/ml 14 ng/ml 20 μ g/ml 11 μ g/ml 100 ng/ml 2 ng/ml
NPC medium, phase 1 (NPC1)	Advanced DMEM/F12 Pen/Strep GlutaMAX™ supplement B-27 supplement SB431542 LDN193189 XAV939	1 % (v/v) 1 % (v/v) 1 % (v/v) 10 μ M 1 μ M 2 μ M
NPC medium, phase 2 (NPC2)	Advanced DMEM/F12 Pen/Strep GlutaMAX™ supplement B-27 supplement LDN193189 XAV939	1 % (v/v) 1 % (v/v) 1 % (v/v) 200 nM 2 μ M
NPC medium, phase 3 (NPC3)	Advanced DMEM/F12 Pen/Strep GlutaMAX™ supplement B-27 supplement FGF (147)	1 % (v/v) 1 % (v/v) 1 % (v/v) 20 ng/ml
Neuronal differentiation medium, phase 1 (ND1)	DMEM/F12 with glutamine Pen/Strep GlutaMAX™ supplement N2-supplement B-27 supplement NEAA Glucose CaCl ₂ Ascorbic acid LM22A LM22B PD-0332991 DAPT	1 % (v/v) 1 % (v/v) 0.5 % (v/v) 1 % (v/v) 1 % (v/v) 1.6 mg/ml 1.8 mM 200 μ M 1 μ M 1 μ M 2 μ M 5 μ M
Neuronal differentiation medium, phase 2 (ND2)	DMEM/F12 with glutamine Pen/Strep GlutaMAX™ supplement N2-supplement B-27 supplement NEAA Glucose Ascorbic acid LM22A LM22B PD-0332991	1 % (v/v) 1 % (v/v) 0.5 % (v/v) 1 % (v/v) 1 % (v/v) 1.6 mg/ml 1.8 mM 200 μ M 1 μ M 1 μ M

Materials

	DAPT CHIR99021 Forskolin GABA	2 μ M 5 μ M 3 μ M 10 μ M 300 μ M
Neuronal differentiation medium, phase 2.1 (ND2.1)	Neurobasal™ Pen/Strep GlutaMAX™ supplement B-27 supplement Glucose Ascorbic acid LM22A LM22B PD-0332991 DAPT CHIR99021 Forskolin GABA	1 % (v/v) 1 % (v/v) 2 % (v/v) 5 mg/ml 200 μ M 1 μ M 1 μ M 2 μ M 5 μ M 3 μ M 10 μ M 300 μ M
Neuronal differentiation medium, phase 3 (ND3)	Neurobasal™ Pen/Strep GlutaMAX™ supplement B-27 supplement Glucose Ascorbic acid LM22A LM22B PD-0332991 CHIR99021	1 % (v/v) 1 % (v/v) 2 % (v/v) 5 mg/ml 200 μ M 1 μ M 1 μ M 2 μ M 3 μ M
Neuronal differentiation medium, phase 4 (ND4)	Neurobasal™ Pen/Strep GlutaMAX™ supplement B-27 supplement Glucose Ascorbic acid LM22A LM22B PD-0332991	1 % (v/v) 1 % (v/v) 2 % (v/v) 5 mg/ml 200 μ M 1 μ M 1 μ M 2 μ M
Neuronal differentiation medium, phase 5 (ND5)	Advanced MEM Pen/Strep GlutaMAX™ supplement B-27 supplement Glucose Ascorbic acid LM22A LM22B PD-0332991 Bryostatin 1	Advanced MEM 1 % (v/v) 1 % (v/v) 2 % (v/v) 5 mg/ml 200 μ M 1 μ M 1 μ M 2 μ M 0.27 nM
3D Neural induction medium	DMEM/F12	93.3 %

Materials

	N2 B27 cAMP 2-Mercaptoethanol LDN-193189 A83-01 XAV939 GlutaMAX NEAA D-Glucose Heparin KOSR Penicillin/Streptomycin	0.5 % (v/v) 1 % 300 ng/ml 50 μ M 200 nM 500 nM 2 μ M 1 % (v/v) 1 % (v/v) 4.44 mM 10 μ g/ml 2% (v/v) 1% (v/v)
3D Neuronal differentiation medium	DMEM/F12 N2 B27 cAMP 2-Mercaptoethanol GlutaMAX NEAA D-Glucose Insulin KOSR Penicillin/Streptomycin	93.3 % 0.5 % (v/v) 1 % 300 ng/ml 50 μ M 1 % (v/v) 1 % (v/v) 4.44 mM 2.5 μ g/ml 2 % (v/v) 1 % (v/v)
3D Neuronal maturation medium	DMEM/F12 N2 B27 cAMP 2-Mercaptoethanol GlutaMAX NEAA D-Glucose L-Ascorbic Acid GDNF Geltrex™ Insulin LM22A LM22B Penicillin/Streptomycin	93.3 % 0.5 % (v/v) 1 % 300 ng/ml 50 μ M 1 % (v/v) 1 % (v/v) 4.44 mM 200 μ M 10 ng/ml 30 μ g/ml 2.5 μ g/ml 1 μ M 1 μ M 1 % (v/v)
Wash medium	DMEM with GlutaMAX™ Pen/Strep	1 % (v/v)
iPSC freezing medium	KnockOut™ Serum Replacement iPSC base medium supplemented with Pen/Strep, LAAP and Sodium selenite DMSO Y-27632	50 % (v/v) 40 % (v/v) 10 % (v/v) 20 μ M
NPC freezing medium	KnockOut™ Serum Replacement	70 % (v/v)

Materials

	Cytobuffer DMSO Y-27632	30 % (v/v) 10 % (v/v) 10 μ M
--	-------------------------------	--

Table 6: Composition of buffers, supplements and solutions

Name	Added components	Final concentration
Artificial cerebrospinal fluid (ACSF)	NaCl MgCl ₂ CaCl ₂ KCl Glucose NaHCO ₃ NaH ₂ PO ₄ adjust pH to 7.3 osmolarity 300 mOsm	125 mM 1 mM 2 mM 2.5 mM 10 mM 25 mM 1.25 mM
Borate buffer	Boric acid H ₂ O adjust pH to 8.4 with NaOH	25 mM
Cytobuffer	Myo-Inositol Polyvinylalcohol DPBS	240 mM 5 mg/ml (w/v) 0.2x
Glucose stock solution	Glucose H ₂ O 0.2 μ m sterile-filtered	400 mg/ml
Imaging buffer	HEPES pH 7.4 NaCl KCl CaCl ₂ MgCl ₂ Glucose	20 mM 140 mM 2.5 mM 1.8 mM 1 mM 10 mM
Intracellular solution	K-gluconate KCl Na-phosphocreatine Mg-ATP GTP EGTA HEPES adjust pH to 7.3 osmolarity 300 mOsm	115 mM 20 mM 10 mM 4 mM 0.3 mM 0.2 mM 10 mM
N2-supplement	DMEM/F12 with glutamine Pen/Strep Insulin Progesterone Putrescine Sodium selenite Transferrin	70 % (v/v) 1 % (v/v) 500 μ g/ml 630 ng/ml 1.611 mg/ml 520 ng/ml 10 mg/ml
PEI coating pre-dilution	Polyethyleneimine (PEI)	1 % (v/v)

Materials

	H ₂ O	
Pluronic coating solution	Pluronic F-127 DPBS	50 mg/ml
Stimulation buffer	HEPES pH 7.4 NaCl KCl CaCl ₂ MgCl ₂ Glucose	20 mM 140 mM 8 mM 4 mM 1 mM 10 mM

5.2 Molecular biology

5.2.1 Bacterial culture

Competent *Escherichia coli* (*E. coli*) DH5 α were obtained from New England Biolabs (#C2987H).

Table 7: Media for bacteria cultivation and transformation

Name	Added components	Final concentration
LB medium	LB medium powder Ampicillin	20 % (w/v) 100 μ g/ml
LB agar	LB medium powder Agar (Bacto™) Ampicillin	20 % (w/v) 15 % (w/v) 100 μ g/ml
SOC medium	Bacto-Tryptone Yeast Extract NaCl KCl MgCl ₂ MgSO ₄ Glucose	2 % (w/v) 0.5 % (w/v) 10 mM 2.5 mM 10 mM 10 mM 200 mM

5.2.2 Enzymes

Table 8: Enzymes for molecular biology and cloning

Enzyme	Cat. number	Manufacturer
DNase I, amplification grade	AMPD1-1KT	Sigma-Aldrich (Darmstadt, Germany)
DNase I, cell culture	10104159001	Sigma-Aldrich (Darmstadt, Germany)
GoTaq® G2 Flexi DNA Polymerase	M780B	Promega (Madison, USA)
LongAmp® Taq DNA Polymerase	M0323S	New England Biolabs (Ipswich, USA)
Proteinase K	405-001	GeneON Bioscience (Ludwigshafen, Germany)

Materials

T4 DNA Ligase	M0202	New England Biolabs (Ipswich, USA)
T4 Polynucleotide Kinase	M0201	New England Biolabs (Ipswich, USA)
Taq DNA Polymerase	331610	Biozym (Hessisch Oldendorf, Germany)
BbsI	R0539S	New England Biolabs (Ipswich, USA)

5.2.3 Plasmids

Table 9: Plasmids used for cloning and *OSTN* mutant cell lines

Name	Backbone	Insert (promoter-transgene)	Application	Cat. number	Source
pSpCas9(BB)-2A-Puro	px459	U6-empty CMV-Cas9-T2A-Puromycin	cloning	62988	Addgene (Watertown, USA)
OSTN gRNA-plasmid	px459	U6- OSTN gRNA CMV-Cas9-T2A-Puromycin	nucleofection	N/A	this thesis
Musclin CRISPR/Cas9 KO plasmid (h)			nucleofection	Sc-407576	Santa Cruz Biotechnology, Inc. (Dallas, USA)
Musclin HDR plasmid (h)			Nucleofection	Sc-407576-HDR	Santa Cruz Biotechnology, Inc. (Dallas, USA)

5.2.4 Primers, oligonucleotides and PCR components

All primers were obtained from Integrated DNA Technologies, Inc. (Coralville, USA). Lyophilized primers were reconstituted at 100 μ M in nuclease-free H₂O for at least 30 min at 37°C and 400 rpm.

Table 10: Primers for RT-PCR and qPCR

Primer name (Gene)	forward/reverse	Sequence (5' → 3')
18S	forward reverse	AAACGGCTACCACATCCAAG CCTCCAATGGATCCTCGTTA
ASCL1	forward reverse	CGCGGCCAACAAGAAGATG CGACGAGTAGGATGAGACCG
DLX1	forward reverse	GATCCGTAAACCCAGGACGA ATCTTGACCTGAGTCTGTGTGAG
DLX2	forward reverse	CTCACCCAGACTCAGGTCAAAA CTCCGAGGGGATCTCACCA
FOXG1	forward reverse	CCCTCCCATTTCTGTACGTTT CTGGCGGCTCTTAGAGAT
hU6	forward	GAGGGCCTATTTCCCATGATT
GAD1	forward reverse	ATCCTGGTTGACTGCAGAGAC CCAGTGGAGAGCTGGTTGAA
GRIA2	forward reverse	GGATCCTCATTAGAACCAGT TGAGGGCACTGGTCTTTTCC
GRIN1	forward reverse	GGCAACACCAACATCTGGAA CCATCCGCATACTTGGAAGAC
GRIN2B	forward reverse	CTCACCCCTTTCCGCTTT AAGGCATCCAGTTTCCCTGTT
GSX2	forward reverse	ATGTCGCGCTCCTTCTATGTC CAAGCGGGATGAAGAAATCCG
hU6	forward	GAGGGCCTATTTCCCATGATT
IL-1 β	forward reverse	GCTCGCCAGTGAAATGATGG AGATTTCGTAGCTGGATGCCG
Mycoplasma	forward reverse	GGGAGCAAACAGGATTAGATACCCT TGCACCATCTGTCACTCTGTTAACCTC
NES	forward reverse	GGCGCACCTCAAGATGTCC CTTGGGGTCCCTGAAAGCTG
OTX2	forward reverse	TGCAGGGGTTCTTCTGTGAT AGGGTCAGAGCAATTGACCA
OSTN (by Ataman et al. (172))	forward reverse	CAGGAAAAGTCCTCTCAGTAGATG GCAAGAGTTTTGCTGTCAGGTCA
OSTN (genotyping for PX459 clones)	forward reverse	TACCATTTGCCTCTAACAGTCCT TCTGTAAGCTAGTTTCCATTACCTC
OSTN (cassette)	reverse	TGTCCTACTCGACAATCAGC
OSTN (genotyping Santa Cruz)	forward reverse	CTCTGGGTGGAGTCTAAGGGA AGCCTCTGGAATTTGAAAGCCG
VGLUT2	forward reverse	TCAGATTCCGGGAGGCTACA TGGGTAGGTCACACCCTCAA
VGLUT1	forward reverse	AGCTGGGATCCAGAGACTGT CCGAAAACCTCTGTTGGCTGC
SNAP25	forward	AGTTGGCTGATGAGTCGCTG

Materials

	reverse	TCATGCCTTCTTCGACACGA
SV2	forward reverse	AACCTAGACCAGGCACTCAT ACCCCTCCCCACAGTTACTTA
SYN	forward reverse	CAGCTCAACAAATCCCAGTCTC GGTCTCAGCTTTACCTCGT
SYP	forward reverse	GACTATGGGCAGCAAGGCTA GGCTTCACTGACCAGACTACA
TUBB3	forward reverse	ATGGACAGTGTCCGCTCAGG TCACACTCCTTCCGCACCA

Table 11: Oligonucleotides and gRNA for cloning

Name	Sequence (5' → 3')
OSTN gRNA sense	CACCGACACTGACACTGTGGAGCTC
OSTN gRNA antisense	AAACGAGCTCCACAGTGTCAGTGTC
OSTN ssOligo	ATGCTAACTATGACATATGTAACCCTTAGATGCTGGACTG GAGATTGGCATAGTGCACATTTATCCTGGCTGTGACACT GACACTGTGGAGCTCAGGAAA

Table 12: Substances for PCR reaction mix

Substance	Concentration	Cat. number	Manufacturer
Reaction buffer	1x	331610	Biozym (Hessisch Oldendorf, Germany)
dNTPs	each 200 µM	SL-Set-S-dNTPs	Steinbrenner Laborsysteme (Wiesenbach, Germany)
Primers	each 400 nM	N/A	Integrated DNA Technologies (Coralville, USA)
Taq DNA Polymerase	0.625 U	331610	Biozym (Hessisch Oldendorf, Germany)
cDNA / genomic DNA	10 ng / 200 ng	N/A	N/A
DMSO (for genomic DNA only)	1% (v/v)	D5879	Sigma-Aldrich (St. Louis, USA)

Table 13: Substances for qPCR reaction mix

Substance	Concentration	Cat. number	Manufacturer
Reaction buffer	1x	M890A	Promega (Madison, USA)
MgCl ₂	2.5 mM	A351B	Promega (Madison, USA)
dNTPs	each 200 µM	SL-Set-S-dNTPs	Steinbrenner Laborsysteme (Wiesenbach, Germany)
Primers	each 200 nM	N/A	Integrated DNA Technologies (Coralville, USA)
DMSO	4 % (v/v)	D5879	Sigma-Aldrich (St. Louis, USA)
Syber® Green I	1x	S9430	Sigma-Aldrich (St. Louis, USA)

Materials

ROX	25 nM	A351513	GENAXXON (Ulm, Germany)
GoTaq [®] DNA Polymerase	0.75 U	M780B	Promega (Madison, USA)
cDNA	10 ng	N/A	N/A

5.2.5 Kits

Table 14: Commercial kits

Kit	Cat. number	Manufacturer
Cell Line Nucleofector [™] Kit V	VCA-1003	Lonza (Basel, Switzerland)
ExtractMe [®] Genomic DNA Kit	EM13-050	BLIRT S.A. (Gdańsk, Poland)
iScript [™] cDNA synthesis kit	17088991BUN	Bio-Rad Laboratories (Hercules, USA)
peqGOLD Gel extraction kit	12-2501-01	VWR (Radnor, USA)
peqGOLD Plasmid miniprep kit	732-2780	VWR (Radnor, USA)
Pierce [™] BCA Protein-Assay	23225	Thermo Fisher Scientific (Waltham, USA)
PureLink [™] HiPure Plasmid Filter Midiprep Kit	K210015	Thermo Fisher Scientific (Waltham, USA)
Qubit RNA BR Assay-Kit	Q10210	Thermo Fisher Scientific (Waltham, USA)
RNA 6000 Nano kit	5067-1511	Agilent Technologies (Santa Clara, USA)

5.2.6 Antibodies and fluorescent probes

Table 15: Primary antibodies

Antigen	Host	Dilutions	Cat. number	Manufacturer
Actin	rabbit	1:10000	4970	Cell Signaling Technology (Danvers, USA)
ANKG (N106/65)	mouse	1:100	75-147	NeuroMab (Davis, USA)
FOXG1	rabbit	1:100	NCFAB	Tebu-Bio (Offenbach am Main, Germany)
CTIP2	rat	1:500	ab18465	Abcam (Cambridge, US)
GAD65 (GAD2)	mouse	1:200	844502	Biologend (San Diego, USA)
GFAP	mouse	1:500	173011	Synaptic Systems (Göttingen, Germany)
HUC/D	mouse	1:500	A21271	Thermo Fisher Scientific (Waltham, USA)

Materials

MAP2	chicken	1:7000	822501	Biologend (San Diego, USA)
mCherry	rabbit	1:200	43590S	Cell Signaling Technologies (Danvers, USA)
Nestin	mouse	1:600	MAB1259	R&D Systems (Minneapolis, USA)
NeuN	rabbit	1:400	MAB377	EMD Millipore (Burlington, USA)
OCT3/4	mouse	1:500	sc-5279	Santa Cruz Biotechnology, Inc. (Dallas, USA)
OSTN	mouse	1:200 (IF) 1:1000 (WB)	sc-365631	Santa Cruz Biotechnology, Inc. (Dallas, USA)
PAX6	rabbit	1:500	901301	Biologend (San Diego, USA)
PSD95	rabbit	1:250	810401	Biologend (San Diego, USA)
PVIM	mouse	1:1000	D076-3	MBL International (Woburn, USA)
S100 β	mouse	1:2000	S2532	Sigma-Aldrich (St. Louis, USA)
SOX2	rabbit	1:400	3579	Cell Signaling Technology (Danvers, USA)
Synapsin I/II/III	mouse	1:500 (IF) 1:4000 (WB)	853701	Biologend (San Diego, USA)
TAU	guinea pig	1:750	314004	Synaptic Systems (Göttingen, Germany)
TBR1	rabbit	1:500	20932-1-ap	Proteintech (Rosemont, USA)
TUBB3	guinea pig	1:750	302 304	Synaptic Systems (Göttingen, Germany)
VGLUT1	guinea pig	1:400	135304	Synaptic Systems (Göttingen, Germany)

Table 16: Secondary antibodies

Antigen	Host	Dilution	Cat. number	Manufacturer
anti-chicken IgY Alexa Fluor-488	goat	1:1000	A11039	Thermo Fisher Scientific (Waltham, USA)
anti-chicken IgY Alexa Fluor-633	goat	1:1000	A21103	Thermo Fisher Scientific (Waltham, USA)
anti-goat IgG Alexa Fluor-488	donkey	1:1000	A11055	Thermo Fisher Scientific (Waltham, USA)
anti-guinea pig IgG Alexa Fluor-488	goat	1:1000	A11073	Thermo Fisher Scientific (Waltham, USA)
anti-guinea pig IgG Alexa Fluor-555	goat	1:1000	A21435	Thermo Fisher Scientific (Waltham, USA)
anti-guinea pig IgG Alexa Fluor-647	donkey	1:1000	A21450	Thermo Fisher Scientific (Waltham, USA)
anti-mouse IgG Alexa Fluor-488	goat	1:1000	A11001	Thermo Fisher Scientific (Waltham, USA)
anti-mouse IgG Alexa Fluor-568	goat	1:1000	A11004	Thermo Fisher Scientific (Waltham, USA)
anti-mouse IgG Alexa Fluor-647	goat	1:1000	A21236	Thermo Fisher Scientific (Waltham, USA)

Materials

anti-rabbit IgG Alexa Fluor-488	goat	1:1000	A11008	Thermo Fisher Scientific (Waltham, USA)
anti-rabbit IgG Alexa Fluor-555	goat	1:1000	A21428	Thermo Fisher Scientific (Waltham, USA)
anti-rat IgG Alexa Fluor-555	goat	1:1000	A21434	Thermo Fisher Scientific (Waltham, USA)
Anti-mouse DyLight™ 680	goat	1:15000	5470S	Cell Signaling Technologies (Danvers, USA)
Anti-mouse DyLight™ 800	goat	1:15000	5257S	Cell Signaling Technologies (Danvers, USA)
Anti-rabbit DyLight™ 680	goat	1:15000	5366S	Cell Signaling Technologies (Danvers, USA)
Anti-rabbit DyLight™ 800	goat	1:15000	5151S	Cell Signaling Technologies (Danvers, USA)

Table 17: Fluorescent probes

Reagent	Concentration	Cat. number	Manufacturer
DAPI	300 nM	422801	Biologend (San Diego, USA)
Fluo-4 AM	1 μ M	20552	AAT Bioquest (Sunnyvale, USA)

5.2.7 Buffers and solutions

Table 18: Self-made buffers and solutions

Buffer / Solution	Components	Concentration
APS stock solution	APS	10 % (w/v) in H ₂ O
DAPI staining solution	DAPI	300 nM in PBS
DEPC-H ₂ O	DEPC	0.1 % (v/v) in H ₂ O
DNA isolation lysis buffer	Tris-HCl, pH 8.5 EDTA SDS NaCl	100 mM 5 mM 0.2 % (w/v) 200 mM
DNA sample buffer (10X)	Tris-HCl, pH 7.6 Bromophenol blue Glycerol	50 mM 0.25 % (w/v) 60 %
Embedding solution	H ₂ O Sucrose Gelatine	10 % (w/v) 7.5 % (w/v)
Mounting solution	Tris-HCl, pH 8.5 Glycerol Mowiol DABCO®	100 mM 25 % 10 % 0.6 %
PBS	NaCl	137 mM

Materials

	KCl Na ₂ HPO ₄ KH ₂ HPO ₄	2.7 mM 10.0 mM 1.8 mM
PFA solution	PFA adjust pH to 7.2	4 % (w/v) in PBS
Protein lysis buffer	Tris-HCl, pH 7.4 NaCl SDS EDTA Phosphatase inhibitor Protease inhibitor	50 mM 150 mM 0.2 % (w/v) 25 mM 1 tablet / 10 ml 1 tablet / 10 ml
SDS stock solution	SDS	10 % (w/v) in H ₂ O
SDS-PAGE Anode buffer (1X)	Tris-HCl, pH 8.8	200 mM
SDS-PAGE polyacrylamide gel buffer	Tris-HCl pH 8.45 SDS	3 M 0.3 % (w/v)
SDS-PAGE sample buffer (6X)	Tris-HCl, pH 6.8 SDS Glycerol 2-Mercaptoethanol Bromophenol blue	93.75 mM 6 % 6 % 9 % 0.25 %
SDS-Polyacrylamide separating gel	SDS-PAGE polyacrylamide gel buffer Bis/Acrylamide Glycerol Ammonium persulfate TEMED	33.3 % (v/v) 10 % (v/v) 10 % (v/v) 0.028 % (w/v) 0.09 % (v/v)
SDS-Polyacrylamide stacking gel	SDS-PAGE polyacrylamide gel buffer Bis/Acrylamide Ammonium persulfate TEMED	24.8 % (v/v) 3.84 % (v/v) 0.0672 % (w/v) 0.224 % (v/v)
Sucrose solution	PBS Sucrose	30 % (v/v)
TAE (1X)	Tris EDTA Acetic acid	40 mM 1 mM 20 mM
TBS (10X)	Tris-HCl, pH 7.4 NaCl KCl	248 mM 1.37 M 26.8 mM
TBS-T (1X)	TBS (10X) Tween® 20	10 % (v/v) 0.1 % (v/v)
Tris-glycine buffer (10x)	Tris-HCl, pH 8.8 Glycine	250 mM 1.92 M
Triton X-100 stock solution	Triton X-100	10 % (v/v) in PBS
Western Blot transfer buffer	Tris-glycine buffer (10X) Methanol SDS	10 % (v/v) 20 % (v/v) 0.08 % (v/v)

Table 19: Commercial buffers and solutions

Buffer / Solution	Cat. number	Manufacturer
DNA Polymerase buffer (10X)	311611	Biozym (Hessisch Oldendorf, Germany)
GoTaq® DNA Polymerase buffer (10X)	M780B	Promega (Madison, USA)
LongAmp® Taq Reaction Buffer (5X)	B0323S	New England Biolabs (Ipswich, USA)
Restriction buffer 2.1 (10X)	B7202S	New England Biolabs (Ipswich, USA)
RNA - Solv reagent	R6830-02	VWR (Radnor, USA)
T4 DNA ligase buffer (10X)	B0202S	New England Biolabs (Ipswich, USA)
TriFast™ peqGold	30-2010	VWR (Radnor, USA)
Tris-Tricine-SDS buffer (10X)	T1165	Sigma-Aldrich (St. Louis, USA)

5.2.8 Reagents and chemicals

Table 20: Molecular biology reagents

Name	Cat. number	Manufacturer
1 kb marker	N0468S	New England Biolabs (Ipswich, USA)
100 bp marker, Quick-Load®	N0467S	New England Biolabs (Ipswich, USA)
Adult brain total RNA, human	R1234035-50-BC	BioCat (Heidelberg, Germany)
dNTPs	147850010	Steinbrenner (Laborsysteme Wiesenbach, Germany)
Fetal brain total RNA, human	1F01-50	Tebu Bio (Le-Perray-en-Yvelines, France)
peqGREEN DNA/RNA binding dye	peqI37-5010	VWR (Radnor, USA)
Protein marker PS 10 plus	310003	GeneOn (Ludwigshafen am Rhein, Germany)
RNaseAWAY	10666421	Thermo Fisher Scientific (Waltham, USA)
SYBR® Green nucleic acid stain	S9430	Sigma-Aldrich (St. Louis, USA)

Table 21: Chemicals

Chemical	Cat. number	Manufacturer
2-Mercaptoethanol	805740	Merck KGaA (Darmstadt, Germany)
2-Propanol	1157	Th. Geyer (Renningen, Germany)
30% Bis/acrylamide	3029.1	Carl Roth (Karlsruhe, Germany)
37% HCl	836.1000	Th. Geyer (Renningen, Germany)
Acetic acid	33209	Sigma-Aldrich (St. Louis, USA)

Materials

Agar (Bacto™)	214010	BD Biosciences (Franklin Lakes, USA)
Agarose	A9539	Sigma-Aldrich (St. Louis, USA)
Ammonium persulfate	A3678	Sigma-Aldrich (St. Louis, USA)
Ampicillin	A9518	Sigma-Aldrich (St. Louis, USA)
Bacto-Tryptone	211705	BD Biosciences (Franklin Lakes, USA)
Boric acid	15583	Thermo Fisher Scientific (Waltham, USA)
Bovine serum albumin (BSA)	A3294	Sigma-Aldrich (St. Louis, USA)
Bromophenol blue	B8026	Sigma-Aldrich (St. Louis, USA)
Chloroform	32211	Sigma-Aldrich (St. Louis, USA)
DABCO	0718.2	Carl Roth (Karlsruhe, Germany)
DEPC	K028.1	Carl Roth (Karlsruhe, Germany)
EDTA	E3889	Across organics (Fair Lawn, USA)
Ethanol	2246.1000	Th. Geyer (Renningen, Germany)
Fetal bovine serum (FBS)	10270-106	Thermo Fisher Scientific (Waltham, USA)
Gelatine	G1890	Sigma-Aldrich (St. Louis, USA)
Glycerol	15523	Sigma-Aldrich (St. Louis, USA)
Glycine	10070150	Thermo Fisher Scientific (Waltham, USA)
KH ₂ PO ₄	1648	Th. Geyer (Renningen, Germany)
KCl	1632	Th. Geyer (Renningen, Germany)
LB medium powder	X968.4	Carl Roth (Karlsruhe, Germany)
Methanol	0082.1	Carl Roth (Karlsruhe, Germany)
MgCl ₂	A351B	Promega (Madison, USA)
MgSO ₄	105886	Merck KGaA (Darmstadt, Germany)
Milk powder	T145.3	Carl Roth (Karlsruhe, Germany)
Mowiol®4-88	0713.1	Carl Roth (Karlsruhe, Germany)
Na ₂ HPO ₄	8622	Th. Geyer (Renningen, Germany)
NaCl	1367	Th. Geyer (Renningen, Germany)
Paraformaldehyde (PFA)	16005	Sigma-Aldrich (St. Louis, USA)
Phosphatase inhibitor mini tablets	A32957	Thermo Fisher Scientific (Waltham, USA)
Polyethyleneimine (PEI)	P3143	Sigma-Aldrich (St. Louis, USA)
Protease inhibitor mini tablets	A32955	Thermo Fisher Scientific (Waltham, USA)
Puromycin dihydrochloride	540222	Merck KGaA (Darmstadt, Germany)
ROX	A351513	GENAXXON (Ulm, Germany)
SDS, pellets	CN30.1	Carl Roth (Karlsruhe, Germany)
Sodium hydroxide, pellets	6771.2	Carl Roth (Karlsruhe, Germany)
Sucrose	S9378	Sigma-Aldrich (St. Louis, USA)
TEMED	T9281	Sigma-Aldrich (St. Louis, USA)
TRIS-HCl pH 8.5	4855.5	Carl Roth (Karlsruhe, Germany)
Triton X-100	1.08603.1000	Merck KGaA (Darmstadt, Germany)
Trypan Blue	17-942E	Lonza (Basel, Switzerland)
Tween® 20	P2287	Sigma-Aldrich(Darmstadt, Germany)
Yeast Extract	212750	BD Biosciences (Franklin Lakes, USA)

5.3 Consumables

Table 22: Consumables

Consumable	Format	Cat. number	Manufacturer
Blotting membranes	0.2 µm PVDF Nitrocellulose	GE10600021 GE10600001	GE Healthcare Life Science (Chicago, USA)
Bottle top filters	500 ml 1000 ml	15983307 15993307	Thermo Fisher Scientific (Waltham, USA)
Cell scrapers		sc-395251	Santa Cruz Biotechnology (Dallas, USA)
Coverslips	12 mm	631-1577	VWR (Radnor, USA)
Cryotubes	1 ml	123280	Greiner (Kremsmünster, Austria)
Luna™ reusable slides		L12011	Logos Biosystems (Anyang, South Korea)
Microscopy slides		H868.1	Carl Roth (Karlsruhe, Germany)
Microscopy slides Epredia™ SuperFrost Plus™		10149870	Thermo Fisher Scientific (Waltham, USA)
Pasteur pipettes		7691061	Th. Geyer (Renningen, Germany)
PCR strip tubes	8 x 200 µl	710971	Biozym (Hessisch Oldendorf, Germany)
Petri dishes	Ø 10 cm	633180	Greiner (Kremsmünster, Austria)
Pipette tips	10 µl 200 µl 1250 µl	70.1130 70.760.002 70.1186	Sarstedt (Nümbrecht, Germany)
Pipetting reservoirs	25 ml	B3125-50	Parmer GmbH (Cole- Wertheim, Germany)
qPCR plate seals		4ti-0500	Steinbrenner Laborsysteme (Wiesenbach, Germany)
qPCR plates	96-well	4ti-0910/C	Steinbrenner Laborsysteme (Wiesenbach, Germany)
Reaction tubes	0.2 ml 0.5 ml 1.5 ml 2.0 ml	72.737.002 72.699 72.690.001 72.695.200	Sarstedt (Nümbrecht, Germany)
Scalpel Cutfix®		9409814	Th. Geyer (Renningen, Germany)
Screw cap tubes	15 ml 50 ml	62.554.502 62.547.254	Sarstedt (Nümbrecht, Germany)
Serological pipettes	5 ml	86.1253.001	Sarstedt (Nümbrecht, Germany)
	10 ml	86.1254.001	
	25 ml	86.1685.001	
	50 ml	7695555	Th. Geyer (Renningen, Germany)
Syringe filters	0.2 µm	83.1826.001	Sarstedt (Nümbrecht, Germany)
Syringes	50 ml	94.6077.137	Sarstedt (Nümbrecht, Germany)
TC dishes	Ø 3.5 cm	83.3900.500	Sarstedt (Nümbrecht, Germany)
	Ø 6 cm	83.3901.002	

Materials

	Ø 10 cm, Cell+	83.3902.300	
TC plates	6-well	83.3920.005	Sarstedt (Nümbrecht, Germany)
	24-well, Cell+	83.3922.300	
	48-well, Cell+	83.3923.300	
	96-well, Cell+	83.3924.005	
Tissue-Tek® Cryomold®	10x10 mm	4565	Sakura Finetek (Torrance, USA)
Western blot filter tissues		115-2166	VWR (Radnor, USA)
U bottom plates	96-well	83.3925.500	Sarstedt (Nümbrecht, Germany)

5.4 Technical Equipment

Table 23: Notable laboratory equipment

Name	Appliance	Manufacturer
5415 D	Centrifuge	Eppendorf (Hamburg, Germany)
5810	Centrifuge, plates	Eppendorf (Hamburg, Germany)
Bioanalyzer 2100	Electrophoresis RNA quality control	Agilent Technologies (Santa Clara, USA)
BP121S	Analytical balance	Sartorius (Göttingen, Germany)
Branson Sonifier 250	Sonication device	Thermo Fisher Scientific (Waltham, USA)
CellDiscoverer 7	Microscope	Carl Zeiss (Oberkochen, Germany)
DFC9000 GT	Camera (microscopy)	(Wetzlar, Germany)
DM6 B	Microscope	Leica (Wetzlar, Germany)
DMIL LED	Microscope, brightfield	Leica (Wetzlar, Germany)
EasyPhor Midi	Agarose gel electrophoresis chamber	Biozym (Hessisch Oldendorf, Germany)
GelStick Touch	Agarose gel imaging system	INTAS Science Imaging Instruments GmbH (Göttingen, Germany)
HERAcell 150i	Incubator	Thermo Fisher Scientific (Waltham, USA)
C170 E3		Binder (Tuttlingen, Germany)
II/2b Device	Nucleofector	Lonza (Basel, Switzerland)
Jupiter Class 1 - Vertical flow clean air cabinet	Class I clean air cabinet	Labogene (Allerød, Denmark)
KS 250 basic	Orbital shaker	IKA Labortechnik ® GmbH
Luna™	Automated cell counter	Logos Biosystems (Anyang, South Korea)
Milli-Q Q-POD	Water conditioner	EMD Millipore (Burlington, USA)
Milli-Q® Integral 5	Water purifier	Merck KGaA (Darmstadt, Germany)

Materials

Mini-PROTEAN® Tetra	PAGE equipment	System Bio-Rad Laboratories (Hercules, USA)
Mr. Frosty™	Freezing container	Thermo Fisher Scientific (Waltham, USA)
NanoDrop™ 1000	Micro-Spectrophotometer	Thermo Fisher Scientific (Waltham, USA)
NU-540 Class II Type A2 Biosafety Cabinet	Biosafety Cabinet	Nuaire (Plymouth, USA)
NX50	Cryostat	Cryostar (Hésingue France)
Odyssey IR imaging system	Western blot imager	LI-COR Biosciences (Lincoln, USA)
Pipet Filler S1	Pipetting aid	Thermo Fisher Scientific Scientific (Waltham, USA)
PowerWave™ XS	Microplate reader	BioTek (Bad Friedrichshall, Germany)
Profilab pH597	pH-meter	Xylem Inc. (Rye Brook, USA)
PTC-200	PCR cycler	Bio-Rad Laboratories (Hercules, USA)
QuantStudio 7 Flex	qPCR cycler	Thermo Fisher Scientific (Waltham, USA)
Qubit 4 Fluorometer	DNA, RNA and protein quantification device	Thermo Fisher Scientific (Waltham, USA)
Research® plus	Micropipettes	Eppendorf (Hamburg, Germany)
TCS SP5 II	Confocal Microscope	Leica (Wetzlar, Germany)
Thermomixer comfort	Block heater	Eppendorf (Hamburg, Germany)
Thermomixer comfort 5355	Thermomixer	Eppendorf (Hamburg, Germany)
Trans-Blot® Turbo™	Western blot transfer system	Bio-Rad Laboratories (Hercules, USA)
UF V 700	Freezer -80°C	BINDER GmbH (Tuttlingen, Germany)
VIP plus	Freezer -150°C	Panasonic (Kadoma, Japan)
Z 216 MK	Centrifuge, refrigerated	Hermle (Wehingen, Germany)
Z 366	Centrifuge, cell culture	Hermle (Wehingen, Germany)

5.5 Software

Table 24: Computer Software

Computer program	Supplier
Affinity Designer 2	Serif (Europe) Ltd (West Bridgford, UK)
ApE – A plasmid editor	M. Wayne Davis
BioRender.com	BioRender (Toronto, Canada)
Excel 2016	Microsoft (Redmond, USA)
IBM SPSS Statistics 25/26	IMB (Armonk, USA)
Image Studio v 2.0	Li-Cor (Lincoln, USA)
ImageJ (FIJI)	National Institutes of Health (Rockville, USA)
Leica Application Suite AF	Leica (Wetzlar, Germany)
Leica Application Suite X	Leica (Wetzlar, Germany)
MATLAB	The MathWorks, Inc. (Natick, USA)
Mendeley reference manager	Mendeley Ltd. (London, UK)
Prism 5	GraphPad (San Diego, USA)
QuantStudio qPCR software	Thermo Fisher Scientific (Waltham, USA)
R Studio	RStudio PBC, open source
Word 2016	Microsoft (Redmond, USA)
ZEN	Carl Zeiss (Oberkochen, Germany)

6. Methods

6.1 Cell culture

All cells were cultivated in incubators with a constant humidity of 95 %, at 37 °C and CO₂ levels of 5 %. Media were stored at 4 °C and adjusted to room temperature (RT) before use. All buffers and media used in cell culture were prepared under sterile conditions or sterile filtered after preparation. All cell culture media and buffer recipes are listed in table 5 and 6.

6.1.1 Cultivation of hiPSCs

Human iPSCs were cultivated on Geltrex™ coated tissue culture plates. Geltrex™ was used in a dilution 1:50-1:100 in wash medium and coated overnight (ON) at 4 °C or for 30 minutes at 37 °C. HiPSCs were cultivated as colonies in iPSC medium and medium was changed daily, cells were passaged once they grew near confluency. The iPSC medium is based on a previous publication by Chen et al. (253). HiPSC cultures were regularly tested for their cell line identity and mycoplasma contamination by PCR. For hiPSC passaging, cells were washed once with 0.5 mM ethylenediamine tetraacetic acid (EDTA) in PBS and then incubated with 0.5 mM EDTA/PBS for 4-5 min at RT. EDTA/PBS was then aspirated and cells were carefully detached by rinsing the well with iPSC medium supplemented with 5 µM Y-27632 (for one day).

6.1.2 Generation of neural progenitors

HiPSCs were grown to a density of 70-80 % to initiate differentiation into neural progenitors. Media was changed from iPSC medium to NPC1 medium, which contained small molecules for dual SMAD inhibition (LDN-193189 and SB-431542) to prevent differentiation into meso- and endoderm and to generate NPCs specific for the ectodermal germ layer as previously described by Chambers et al. (214). The addition of Wnt pathway inhibitor XAV-939 prevented a posteriorization of the progenitors and enhanced the generation of forebrain NPCs. To expand the NPCs and promote proliferation, cells were supplemented with FGF2 for some passages (NPC3 medium).

The cells were passaged on day four in a ratio of 1:2 and kept four more days in NPC1 medium. The cells were passaged by incubation with TrypLE™ Express for 5-7 min at 37°C and were then detached with wash medium and centrifuged for 4 min at 1,200 xg. The supernatant was removed and the cell pellet was dissociated with the plating medium supplemented with 5 µM Y-27632. On day eight the cells were passaged again, as previously described, in a ratio of 1:2 and were maintained in NPC2 medium for eight days without splitting. Following this eight-day period, cells were passaged in a ratio of 1:2 and plated in NPC3 medium. Cells were kept in this medium for 1-2 more passages. In phase three cells were either prepared for the final differentiation into cortical neurons or frozen in NPC freezing medium with 10 µM Y-27632 for

later use. NPCs were cultivated on Geltrex™ coated tissue culture plates and media changes ensued daily. Y-27632 was removed the day after the split.

6.1.3 Generation of cortical neurons

For most experiments, NPCs were differentiated into cortical neurons. Therefore, the aforementioned NPCs were terminally differentiated in a multi-step protocol based on previously published work by other research groups (261,262).

Prior to coating, glass coverslips were pre-treated with 37 % hydrochloric acid (HCl) for several hours on an orbital shaker at RT. The coverslips were then thoroughly washed multiple times with H₂O and 70% ethanol an air-dried and then autoclaved. For neuronal cultures, tissue culture plates and coverslips were coated with PEI/Laminin. Therefore, wells were incubated with 0.005% PEI in borate buffer for 10-15 min at RT. Plates were then thoroughly washed 3x with H₂O and then dried at RT. Finally, 1:400 laminin in PBS (+Ca²⁺, +MgCl₂) was added to the plates and the coating took place either ON at 4 °C or for 30 min at 37 °C.

Following the NPC stage was the terminal differentiation which was conducted by adaptation of previously published protocols by Kemp et al. and Telezhkin et al. (261,262). The induction of the terminal neuronal differentiation was initiated by the application of γ -secretase inhibitor DAPT in combination with cyclin D-dependent kinase 4/6 (CDK4/6) inhibitor PD-0332991 and tyrosine receptor kinase B and C (TRKB and TRKC) receptor agonists LM22A and LM22B. This combination suppressed cell division and in combination with Wnt and cAMP/CREB pathway activators CHIR99021 and forskolin promoted neuronal differentiation. In addition, a high CaCl₂ concentration and the supplementation of GABA imitated the conditions during fetal brain development. For the final maturation of neurons, Bryostatin 1 was added which promotes synapse development

Thus, neural differentiation was initiated by changing the NPC3 medium to ND1 medium to promote NPCs' exit of the cell cycle and development into neurons. The start of neural differentiation was considered as d0 of the terminal differentiation.

The young neurons were split on d1 onto the final format and kept in ND1 medium. If necessary, DNase I was used during the split to prevent DNA contamination of the cells. Neurons were split by incubation with TrypLE™ Express for 3-5 minutes at 37°C and subsequent resuspension in wash medium and then centrifugation for 4 min at 800-900 xg. After resuspension, cells were counted with an automated cell counter (Luna™) and then plated in ND1 medium supplemented with 10 μ M Y-27632 until the next medium change. Usually 48 well plates (150,000 cells/well), 24 well plates (ca. 200,000 cells/well) with

coverslips and 6 wells (3-6 million cells/well) were used for neuronal cultures, depending on the experiment.

After the initial 3d phase, media was switched to ND2 medium, which was further promoting differentiation of NPCs into neurons and simultaneously induced maturation of neurons. Neurons were kept in ND2 medium for four days. On d7, medium was switched with a half media change to ND2.1 medium. On d10, medium was exchanged halfway with ND3 medium which promoted survival of neurons and their maturation. A week later, medium was fully changed to ND4 medium which mainly promoted neural maturation. The final maturation medium (ND5) was applied to the cells with a half medium change on d24 of the terminal differentiation and cells were kept in this media until the required age was reached for the experiments (ranging from d42-d105). If not stated otherwise, neuron medium was changed halfway twice a week.

6.1.4 Treatment of cortical neurons

To investigate the influence of specific molecules/ activation of specific pathways on neuronal function and molecular phenotypes, cortical neurons were treated with various components. To facilitate morphological analysis in a dense, mature culture, neurons were transduced with an adeno-associated virus (AAV) 2-3 weeks prior to the time point of analysis. The AAV (AVV_CaMKIIa p-hCHR2(134a)-mcherry) was kindly provided by the laboratory of Prof. Grinevich. The AAV lead to an expression of mcherry fluorescent protein under the calcium/calmodulin-dependent protein kinase IIa (CaMKIIa) promoter.

To investigate phenotype attribution to OSTN signaling, neuronal cultures were treated with 100 nM (rh)OSTN for 7d. 200nM AP-811, another antagonist for NPRC competing with OSTN for receptor binding, was applied for 8d either as a single treatment or in combination with 100 nM OSTN. In case of combination, cells were first incubated ON with AP-811 to block NPRC, followed by the combination of AP-811 and OSTN. To determine if phenotypes are attributed to IL-1 β signaling, neuronal cultures were treated with 50 ng/ml IL-1 β for and 100 ng/ml IL-1Ra (IL-1 receptor antagonist) either as single treatments or in combination for 5d. In case of a combination treatment, the cells were pre-incubated with IL-1Ra for 1h to block IL-1R before IL-1 β was added. If treatments of these four components was combined the respective inhibitors (AP-811 or IL-1Ra) were applied prior to their counterparts in the previously described manner. Treatments were permanently (for the indicated duration) in the media and refreshed with every media change. Please note that treatment results are partially preliminary (due to N numbers, indicated in Results part).

6.1.5 Co-culture with mouse derived astrocytes for electrophysiological measurements

For electrophysiological measurements cortical neurons were co-cultured with astrocytes. Therefore, mouse derived glial progenitors maintained in astrocyte medium (Table 5) were detached with TrypLE™ Express (5 min, 37 °C) centrifuged in wash medium 4 min at 1200 xg and plated on PEI/Laminin coated coverslips (described in the previous section) in a density of ca. 70,000-90,000 cells per well of a 24 well plate. They were kept in astrocyte medium for another two days then the medium was switched to astrocyte differentiation media (Table 5). After differentiating the mouse glial progenitors for two days into astrocytes, cortical neurons were seeded on top in a density of 200,000 cells per well. Starting from the day of co-culture, cells were kept in the different ND media without containing PD-0332991 according to the different terminal differentiation phases.

6.1.6 Cryopreservation of cells

Cells were cryopreserved either as hiPSCs or as neural progenitor cells (NPC). To freeze hiPSCs, cells were detached with EDTA, as previously described, but instead of iPSC medium wash media was used to rinse off the cells. Cells were then centrifuged for 4-5 minutes at 500 xg. After centrifugation, the medium was aspirated, and cells were carefully resuspended in cold iPSC cryomedium and transferred into cryotubes. For long-term storage cryotubes were transferred to -150°C or to liquid nitrogen. In order to freeze NPCs, cells were detached with TrypLE™ Express and the cell pellet was resuspended in cold NPC cryomedia and transferred into cryo-tubes.

Cryotubes were then transferred into a Mr. Frosty™ freezing container with a cooling rate of -1 °C/min which was subsequently stored at -80 °C for 24 h and then stored at -150 °C until further use.

6.1.7 Defrosting of hiPSCs and neural progenitors

To defrost hiPSCs or neural progenitors, tubes with pre-warmed wash medium were prepared and cryotubes were defrosted at 37 °C as fast as possible. Once the cells were almost completely defrosted, the remaining ice was melted with the warm wash medium and cells were transferred and centrifuged at 500 xg (hiPSCs) or 1200 xg (progenitors). Supernatant was discarded and cells were plated in the respective culture medium supplemented with 5-10 μM Y-27632.

6.1.8 Organoid generation

Organoid generation and processing were performed in collaboration with Dr. Andrea C. Rossetti (Hector Institute for Translational Brain Research, Central Institute of Mental Health,

Mannheim, Germany). Organoids were generated like previously published (298,299). When hiPSCs reached a sufficient density, cells were detached with TrypLE™ Express, counted and seeded (~9000 cells/well) in a 96 well plate (U-bottom) coated with Pluronic coating solution (Table 6) for 10 min at RT to prevent attachment of the cells to the plate bottom. Cells were plated in iPSC medium supplemented with 50 μ M Y-27632 and formed embryoid bodies (EBs) by self-assembly and medium was changed every other day. On day 5, medium was changed to 3D neural induction medium and changed every other day. At day 8, organoids were embedded in Geltrex™ to provide structural support and were subsequently transferred into 6 cm dishes (coated with Pluronic). From now on, organoids were cultivated on an orbital shaker. On day 10 the medium was changed to 3D neural differentiation medium and medium changes were done every 3-4 days. On day 35, medium was changed to 3D maturation medium and was changed every 3-4 days.

For processing, organoids were incubated with 4% PFA for 10-15 min at RT, then PFA was removed and samples were washed with PBS several times for 10 min at RT. Afterwards, samples were transferred into a 30 % sucrose solution ON at 4 °C to reduce crystal formation during the freezing process. In collaboration with Dr. Rossetti and Helene Schamber, organoids were then embedded in gelatine solution and frozen in an ethanol and dry ice freezing bath. Samples were now either stored at -80 °C or sliced at the cryostat to a thickness of ca. 20 μ m and collected on SuperFrost™ microscope slides. The staining procedure is the same as described in section 6.5.4, only the samples on the slides had to be circled with a liquid barrier pen prior to the staining.

6.2 Generation of isogenic *OSTN* mutant lines via CRISPR/Cas9

To generate a genetic situation that resembles the SCZ line, the aim was to either knockout or at least disrupt the *OSTN* gene to render the protein useless. This could be achieved by introducing a frameshift mutation leading to a premature stop codon.

6.2.1 Generation of an *OSTN*-targeting CRISPR/Cas9 plasmid

Next to a commercially available CRISPR/Cas9 system by Santa Cruz, the PX459 V2.0 plasmid (initially designed by the Feng Zhang Lab (300), available on Addgene) was used. This plasmid encodes for the *Streptococcus pyogenes* Cas9 enzyme fused to a puromycin N-acetyltransferase via a T2A sequence, a β -lactamase for ampicillin resistance and a restriction site for the insertion of a target-specific guide RNA (gRNA).

Initially, the plasmid was digested and gRNAs were phosphorylated and annealed with the protocols shown in Table 25+26.

Table 25: Protocols for backbone digestion and gRNA phosphorylation reaction mixes

Backbone digestion		gRNA phosphorylation and annealing	
1 µg	PX459 V2.0 plasmid	1 µl	sense gRNA (100 µM)
1 µl	BbsI	1 µl	antisense gRNA (100 µM)
2 µl	10x restriction buffer 2.1	1 µl	10x T4 ligation buffer
to 20 µl	ddH ₂ O	0.5 µl	T4 PNK
		6.5 µl	ddH ₂ O

Table 26: Program for backbone digestion and gRNA phosphorylation

Backbone digestion		gRNA phosphorylation and annealing	
37 °C	1 h	Phosphorylation	37 °C 30 min
		Annealing	95 °C 5 min
			Down to 25 °C 5 °C/min

Afterwards, the plasmid digestion was checked with agarose gel electrophoresis and then purified with the peqGOLD Gel extraction Kit according to the manufacturer's protocol (section 6.4.8). This step was followed by the ligation of the phosphorylated gRNAs with the digested backbone. Therefore, a reaction mix was prepared as depicted in Table 27 and the mix was incubated at RT for 1 h.

Table 27: Composition for ligation reaction mix

Ligation	
50 ng	Digested plasmid (backbone)
1 µl	Phosphorylated and annealed gRNA duplex
1 µl	10x T4 ligation buffer
1 µl	T4 DNA ligase
to 10 µl	ddH ₂ O

6.2.2 Transformation of competent *E. coli*

The final plasmid was amplified with competent *E. coli* DH5 α bacteria. Therefore, 5 μ l of the ligated plasmid were added to 50 μ l of bacteria suspension and incubated on ice for 15 min. The bacteria were then heat shocked by placing the tube in a heating block which was pre-heated to 42 °C for 40 s. Afterwards, the tube was put on ice immediately for 2 min before adding 300 μ l SOC medium (Table 7). The sample was incubated at 37 °C while shaking at 650 rpm for 1 h in a ThermoMixer[®]. Finally, bacteria were plated on 10 cm LB-agar plates supplemented with 100 μ g/ml ampicillin and incubated ON at 37 °C. The following day single colonies were picked to inoculate 5 ml of LB medium (Table 7) supplemented with 100 μ g/ml ampicillin. Freshly inoculated tubes were incubated ON at 37 °C while shaking at 400 rpm.

6.2.3 Plasmid DNA isolation from *E. coli*

Inoculated 5 ml tubes were checked for bacteria growth, if the optic density significantly increased ON then DNA was isolated from these bacteria samples. For small volumes the peqGOLD Plasmid miniprep Kit (VWR) was used and isolation was performed according to the manufacturer's protocol. In the final step, DNA was eluted with 30 μ l ddH₂O and DNA concentration was measured with the NanoDrop[™] 1000 spectrophotometer. For large-scale plasmid DNA production, about 200 ml of LB medium were inoculated with leftover bacteria suspension of miniprep inoculation and incubated ON at 37 °C while skating at 400 rpm. The next day, bacteria cultures were centrifuged at 4,600 x g for 10 min. To isolate plasmid DNA from large samples, the PureLink[™] HiPure Plasmid Filter Midiprep Kit (Thermo Fisher Scientific) was used according to the manufacturer's instructions. Centrifugation steps for precipitation and washing were performed at lower velocity (4,600 x g) due to technical limitations but to compensate, duration of centrifugation was increased to 1 h and 2 h respectively. DNA concentrations were measured with the NanoDrop[™] 1000 spectrophotometer and plasmids were checked for the correct integration of gRNAs by Sanger sequencing using the hU6 forward primer (Table 10). FASTA sequences were analyzed with the ApE plasmid editor software. Plasmid DNA was stored at -20 °C.

6.2.4 Nucleofection of hiPSCs and clone validation

Genetic adjustment of a control cell line (in the following referred to as wild type (WT)) into homo- or heterozygous *OSTN* mutant cell lines was achieved with two CRISPR/Cas9 systems. The first system is a commercial CRISPR/Cas9 system by Santa Cruz (Table 9), which was ready to use after reconstitution of the plasmids according to the manufacturer's instructions. The second system was a self-designed CRISPR/Cas 9 system based on the commercially available PX459 plasmid (available at Addgene, generated by the Feng Zhang lab (300), Table

9). This plasmid was adjusted as described in section 5.2.1 and a single-stranded oligodeoxynucleotide (ssODN) was designed according to the chosen gRNAs.

To generate a *OSTN* mutant cell line, a low passage of a mycoplasma-free, control hiPSC line was chosen. HiPSCs were grown to an appropriate density to yield 2-3 million cells in a well. Before starting, all reagents of the Lonza Cell Line Nucleofector Kit V (Table 14) were adjusted to RT and cells were pre-incubated with 5 μ M RI for 30-60 min and then detached with TrypLE™ Express. HiPSCs were incubated up to 8 min with TrypLE™ Express and if possible TrypLE™ Express was removed from the cells to minimize stress for the cells. The hiPSCs were removed from the well with a minimal amount (~2 mL) of wash medium (Table 5) and were then counted with Trypan Blue (Table 21) using an automated cell counter (Luna™) (Table 23). About one million cells were transferred into a 2 mL tube and centrifuged for 5 min at 500 xg at RT. The rest of the cells were centrifuged as well, with the same specifications. Meanwhile, a Geltrex™-coated 6 well plate was prepared with iPSC medium without antibiotics supplemented with 10 μ M Y-27632. On two wells, hiPSCs which didn't undergo genetic modification were plated, at a density of about 250,000 cells/well, as a selection control and for SNP karyotyping. For the Santa Cruz system only, some (50,000-75,000 cells/well) non-modified cells were plated to act as support-cells for the nucleofected cells in the remaining 4 wells. The one million cells in the 2 mL tube were completely cleared of the wash medium and were then carefully resuspended in 82 μ l Nucleofector™ Solution V, 18 μ l Supplement 1 and a total of 6 μ g (for PX459 based approach, 4 μ g of ssODN + 2 μ g *OSTN* gRNA PX459 plasmid) or 2 μ g (Santa Cruz system, 1 μ g of each plasmid) of DNA. The cell suspension was transferred to the nucleofection cuvette avoiding any air bubbles and placed in the nucleofection device. The cells were electroporated with the B-023 program of the Lona Cell Line Nucleofector. Afterwards, cells were transferred back into the 2 mL tube and the volume was added up to 1 ml with antibiotics-free iPSC medium supplemented with 10 μ M Y-27632. Cells were then plated in different densities on 4 wells of the 6 well plate (400,000; 300,000; 200,000 and 100,000 cells/well). Cells were kept in antibiotics-free iPSC medium for 2d, then media was switched to standard iPSC medium. The PX459 construct introduces a transient resistance to puromycin, while the Santa Cruz construct introduces a permanent puromycin resistance. Based on that, the puromycin selection for the PX459 construct started 2-3 d after the nucleofection with 0.33 μ g/mL puromycin and lasted for max. 3d. For the Santa Cruz construct, the selection started 2-4d after the nucleofection at the same puromycin concentration and lasted for several days up to two weeks. Once the puromycin control well (non-modified cells) was empty, the puromycin selection was stopped and cells were allowed to grow into small colonies. The emerging colonies were then picked manually and transferred into Geltrex™-coated 48 well plates (a single colony per well) and slowly split to bigger formats, until there

were enough cells to generate cryo-backups and for characterization via PCR and Sanger sequencing. FASTA sequences were analyzed with the ApE plasmid editor software.

6.3 Live cell analyses

6.3.1 Calcium imaging

For calcium imaging (Ca^{2+} imaging), neurons were plated in a 48 well tissue culture plate coated with PEI/Laminin at a density of 150,000 cells per well. At day 45 (if not stated otherwise) of terminal differentiation cells were stained with 1 μM Fluo4-AM and 0.02% pluronic acid supplemented into the culture medium. Cells were incubated for 30 min at 37 °C in the dark and then washed once with imaging buffer (Table 6) followed by another 30 min incubation with imaging buffer to ensure calcium transients measured were not caused by the medium change. Calcium transients were recorded with the Celldiscoverer 7 (Zeiss) and three positions per well were chosen for each condition. Live imaging was set to 1.5 min continuous recording per position, then switching to the next position and repeat that loop, summing up to three minutes recordings per position. Images were acquired at an interval of 170 ms resulting in a frame rate of ca. 5 frames per second (fps). After incubations, the first measurement was the baseline activity of cells measured in imaging buffer ensued by a change to stimulation buffer with higher calcium and potassium concentrations (301) to stimulate neuronal activity. The stimulation buffer was supplemented with 5 μM gabazine which inhibits potential populations of GABAergic neurons thus disinhibiting glutamatergic neurons leading to maximal stimulation of neuronal activity. After changing to stimulation buffer with gabazine, calcium transients were recorded immediately with the same settings described for baseline recordings, however, new positions per well were chosen due to dye stability and photobleaching issues. Lastly, calcium transients were recorded while cells were in stimulation buffer supplemented with 1 μM tetrodotoxin (TTX) to verify if calcium transients were dependent on voltage-gated sodium channels thus assumably of synaptic origin. For TTX recordings usually 1-2 new positions were chosen but were otherwise recorded with the same settings as previously described.

The calcium transients were extracted with the ZEN software. Transients analyzed with the previously published PeakCaller script for MATLAB (302). Statistics for Ca^{2+} imaging data were performed on means resulting from each position to minimize bias by the analyzed cell numbers.

6.3.2 Electrophysiology

Electrophysiological measurements and analysis were kindly performed by Dr. Mahnaz Davoudi (Hector Institute for Translational Brain Research, Central Institute of Mental Health, Mannheim, Germany) and in cooperation with PD Dr. Georg Köhr (Department of Neurophysiology, Mannheim Center for Translational Neuroscience, University of Heidelberg/Medical Faculty Mannheim, Germany). The preparation and treatment of cells was done by the author of this thesis. Therefore, cells were co-cultured with mouse derived astrocytes. Measurements were carried out around day 55 to 60 of terminal differentiation.

Cells were recorded using an EPC9 amplifier and PatchMaster (HEKA Elektronik GmbH). Neurons were perfused with carbogen (95 % O₂/5 % CO₂)-saturated artificial cerebrospinal fluid (ACSF) at 2 ml/min in a recording chamber at RT. Recording pipets were pulled from borosilicate glass capillaries with a P-97 micropipette puller (Sutter Instrument) and filled with intracellular solution with a resistance of 4 to 6 MΩ. Single neurons were visualized with a Zeiss Axioskop using infrared differential interference contrast video microscopy in the recording chamber. In voltage-clamp, input resistance was determined at -70 mV based on currents evoked by small voltage steps (-3 mV; 300 ms). With increasing depolarizing steps (10 mV; 300 ms) inward and outward currents were evoked. In current-clamp, the resting membrane potential (RMP) was measured and action potentials (APs) were evoked with increasing current injections (10 pA; 300 ms) in ten depolarizing steps. The amplitude of the first evoked AP was analyzed, and the number of all evoked APs was summarized. Further, spontaneous excitatory postsynaptic currents (sEPSCs) were recorded at -70 mV at RT. Recordings were sampled at 20 kHz. The analysis was performed with FitMaster (HEKA Elektronik GmbH) and MiniAnalysis (Synaptosoft).

6.4 Molecular Biology

6.4.1 Harvesting samples

To harvest cells for molecular analyses, cells were washed with cold PBS. Then cold PBS was added to the well, and cells were detached from the well using a cell scraper or the mechanical force of rinsing the well with a pipet. The cells were then transferred into a 1.5 mL Eppendorf tube and centrifuged at 5000 xg for 5 min at 4 °C. Afterwards, supernatant was removed, and samples were stored at either -20 °C or -80 °C until further use.

6.4.2 DNA isolation

Several quality controls of cells require genomic DNA (gDNA), therefore gDNA was isolated either with the Zymo *Quick-DNA* Miniprep Plus Kit according to the manufacturer's protocol or via classical DNA extraction.

For classical DNA extraction cell pellets were dissolved in 150 μ L lysis buffer (table X) supplemented with 1 μ L proteinase K (table X) and incubated for 1 h at 37 °C and 500 rpm in a ThermoMixer®. Subsequently, samples were heated to 95 °C for 10 min after which 105 μ L isopropanol were added to each sample. The samples were then incubated for 30 min at RT while being vortexed every few minutes. This step was followed by a 10 min centrifugation at 12,000 xg to pelletize DNA. DNA pellets were then washed with 70 % ethanol and centrifuged for 10 min at 12,000 xg. The washing step was repeated once more, followed by air-drying the DNA pellet. Lastly, DNA was dissolved in 20-200 μ L water by pipetting up and down and an incubation for 30 min at 37 °C and 400 rpm or an ON incubation at 4 °C. DNA concentrations were measured as described in section 6.4.4 and DNA was stored at -20 °C.

6.4.3 RNA isolation

Cells were harvested and stored as pellets. In order to isolate RNA from samples, cell pellets were dissolved in 1 mL RNA-Solv reagent (VWR, Table 19) by pipetting up and down. Once samples were dissolved, they were incubated for approximately 10 min at RT. Then, 200 μ L of chloroform were added and samples were vortexed for 15 s each and incubated for another 10 min at RT. Subsequently, samples were centrifuged for 5 min at 4 °C and 12.000 xg. Now three phases form, the upper aqueous phase containing the RNA, a white inter-phase containing DNA and at the bottom a phase containing proteins. The aqueous phase was then transferred to a new 1.5 mL tube and 200 μ L isopropanol were added to the samples to precipitate RNA. The chemicals were carefully but thoroughly mixed in the tube by inverting the tubes several times. Samples were stored at -20 °C ON for RNA precipitation. The following day, samples were centrifuged for 25 min at 4°C and 12.000 xg to pelletize precipitated RNA. The supernatant was discarded and RNA pellets were washed with 1 mL 75 % ethanol in diethyl pyrocarbonate-treated (DEPC) water. Samples were then centrifuged for 10 min at 4 °C and 12.000 xg, supernatant was discarded and the washing step was repeated. After the second washing step RNA pellets were air dried until most of the ethanol/DEPC was evaporated. Lastly, RNA pellets were dissolved in 20 μ L DEPC water by pipetting up and down and then shaking for 30 min at 450 rpm and 37 °C in a ThermoMixer® (Eppendorf), followed by a DNase I digest to remove any remaining DNA contaminations. DNase I digest was performed with the DNase I kit (AMPD1-1KT) by Sigma Aldrich (Table 8). For 20 μ L RNA, 2.5 μ L of DNase I and 2.5 μ L of 10x DNase reaction buffer were added to each sample and incubated for 15 min at RT. Then, 2.5 μ L stop solution were added to each sample and samples

were incubated at 70 °C for 10 min. Afterwards RNA concentrations were measured or RNA samples were stored at -80 °C or -150 °C until further use.

6.4.4 Determination of DNA and RNA concentrations

DNA concentrations were measured using a NanoDrop™ fluorometer. RNA concentration of samples was measured using either a NanoDrop™ or a Qubit 4 Fluorometer. For measurements with the Qubit Fluorometer, samples were prepared with the Qubit RNA Broad Range (BR) assay kit according to the manufacturer's protocol. In short, 200 µL working solution was prepared for the 2 standards and each sample. Therefore, the Qubit RNA BR Reagent was diluted 1:200 in Qubit RNA BR Buffer and working solution was transferred into assay tubes, 190 µL for standard 1 and 2 and 199 µL for each sample. Then 10 µL of standard 1 and 2 and 1 µL of each sample were added to their respective assay tube which were then vortexed briefly and incubated in the dark for 2 min. The Qubit Fluorometer was then calibrated with the two standards and afterwards samples were measured.

6.4.5 Complementary DNA (cDNA) synthesis

In order to perform expression analyses like polymerase chain reaction (PCR) or quantitative PCR, isolated RNA was transcribed into cDNA. Reverse transcription was performed with the iScript™ cDNA Synthesis Kit (Table 14) according to the manufacturer's protocol. In short, 500-1000 ng RNA were used and added to 15 µl with RNase free water and 4 µl of 5x reverse transcription buffer and 1 µl of reverse transcriptase were added to each sample (final total volume 20 µl). The cDNA synthesis ensued in a thermal cycler with the cDNA program described in Table 28. CDNA was stored at -20 °C until further use.

Table 28: Cycling program for cDNA synthesis with iScript™ cDNA Synthesis Kit

Cycle step	Temperature	Time in min
Priming	25 °C	5
Reverse transcription	46 °C	20
Enzyme inactivation	95°C	1
	4 °C	∞

6.4.6 Quantitative PCR (qPCR)

Quantitative PCR was performed to analyze gene expression levels. Therefore, RNA was extracted and cDNA was synthesized and diluted in ddH₂O if necessary. QPCR reaction mix was prepared as described in Table 13 and qPCR was run in a 96 well format in a QuantStudio 7 Flex cycler (Thermo Fisher Scientific) with the program described in Table 29. QuantStudio software determined threshold cycle (Ct) values and melting curves. Afterwards, relative fold changes were calculated using the $\Delta\Delta C_t$ method (303) and gene expression was normalized to 18S rRNA.

Table 29: qPCR cycling program

Step	Temperature	Time	Cycles
Hold	50 °C	2 min	1
	95 °C	10 min	1
PCR	95 °C	20 s	1
	60 °C	20 s	40
	72 °C	20 s	1
Melting curve	95 °C	15 s	1
	60 °C	1 min	1
	95 °C	0.05 °C/s	1

6.4.7 Reverse transcriptase PCR (RT-PCR)

RT-PCR was performed on cDNA or DNA to characterize cells or to perform quality controls on the cells. The RT-PCR reaction mix was prepared as described in Table 12 with the Taq DNA Polymerase Kit (Biozym). For cloning steps the LongAmp® Taq Polymerase Kit (NEB) which has a proofreading function was used (program and composition Tables 31 + 32). Amplification of target amplicons was performed with the program in Table 33, if necessary the annealing temperature or elongation time was adjusted. Primers are listed in Table 10. PCR products were analyzed and visualized by agarose gel electrophoresis.

Methods

Table 30: RT-PCR cycling program (Taq DNA Polymerase, Biozym)

Step	Temperature	Time	Cycles
Initial denaturation	95	1 min	1
Denaturation	95 °C	15 s	40
Annealing	60 °C	15 s	
Elongation	72 °C	30 s	
Final elongation	72 °C	5 min	1
	4 °C	∞	

Table 31: Composition of LongAmp® Taq Polymerase reaction mix

Component	Final concentration
LongAmp® Reaction Buffer 5x	1x
dNTPs	300 µM
Primers	400 nM each
LongAmp® Taq DNA Polymerase	2.5 U
Plasmid DNA	10 ng
ddH ₂ O	to 25 µl

Table 32: LongAmp® cycling program

Step	Temperature	Time	Cycles
Initial denaturation	94 °C	30 s	1
Denaturation	94 °C	30 s	30
Annealing	60 °C	60 s	
Elongation	65 °C	50 s/kb	
Final elongation	65 °C	5 min	1
	4 °C	∞	

Cell cultures were regularly tested for mycoplasma contamination, this was done on gDNA and was performed by Helene Schamber. Primers can be found in Table 10 and RT-PCR was run with the cycling program in Table 33.

Table 33: Program mycoplasma PCR

Step	Temperature	Time	Cycles
Initial denaturation	95 °C	1 min	1
Denaturation	95 °C	15 s	35
Annealing	50 °C	15 s	
Elongation	72 °C	10 s	
Final elongation	72 °C	3 min	1
	4 °C	∞	

6.4.8 Agarose gel electrophoresis, gel extraction and sanger sequencing

RT-PCR products were analyzed by gel electrophoresis with gels made of 1-2 % agarose (w/v) in 1x TAE buffer with 1 :15,000 peqGREEN. Samples were mixed with 10x DNA sample buffer (to a concentration of 1x) and were applied to the gel together with a 1 kb or 100 kb marker as reference. The DNA fragments were size-separated by running the gel at 100 V for 45-50 min

and fragments were visualized with a GelStick Touch imaging system (INTAS Science Imaging Instruments GmbH).

For quality control of e.g. cloning steps of plasmids or to validate the mutation in a cell line, DNA fragments were cut out of the agarose gel and were extracted out of the gel with the peqGOLD Gel extraction kit according to the manufacturers protocol. Samples were eluted in 30 μ l elution buffer and DNA concentration was measured. Samples were either frozen at -20 °C until further use or directly sent to Sanger sequencing. Therefore, DNA was adjusted to a concentration according to the Microsynth-Seqlab website (depending on fragment type) in a volume of 12 μ l and 3 μ l of forward or reverse primer were added. For plasmids standard primers could be added by the Sanger sequencing facility (Microsynth-Seqlab Göttingen, Germany). Samples were then sent at RT.

6.4.9 Measurement of RNA integrity

As part of quality control, integrity of RNA was determined using the Agilent 2100 Bioanalyzer Instrument and the Agilent RNA 6000 Nano Kit according to the manufacturer's protocol. Succinctly, kit components were adjusted to RT and RNA ladder was initially heated up to 70 °C for X min, then aliquoted and stored at -80 °C (long-term) or put on ice for direct use. Furthermore, 1 μ l of each RNA sample was heated to 70 °C for 2 min and then stored on ice. The gel was filtered through the provided columns by centrifugation for 10 min at RT and 13.000 x g. Gel dye was briefly vortexed and 1 μ l of dye was added to 65 μ l of gel. This mixture was again briefly vortexed and subsequently centrifuged for 10 min at RT and 13.000 x g. The RNA 6000 Nano chip was coated with 9 μ l gel-dye mixture using the Agilent priming station. According to manufacturer's instructions, the plunger was pulled up to 1 ml and then the station was closed, the plunger was slowly pressed down until it was locked in place. After 30 s, the plunger was released and 9 μ l of gel-dye mix were added to two more wells respectively. To all remaining wells, 5 μ l of RNA detection dye were added and lastly 1 μ l of ladder and sample were added to the respective wells. Afterwards, the chip was vortexed in a vortex mixer (MS3, IKA) for 1 min at 2400 rpm. In the meantime, the electrodes of the instrument were cleaned with RNase away for 1 min and then with RNase free water for another minute, electrodes were then briefly air dried before the instrument was closed after inserting the chip. The chip was measured and analyzed with the eukaryote total RNA nano program.

6.4.10 Bulk RNA sequencing (RNAseq)

Three biological replicates of each condition were prepared for bulk RNAseq. RNA was isolated as described in section 6.4.3 and quality control was performed as described in section 6.4.4 and 6.4.9. Samples with a RNA integrity number (RIN) \geq 7.2 qualified for RNAseq. A minimum amount of 1200 ng RNA in at least 40 μ l volume per sample were sent to the High Throughput

Sequencing Unit of the Genomics & Proteomics Core Facility, German Cancer Research Center (DKFZ) to be processed. In the facility, the library preparation was performed using the TruSeq Stranded protocol (Illumina) and libraries were sequenced to 50 bp on the NovaSeq 6K platform. In the core facility another quality control was run before the samples were cleared for sequencing. Sequencing data was run through an RNAseq processing workflow by the Omics IT and Data Management Core Facility, German Cancer Research Center (DKFZ). Analysis of total counts per feature was performed with R (R Core Team, 2020) and analyzed with the DESeq2 package (304). All features without any counts were removed and for differential testing with DESeq2 the formula "~Batch+Condition" was used. Heatmaps for RNAseq expression data show z-scaled TPM normalized counts. Gene ontology (GO) enrichment analysis was performed with enrichGO from the clusterProfiler package (305).

RNAseq data analysis was performed in close collaboration with Dr. Anne Hoffrichter (Hector Institute for Translational Brain Research, Central Institute of Mental Health, Mannheim, Germany).

6.5 Biochemistry

6.5.1 Protein isolation

Cell pellets were dissolved in 100-150 μ l protein lysis buffer (Table 18), by pipetting up and down. Samples were then incubated at RT for 10 min and then put on ice and incubated for at least 1 h. Samples were then briefly sonicated to get rid of DNA contaminations. Finally, samples were centrifuged at 16,000 x g for 15 min at 4 °C to remove cell debris from the samples. Samples were then stored at -20 °C until further use.

6.5.2 Determination of protein concentration

Protein concentrations were measured colorimetrically using the Pierce™ BCA Protein-Assay kit (Table 14). The assay was performed according to manufacturer's protocol. Samples were diluted 1:5 in ddH₂O and added to a 96 well plate together with the assay reagents mix. The plate was then incubated at 37 °C for 30 min in the dark. Absorption at 562 nm was then measured with a PowerWave™ XS (BioTek) microplate reader and protein concentration were calculated according to the measured BSA standard dilutions. Standard and samples were measured in duplets.

6.5.3 SDS-PAGE and western blot

For western blot/ sodium dodecyl sulfate–polyacrylamid gel electrophoresis (SDS-PAGE) 10 % acrylamide gels were casted into 1.5 mm chambers (Bio-Rad). Therefore, the separation

gel was prepared as described in Table 18 and casted into the chambers. To ensure an even polymerization surface and to avoid any air bubbles the gel was immediately covered with isopropanol. Once the separation gel was fully polymerized, isopropanol was removed and the stacking gel (Table 18) was cast on top of the separation gel. The gels were prepared with combs for 10 or 15 samples. Gels were usually stored ON or up to a week in the fridge wrapped in moist paper towels in a plastic bag. Samples for SDS-PAGE were mixed with 6x SDS-PAGE sample buffer (Table 18) and heated to 95 °C for 5 min, briefly centrifuged and stored on ice until use. Samples were usually used at a final protein concentration of 15-25 µg but sometimes up to 50 µg. To run SDS-PAGE gels were placed in the running chamber. The space between gels was filled with a commercial Tris-Tricine buffer (Table 19) and the rest of the chamber was filled with anode buffer (Table 18). Then combs were removed from the gels and pockets were rinsed with a Hamilton syringe and Tris-Tricine buffer. Now samples and protein ladder (Table 20) were applied to the gels and gel run was started at 20 V until all samples completely entered the stacking gel, afterwards voltage was increased to 120 V and gels were run until the desired separation of proteins was reached. After separation proteins were blotted to a 0.2 µm Nitrocellulose membrane or a PVDF membrane, while PVDF membranes were activated with methanol for ca. 2 min before blotting. Proteins were transferred to the membranes using a semi-dry blotting system (BioRad). Therefore, membranes were placed on paper drenched in blotting buffer (Table 18) in the blotting chambers, then separation gels were placed on top of the membrane and covered with buffer-drenched paper. Air bubbles were removed from the blotting “sandwich” with a small roller. Chambers were closed and blotting was performed with 20 V, 1 A for 30 to 45 min. After blotting, membranes were transferred to 50 ml tubes and covered with blocking solution, which was 5 % (w/v) milk powder in 1x TBS-T (Table 18). to ensure permanent coverage of the membranes with blocking buffer, tubes were incubated on a rolling shaker for 1 h at RT. Finally, primary antibodies (Table 15) were diluted in blocking solution and added to the membrane and incubated on a rolling shaker ON at 4 °C. The next day, membranes were washed three times with 1x TBS-T for 10 min. Secondary antibodies (Table 16) were prepared in 1x TBS-T (for PVDF membranes 0.01 % SDS was added) and incubated in the dark on the membrane for 1 h at RT on a rolling shaker. Subsequently, membranes were washed repeatedly with 1x TBS-T and finally with TBS then ddH₂O to reduce background caused by Tween-20. Proteins were detected using the LI-COR Odyssey IR imaging system and analyzed with Fiji (ImageJ).

6.5.4 Immunofluorescence staining

To prepare cells on coverslips for immunofluorescence stainings, cells were washed once with PBS and then incubated with cold 4 % paraformaldehyde (PFA) in PBS for 10 min at RT or ice-cold methanol for 5 min at -20 °C. After incubation, cells were washed at least three times with PBS. Cells were then either directly used for staining or stored at 4 °C until further use.

After the PBS wash, cells were covered with blocking solution containing either Triton-X (10 % FBS/PBS + 0.1-0.3 % Triton-X) and incubated for 1 h at RT or saponin (10 % FBS/PBS + 0.05 % saponin) and were incubated for ca. 15 min at RT. Primary antibodies were diluted (for antibody dilutions see Table 15) in blocking solution (Triton-X) or antibody solution (saponin), mixed well and subsequently centrifuged at 10,000 x g and 4 °C for 5 min to avoid antibody aggregates on the samples. Samples were then incubated with primary antibodies at 4 °C ON. The next day, samples were washed three times with respective blocking solution. Secondary antibodies carrying a fluorophore, were diluted (dilutions Table 16) in blocking solution or antibody solution, mixed well and centrifuged at 10,000 x g and 4 °C for 5 min to avoid antibody aggregates on the samples. The samples were incubated with the secondary antibodies for 45 min at RT. Then, samples were washed with PBS and incubated with 4',6-Diamidino-2-phenylindol (DAPI) in PBS for 10 min at RT to label nuclear DNA and washed again with PBS afterwards. Two final washing steps were performed using Milli-Q® water to avoid any salt crystal formation on the coverslips. Samples were then mounted with Mowiol on glass slides and dried ON at RT. After mounting and drying, samples were stored at 4 °C.

6.6 Microscopy - image acquisition

Images of IFs were taken with the fluorescence microscope DM6B (Leica) with the Leica imaging software LasX (Leica). Images were acquired with the 20x or 40x objectives.

The Celldiscoverer 7 (Zeiss) and the corresponding ZEN software was used for brightfield images and live cell imaging using the 20x objective with a 0.5x zoom.

Images were processed with ImageJ and most analyses were performed with ImageJ plugins.

6.7 Analyses

Image analyses were performed blinded.

6.7.1 Early outgrowth assay

To analyze the early morphological development of neurons, neurons were plated on PEI/Laminin-coated coverslips in a low density 30,000-40,000 cells/coverslip. Cells were fixed with 4 % PFA at the designated time points and subsequently stained as previously described. After image acquisition, the images were analyzed with the NeuronJ plugin (ImageJ) to measure length and branchpoints of the cells.

6.7.2 Sholl analysis

To analyze the morphology of mature neurons in a dense (more physiological) culture (200,000 cells/cover slip), 2-3 weeks prior the analysis cells were transduced with an AAV (AVV_CaMKIIa p-hCHR2(134a)-mcherry) kindly provided by the Grinevich Lab (Central Institute for Mental Health). The low transduction efficiency led to single neuron labeling which enabled the morphological analysis. Cells were fixed with 4 % PFA and stained for mcherry and other markers. After image acquisition, neurons were manually traced based on the mcherry signal and then analyzed with the ImageJ Sholl program (306). Sholl radii were set every 15 μm until 300 μm from the soma. The total length of neurons was calculated based on the Sholl results, the first radius was equated to the number of primary neurites and the sum of intersections was calculated from all intersections of each cell.

6.7.3 Analysis of synaptic proteins

To analyze the density of synaptic proteins (SYN, PSD95) ROIs were selected based on the structural protein (Microtubule Associated Protein 2 (MAP2)). Then puncta were measured with the ComDet v.0.4.1 plugin (ImageJ) and the lengths of the selected ROIs were determined. The number of single and colocalized puncta per 100 μm neurite were calculated. Puncta and colocalization were always measured with the same size and distance parameters.

6.7.4 Statistical analysis

Data are presented as means \pm standard error of the mean (SEM). The number of biological replicates is indicated in the respective figure descriptions. Statistical analysis was either performed with GraphPad Prism5 or SPSS. Datasets were tested for normality with the Kolmogorov-Smirnov test. If normality was not given, a Mann-Whitney-U test was performed, when two groups were compared. If several groups were compared for one dependent variable, a Kruskal-Wallis test (with Dunn's post hoc test) was performed. Significance levels compared to controls are indicated as * $p < 0.05$, ** $p < 0.01$, *** $p < 0.001$ and not significant (ns) $p > 0.05$.

6.7.5 Visualization

Bar graphs, scatter plots and Sholl graphs were generated with GraphPad Prism 5 and bar graphs (qPCR) were generated with MS Excel. Bulk RNAseq-related graphs were generated with R by Dr. Anne Hoffrichter (Hector Institute for Translational Brain Research, Central Institute of Mental Health, Mannheim, Germany). Schematic representations were generated with BioRender.com as indicated.

7. Results

7.1 hiPSC quality control revealed a chromosomal aberration in the SCZ patient

After reprogramming iPSC cells have to pass through several quality controls. These include the verification of expression of pluripotency markers, a regular test for mycoplasma contamination and SNP karyograms to ensure the reprogramming process did not interfere with the chromosomal integrity of the cells (SNP karyograms were already available in the laboratory for "Ctrl", "SCZ" and "WT" lines and were outsourced to an external facility). First, all hiPSCs used in this work were positive for the pluripotency markers SOX2 and OCT3/4 (representative images Figure 10C). Interestingly, one SCZ patient-derived cell line (SCZ) showed a peculiar chromosomal anomaly in the SNP karyogram (Figure 10A). Specifically, a more in-depth analysis revealed a heterozygous deletion of the genetic locus 3q28 (Figure 10B) which was not identified in the respective first-degree relative-derived cell line (Ctrl). To ensure that this deletion was not a consequence of the reprogramming process, a subsequent SNP karyogram was performed on the somatic donor cells (PBMCs) and the heterozygous 3q28 deletion was confirmed to be a patient-specific genetic anomaly.

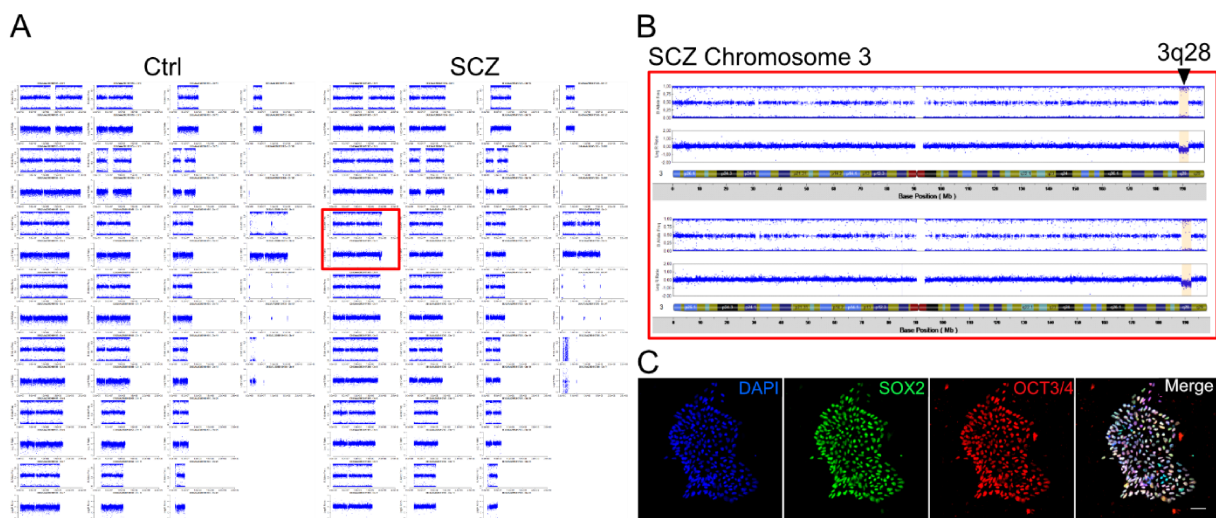


Figure 10: Quality control of hiPSCs representative for Ctrl and SCZ

A) SNP karyogram of Ctrl and SCZ hiPSCs, red square labels chromosome 3 of SCZ. **B)** Zoom in on SNP karyogram of chromosome 3 of SCZ. The black triangle marks the 3q28 locus identifying the heterozygous deletion. **C)** Representative images of hiPSC pluripotency markers. Scale bar = 50 μ m

7.2 Generation of isogenic *OSTN* mutant hiPS cell line

In-depth research of the genetic landscape of genetic locus 3q28, revealed two interesting candidate genes out of around 40 genes (Table S1), namely the osteocrin gene (*OSTN*, alternative name musclin) and the interleukin-1 receptor accessory protein gene (*IL1RAP*). As already described in the introduction, these genes and the respective proteins can influence neuronal properties, thus being interesting in the context of SCZ pathophysiology.

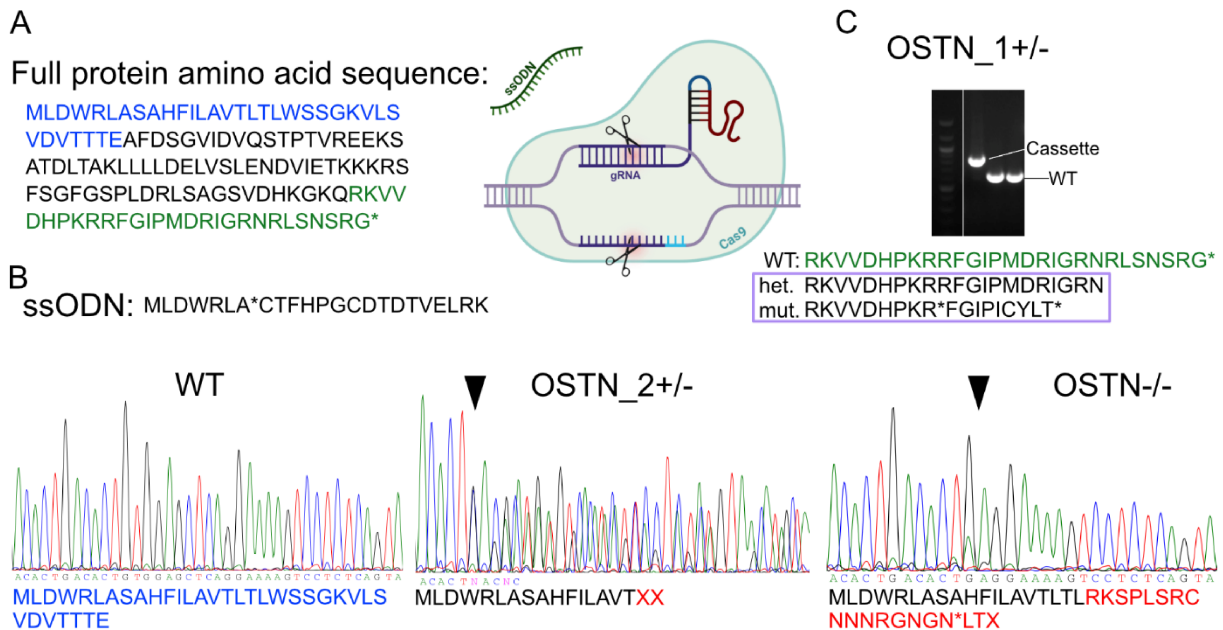


Figure 11: Generation of *OSTN* mutant hiPS cell line with CRISPR/Cas9

Two different CRISPR/Cas9 systems were used to generate an *OSTN* mutant hiPS cell line based on a healthy control cell line (WT). **A**) Amino acid sequence of full length *OSTN* protein. The blue sequence labels the sequence which was targeted by the self-designed CRISPR/Cas9 system (based on PX459 plasmid). The green amino acid sequence depicts one of three targets of the commercial CRISPR/Cas9 system (Santa Cruz) which was successfully targeted in this project. **B**) Amino acid sequence of ssODN. Sequencing chromatograms and amino acid sequences of WT, heterozygous *OSTN* mutant *OSTN*_2+/- and homozygous *OSTN* mutant *OSTN*-/-. Black arrow heads mark the start of the mutation. **C**) RT-PCR results for *OSTN*_1+/- as validation of cassette integration of the commercial CRISPR/Cas9 system. Genetic alteration and heterozygosity were confirmed by wildtype band and subsequent sequencing (amino acid sequences). Asterisks indicate stop codon, red amino acids are changed sequences due to CRISPR/Cas9, *OSTN*-/- has a deletion of 8 base pairs and subsequently displays a frameshift mutation with a premature stop codon. CRISPR/Cas9 scheme was created with BioRender.com

To validate the influence of *OSTN* in a potential molecular phenotype, I generated a dedicated cellular model by targeting *OSTN* gene with two CRISPR/Cas9 systems. On one hand, I chose a system based on the PX459 plasmid (available on Addgene). More in detail, I designed and integrated a single gRNA into the plasmid then I designed a ssODN to obtain a frameshift mutation and eventually to a premature stop codon (targeted region in protein sequence in blue Figure 11A). With this system, there was no permanent integration of any parts of the CRISPR/Cas9 system. Thus, the insertion of the specific mutation into the *OSTN* gene was confirmed by Sanger sequencing (Figure 11B). The second approach involved the use of a

commercial system targeting the *OSTN* gene with three different gRNAs and respective homolog directed repair (HDR) plasmids (targeted region in protein sequence in green Figure 11A). This system, if successful, would lead to a permanent integration of the cassette, which can be detected by RT-PCR (Figure 11C) and can further be confirmed by Sanger sequencing. The success rate of the commercial system was relatively low, with only one clone with a heterozygous mutation. This clone will be referred to as *OSTN*₁^{+/-}. The approach with the adjusted PX459 plasmid was more effective, resulting in several clones with heterozygous and homozygous mutations, despite the caveat of having not identical mutations among the clones. Out of the cohort of validated clones derived from the PX459 plasmid approach one heterozygous and one homozygous clone were chosen for further analyses (named *OSTN*₂^{+/-} and *OSTN*^{-/-} respectively).

7.3 Generation and Characterization of hiPSC-derived cortical neurons

7.3.1 Generation and validation of hiPSC-derived cortical neurons

For the majority of the experiments presented in this thesis, hiPSCs were differentiated into cortical neurons passing through an intermediate NPC phase. The identity of the cells and -in general- the quality of the cell culture protocol (Figure 12), were characterized during the differentiation stages with immunofluorescence and RT-PCR.

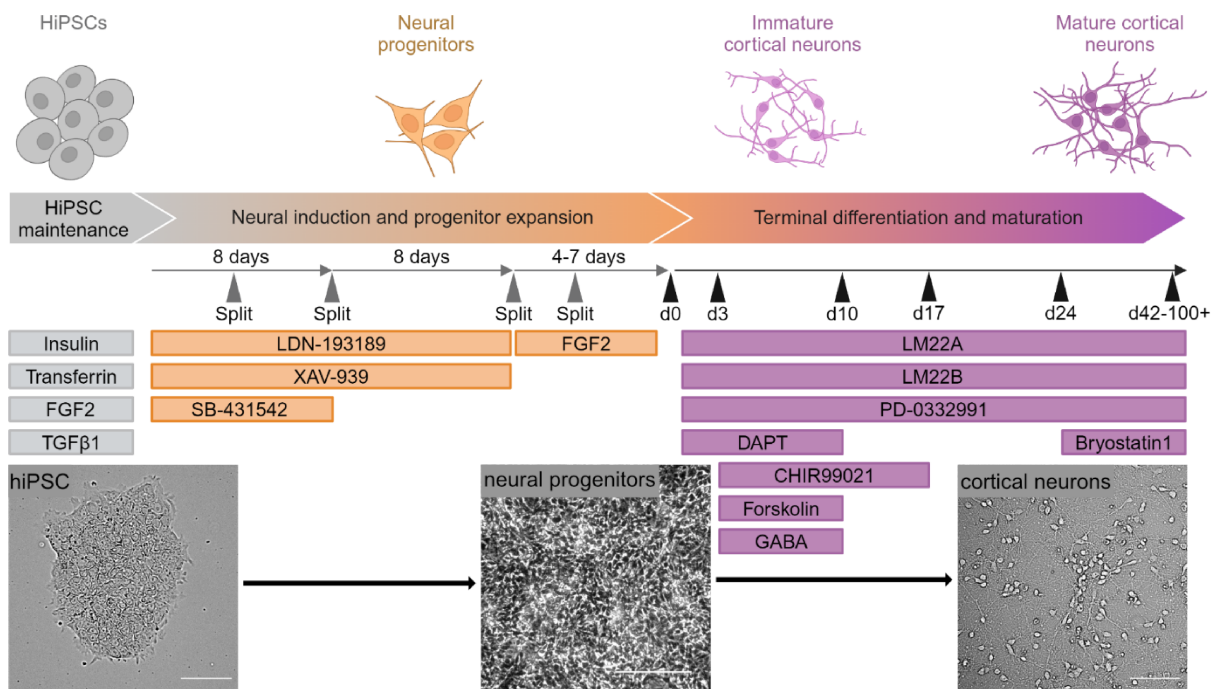


Figure 12: Overview of differentiation protocol from hiPSCs to cortical neurons

Scheme of cell differentiation protocol indicating the different factors and small molecules used in the different phases of the protocol. The duration of the different phases is indicated above the small

Results

molecules. Depicted at the bottom of the figure are representative brightfield pictures of hiPSCs, NPCs and cortical neurons (from left to right). Scale bars = 100 μ m, differentiation diagram was created with BioRender.com

NPCs were tested for general progenitor marker Nestin (NES), for their regional identity by checking for marker expression such as forkhead box G1 (FOXG1) and paired box 6 (PAX6) and SOX2 (Figure 13A), as well as screening for the absence of markers that suggest an undesired patterning (not shown) of NPCs. A validation of the immunostaining was achieved by RT-PCR, confirming further markers for their expression patterns. As shown in figure 13B, the NPCs expressed region specific markers such as orthodenticle homeobox 2 (*OTX2*) and *FOXG1* and displayed low expression of ventral markers like *DLX1* and *DLX2*. Neuronal cultures were also checked for their composition and purity. Therefore, neurons were stained for specific cortical layer markers t-box brain 1 (TBR1, cortical layer VI) and CTIP2 (cortical layer V) and for general pan-neuronal markers such as MAP2, TAU, TUBB3 and neuronal nuclei (NEUN). Furthermore, neuronal cultures were stained for VGLUT1 and GAD2, to validate the efficiency of the protocol in differentiating NPCs in cortical glutamateric neurons. Indeed, the staining showed high levels of the glutamatergic marker VGLUT1 and only a low percentage of GABAergic neurons. Additionally, neuronal cultures were evaluated for astrocyte contamination by staining for GFAP and S100B (Figure 13C), which showed very low amounts of astrocytes. The neuronal characterization by immunostaining was supported by gene expression analyses. With RT-PCR the expression of neuronal subtype markers (*VGLUT1,2* and *GAD1*), neuronal receptors (*GRIN1*, *GRIN2B* and *GRIA2*) and synaptic markers (*SYN*, *SV2*, *SNAP25* and *SYP*) was validated (Figure 13D). This further corroborated the glutamatergic identity of the neuronal cultures and indicated ongoing maturation.

Results

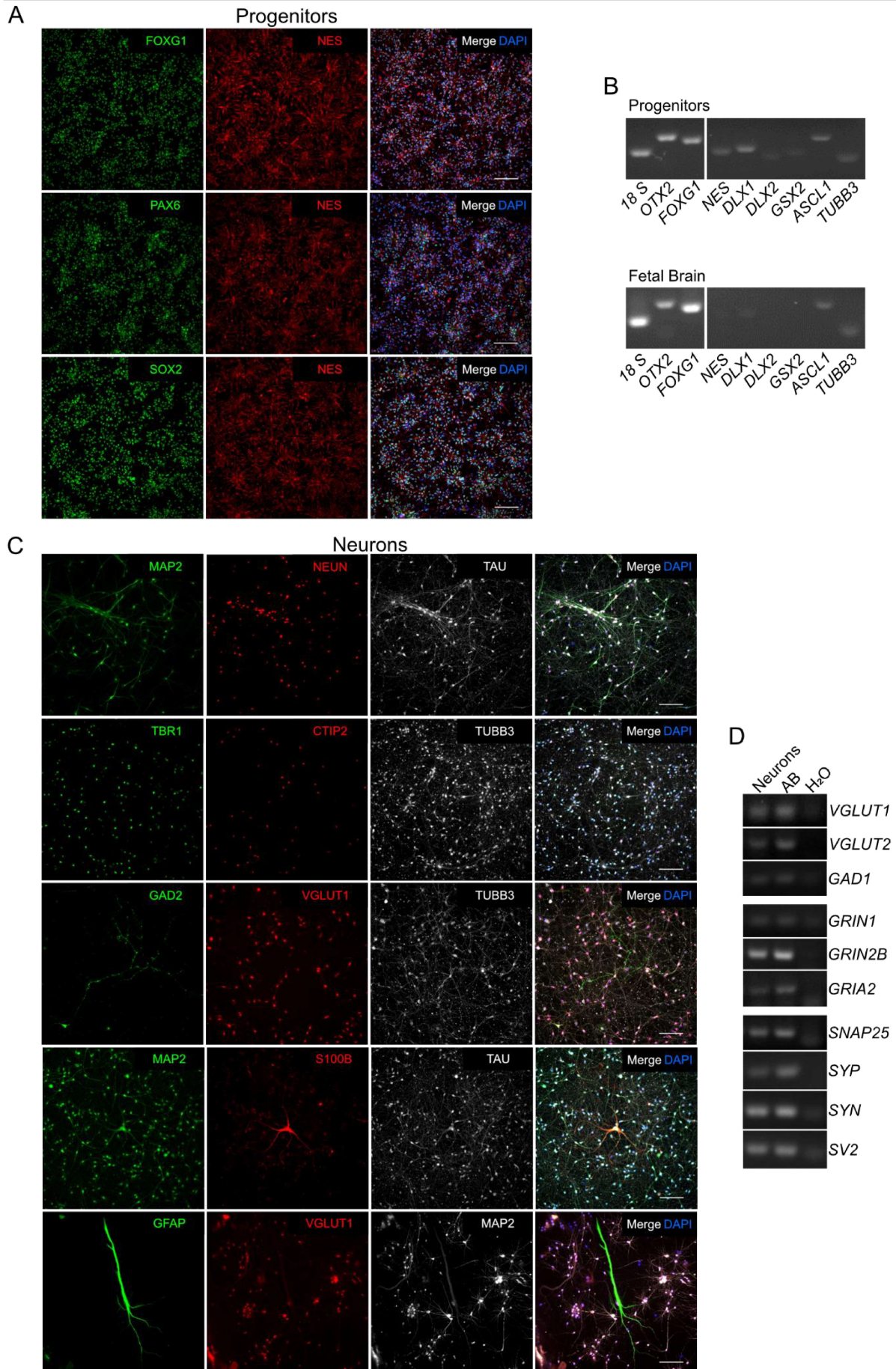


Figure 13: Characterization of NPCs and neuronal cultures

At different stages of neuronal differentiation cells underwent quality control by checking for the regional identity via IF and RT-PCR. **A)** Representative images of progenitor staining for regional identity markers FOXG1, PAX6, SOX2 and general progenitor marker NES. **B)** Representative RT-PCR of progenitors and fetal brain (positive control) for neural progenitor regionalization markers (*OTX2*, *FOXG1*, *DLX1*, *DLX2*, *GSX2*) and general neural progenitor markers (*NES*, *ASCL1*, *TUBB3*). **C)** Representative images of neuronal stainings around d42 of terminal differentiation. Neurons express neuronal markers NEUN, MAP2, TAU, TBR1, CTIP2, TUBB3 and VGLUT1 with low contamination of the culture with astroglia (GFAP, S100B) and GABAergic neurons (GAD2). **D)** Representative RT-PCR of neurons and adult brain (AB, as positive control) of neuronal subtype markers (*VGLUT1* (gene: *SLC17A7*), *VGLUT2* (gene: *SLC17A6*) and *GAD1*), neuronal receptors (*GRIN1*, *GRIN2B*, and *GRIA2*) and synaptic markers (*SYP*, *SYN*, *SV2* and *SNAP25*). Scale bars = 100 μ m.

Overall, neuronal cultures were highly pure consisting of mainly glutamatergic neurons expressing cortical layer markers for layers V/VI with very low contamination by astroglia and GABAergic neurons. Furthermore, neurons expressed various general neuronal markers including synaptic proteins and receptors necessary for neuronal function, proving the effectiveness of the differentiation protocol.

7.3.2 Neuronal cultures show low expression of *OSTN*

The expression of *OSTN* was investigated with several methods such as IF, qPCR, RT-PCR and SDS-PAGE and western blot. *OSTN* was previously shown to be expressed in human and primate brains exclusively and was hypothesized by Ataman et al. to be expressed in a MEF2C-dependent manner, induced by neuronal activity and have a ramification-limiting effect (172). This working hypothesis (Figure 14A) was adopted as a basis for experiments presented in the following paragraph.

Neuronal cultures were first tested for the presence of *OSTN* via IF, with cells displaying a dotted signal when stained with a specific antibody (Figure 14B). Albeit *OSTN* was detectable by IF, it was not possible to confirm its presence by SDS-PAGE and western blot, most likely due to low expression levels since recombinant *OSTN* (positive control) was well detected (Figure 14C). Furthermore, as suggested by Ataman et al., I tested the inducibility of *OSTN* expression with an depolarizing stimulus (172). This was done by KCl stimulation on Ctrl and SCZ neurons (d52) in a proof of principle approach (low N). According to qPCR, *OSTN* mRNA levels were increased in neurons after initial silencing with TTX followed by a 6 h KCl stimulus (55 mM) compared to the respective non-treated neurons (Figure 14D). The fold change for *OSTN* could be detected as +2.45 folds in Ctrl neurons and 3.24 folds in SCZ neurons (normalization on untreated Ctrl). Interestingly, unstimulated SCZ neurons showed a slight decrease when normalized on untreated Ctrl).

Results

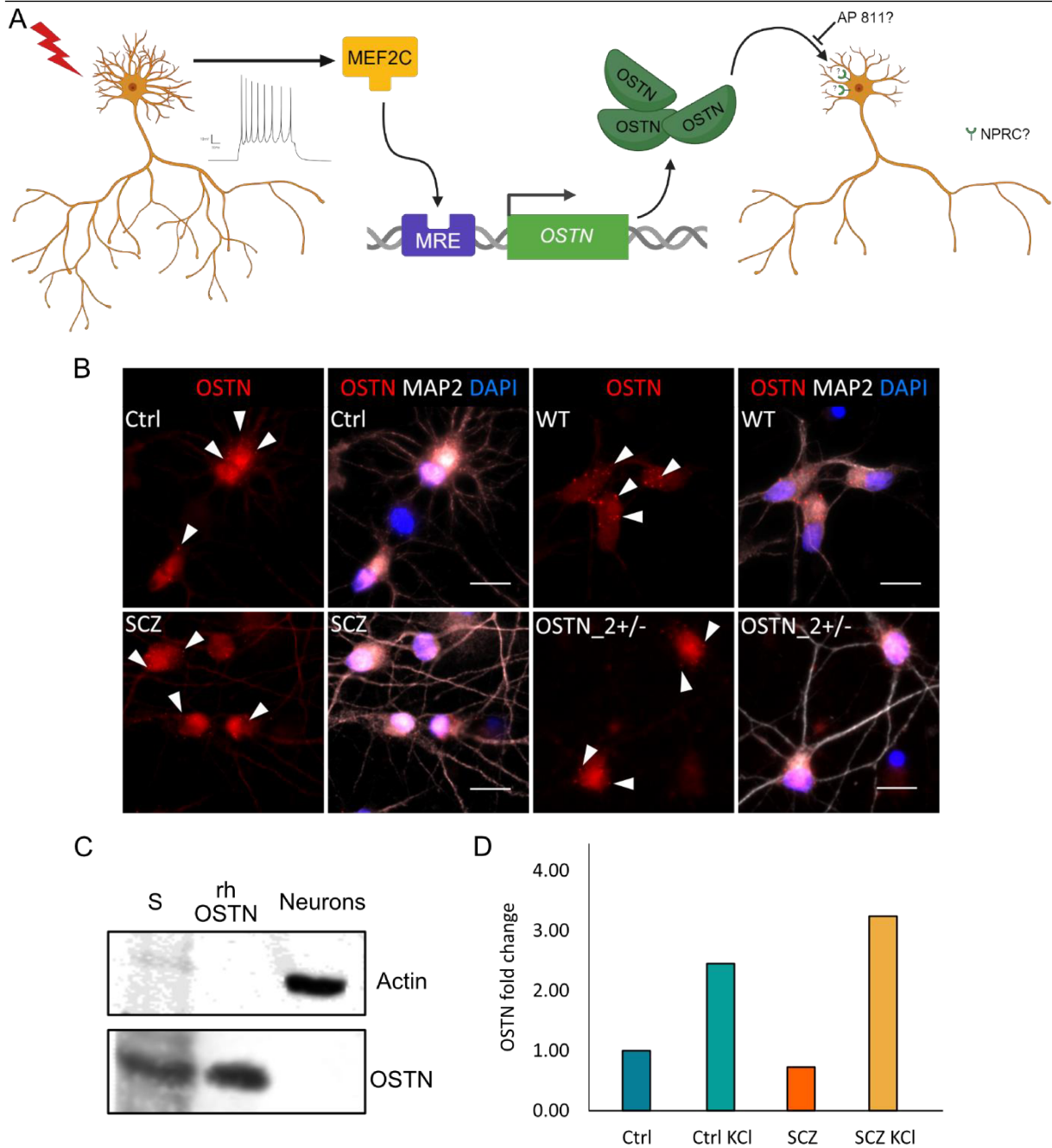


Figure 14: OSTN expression in neuronal cultures

A) Hypothesis how *OSTN* is expressed and its effects on neurons based on Ataman et al. (172). *OSTN* expression is induced by MEF2C and increased upon increased neuronal activity. *OSTN* then reduces neuronal ramification. In the periphery *OSTN* is known to act via the NPRC receptor which may be the case in neurons as well but remains to be confirmed. Created with BioRender.com. **B)** Representative images of *OSTN* IF for Ctrl, SCZ, WT and *OSTN*_{2+/-} neuronal cultures. White arrow heads indicate *OSTN* puncta. Scale bars = 15 μm. **C)** Western blot of rh*OSTN* as positive control and neurons. S is the protein standard. **D)** Test of inducibility of *OSTN* with KCl stimulation. QPCR showed increase in *OSTN* expression after TTX synchronization and subsequent KCl stimulation (6 h, 55 mM) in Ctrl and SCZ neurons (proof of principle). Normalized to Ctrl, data presented as mean, N = 1, n = 3 technical replicates.

These results further corroborated a low *OSTN* expression since expression detection without stimulation happened at rather high cycle numbers (~35 cycles). In summary *OSTN* was

detected and hence expressed by the neurons although at low levels and its levels were modulated by neuronal depolarization as shown in the literature.

7.3.3 RNAseq gene ontology (GO) term analysis uncovered research foci

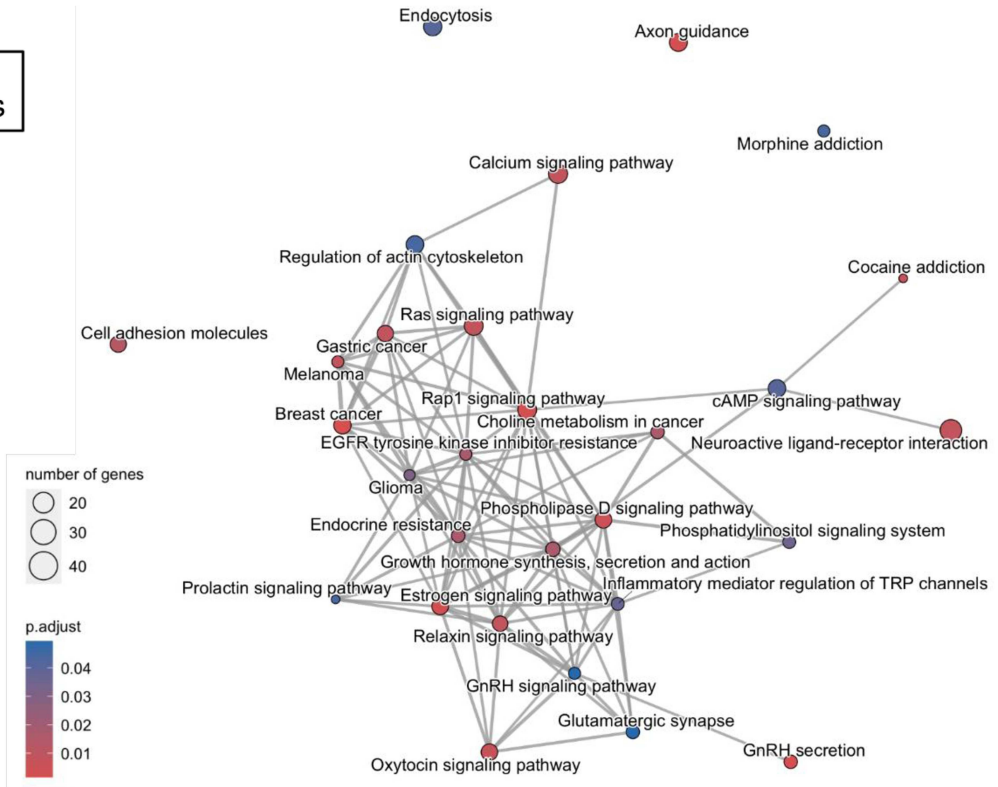
To unravel cellular mechanisms and pathways that are affected by the heterozygous 3q28 deletion and specifically by an *OSTN* mutation, neuronal cultures of Ctrl, SCZ, WT, *OSTN*_1+/- and *OSTN*-/- at d42 of the terminal differentiation were processed for whole transcriptome RNA bulk sequencing. After a successful sequencing granted by the bioinformatic quality control, lists of differentially expressed genes (DEG) were generated and used to perform GO enrichment and Kyoto Encyclopedia of Genes (KEGG) analyses. Significantly enriched GO terms contain clusters of genes that are involved in specific processes and are differentially expressed between the SCZ lines and the control, a feature that is useful to extrapolate fields of interest for further investigation. The KEGG and GO analyses for biological process, molecular function and cellular component for Ctrl and SCZ neurons revealed, among others, enrichment of terms related to neuronal growth and morphology like axon guidance, regulation of actin cytoskeleton (Figure 15A), axon development, axonogenesis, regulation of axonogenesis, regulation of neurogenesis (Figure 15B), actin binding (Figure 15C), growth cone and site of polarized growth (Figure 15D). Another field of interest that arose in the GO analysis was synapses and functionality, since the following GO terms were enriched among others: neuroactive ligand-receptor interaction (Figure 15A), modulation of chemical synaptic transmission, regulation of trans-synaptic signaling, synapse organization, synapse assembly (Figure 15B), voltage-gated potassium channel activity, voltage-gated channel activity, calcium ion transmembrane transporter activity, glutamate receptor binding (Figure 15C), postsynaptic density, glutamatergic synapse, dendritic spine, synaptic membrane, neuron to neuron synapse, etc. (Figure 15D). These GO term enrichments were a corroboration of morphology, development and synapses as fields of interest for further experiments.

The comparison between WT, *OSTN*_1+/- and *OSTN*-/- RNAseq data likewise revealed GO term enrichment in similar fields of interest such as, for *OSTN*_1+/- line, neuropeptide signaling pathway (Figure 16A), neuropeptide receptor binding, neuropeptide receptor activity (Figure 16B), axon terminus, neuron projection terminus, distal axon, postsynaptic membrane and neuron to neuron synapse (Figure 16C), while for *OSTN*-/-, terms like axon guidance, axonogenesis, neuron projection guidance and axon development (Figure 16D), neuron projection terminus and axon terminus (Figure 16E) were found to be enriched. These results represented the foundations of subsequent analyses in the wet lab.

Results

A

KEGG analysis



B

Biological process

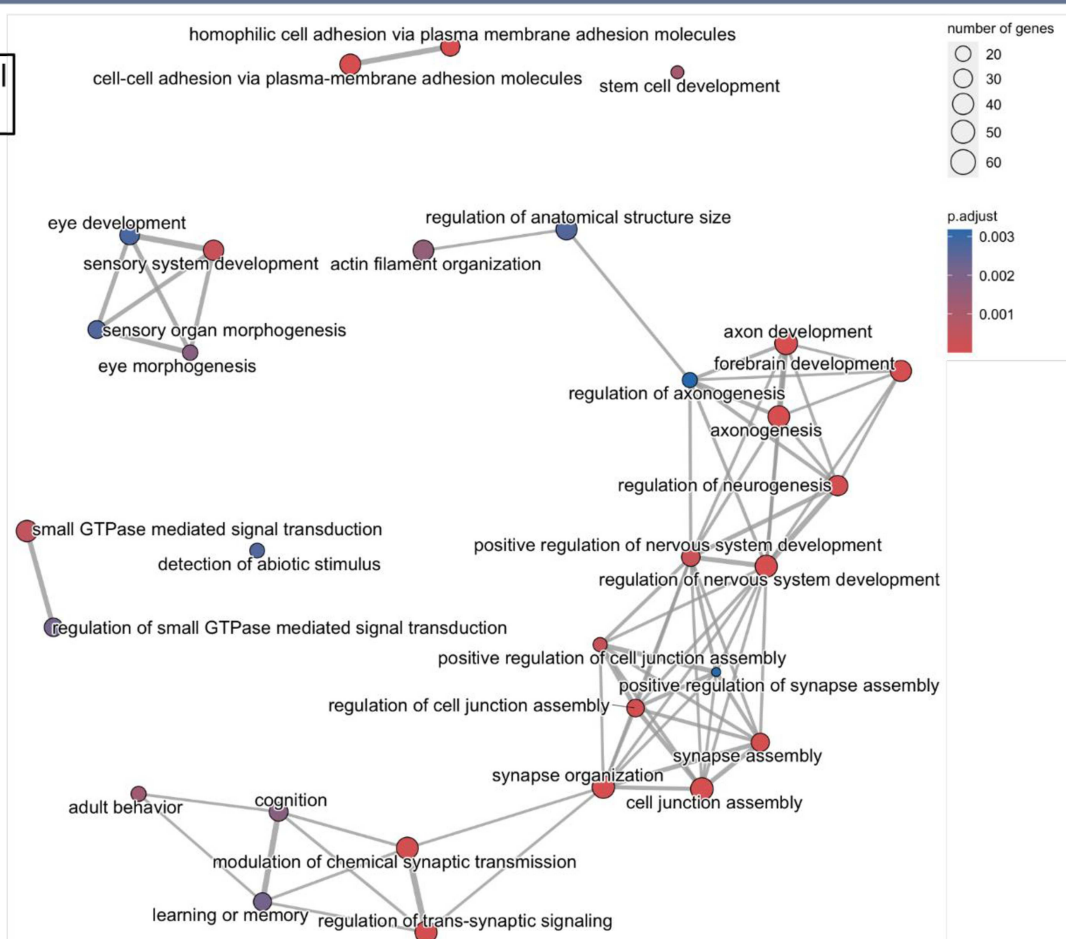
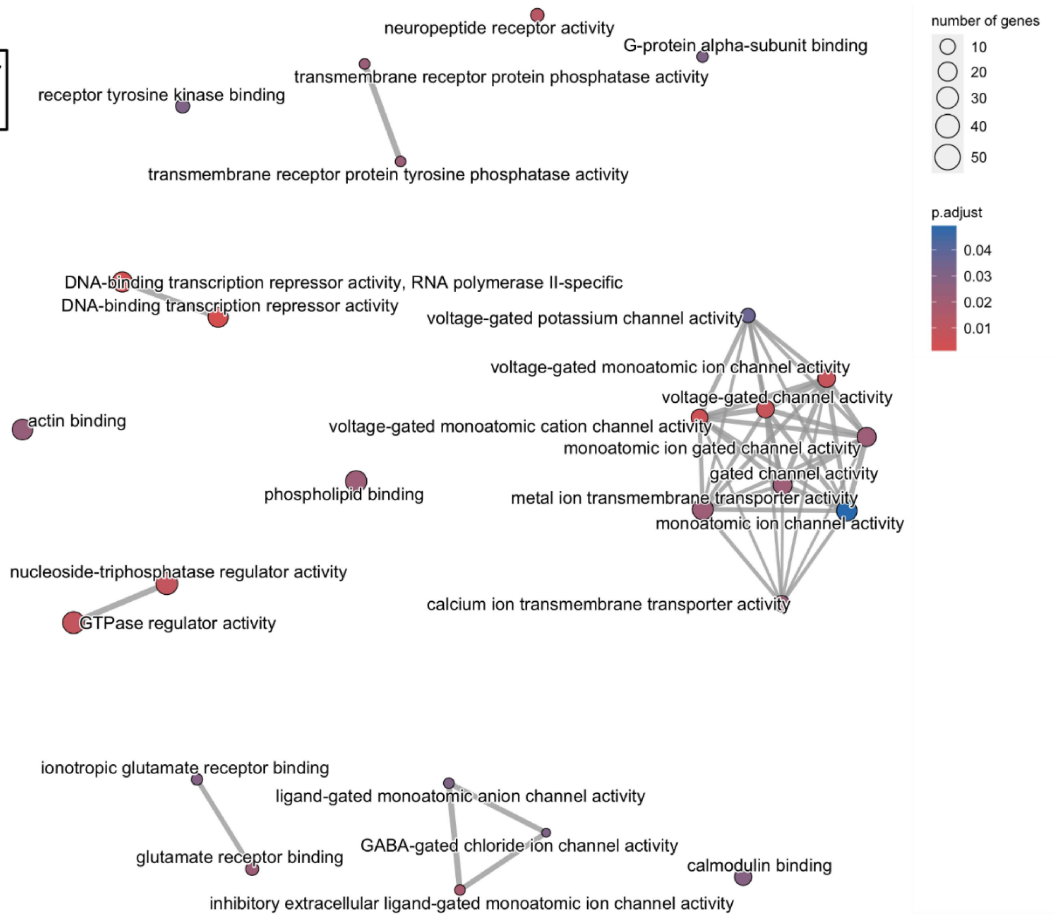


Figure continued on the next page.

Results

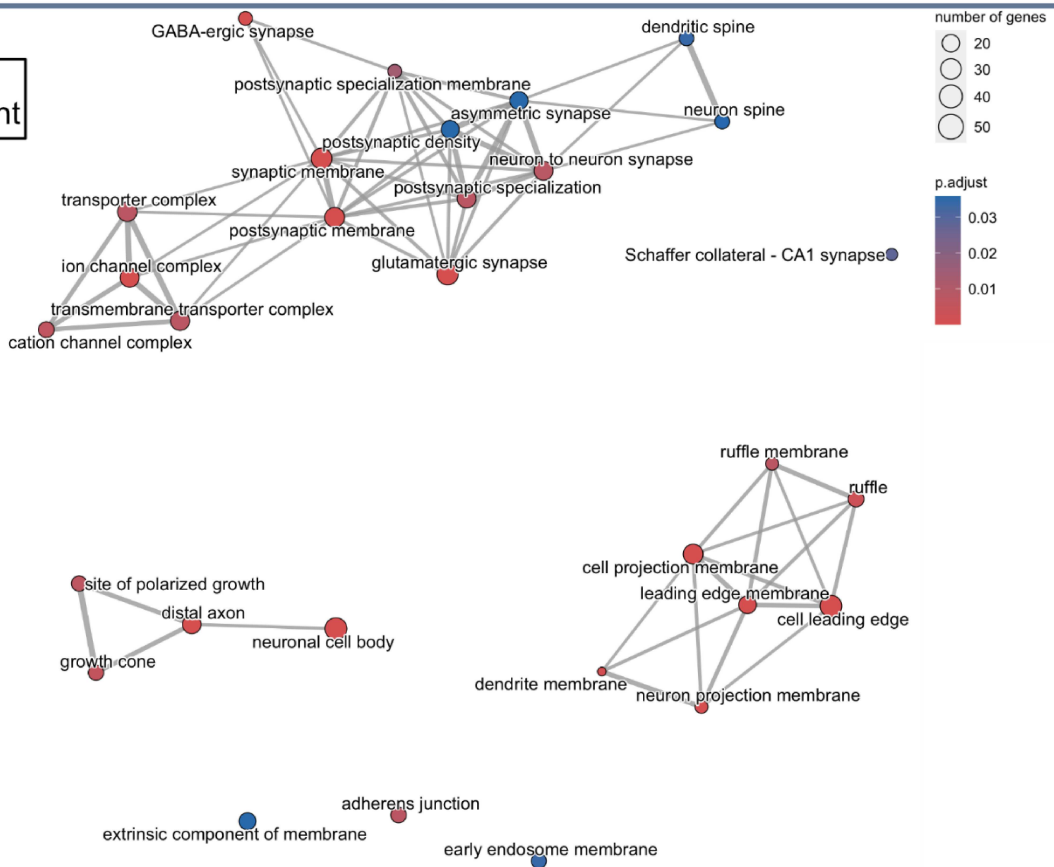
C

Molecular function



D

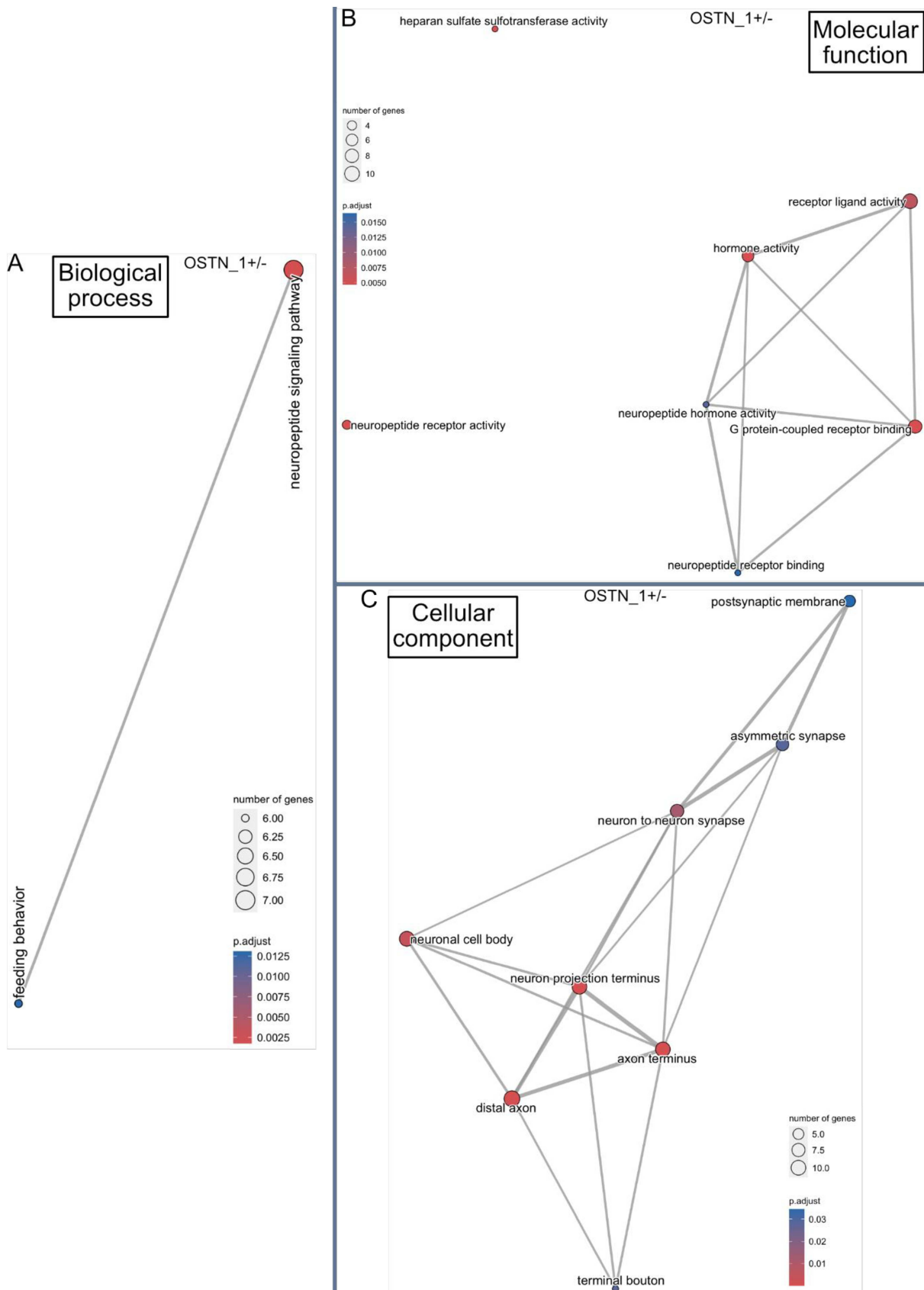
Cellular component



Results

Figure 15: GO term enrichment of d42 Ctrl and SCZ neurons

Semantic clustering of enriched GO terms for SCZ vs. Ctrl neuronal cultures categorized in **A) KEGG**, **B) Biological process**, **C) Molecular function** and **D) Cellular component**. N = 3 individual batches per cell line. Statistics and graphs by Dr. Anne Hoffrichter.



Results

Figure continued from previous page.

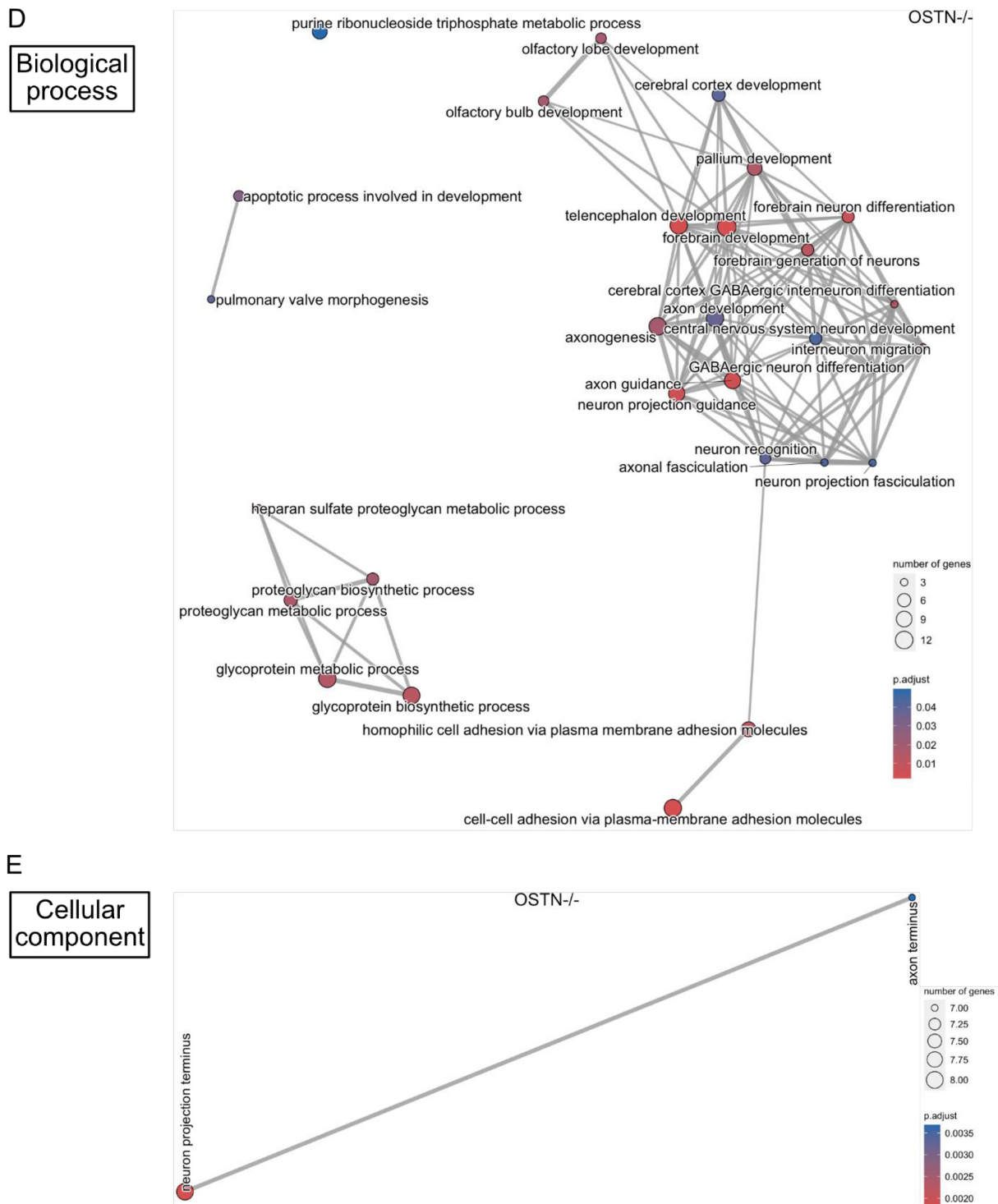


Figure 16: GO term enrichment of d42 WT, OSTN₁^{+/-} and OSTN^{-/-} neurons

Semantic clustering of enriched GO terms categorized in **A)** Biological process for OSTN₁^{+/-}, **B)** Molecular function for OSTN₁^{+/-} vs. WT, **C)** Cellular component for OSTN₁^{+/-} vs. WT, **D)** Biological process for OSTN^{-/-} vs. WT and **E)** Cellular component for OSTN^{-/-} vs. WT neuronal cultures. N = 2-3 individual batches per cell line (OSTN^{-/-} N = 2). Statistics and graphs by Dr. Anne Hoffrichter.

7.4 Heterozygous 3q28 deletion impacts neuronal morphology

In the following analyses, starting from section 7.4.6, some results are preliminary due to low N numbers that are indicated in the figure captions. This especially refers to some of the treatments used.

7.4.1 Impact of heterozygous 3q28 deletion on morphology-related genes

An impact of the heterozygous 3q28 deletion on neuronal morphology was already apparent from the GO term analysis described in the previous section. More in detail, DEG analysis showed several genes directly and indirectly involved in neuronal outgrowth to be expressed significantly different between SCZ and Ctrl (Figure 17A).

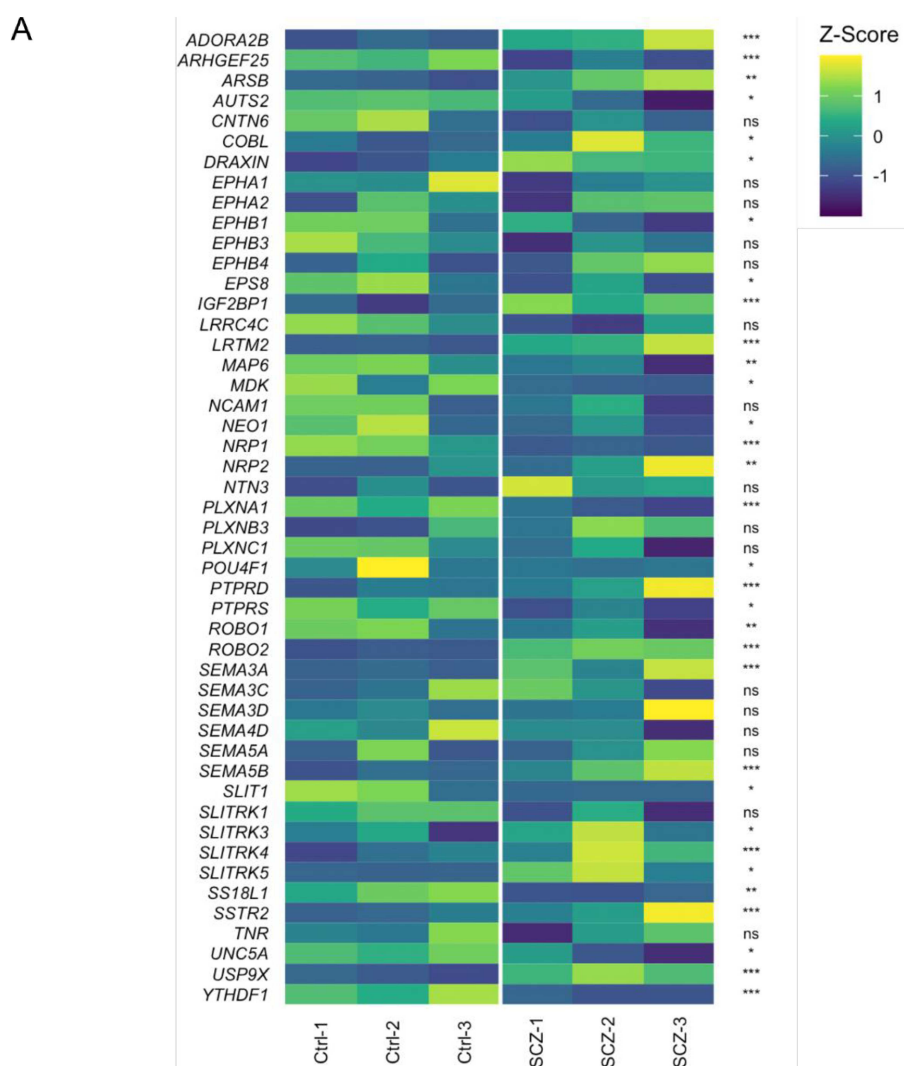


Figure continued on the next page.

Results

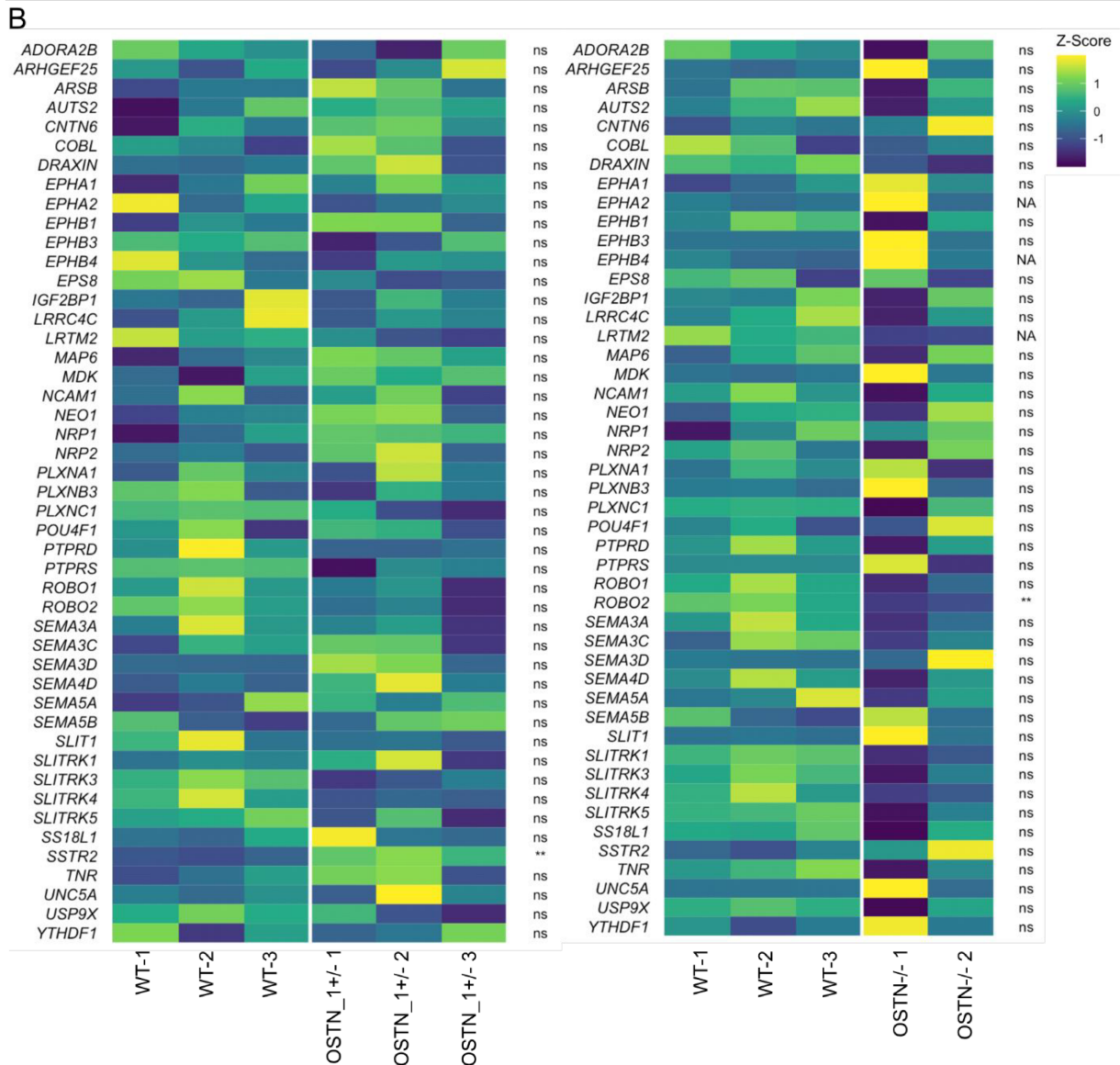


Figure 17: Differentially expressed genes related to neuronal morphology of d42 neurons

Genes listed are involved in axon guidance, neurite outgrowth and branching. **A**) Heatmap (z-scaled) of gene expression for Ctrl vs. SCZ neurons (RNAseq). **B**) Heatmaps (z-scaled) of gene expression for WT vs. OSTN_{1+/-} and WT vs. OSTN^{-/-} neurons (RNAseq). Benjamini-Hochberg adjusted p-values calculated with Wald test, * $p < 0.05$, ** $p < 0.01$, *** $p < 0.001$, Heatmaps and statistics by Dr. Anne Hoffrichter.

As an example, genes that are known to be involved in axon guidance such as a member of the ephrin family (ephrin type-B receptor 1: *EPHB1*) and semaphorins (*SEMA3A*, *SEMA5B*), but also genes involved in processes such as axon guidance, neurite outgrowth and branching: arylsulfatase B (*ARSB*), cordon-bleu WH2 repeat protein (*COBL*), dorsal inhibitory axon guidance protein (*DRAXIN*), neuropilin 2 (*NRP2*), protein tyrosine phosphatase receptor type D (*PTPRD*), roundabout guidance receptor 1 (*ROBO1*), *ROBO2*, slit guidance ligand 1 (*SLIT1*), somatostatin receptor 2 (*SSTR2*), unc-5 netrin receptor A (*UNC5A*) etc.

Between WT and OSTN_{1+/-} only *SSTR2* could be detected as significantly differently expressed, while between WT and OSTN^{-/-} only *ROBO2* was significantly differently

expressed (Figure 17B). The remaining genes from the list were not significantly different, however several genes showed an interesting modulation trend.

7.4.2 Increased neurite length in young neurons with heterozygous 3q28 deletion

As already described in the introduction the 3q28 locus harbors two genes -*OSTN* and *IL1RAP*- that might be involved in the modulation of neuronal morphology. On one side, *OSTN* was found to be evolutionarily repurposed in human and primate brains to limit neuronal ramification especially following increased neuronal activity (172). On the other, *IL-1RAP* as an essential part of the *IL-1 β* signaling pathway, takes effect on neuronal morphology as well since *IL-1 β* signaling was shown to reduce neuronal ramification (138,163,165). Therefore, also in light of the results of the sequencing analyses, I pursued the investigation of neuronal morphology, first, in an early outgrowth assay. For this purpose, Ctrl and SCZ iPSC-derived neurons were stained for the pan-neuronal markers MAP2 and TAU on day 3 and 5 after plating (Figure 18A). Three parameters were determined: 1. the total length of neurons; 2. total number of neurites and 3. the number of branchpoints (Figure 18B). The total length of neurons was not significantly different between Ctrl and SCZ on d3 (Ctrl = $251.6 \pm 5.44 \mu\text{m}$ and SCZ = $266.7 \pm 5.662 \mu\text{m}$), while on d5 SCZ neurons were overall significantly bigger than Ctrl neurons (Ctrl = $267.2 \pm 7.384 \mu\text{m}$, SCZ = $316.1 \pm 8.921 \mu\text{m}$). Additionally, the size increase of SCZ neurons was significant from d3 to d5. The total number of neurites on d3 was significantly lower in SCZ neurons (Ctrl = 4.397 ± 0.1278 , SCZ = 4.002 ± 0.1465) but this difference was diminished on d5, and no significant difference was observed between Ctrl and SCZ cells (Ctrl = 5.125 ± 0.1525 , SCZ = 4.987 ± 0.1772). Moreover, both Ctrl and SCZ neurons showed significant increase in the total number of neurites on d5 compared to d3. Lastly, going along with the results of the total number of neurites, the number of branch points on d3 was significantly lower in SCZ neurons (Ctrl = 1.673 ± 0.1116 , SCZ = 1.491 ± 0.1208). On d5 I did not find a significant difference between the lines (Ctrl = 2.210 ± 0.1413 , SCZ = 2.386 ± 0.1583), although SCZ neurons displayed a tendency to surpass Ctrl neurons in the number of branch points. SCZ neurons also showed a significant increase of branch points from d3 to d5.

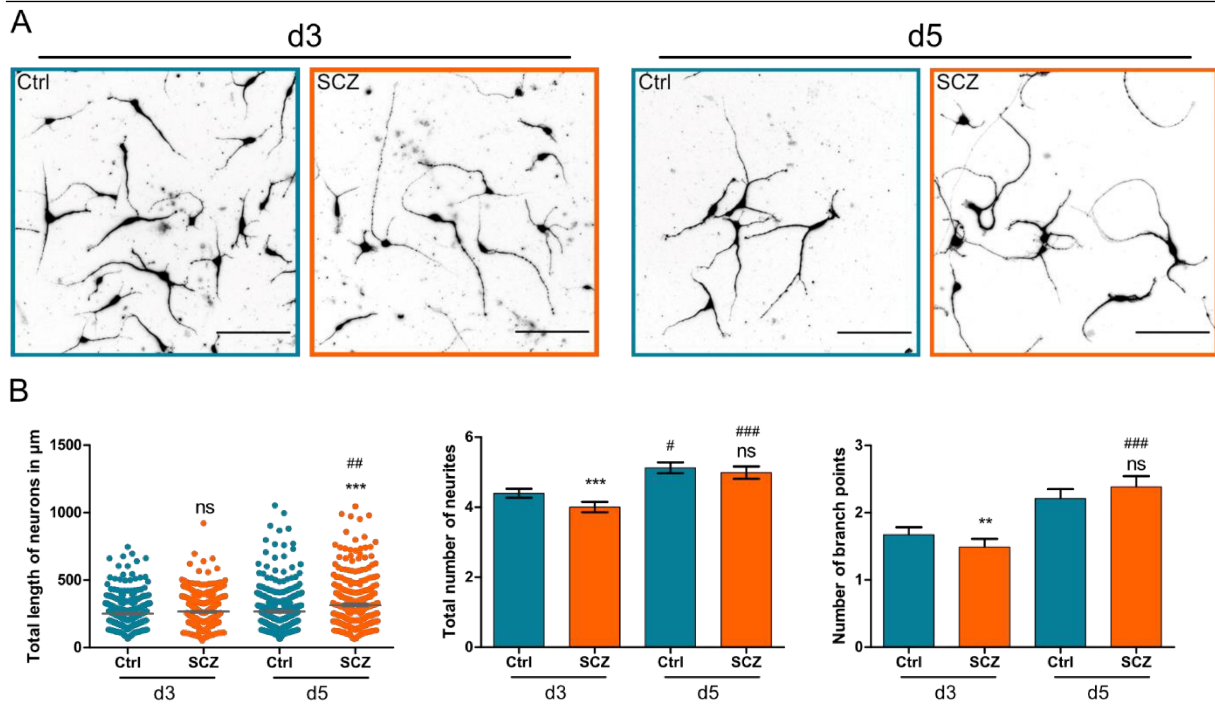


Figure 18: Early outgrowth assay of Ctrl and SCZ neurons

A) Representative binary images of Ctrl and SCZ neurons on d3 and d5 of the assay. Scale bars = 100 μm . **B)** Analysis results of the early outgrowth assay, total length of neurons in μm , total number of neurites and number of branch points (from left to right). Results are presented as mean \pm SEM, N = 2 individual batches, n = 376-401 cells per line and time point, Kruskal-Wallis test with Dunn's multiple comparison test, * compares Ctrl vs. SCZ, # compares time point Ctrl vs. Ctrl/SCZ vs. SCZ, */# $p < 0.05$, **/### $p < 0.01$, ***/### $p < 0.001$, ns = not significant.

7.4.3 SCZ neurons display higher ramification and an increased size compared to Ctrl cells (d55-60)

To investigate more mature, complex and functional neurons and to verify the phenotype of SCZ neurons, dense neuronal cultures were transduced with an AAV expressing mCherry under the CaMKIIa promoter. After two to three weeks, low efficiency transduction led to a sparse labeling with mCherry. The morphological analyses were then run on d55-60 neurons stained for MAP2 and mCherry. The mCherry⁺ neurons were traced and Sholl analysis was performed at a radius step size of 15 μm (306). Representative tracings are depicted in Figure 19A). Based on the Sholl analysis additional parameters could be calculated such as the number of primary neurites, sum of intersections and the total length of neurons. The morphological analysis of Ctrl and SCZ neurons showed that at 30 μm from the soma both cell lines had the highest number of intersections (Ctrl 15.58 ± 0.4066 , SCZ 11.62 ± 0.2557). Starting from 60-195 μm from the soma, the number of intersections between Ctrl and SCZ were significantly higher in SCZ neurons (largest difference at 75 μm Ctrl 5.377 ± 0.3078 , SCZ 7.906 ± 0.2632). From 210-300 μm there was no significant difference in neuronal complexity (Figure 19B). Ctrl neurons had significantly higher numbers of primary neurites (Ctrl $11.66 \pm$

Results

0.3131; SCZ 10.49 ± 0.249), but the sum of intersections (Ctrl 77.74 ± 2.743 ; SCZ 92.83 ± 2.515) and the total length in μm (Ctrl $1166 \pm 41.15 \mu\text{m}$; SCZ $1393 \pm 37.73 \mu\text{m}$) showed higher values for SCZ neurons amounting to overall bigger and more ramified neurons in the SCZ context (Figure 19C).

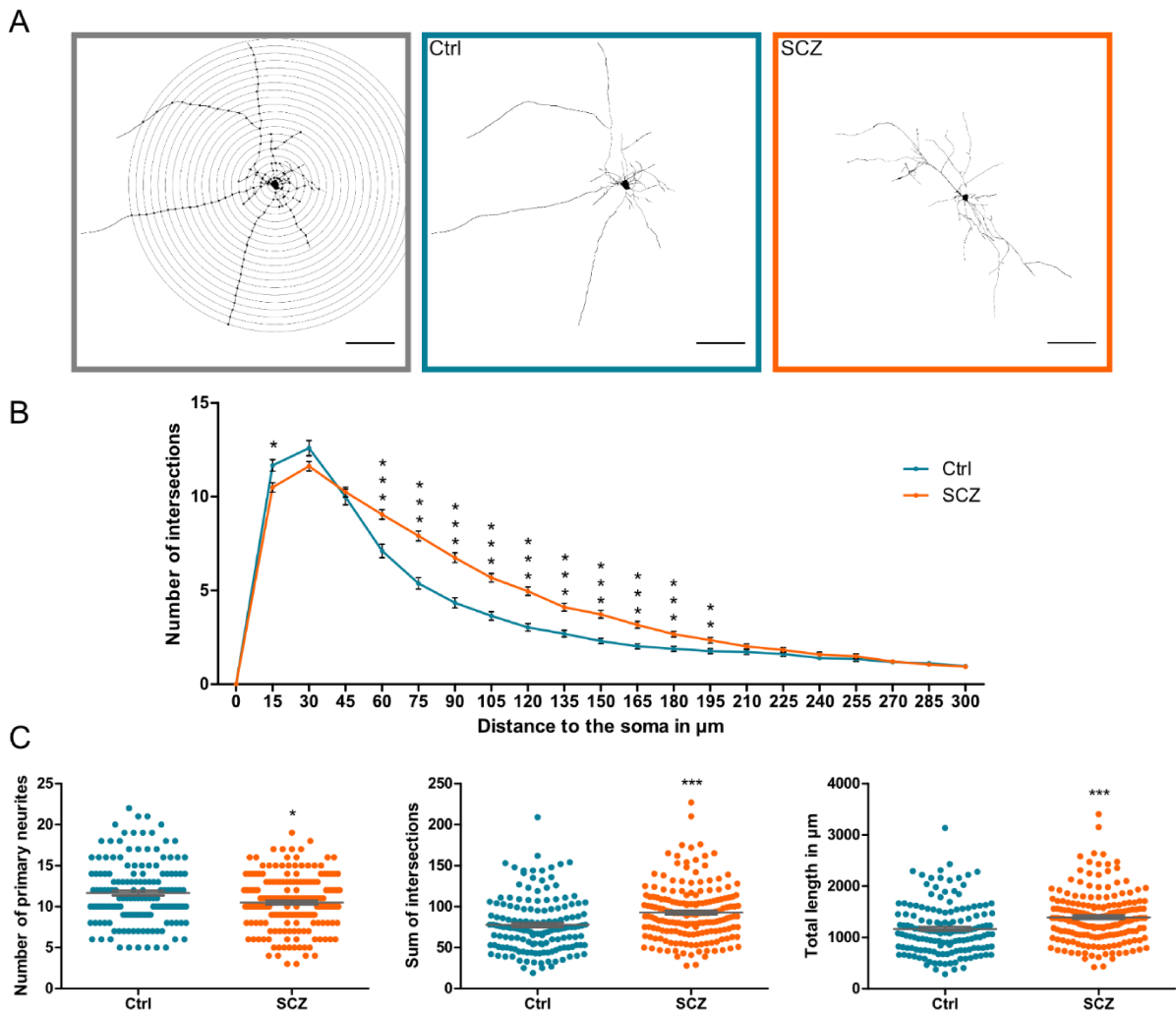


Figure 19: Sholl analysis of Ctrl and SCZ neurons (d55-60)

Neuronal cultures were transduced with an AAV that enables mCherry expression under the CaMKII α promoter and subsequently analyzed. **A)** Representative images of Sholl analysis principle and reconstructed Ctrl and SCZ neurons. Sholl circle image is enclosed in a gray frame. Scale bars = 100 μm . **B)** Results of Sholl analysis Ctrl vs. SCZ neurons, plotted are the number of intersections and the distance to the soma. Sholl radius step size = 15 μm . **C)** Results of further morphology parameters: number of primary neurites, sum of intersections and the total length of neurons. N = 3 batches, Ctrl n = 151 neurons, SCZ n = 180 neurons, data presented as mean \pm SEM, Kruskal-Wallis test with Dunn's multiple comparison test, * $p < 0.05$, ** $p < 0.01$, *** $p < 0.001$

7.4.4 Investigation of *OSTN* impact on neuronal morphology as a 3q28-located gene

In order to validate the morphological phenotype of Ctrl and SCZ neurons and to pinpoint the influence of specifically *OSTN* on neuronal morphology, *OSTN* mutant lines were analyzed in the same way. Therefore, WT, *OSTN*_1+/-, *OSTN*_2+/- and *OSTN*-/- neurons (d55-60) were transduced with the AAV (as previously described) and Sholl analysis was performed on mCherry⁺ neurons (Figure 20A). The results of *OSTN*_1+/- and *OSTN*-/- should be seen as preliminary, since a higher sample size would be necessary to make a statistically valid point. Nonetheless, *OSTN*_1+/- and *OSTN*-/- display the highest number of intersections at 15 μ m from the soma (*OSTN*_1+/- 11.9 ± 0.6962 ; *OSTN*-/- 9.125 ± 0.7347), while WT neurons display it at 30 μ m (12.366 ± 0.725) and *OSTN*_2+/- at 45 μ m (11.155 ± 0.5086). *OSTN*-/- neurons showed significantly less intersections than WT from 30-255 μ m from the soma, while *OSTN*_1+/- displayed significantly less intersections from 60-105 μ m and only from 210-300 μ m there was a non-significant trend that *OSTN*_1+/- had slightly more intersections than WT neurons. Heterozygous *OSTN*_2+/- neurons showed significantly more intersections than WT neurons from 60-105 μ m, further distal from the soma, WT neurons had slightly more intersections (Figure 20B). *OSTN*_2+/- neurons were shown to have significantly fewer primary neurites than WT neurons (WT 11.23 ± 0.4927 ; *OSTN*_2+/- 8.68 ± 0.279), whereas there were no considerable differences of WT towards *OSTN*_1+/- (11.9 ± 0.696) or *OSTN*-/- (9.125 ± 0.735) neurons. For the two parameters sum of intersections and total length, the only significant difference was between *OSTN*-/- and WT neurons (WT sum of intersections 102.4 ± 7.461 ; total length $1535 \pm 111.9 \mu$ m) while *OSTN*-/- neurons (*OSTN*-/- sum of intersections 40.25 ± 2.741 ; total length $603.8 \pm 41.12 \mu$ m) displayed lower values. The heterozygous clones merely showed non-significant tendencies for sum of intersections (*OSTN*_1+/- 71.97 ± 5.739 ; *OSTN*_2+/- 95.36 ± 4.196) and total length (*OSTN*_1+/- $1080 \pm 86.09 \mu$ m; *OSTN*_2+/- $1430 \pm 62.94 \mu$ m) which amounted to overall lower values than WT neurons (Figure 20C).

Results

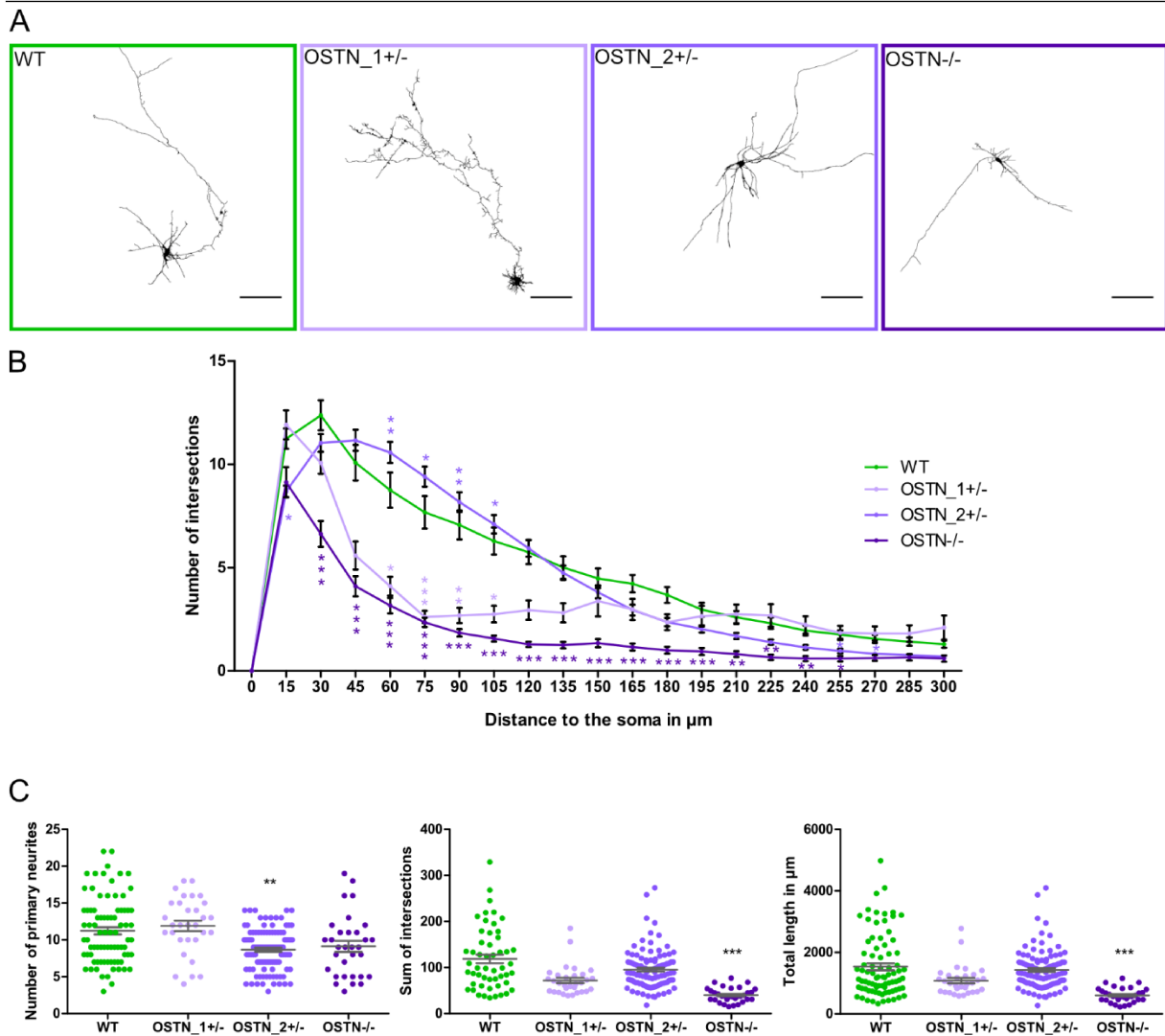


Figure 20: Sholl analysis of WT and *OSTN* mutant neurons (d55-60)

Neuronal cultures were transduced with an AAV that enables mCherry expression under the CaMKII α promoter and subsequently analyzed. **A)** Representative images of reconstructed WT, *OSTN_1*^{+/-}, *OSTN_2*^{+/-} and *OSTN*^{-/-} neurons. Scale bars = 100 μ m. **B)** Results of Sholl analysis, WT vs. *OSTN_1*^{+/-}, *OSTN_2*^{+/-} and *OSTN*^{-/-} neurons, plotted are the number of intersections and the distance to the soma. Sholl radius step size = 15 μ m. **C)** Results of further morphology parameters: number of primary neurites, sum of intersections and the total length of neurons. WT N = 3 batches, n = 82 neurons, *OSTN_1*^{+/-} N = 1 batch, n = 31 neurons, *OSTN_2*^{+/-} N = 3 batches, n = 103 neurons, *OSTN*^{-/-} N = 1 batch, n = 32 neurons, data presented as mean \pm SEM, Kruskal-Wallis test with Dunn's multiple comparison test, * $p < 0.05$, ** $p < 0.01$, *** $p < 0.001$

In summary, the phenotype of SCZ neurons could not exactly be replicated for the *OSTN* mutant neurons, however especially for the WT cells it must be mentioned that a strong batch variation occurred. This is in line with the intrinsic variability of the iPSC system that together with a high fidelity to human physiology can bring high variation in the output of the analysis. This should be addressed by increasing the number of batches. To demonstrate this variability, single WT batches were plotted (Appendix Figure S1). Before batch 3, that seemingly behaves atypical compared to the other two batches, was included, the phenotypes of WT and

OSTN₂^{+/-} were closer to the SCZ neuron phenotype, which can be seen in Figure S2 (Appendix) to illustrate the influence of single batches and batch variability.

7.4.5 Neuronal cultures respond to IL-1 β pathway activation

After the identification of morphological phenotypes in SCZ neurons and a partial reproducibility of these observations also in *OSTN* mutant cells, new questions arose. First as mentioned before, another candidate gene was identified on the 3q28 locus, *IL1RAP* which is an essential co-receptor in the IL-1 β pathway. Hence, I decided to investigate if the IL-1 β pathway impacted neuronal morphology like it has been previously hypothesized (163,165). IL-1 β signaling in neurons supposedly reduces neuronal ramification similar as *OSTN* (Figure 21A). Therefore, cells were initially treated with IL-1 β to determine via qPCR if cells were responsive to this signaling. Ctrl and SCZ neurons were tested and showed an increase in IL-1 β expression after 24 h IL-1 β treatment by 5.21 fold (Ctrl) and 3.95 fold (SCZ) compared to the respective untreated neurons (normalized to untreated neurons respectively, Figure 21B). In conclusion, neurons were responsive to IL-1 β treatment and recombinant IL-1 β was effective.

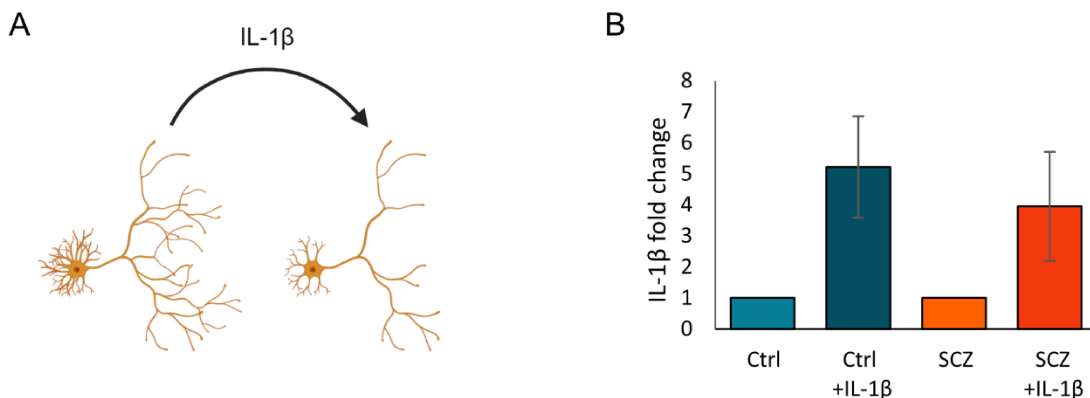


Figure 21: IL-1 β responsiveness of neurons

A) Hypothesized influence of IL-1 β on neuronal morphology. Created with BioRender.com. **B)** Results of qPCR of d42 neurons with or without IL-1 β treatment. N = 3, data presented as mean \pm SEM

7.4.6 Influence of *OSTN* and IL-1 β pathways on Ctrl and SCZ neuronal morphology

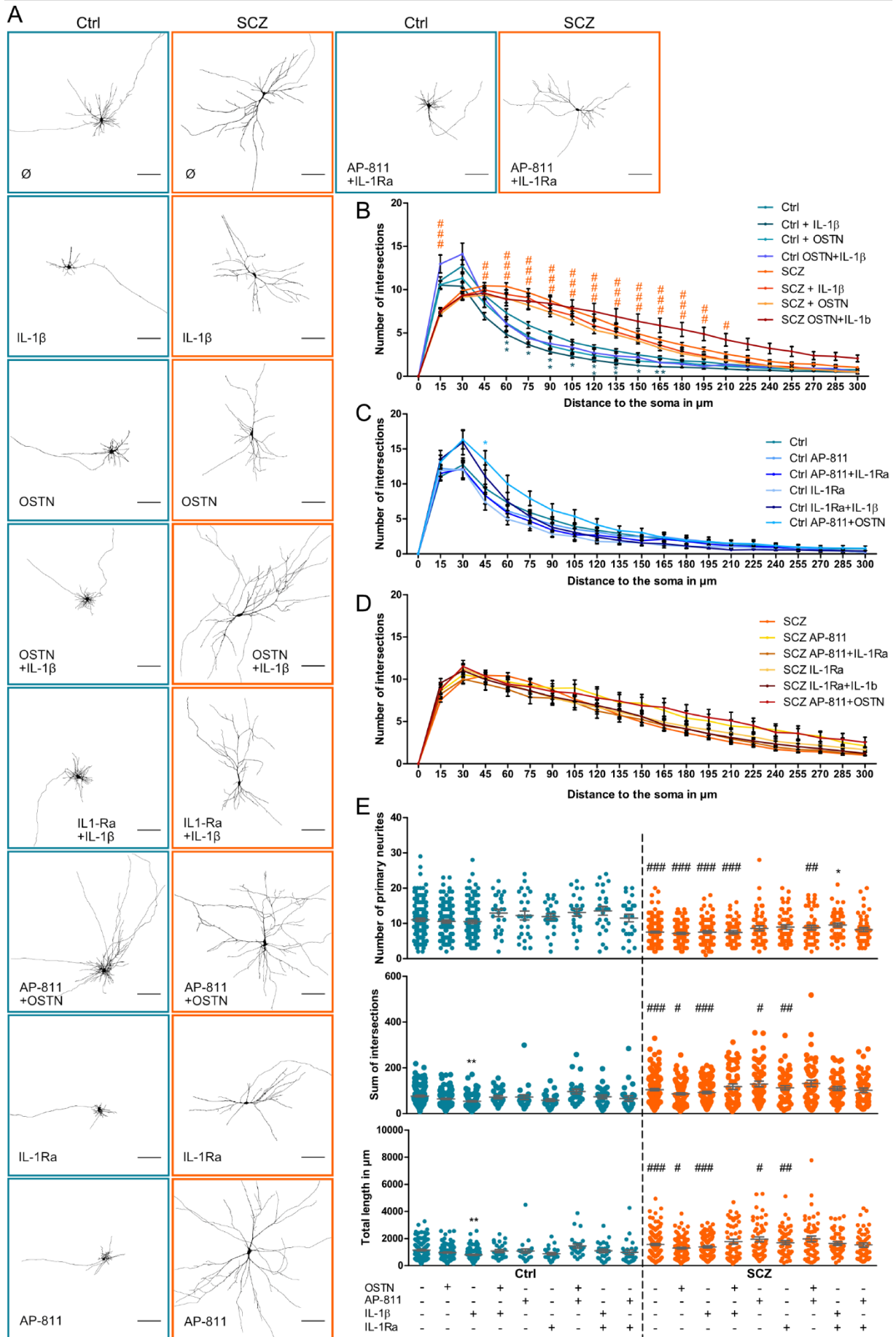
Following the validation of the IL-1 β induced neuronal response, the next experiments were designed to determine the influence of the IL-1 β pathway on the neuronal morphology. Furthermore, to deepen the investigation of the influence of a heterozygous 3q28 deletion on neuronal morphology the combination of the *OSTN* mutation and interference with the IL-1 β pathway were analyzed. Additionally, it was tested if the neuronal phenotypes could be rescued by stimulation or inhibition of the respective pathway. Therefore, complex combinations of

Results

pathway antagonists and agonists of the IL-1 β pathway (IL-1 β as agonist, IL-1Ra as antagonist) and OSTN pathway (OSTN supplementation and AP-811 as another competitive NPRC antagonist) were applied on Ctrl, SCZ, WT and OSTN_2+/- neuronal cultures that were transduced with the AAV. The following combinations were investigated in this preliminary experiment: untreated, 50 ng/ml IL-1 β (5d), 100 nM OSTN (7d), 100 nM OSTN (7d) + 50 ng/ml IL-1 β (5d), 100 ng/ml IL-1Ra (5d) + 50 ng/ml IL-1 β (5d), 200 nM AP-811 (8d) + 100 nM OSTN (7d), 100 ng/ml IL-1Ra (5d), 200 nM AP-811 (8d) and 200 nM AP-811 (8d) + 100 ng/ml IL-1Ra (5d). The experiment was performed on d55-60 AAV-transduced neurons.

The results of the Sholl analysis of this initial experiment on Ctrl and SCZ neurons suggested that some of the treatment combinations indeed had the potential to alter neuronal morphology (Figure 22A). The first Sholl graph plots untreated, IL-1 β , OSTN and OSTN+IL-1 β for Ctrl and SCZ neurons, statistics marked with asterisks compares within the group (same cell line, and always vs. "untreated") e.g. Ctrl+IL-1 β vs. untreated Ctrl; statistics marked with a rhombus compares the two cell lines' untreated condition (Figure 22B). The conditions untreated, IL-1 β and OSTN were performed with a statistical valid N number while the other treatment conditions were initial experiments and need further validation. The Ctrl neurons treated with IL-1 β showed significantly reduced number of intersections from 60-165 μ m from the soma and in general trended (non-significant) towards fewer intersections starting already from 30 μ m from the soma. The other treatments were not significantly different from the untreated neurons, however OSTN treatment led to an overall reduction in intersections starting at 30 μ m from the soma. The combination of IL-1 β and OSTN treatment of Ctrl neurons did not induce significant differences in intersections but showed a higher number at 15-30 μ m and a general reduction starting at ca. 45 μ m from the soma, aligning with OSTN treated Ctrl neurons. The results for SCZ neurons were less clear since there were no significant differences but only very subtle trends toward less intersections of neurons with IL-1 β and OSTN single treatments (starting at 30 μ m from the soma). The combination treatment of IL-1 β +OSTN showed less intersections from 30-105 μ m from the soma, but then even displayed higher number of intersections starting at 120 μ m from the soma compared to the untreated SCZ neurons. Of note, statistically significant differences between Ctrl and SCZ (untreated) could be reproduced from former experiments. For better clarity and comprehensibility, the next two graphs show the remaining treatments plotted separately for Ctrl and SCZ. Further, my focus in this initial experiment was to determine the changes upon treatment within the same cell line, albeit in the future comparison between the cell lines will be important.

Results



Results

Figure 22: Modulation of OSTN and IL-1 β pathways impacts morphology in Ctrl and SCZ neurons

Neuronal cultures were transduced with an AAV that enables mCherry expression under the CaMKIIa promoter and subsequently analyzed. **A)** Representative images of reconstructed Ctrl and SCZ d55-60 neurons with different treatments. Scale bars = 100 μ m. Sholl analysis results, **B)** first graph depicts Ctrl and SCZ untreated condition and pathway agonist treatments, **C)** second and **D)** third graph depict untreated and remaining treatment conditions for Ctrl and SCZ neurons separately. **E)** Graphs of morphological parameters number of primary neurites, sum of intersections and total length in μ m with all treatment conditions. Treatments for this analysis: 8d 200 nM AP-811, 7d 100 nM OSTN, 5d 100 ng/ml IL-1Ra, 5d 50 ng/ml IL-1 β , duration and concentrations for combined treatments were the same. Untreated, OSTN, IL-1 β : Ctrl N = 3-4 batches, n = 111-135 neurons per condition and SCZ N = 3-5 batches, n = 111-169 neurons per condition, remaining treatments: Ctrl N = 1 batch per condition, n = 25-26 neurons per condition and SCZ N = 2 batches per condition, n = 50-52 neurons per condition, partially preliminary results due to low N numbers, data presented as mean \pm SEM, Kruskal-Wallis test with Dunn's multiple comparison test, * describe comparison within the group (treatment vs. untreated of the same cell line), # describes comparison between groups (between cell lines and the respective treatment counterpart) */# $p < 0.05$, **/### $p < 0.01$, ***/#### $p < 0.001$

However, except for Ctrl AP-811+OSTN at 45 μ m (Ctrl 9.37 ± 0.5736 ; Ctrl AP-811+OSTN 13.36 ± 1.39) no significant differences were uncovered (Figure 22C). For Ctrl neurons treated with AP-811, IL-1Ra and AP-811+IL-1Ra a subtle trend towards less intersections between 45-135 μ m from the soma was detectable. IL-1Ra+IL-1 β and AP-811+OSTN showed more intersections from 15-45 μ m from the soma, where IL-1Ra+IL-1 β started to align with the rest of the treatments at fewer intersections. AP-811+ OSTN however only started to align at 165 μ m from the soma and was shown to have more intersections closer to the soma. SCZ neurons showed less clear differences and close to the soma the different treatments almost aligned (Figure 22D). Starting at 105 μ m AP-811+OSTN and AP-811 were shown to have more intersections while the other treatments aligned with the untreated neurons or displayed only a subtle difference towards more intersections. The additional three morphological parameters showed barely significant differences between the treatments (Figure 22E). SCZ neurons treated with IL-1Ra+IL-1 β showed significantly more primary neurites (SCZ untreated 7.544 ± 0.2498 ; IL-1Ra+IL-1 β 9.56 ± 0.527) and Ctrl neurons treated with IL-1 β were shown to have less intersections in total (Ctrl untreated 76.44 ± 3.691 ; IL-1 β 53.57 ± 2.717) and thus have overall significantly smaller neurons (Ctrl untreated $1147 \pm 55.36 \mu$ m; IL-1 β $803.5 \pm 40.76 \mu$ m). Further significant differences only were shown between the two cell lines comparing the respective counterparts. SCZ neurons treated with OSTN, IL-1 β , OSTN+IL-1 β , AP-811+OSTN and untreated (SCZ range 7.18 ± 0.267 to 8.82 ± 0.6284) displayed significantly fewer primary neurites than their Ctrl neuron counterparts (Ctrl range 10.5 ± 0.4799 to 13.12 ± 0.9888). The parameters sum of intersections and total length were shown to be significantly higher in SCZ neurons treated with OSTN, IL-1 β , OSTN+IL-1 β , AP-811, IL-1Ra and untreated (Ctrl range sum of intersections 53.57 ± 2.717 to 76.44 ± 3.691 ; total length $803.5 \pm 40.76 \mu$ m to $1147 \pm 55.36 \mu$ m; SCZ range sum of intersections 86.32 ± 4.696 to 129.5 ± 12.08 ; total length $1295 \pm 70.44 \mu$ m to $1942 \pm 181.1 \mu$ m).

In conclusion, Ctrl neurons treated with OSTN, IL-1 β and OSTN+IL-1 β showed a reduction in ramification with significant results for IL-1 β treatment, while SCZ neurons showed similar, but far less prominent modulations.

7.4.7 Influence of OSTN and IL-1 β pathways on WT and OSTN₂^{+/-} neuronal morphology

The same treatment conditions were applied to mCherry transduced neuronal cultures of WT and OSTN₂^{+/-} and the analysis was performed at d55-60. For this initial experiment OSTN₂^{+/-} was chosen due to its heterozygous mutation in the early coding sequence of OSTN which is assumably the closest representation of the SCZ context. The Sholl analysis results indicated differences upon some treatments (Figure 23A). Due to technical issues, there is no data on WT treated with IL-1 β and OSTN respectively. Thus, the top Sholl graph plots only untreated and OSTN+IL-1 β for the WT but untreated, IL-1 β , OSTN and OSTN+IL-1 β for OSTN₂^{+/-} (Figure 23B). Between the two WT conditions no significant differences could be detected, the treated condition even tended to have slightly more intersections (30-150 μ m from soma). OSTN₂^{+/-} neurons displayed significantly fewer intersections for the IL-1 β treatment at 60-90 μ m (largest difference at 75 μ m untreated 9.398 ± 0.485 , IL-1 β 5.08 ± 0.58), but already starting from 30-150 μ m from the soma less intersections were observed compared to the untreated condition. In the distal regions from the soma, starting from 180 μ m, IL-1 β treated OSTN₂^{+/-} neurons had more intersections reaching significance at 255-300 μ m from the soma (largest difference at 255 μ m untreated 0.961 ± 0.109 ; IL-1 β 2.12 ± 0.307). The double treatment led to fewer intersections in the range of 15-165 μ m from the soma and then aligned with the untreated condition. OSTN treated OSTN₂^{+/-} neurons displayed more intersections proximal to the soma (15-45 μ m), then at 60-225 μ m from the soma displayed less intersections than the untreated condition however no significances could be detected. For the remaining analyzed radii, OSTN treated neurons were aligned in the number of intersections with untreated and OSTN+IL-1 β treated neurons. Significant differences between untreated WT and OSTN₂^{+/-} were already described in Figure 20 (same batches). The subsequent two Sholl graphs depict the remaining treatment conditions (as previously described for Figure 22) for WT and OSTN₂^{+/-} separately. Altogether, in the graph (Figure 23C) representing the WT condition, all treatments induced more intersections at 15-105 μ m from the soma (e.g. at 30 μ m untreated 12.366 ± 0.725 ; treatments range 13.824 ± 0.998 to 16.2 ± 1.175) and then were shown to roughly align with the untreated WT starting at 120/135 μ m from the soma. Nonetheless, the only significant differences occurred at 45 μ m for AP-811, AP-811+IL-1Ra and IL-1Ra+IL-1 β treated neurons (largest difference untreated 10.073 ± 0.856 ; IL-1Ra+IL-1 β 14.7 ± 1.21), at 60 μ m for AP-811 and IL-1Ra+IL-1 β treated

Results

neurons (largest difference untreated 8.744 ± 0.847 ; IL-1Ra+IL-1 β 13.04 ± 1.206) and lastly at 75 μm from the soma for IL-1Ra+IL-1 β treated neurons (untreated 7.671 ± 0.792 ; IL-1Ra+IL-1 β 11.26 ± 1.065), all of which displayed more intersections than the untreated WT. The third Sholl graph (Figure 23D) depicts the same treatment conditions but for OSTN₂^{+/-} neurons, which in these preliminary results exhibit different effects. The untreated condition showed generally more intersections proximal to the soma (15-120 μm) than all the displayed treatment conditions. Except AP-811 condition, results were aligned among the other conditions at 15-30 μm from the soma, then starting at 45 μm AP-811 and IL-1Ra+IL-1 β condition roughly aligned at fewer intersections than the other conditions which also roughly aligned among themselves. Significant differences solely occurred for AP-811 at 60-120 μm (largest difference at 75 μm untreated 9.398 ± 0.485 ; AP-811 5.182 ± 0.686) and IL-1Ra+IL-1 β at 60-90 μm from the soma (largest difference at 75 μm untreated 9.398 ± 0.485 ; IL-1Ra+IL-1 β 5.44 ± 0.714) displaying less intersections compared to the untreated neurons. IL-1Ra and AP-811+OSTN were shown to have slightly more intersections starting at 150-270 μm , AP-811 continuously displayed less intersections until 255 μm , whereas the remaining conditions roughly aligned with the untreated condition starting at 180 μm from the soma and all conditions aligned at 285-300 μm (Figure 23D). Morphological parameters number of primary neurites (WT range 11.23 ± 0.493 to 13.22 ± 0.817), sum of intersections (WT range 102.4 ± 7.461 to 121.5 ± 9.4) and total length (WT range $1535 \pm 111.9 \mu\text{m}$ to $1822 \pm 141 \mu\text{m}$) did not show any significant differences between the WT treatment conditions (Figure 23E), however OSTN+IL-1 β treatment of OSTN₂^{+/-} neurons showed significantly fewer primary neurites (untreated 8.68 ± 0.279 ; OSTN+IL-1 β 5.92 ± 0.476). The sum of intersections and total length were shown to be significantly lower in AP-811 and IL-1Ra+IL-1 β treated OSTN₂^{+/-} neurons compared to the untreated condition (sum of intersections untreated 95.36 ± 4.196 ; AP-811 58.18 ± 7.306 ; IL-1Ra+IL-1 β 66.64 ± 5.017 ; total length untreated $1430 \pm 62.94 \mu\text{m}$; AP-811 $872.7 \pm 109.6 \mu\text{m}$; IL-1Ra+IL-1 β $999.6 \pm 75.25 \mu\text{m}$). When compared to the respective counterpart (WT vs. OSTN₂^{+/-}), the number of primary neurites was significantly lower in OSTN₂^{+/-} in all conditions except for OSTN and IL-1 β (OSTN₂^{+/-} range 5.92 ± 0.476 to 8.68 ± 0.279), which could not be acquired in WT neurons. The other two morphology parameters were also significantly lower in OSTN₂^{+/-} with OSTN+IL-1 β , AP-811 and IL-1Ra+IL-1 β .

Results

Figure 23: Modulation of OSTN and IL-1 β pathways impacts morphology in WT and OSTN₂^{+/-} neurons

Neuronal cultures were transduced with an AAV that enables mCherry expression under the CaMKII α promoter and subsequently analyzed. **A)** Representative images of reconstructed WT and OSTN₂^{+/-} d55-60 neurons with different treatments. IL-1 β and OSTN treatments missing for WT neurons due to technical issues. Scale bars = 100 μ m. Sholl analysis results, **B)** first graph depicts WT and OSTN₂^{+/-} untreated condition and pathway agonist treatments, **C)** second and **D)** third graph depict untreated and remaining treatment condition for WT and OSTN₂^{+/-} neurons separately. **E)** Graphs of morphological parameters number of primary neurites, sum of intersections and total length in μ m with all treatment conditions. Treatments for this analysis: 8d 200 nM AP-811, 7d 100 nM OSTN, 5d 100 ng/ml IL-1Ra, 5d 50 ng/ml IL-1 β , duration and concentrations for combined treatments were the same. WT untreated N = 3 batches, n = 82 neurons, WT treatments N = 2, n = 50-52 neurons per condition, OSTN₂^{+/-} untreated N = 3 batches, n = 103 neurons; OSTN₂^{+/-} OSTN N = 2 batches, n = 74 neurons, OSTN₂^{+/-} other treatments N = 1 batch per condition, n = 22-25 neurons per condition; partially preliminary results due to low N numbers, data presented as mean \pm SEM, Kruskal-Wallis test with Dunn's multiple comparison test, * describe comparison within the group (treatment vs. untreated of the same cell line), # describes comparison between groups (between cell lines and the respective treatment counterpart), */# $p < 0.05$, **/## $p < 0.01$, ***/### $p < 0.001$

The remaining conditions were also reduced in OSTN₂^{+/-} compared to WT (WT ranges see above; OSTN₂^{+/-} sum of intersections overall range 58.18 ± 7.306 to 95.36 ± 4.196 ; total length overall range $872.7 \pm 109.6 \mu$ m to $1430 \pm 62.94 \mu$ m), but without significance (Figure 23E).

In sum, OSTN₂^{+/-} neurons treated with OSTN, IL-1 β and OSTN+IL-1 β displayed a reduction of Sholl intersections albeit only significant for IL-1 β treatment, which is in line with the results of Ctrl and SCZ neurons. WT neurons could not be analyzed for OSTN and IL-1 β treatment, however all other treatments led to increased ramification (only partially significant). Nonetheless, these results are preliminary and need further investigation for proper evaluation.

7.5 Heterozygous 3q28 deletion affects synapses

The GO term analysis of the RNAseq data of d42 Ctrl and SCZ neurons, as well as WT, OSTN₁^{+/-} and OSTN^{-/-} neurons, indicated an impact of the heterozygous 3q28 deletion on synaptic genes, and genes related to synaptic function and dendritic spine morphogenesis. Therefore, I decided to focus my investigation into the synaptic compartment of the cell lines used in this study.

7.5.1 Mature SCZ neurons display increased synapse density

The first experimental point was the RNAseq data in d42 neurons. Here, I found that pre- and postsynaptic genes were differentially expressed in SCZ neurons compared to WT. For example, cerebellin 2 precursor (*CBLN2*), NMDAR subunit *GRIN2C*, glutamate metabotropic receptor 3 (*GRM3*), leucine zipper tumor suppressor family member 3 (*LZTS3*), neuropilin and tolloid like 2 (*NETO2*), protein tyrosine phosphatase receptor type D (*PTPRD*), SH3 and multiple ankyrin repeat domains 2 (*SHANK2*), shisa family member 6 (*SHISA6*), *SYN3* and synaptopodin (*SYNPO*) (Figure 24A). Furthermore, genes related to the SNARE complex and hence vesicle release, displayed differential expression as well, for instance synaptotagmins (*SYT13*, *SYT17*) and *SNAP25* (Figure 24B). To confirm the modulation of synaptic proteins, I performed SDS-PAGE and western blot analysis on d42 Ctrl and SCZ neurons. Here, a slight difference (yet non-significant) occurred for *SYN1* with SCZ neurons showing slightly lower levels than Ctrl (Figure 24C). However, synaptic marker distribution patterns suggested that neurons need more time to be fully mature, especially regarding synapses. Hence, a later time point was chosen for synapse analysis. Neurons were cultivated up to d105 and IF was performed for synaptic markers *SYN* and *PSD95*, and structural marker *MAP2* (Figure 24D). Afterwards, synaptic markers were quantified as *SYN* or *PSD95* particles per 100 μm neurite. Further, the amount of colocalization of these markers was quantified as well. At d105 SCZ neurons displayed significantly more *SYN* and *PSD95* particles/ 100 μm neurite (*SYN* Ctrl 29.02 ± 0.809 ; SCZ 39.67 ± 0.958 ; *PSD95* Ctrl 28.43 ± 1.572 ; SCZ 46.65 ± 2.206) as well as significantly more colocalization (Ctrl 8.022 ± 0.465 ; SCZ 15.03 ± 0.741 ; Figure 24E).

Results

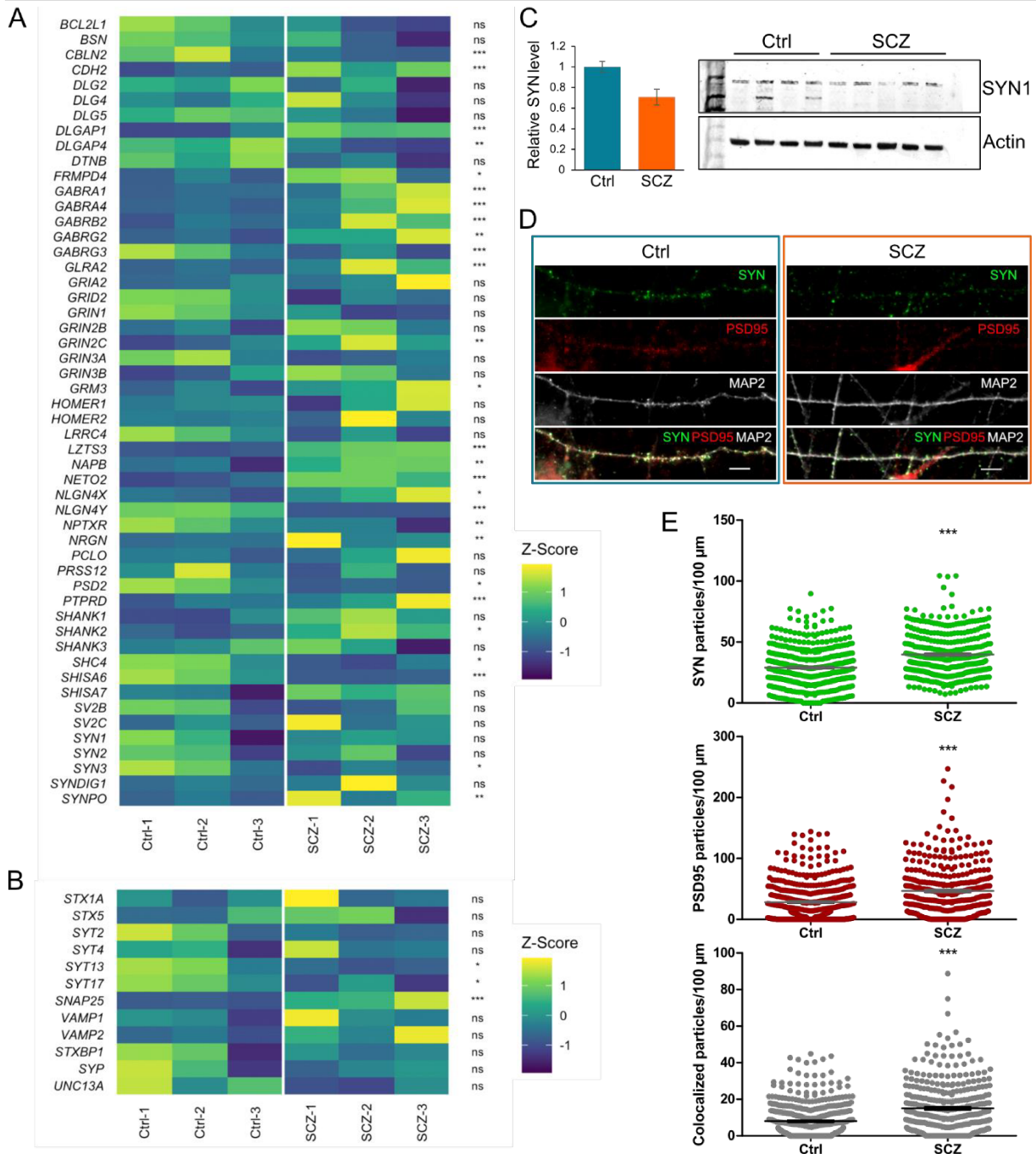


Figure 24: SCZ neurons display an increase in synapse density at late time points

Analyses of synapses of Ctrl and SCZ neurons at an early (d42) and late time point (d~105). **A**) Heatmap (z-scaled) of gene expression of genes related to synapses for d42 Ctrl and SCZ neurons (RNAseq). **B**) Heatmap (z-scaled) of gene expression of genes related to the SNARE complex for d42 Ctrl and SCZ neurons (RNAseq). **C**) Western blot and quantification of d42 Ctrl and SCZ neurons for SYN1. Normalized to Ctrl. **D**) Representative close-up images of d~105 Ctrl and SCZ neurites. IF for SYN and PSD95. Scale bars = 10 μm. **E**) Quantitative analysis of SYN and PSD95 particles and the SYN/PSD95 particle colocalization per 100 μm neurite. RNAseq N = 3, Western Blot N ≥ 4, IFs Ctrl N = 6 batches, Ctrl n = 427 neurites, SCZ N = 5 batches, SCZ n = 359 neurites, data presented as mean ± SEM, Heatmaps: Benjamini-Hochberg adjusted p-values calculated with Wald test, Scatter dot plots: Mann-Whitney U test, * $p < 0.05$, ** $p < 0.01$, *** $p < 0.001$, Heatmaps and heatmap statistics by Dr. Anne Hoffrichter.

Results

Additional genes related to synaptic receptors and adhesion molecules were analyzed in the RNAseq data (d42), since those genes can as well influence synaptic function, synapse formation and neurite growth. It was shown that NMDAR subunit *GRIN2C* and some GABAR subunits (*GABRA1*, *GABRA4*, *GABRB2*, *GABRG2*, *GABRG3*) were significantly different in SCZ neurons (Figure 25A). Furthermore, several adhesion molecule genes could be detected to be significantly differentially expressed some of which are likely associated with SCZ. Genes encoding for cadherins and protocadherins (*CDH2*, *PCDH17*, *PCDHGB1*), neuregulin 1 (*NRG1*), contactin associated protein 2 (*CNTNAP2*), and further adhesion molecules like DS cell adhesion molecule (*DSCAM*), *DSCAM* like 1 (*DSCAML1*) and dyslexia-associated protein *KIAA0319* (*KIAA0319*) were identified to be significantly different between Ctrl and SCZ (Figure 25B).

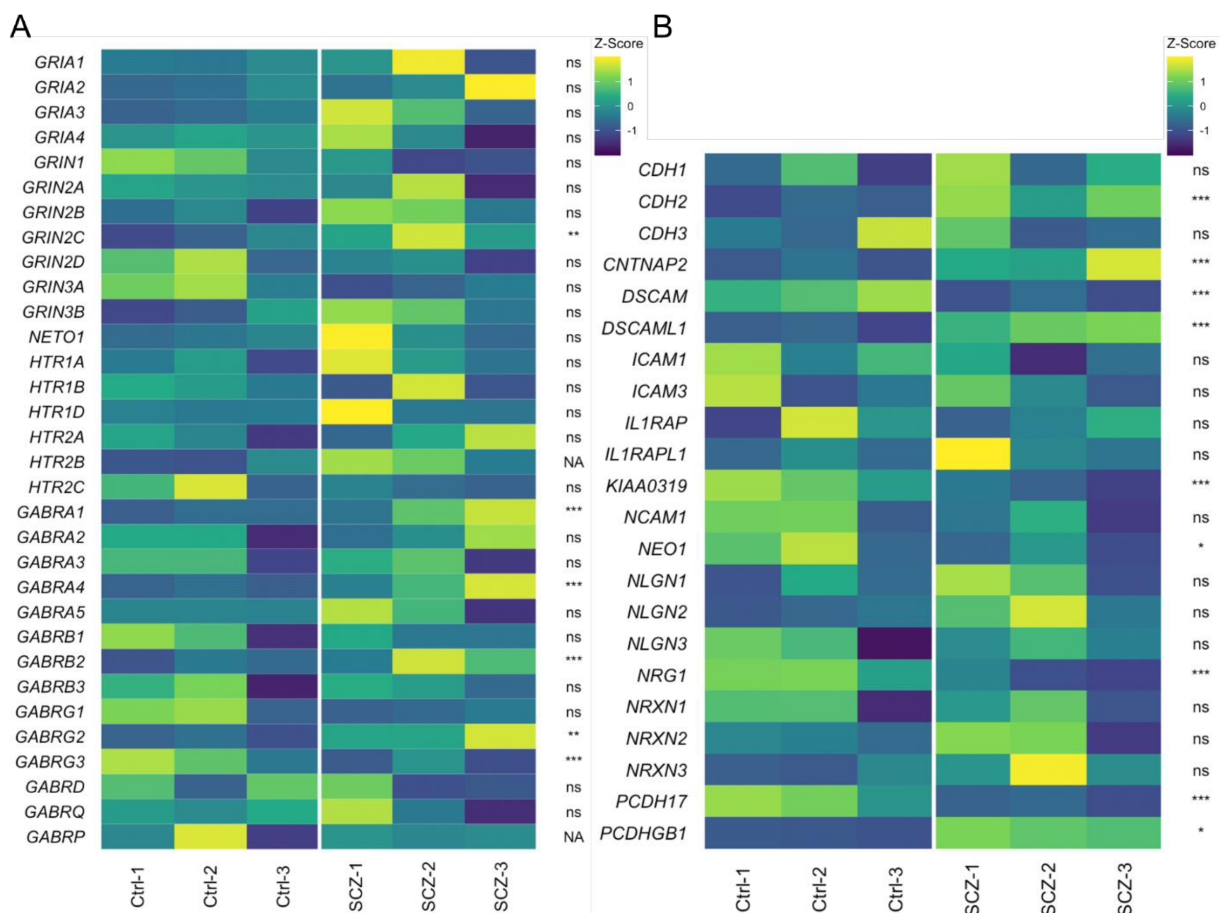


Figure 25: Heterozygous 3q28 deletion elicits differential expression of genes encoding for synaptic receptors and adhesion molecules

Heatmaps (z-scaled) of genes encoding for synaptic receptors and adhesion molecules to analyze RNAseq data of d42 neurons. **A)** Ctrl and SCZ neurons data on synaptic receptors. **B)** Ctrl and SCZ neurons data on adhesion molecules. N = 3, Benjamini-Hochberg adjusted p-values calculated with Wald test, * $p < 0.05$, ** $p < 0.01$, *** $p < 0.001$, Heatmaps and statistics by Dr. Anne Hoffrichter.

7.5.2 Mutation of *OSTN* impacts synapse density

For the analysis of for the WT, *OSTN*_1+/-, *OSTN*_2+/- and *OSTN*-/- neurons, I used the same approach described in the previous section. RNAseq data of WT, *OSTN*_1+/- and *OSTN*-/- from d42 of terminal differentiation, revealed DEG related to synapses as well (Figure 26), albeit clearly less than in the Ctrl and SCZ comparison. Compared to the WT control neurons, both, *OSTN*_1+/- and *OSTN*-/- neurons had a significant difference in expression of serine protease 12 (*PRSS12*), *OSTN*_1+/- had a significant difference in expression of synaptic vesicle glycoprotein 2C (*SV2C*) and *OSTN*-/- in GABAR subunit beta 2 (*GABRB2*) (Figure 26A). The SNARE related genes were also investigated in the RNAseq data, however no significant differences were uncovered in d42 neurons (Figure 26B).

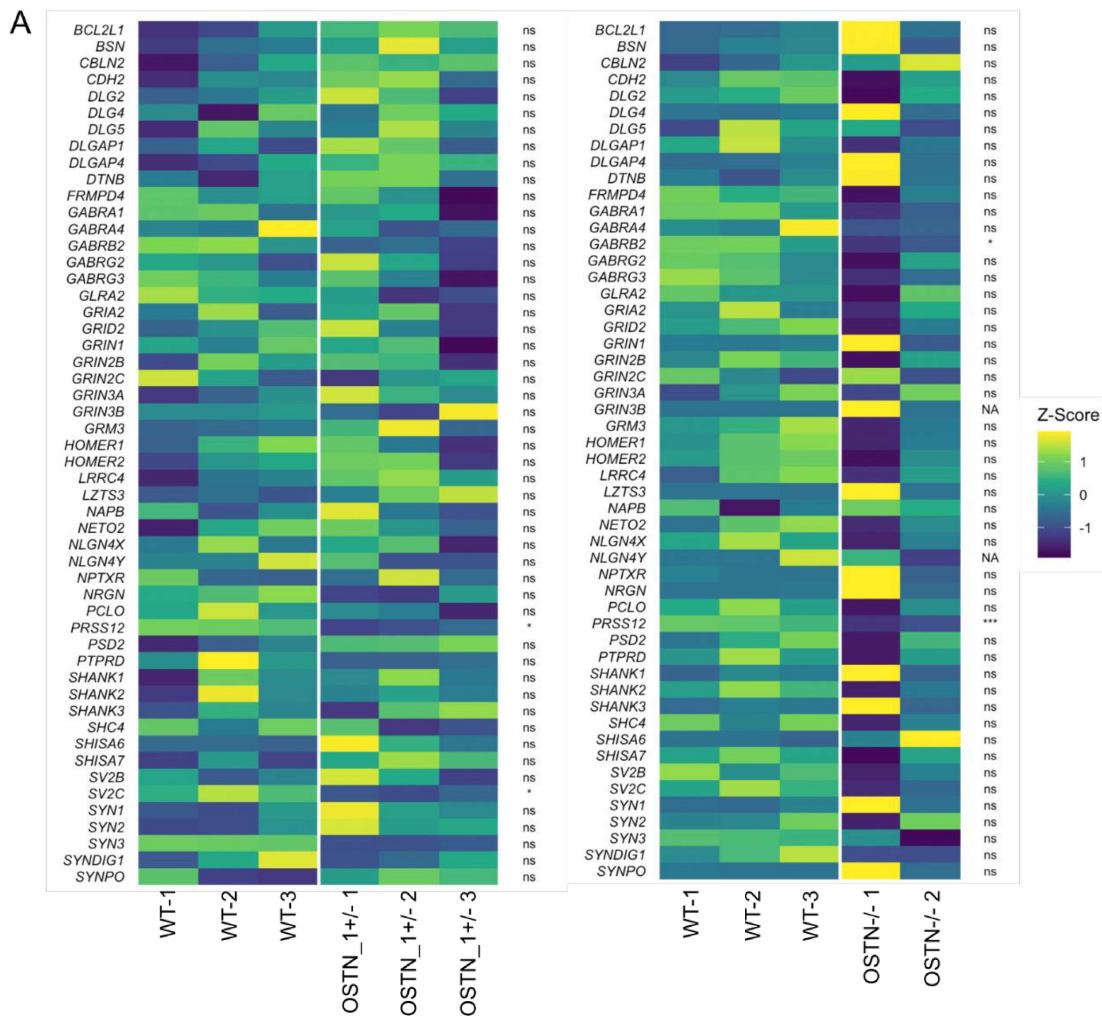


Figure continued on the next page.

Results

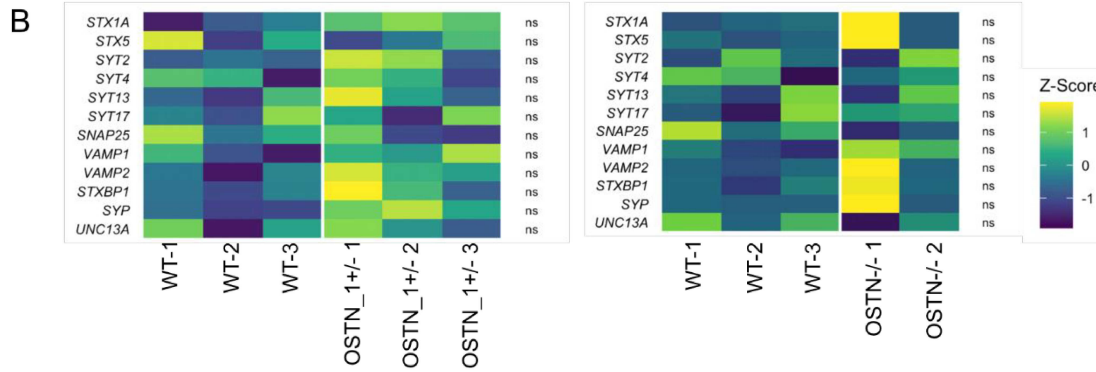


Figure 26: Expression of synapse and SNARE complex related genes in WT, OSTN_1+/− and OSTN-/-

A) Heatmaps (z-scaled) of gene expression of synapse related genes in d42 WT, OSTN_1+/− and OSTN-/- neurons (RNAseq). **B)** Heatmaps (z-scaled) of gene expression of SNARE complex related genes in d42 WT, OSTN_1+/− and OSTN-/- neurons (RNAseq). N= 2-3, Benjamini-Hochberg adjusted p-values calculated with Wald test, * $p < 0.05$, ** $p < 0.01$, *** $p < 0.001$, Heatmaps and statistics by Dr. Anne Hoffrichter.

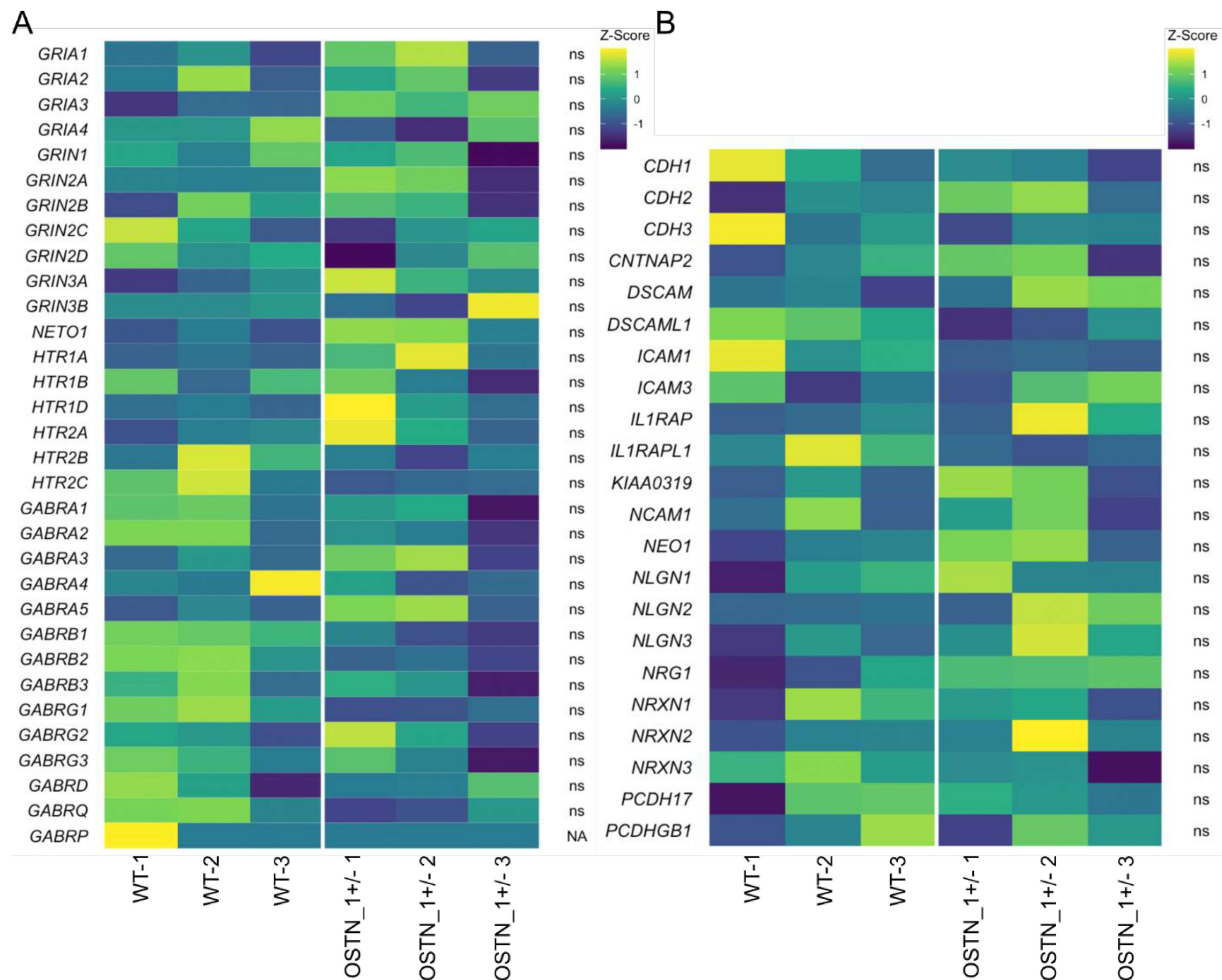


Figure continued on the next page.

Results

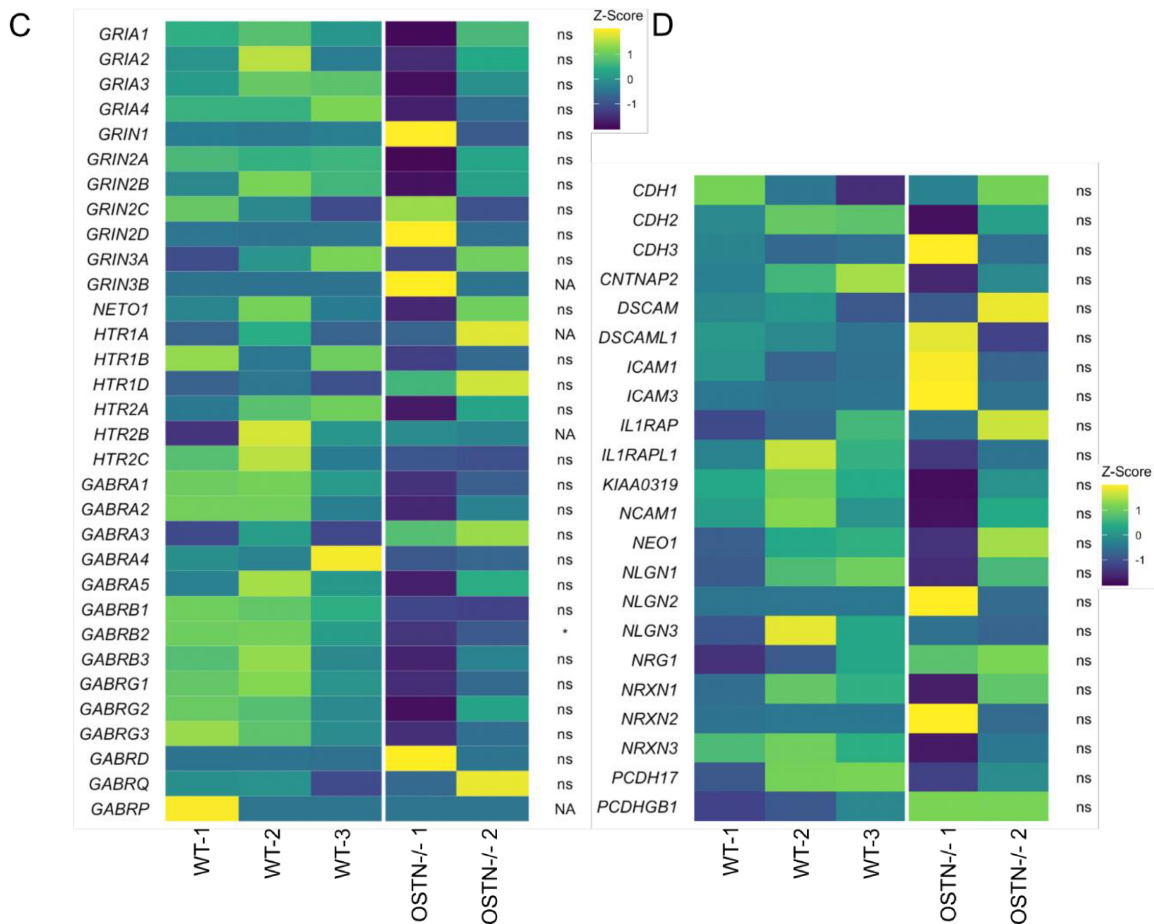


Figure 27: *OSTN* mutation does not significantly change expression of genes encoding for synaptic receptors and adhesion molecules

Heatmaps (z-scaled) of genes encoding for synaptic receptors and adhesion molecules to analyze RNAseq data of d42 neurons. **A)** WT and *OSTN*₁^{+/-} neurons data on synaptic receptors. **B)** WT and *OSTN*₁^{+/-} neurons data on adhesion molecules. **C)** WT and *OSTN*^{-/-} neurons, data on synaptic receptors. **D)** WT and *OSTN*^{-/-} neurons, data on adhesion molecules. N = 2-3, Benjamini-Hochberg adjusted p-values calculated with Wald test, * $p < 0.05$, ** $p < 0.01$, *** $p < 0.001$, Heatmaps and statistics by Dr. Anne Hoffrichter.

After the analysis of synapse and SNARE related genes, the gene analysis of synaptic receptors and adhesion molecules (RNAseq) was performed on WT, *OSTN*₁^{+/-} and *OSTN*^{-/-} data as well to check any influence of *OSTN* mutation on these genes. However, no significant differential expression was found, except for GABAR subunit *GABRB2* in *OSTN*^{-/-} neuronal cultures (Figure 27A-D).

WT, *OSTN*₁^{+/-}, *OSTN*₂^{+/-} and *OSTN*^{-/-} neurons were also cultivated up to d105 for synaptic analysis. IFs were performed for SYN, PSD95 and MAP2 (Figure 28A) and the number of SYN and PSD95 particles per 100 μm neurite as well as their colocalization was quantified. Analysis of synaptic markers revealed significantly less SYN particles in all mutant neurons compared to WT neurons (WT 46.49 ± 1.264 ; *OSTN*₁^{+/-} 18.35 ± 2.746 ; *OSTN*₂^{+/-} 36.65 ± 1.25 ; *OSTN*^{-/-} 36.38 ± 2.046). The amount of PSD95 particles per 100 μm was significantly reduced in *OSTN*₁^{+/-} and *OSTN*^{-/-} but not in *OSTN*₂^{+/-} neurons (WT 45.84 ± 3.065 ; *OSTN*₁^{+/-} 8.974

Results

± 1.666 ; OSTN_2+/- 36.88 ± 1.595 ; OSTN-/- 11.36 ± 1.087). This was the same for the colocalization analysis: OSTN_1+/- and OSTN-/- displayed significantly less colocalization, while for OSTN_2+/- the phenotype was less evident (WT 16.58 ± 1.076 ; OSTN_1+/- 3.178 ± 0.911 ; OSTN_2+/- 13.33 ± 0.7065 ; OSTN-/- 5.041 ± 0.551 ; Figure 28B).

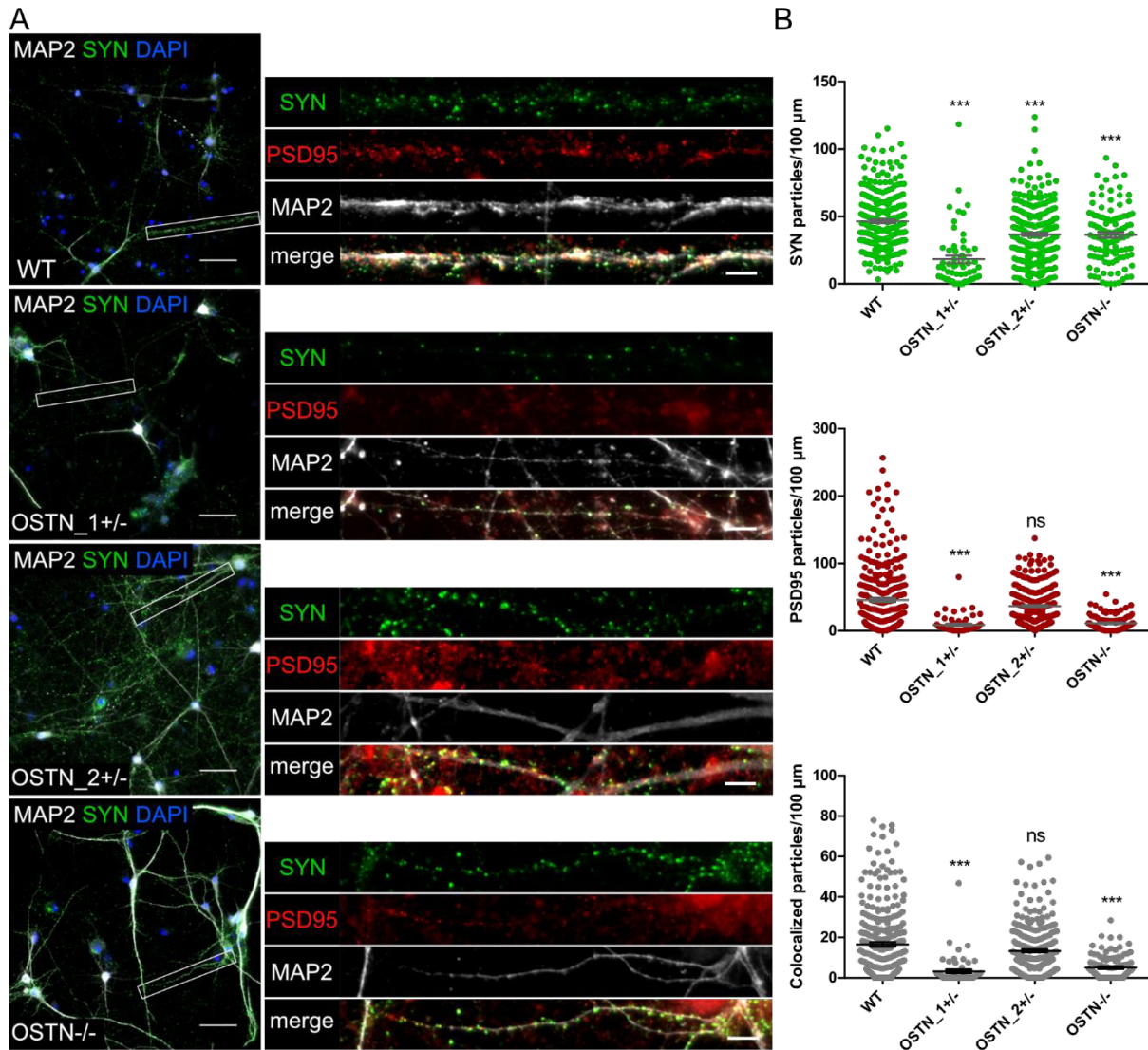


Figure 28: Mutation of *OSTN* gene reduces synapse density in mature neurons (d105)

Analysis of ca. d105 WT, OSTN_1+/-, OSTN_2+/- and OSTN-/- neurons to evaluate the influence of an *OSTN* mutation on synapses of mature neurons. **A)** Representative images of IF for SYN, PSD95 and MAP2. Scale bars = 50 μm; 10 μm. **B)** Quantitative analysis of SYN particles, PSD95 particles and the SYN/PSD95 particle colocalization per 100 μm neurite. WT N=3 batches, n = 280 neurites, OSTN_1+/- N = 1 batches, n = 60 neurites, OSTN_2+/- N = 4 batches, n = 280 neurites, OSTN-/- N = 2 batches, n = 110 neurites, data presented as mean \pm SEM, Kruskal-Wallis test with Dunn's multiple comparison test, * $p < 0.05$, ** $p < 0.01$, *** $p < 0.001$, ns = not significant.

7.5.3 Influence of OSTN and IL-1 β pathway modulation on synapses

After considering that the IL-1 β pathway can influence synapses and after the preliminary morphological data on OSTN and IL-1 β pathway activation and inhibition, I decided to analyze synapses with the same treatment conditions mentioned in previous sections (7.4.6; 7.4.7). Two timepoints were chosen for this analysis: on the one hand SYN particles were analyzed on the mCherry⁺ neurons at d55-60 (the same neurons which were analyzed for morphology in Figure 22 and 23, thus particles were determined per area) and on the other hand SYN and PSD95 particles and their colocalization were analyzed at around d105 with the different treatments described in section 7.4.6. The analysis of mCherry⁺ Ctrl and SCZ neurons (Figure 29A) exposed to the previously described treatment combinations, revealed significant differences in SYN particles per 100 μm^2 neurite.

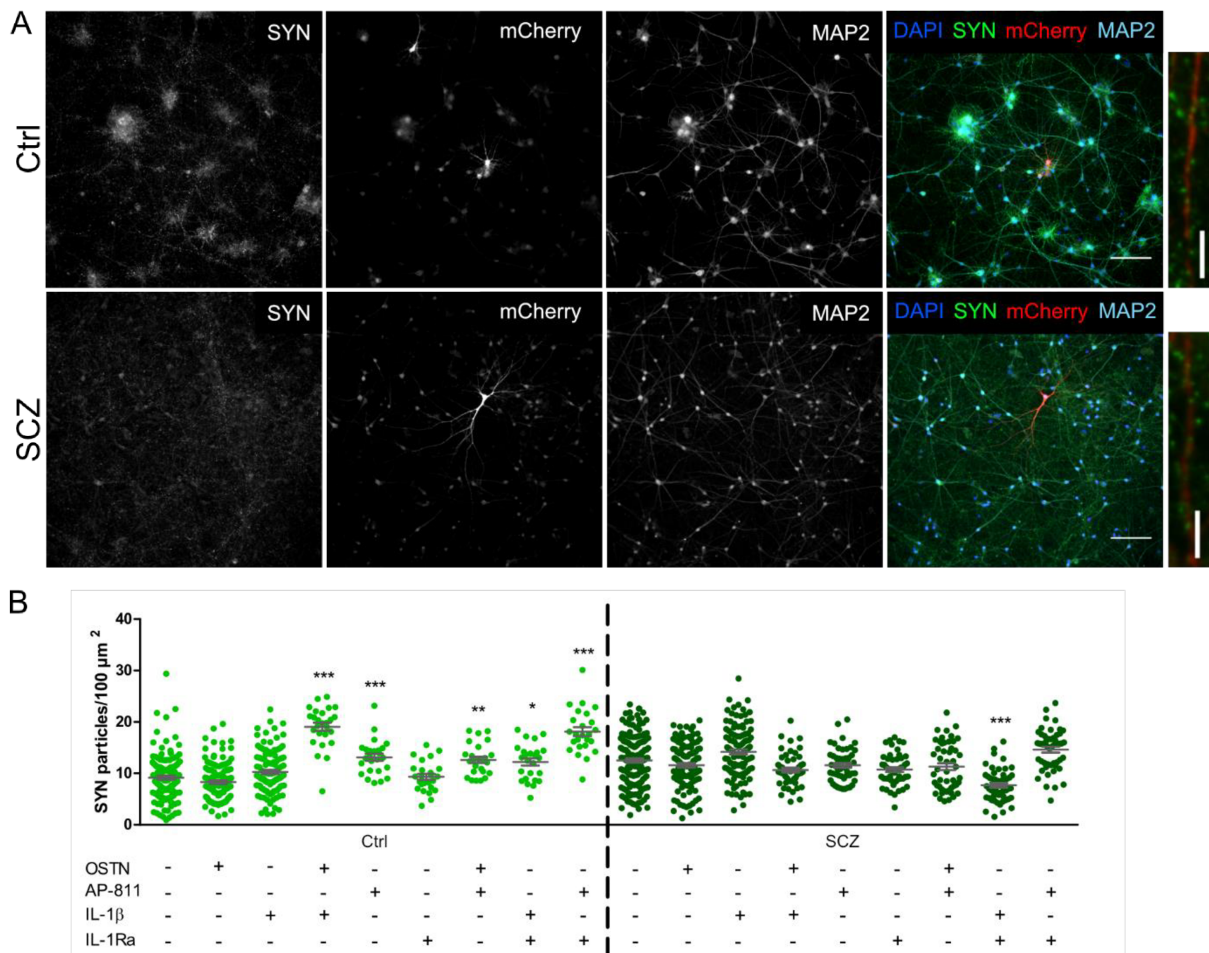


Figure 29: Modulation of OSTN and IL-1 β pathways impacts synapsin particle density mainly in Ctrl neurons (d55-60)

SYN particle density was analyzed on mCherry⁺ Ctrl and SCZ neurons with and without combinations of OSTN and IL-1 β pathway activation and inhibition. **A)** Representative IF for SYN, mCherry and MAP2 of AAV transduced Ctrl and SCZ neurons. Scale bars = 100 μm ; 10 μm . **B)** Quantitative analysis of SYN particles per 100 μm^2 for Ctrl and SCZ neurons. Treatments for this analysis: 8d 200 nM AP-811, 7d 100 nM OSTN, 5d 100 ng/ml IL-1Ra, 5d 50 ng/ml IL-1 β , duration and concentrations for combined treatments were the same. Ctrl untreated N = 4 batches, n = 134 neurons, OSTN and IL-1 β N = 3 batches, n = 111-116 neurons per condition, remaining treatments N = 1 batch, n = 25-26 neurons per condition, SCZ

Results

untreated N = 5 batches, n = 157 neurons, OSTN and IL-1 β N = 3 batches, n = 111-115 neurons per condition, remaining treatments N = 2 batches, n = 50-52 neurons per condition, data presented as mean \pm SEM, Kruskal-Wallis test with Dunn's multiple comparison test, * $p < 0.05$, ** $p < 0.01$, *** $p < 0.001$

In Ctrl neurons SYN particles/100 μm^2 were significantly increased for OSTN+IL-1 β (19.05 ± 0.785), AP-811 (13.13 ± 0.679), AP-811+OSTN (12.61 ± 0.609), IL-1Ra+IL-1 β (12.21 ± 0.7003) and AP-811+IL-1Ra (18.11 ± 0.872) compared to untreated Ctrl (9.164 ± 0.381) neurons. In SCZ neurons the only significance was observed as a reduction of SYN particles/100 μm^2 neurite for the IL-1Ra+IL-1 β treatment condition (7.68 ± 0.452) compared to untreated SCZ neurons (12.52 ± 0.395 ; Figure 29B).

The same analysis was performed on WT and OSTN₂^{+/-} neurons (Figure 30A). For both, WT and OSTN₂^{+/-} neurons, treatments in general led to reduced SYN particles/100 μm^2 . Data for WT treated with OSTN and IL-1 β are missing (technical issues). However, a significant reduction in SYN particles/100 μm^2 neurite in WT neurons could be observed for IL-1Ra (11.01 ± 0.502), AP-811+OSTN (11.32 ± 0.501), IL-1Ra+IL-1 β (8.825 ± 0.441) and AP-811+IL-1Ra (11.27 ± 0.567) treatment conditions compared to untreated WT (13.8 ± 0.586) neurons. Whereas in OSTN₂^{+/-} neurons there was also a reduction in SYN particles/100 μm^2 neurite but for OSTN (10.67 ± 0.426), OSTN+IL-1 β (9.376 ± 0.465), IL-1Ra (10.51 ± 0.413), AP-811+OSTN (10.23 ± 0.349), IL-1Ra+IL-1 β (10.34 ± 0.647) and AP-811+IL-1Ra (9.66 ± 0.451) compared to untreated OSTN₂^{+/-} (13.27 ± 0.494) neurons (Figure 30B).

Results

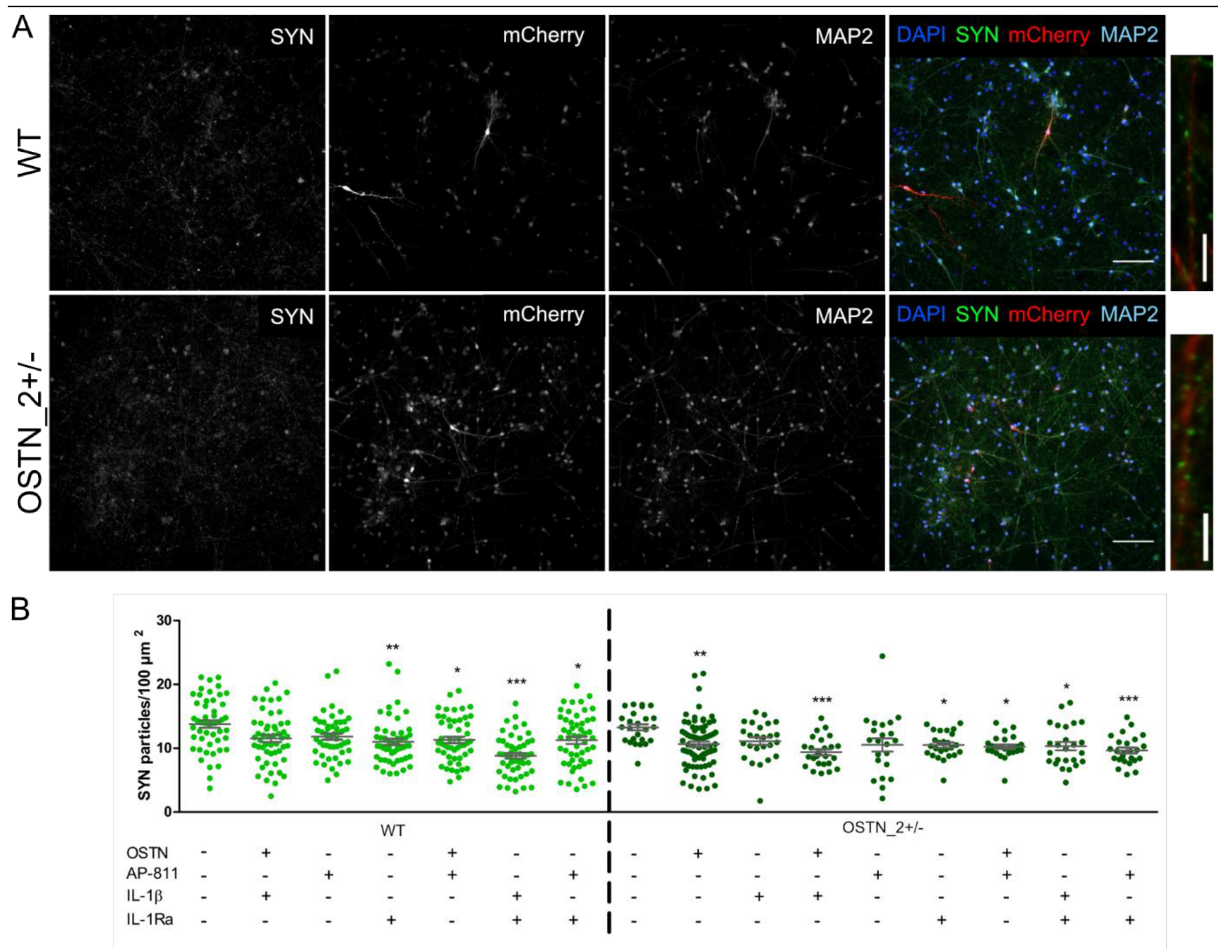


Figure 30: Modulation of OSTN and IL-1β pathways impacts synapsin particle density in WT and OSTN_2+/- neurons (d55-60)

SYN particle density was analyzed on mCherry⁺ WT and OSTN_2+/- neurons with and without combinations of OSTN and IL-1β pathway activation and inhibition. **A)** Representative IF for SYN, mCherry and MAP2 of AAV transduced WT and OSTN_2+/- neurons. Scale bars = 100 μm; 10 μm. **B)** Quantitative analysis of SYN particles per 100 μm² for WT and OSTN_2+/- neurons. Treatments for this analysis: 8d 200 nM AP-811, 7d 100 nM OSTN, 5d 100 ng/ml IL-1Ra, 5d 50 ng/ml IL-1β, duration and concentrations for combined treatments were the same. WT N = 2 batches, n = 50-52 neurons per condition, OSTN_2+/- OSTN N = 2 batches, n = 75 neurons, remaining treatments N = 1 batch, n = 22-25 neurons per condition, data presented as mean ± SEM, Kruskal-Wallis test with Dunn's multiple comparison test, * $p < 0.05$, ** $p < 0.01$, *** $p < 0.001$

Next, mature neurons around d105 were analyzed with the same treatments. Here, SYN and PSD95 particles and their colocalization were quantified. In Ctrl neurons, no significant differences in SYN particles/100 μm were detected, while in SCZ neurons treatments with IL-1β (47.26 ± 1.041), OSTN+IL-1β (43.15 ± 1.11), AP-811 (44.69 ± 1.031) and IL-1Ra (47.92 ± 1.213) significantly increased SYN particles/100 μm compared to untreated SCZ (38.25 ± 1.324) neurons (Figure 31A).

Results

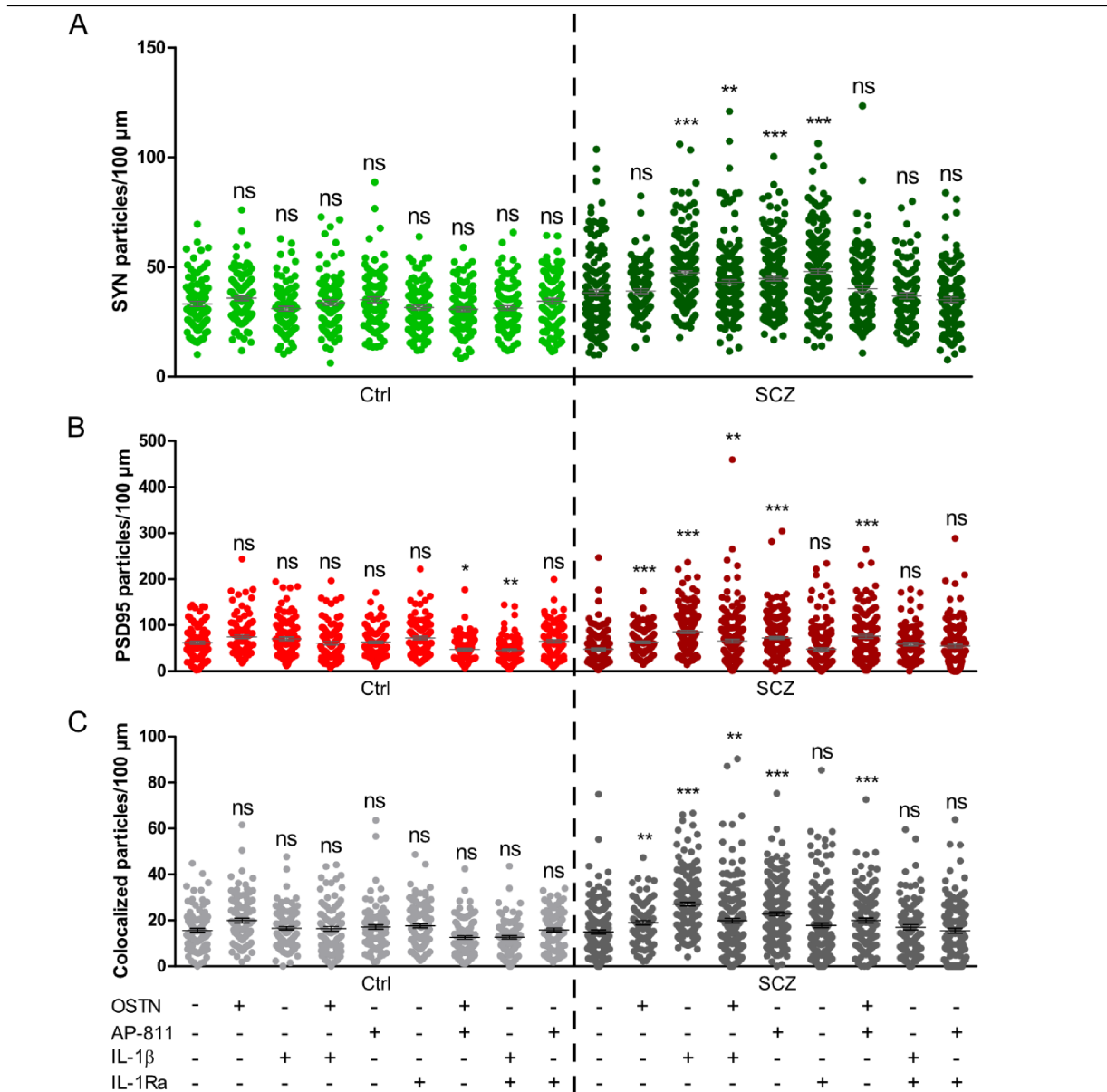


Figure 31: Modulation of OSTN and IL-1 β pathways impacts synaptic particle density mainly in d105 SCZ neurons

SYN and PSD95 and their colocalization particle density was analyzed in d105 Ctrl and SCZ neurons with and without combinations of OSTN and IL-1 β pathway activation and inhibition. **A)** Quantitative analysis of SYN particles per 100 μm . **B)** Quantitative analysis of PSD95 particles per 100 μm . **C)** Quantitative analysis of SYN and PSD95 particle colocalization per 100 μm . Treatments for this analysis: 8d 200 nM AP-811, 7d 100 nM OSTN, 5d 100 ng/ml IL-1Ra, 5d 50 ng/ml IL-1 β , duration and concentrations for combined treatments were the same. Ctrl N = 1 batch, n = 100-101 neurites per condition, SCZ N = 2 batches, n = 140-200 neurites per condition, OSTN and IL-1Ra+IL-1 β N = 1, n = 100 neurites per condition, data presented as mean \pm SEM, Kruskal-Wallis test with Dunn's multiple comparison test, * $p < 0.05$, ** $p < 0.01$, *** $p < 0.001$, ns = not significant.

PSD95 particles/100 μm were significantly reduced in Ctrl neurons (Ctrl untreated 61.94 ± 3.461) treated with AP-811+OSTN (47.19 ± 2.621) and IL-1Ra+IL-1 β (45.03 ± 2.543), whereas in SCZ neurons treated with OSTN (62.8 ± 2.921), IL-1 β (85.72 ± 2.916), OSTN+IL-1 β (65.49 ± 3.841), AP-811 (72.17 ± 2.969) and AP-811+OSTN (75.9 ± 4.436) PSD95 particles/100 μm were significantly increased (SCZ untreated 47.63 ± 2.528 ; Figure 31B). The colocalization of

Results

both particles/100 μm was not significantly different for any condition of Ctrl neurons. In SCZ neurons on the other hand, colocalization/100 μm was significantly higher in treatment conditions OSTN (18.96 ± 0.881), IL-1 β (27.03 ± 0.856), OSTN+IL-1 β (19.89 ± 0.995), AP-811 (22.79 ± 0.849) and AP-811+OSTN (19.95 ± 1.072) compared to untreated SCZ neurons (14.93 ± 0.847 ; Figure 31C).

The same analysis was performed on WT and OSTN₂^{+/-} neurons, however due to technical issues most treatment conditions for OSTN₂^{+/-} neurons could not be analyzed (see Appendix Figure S3).

7.6 Impacts of heterozygous 3q28 deletion on neuronal function

In addition to morphological analyses and analyses of synapses, the aspect of neuronal functionality and neuronal communication arose as a central field of interest. Initially, a measure to indirectly evaluate neuronal functionality was the investigation of the AIS. The AIS is a dynamic structure essential for action potential (AP) generation which regulates neuronal excitability by adjusting its position and length (Figure 32A) (307).

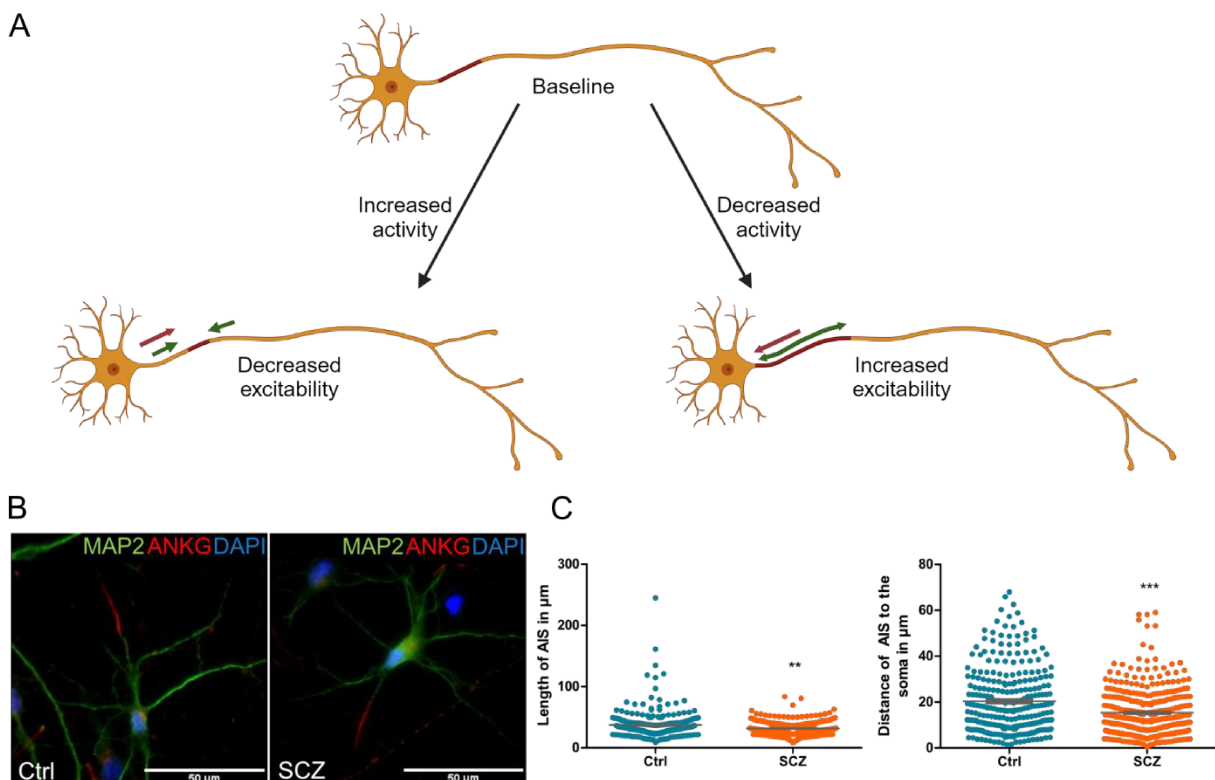


Figure 32: Heterozygous 3q28 deletion affects AIS length and position

The AIS is a dynamic structure between soma and axon that is involved in action potential generation and regulation of neuronal excitability. **A)** Scheme of AIS hypothesis, shift of size and position of AIS regulates excitability of neurons as a reaction to increased or decreased neuronal activity. **B)** Representative images of IF of MAP2 and ANKG for d30-42 Ctrl and SCZ neurons. Scale bar = 50 μm .

Results

C) Quantitative analysis of AIS length and AIS distance to the soma. N= 5 batches, Ctrl n = 282 AIS, SCZ n = 345 AIS, data presented as means \pm SEM, Mann-Whitney U test, * $p < 0.05$, ** $p < 0.01$, *** $p < 0.001$

To gain first insights in neuronal functionality, neurons were fixed and stained for structural protein MAP2 and AIS marker ANKG (Figure 32B). Subsequently, AIS lengths and the distance of the AIS to the soma were measured. Interestingly, I found that SCZ neurons had significantly shorter AIS (Ctrl $37.33 \pm 1.33 \mu\text{m}$; SCZ $31.68 \pm 0.5619 \mu\text{m}$) which were closer to the soma (Ctrl $20.36 \pm 0.8578 \mu\text{m}$; SCZ $15.34 \pm 0.575 \mu\text{m}$) than Ctrl neurons' AIS (Figure 32C).

7.6.1 Calcium imaging uncovers slight variation in neuronal activity

After identifying differences in morphology and synapses, I wanted to get more detailed insight into potential functional differences between Ctrl and SCZ neurons. Calcium imaging allows to record functional data on many neurons at once and enables evaluation of network activity. Therefore, neuronal cultures were labeled with calcium indicator Fluo4-AM and recorded under baseline conditions, stimulation conditions and with TTX to validate the synaptic origin of Ca^{2+} transients (TTX data not shown). On d45, Ctrl and SCZ neuronal cultures were recorded (Figure 33A) and Ca^{2+} transients were analyzed with an analysis script (PeakCaller) previously published by Artimovich et al. (302). Ctrl and SCZ neurons displayed no significant differences in the number of active cells (Ctrl $46.42 \pm 6.39 \%$; SCZ $50.79 \pm 5.27 \%$), average events per active cells (Ctrl 6.066 ± 0.883 ; SCZ 5.428 ± 0.549), average frequency of active cells (Ctrl $0.0927 \pm 0.0089 \text{ Hz}$; SCZ $0.09655 \pm 0.0107 \text{ Hz}$) or in their synchronicity index (Ctrl 0.049 ± 0.0155 ; SCZ 0.069 ± 0.0258 ; Figure 33B). In line with that, synchronization matrixes and raster plots displayed very similar results (Figure 33C, D).

Results

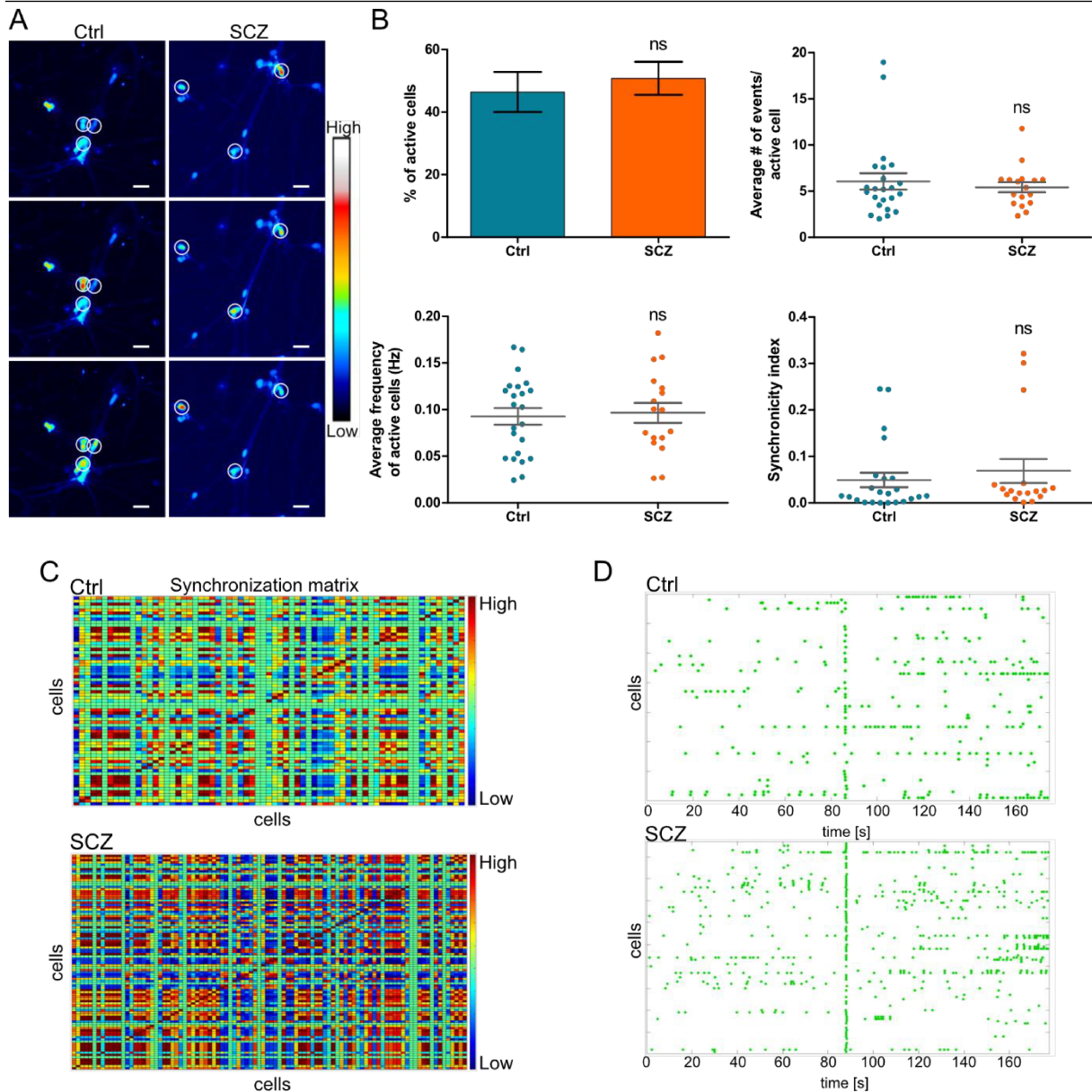


Figure 33: Ctrl and SCZ neurons (d45) do not show significant differences in Ca^{2+} transient frequency under baseline conditions

D45 Ctrl and SCZ neurons were loaded with Fluo4-AM (calcium indicator) and live-cell imaging was performed in imaging buffer to record baseline activity. **A)** Representative extracts from Ca^{2+} imaging videos for Ctrl and SCZ. Cells labeled by white circles and Ca^{2+} transients depicted by color difference. Scale bar = 25 μm . **B)** Quantification of the relative number of active cells, number of events per active cell, average frequency of active cell and synchronicity index of Ctrl and SCZ neuronal cultures. **C)** Representative synchronization matrix and **D)** representative raster plots of cells under baseline conditions. $N = 4-5$ batches, $n = 2-3$ positions/well, data presented as mean \pm SEM, Kruskal-Wallis test with Dunn's multiple comparison test, ns = not significant.

The exposure to a stimulation buffer with high Ca^{2+} and high K^+ concentrations in combination with gabazine, an antagonist of GABA_A receptors, resulted in more Ca^{2+} transients in more cells (Figure 34A). Further, significantly more active cells were detected in SCZ neuronal cultures (Ctrl stim. 33.54 ± 5.56 %; SCZ stim. 57.47 ± 2.64 %) and a significantly higher synchronicity index in stimulated SCZ neurons than Ctrl neurons (Ctrl stim. 0.01856 ± 0.00427 ; SCZ stim 0.04675 ± 0.00654).

Results

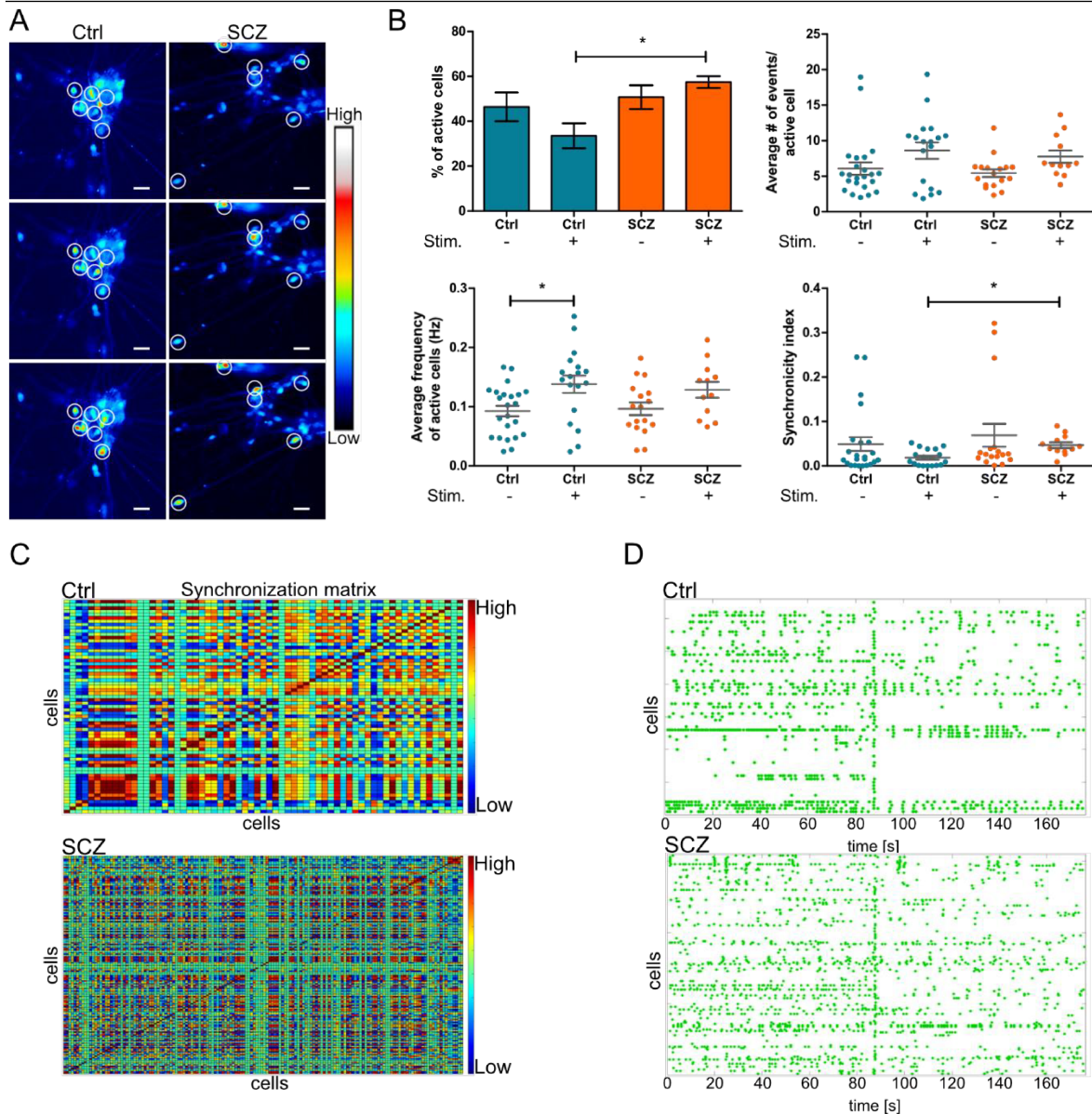


Figure 34: Ctrl and SCZ neurons (d45) show significant differences in number of active cells and synchronicity under stimulating conditions

D45 Ctrl and SCZ neurons were loaded with Fluo4-AM (calcium indicator) and live-cell imaging was performed in stimulation buffer (high Ca^{2+} , high K^+) to record activity under stimulating conditions. **A**) Representative extracts from Ca^{2+} imaging videos for Ctrl and SCZ. Cells labeled by white circles and Ca^{2+} transients depicted by color difference. Scale bar = 25 μm . **B**) Quantification of the relative number of active cells, number of events per active cell, average frequency of active cell and synchronicity index of Ctrl and SCZ neuronal cultures baseline vs. stimulation. **C**) Representative synchronization matrix and **D**) representative raster plot of cells with stimulation buffer. $N = 4-5$ batches, $n = 2-3$ positions/well, data presented as mean \pm SEM, Kruskal-Wallis test with Dunn's multiple comparison test, * $p < 0.05$

Meanwhile, the average number of events per active cell (Ctrl stim. 8.606 ± 1.155 ; SCZ stim. 7.751 ± 0.86) and the frequency of active cells (Ctrl stim. 0.1381 ± 0.01463 ; SCZ stim. 0.1285 ± 0.01348) did not differ significantly from Ctrl neurons (Figure 34B). These results were reflected in the respective synchronization matrix (Figure 34C) and raster plot (Figure 34D).

Results

Ca²⁺ imaging was also performed on WT, OSTN_1+/-, OSTN_2+/- and OSTN-/- neurons at around d45. Cells were labeled with Fluo4-AM and recorded under baseline and stimulation conditions. There were some differences in the numbers of active cells, however the results were slightly ambiguous. OSTN_2+/- neuronal cultures had significantly less active cells in baseline recordings (WT 50.29 ± 4.642 %; OSTN_1+/- 29.58 ± 7.795 %; OSTN_2+/- 8.833 ± 1.512 %; OSTN-/- 35.34 ± 4.16 %; Figure 35A), and these cells displayed less events per cell as well (WT 5.35 ± 0.636; OSTN_1+/- 4.873 ± 0.433; OSTN_2+/- 2.541 ± 0.56; OSTN-/- 4.942 ± 0.327) than WT neurons under baseline conditions (Figure 35B). The average frequency of active cells did not differ significantly between WT, OSTN_1+/-, OSTN_2+/- and OSTN-/- but upon stimulation the frequency of OSTN_2+/- neurons was significantly increased (OSTN_2+/- baseline 0.0587 ± 0.0178 Hz; stim. 0.1182 ± 0.0118 Hz; Figure 35C). Lastly, the synchronicity index increased significantly in OSTN_2+/- neurons upon stimulation (OSTN_2+/- baseline 0.001 ± 0.0006; stim. 0.0595 ± 0.03194) and under baseline conditions it differed significantly between WT (baseline 0.0536 ± 0.0158) and OSTN_2+/- (Figure 35D), displaying a much lower synchronicity index in OSTN_2+/- neurons. Overall, the results on WT and OSTN mutant cell lines were less clear than on Ctrl and SCZ neurons, but partially mimicked some functional traits.

Results

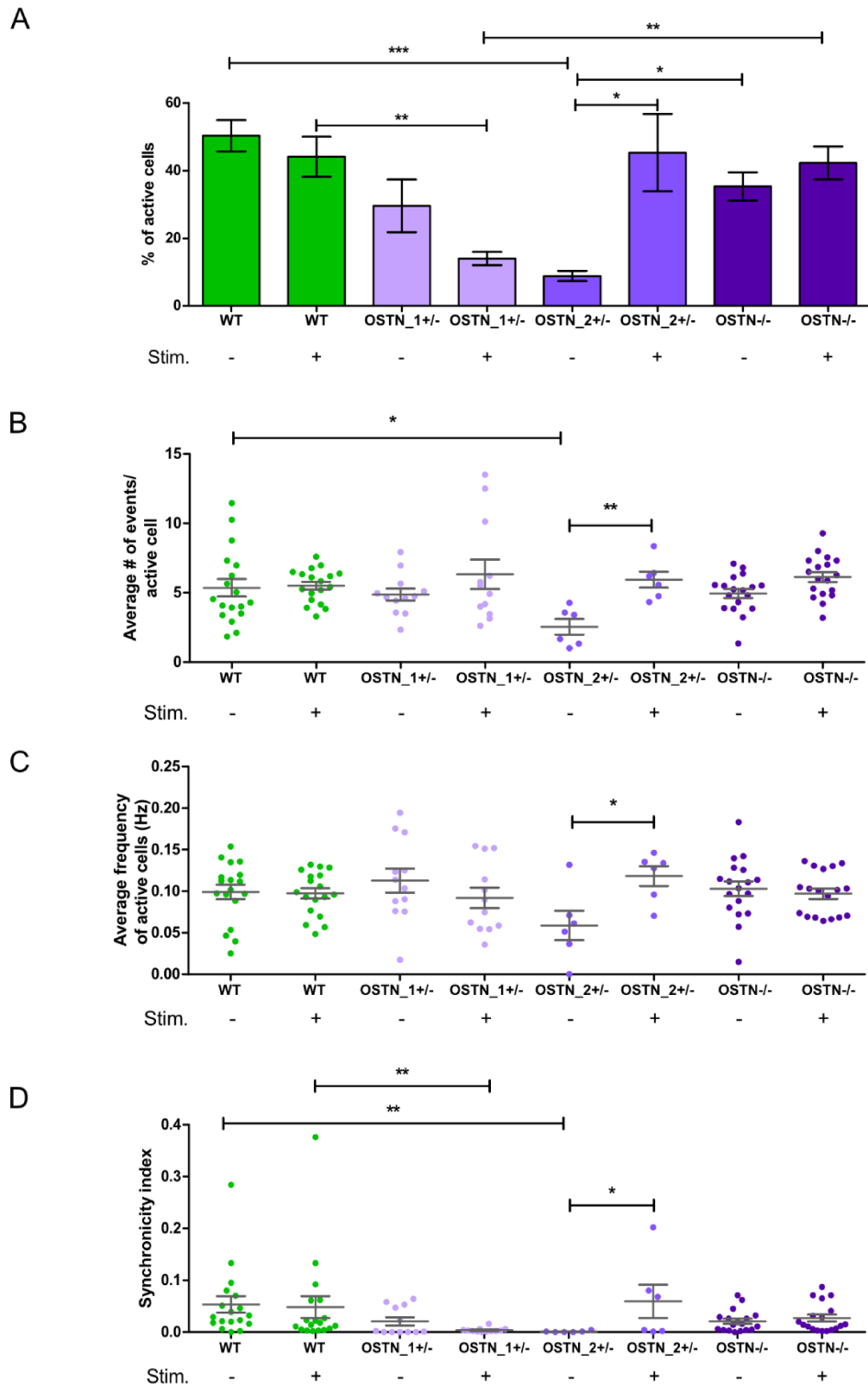


Figure 35: Ca²⁺ imaging of d45 OSTN mutant neuronal cultures reveals mostly subtle influence of OSTN mutation on neuronal activity

D45 neuronal cultures of WT, OSTN_1+/-, OSTN_2+/- and OSTN-/- were loaded with calcium indicator Fluo4-AM and imaged under baseline and stimulating conditions. Quantitative analyses of **A**) relative number of active cells, **B**) average number of events per active cell, **C**) average frequency of active cells and **D**) synchronicity index. WT and OSTN-/- N = 3, OSTN_1+/- N = 2, OSTN_2+/- N = 1 batches, n = 3 positions/well, data presented as mean ± SEM, Kruskal-Wallis test with Dunn's multiple comparison test, * $p < 0.05$, ** $p < 0.01$

Results

Moreover, I treated neuronal cultures with OSTN and IL-1 β pathway modulators to get an idea if these treatments can alter functional aspects of neurons. All in all, there was no significant difference in the percentage of active cells (Figure 36A), no significant difference between the treatments for the average number of events per cell in Ctrl or SCZ neurons (Figure 36B). Solely, the application of stimulation conditions evoked a significant increase in OSTN-treated SCZ neurons for the average number of events per active cell (baseline 4.323 ± 0.5514 ; stim. 9.517 ± 1.122 ; Figure 36B). The only significant differences in the average frequency of active cells were an increase in frequency for untreated Ctrl neurons upon stimulation (baseline 0.09271 ± 0.008846 Hz; stim. 0.1381 ± 0.01463 Hz), the same was true for SCZ neurons treated with OSTN (baseline 0.0813 ± 0.0148 Hz; stim. 0.158 ± 0.0133 Hz) which also showed an increase in frequency upon stimulation (Figure 36C). OSTN (0.1124 ± 0.0328) and AP-811+OSTN (0.122 ± 0.0369) treatments increased the synchronicity index in Ctrl neurons under baseline conditions compared to untreated Ctrl (0.0405 ± 0.0133) neurons under baseline conditions (Figure 36D). Whereas in SCZ neurons there seemed to be some differences, albeit none of them were significant.

Results

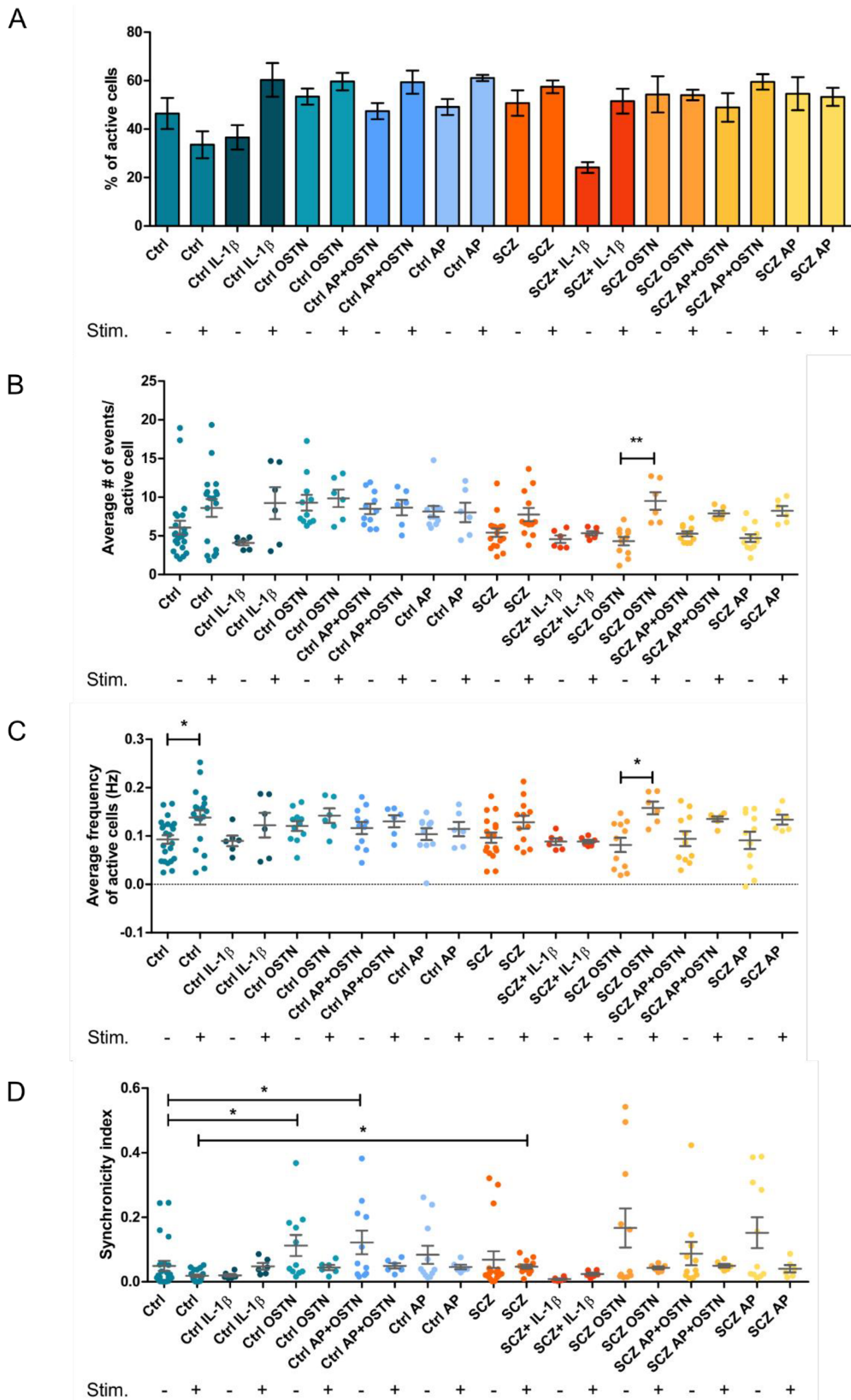


Figure 36: Ca²⁺ imaging of d45 Ctrl and SCZ neuronal cultures with modulation of OSTN and IL-1 β pathways

Ca²⁺ imaging experiment with modulation of OSTN and IL-1 β pathways in d45 Ctrl and SCZ neuronal cultures with and without stimulation. Quantitative analyses of **A**) relative number of active cells, **B**) average number of events per active cell, **C**) average frequency of active cells and **D**) synchronicity index. AP = AP-811 in this Figure, treatments 7d 15 nM OSTN, 8d 100 nM AP-811, 4d 50 ng/ml IL-1 β , duration and concentrations for combined treatments were the same. IL-1 β N = 1, rest N = 3-5 batches,

Results

n = 2-3 positions/well, data presented as mean \pm SEM, data pooled with untreated data sets, Kruskal-Wallis test with Dunn's multiple comparison test, * $p < 0.05$, ** $p < 0.01$

The baseline activity of neuronal cultures (Ctrl, SCZ, WT, OSTN_1+/- and OSTN-/-) was reflected in the expression pattern of activity-related genes (RNAseq data). Except for *JUN* in SCZ neurons, there were no significant differences in the transcript amounts (Figure 37). Although non-significant, a trend towards lower activity could be observed in SCZ and OSTN_1+/- neurons.

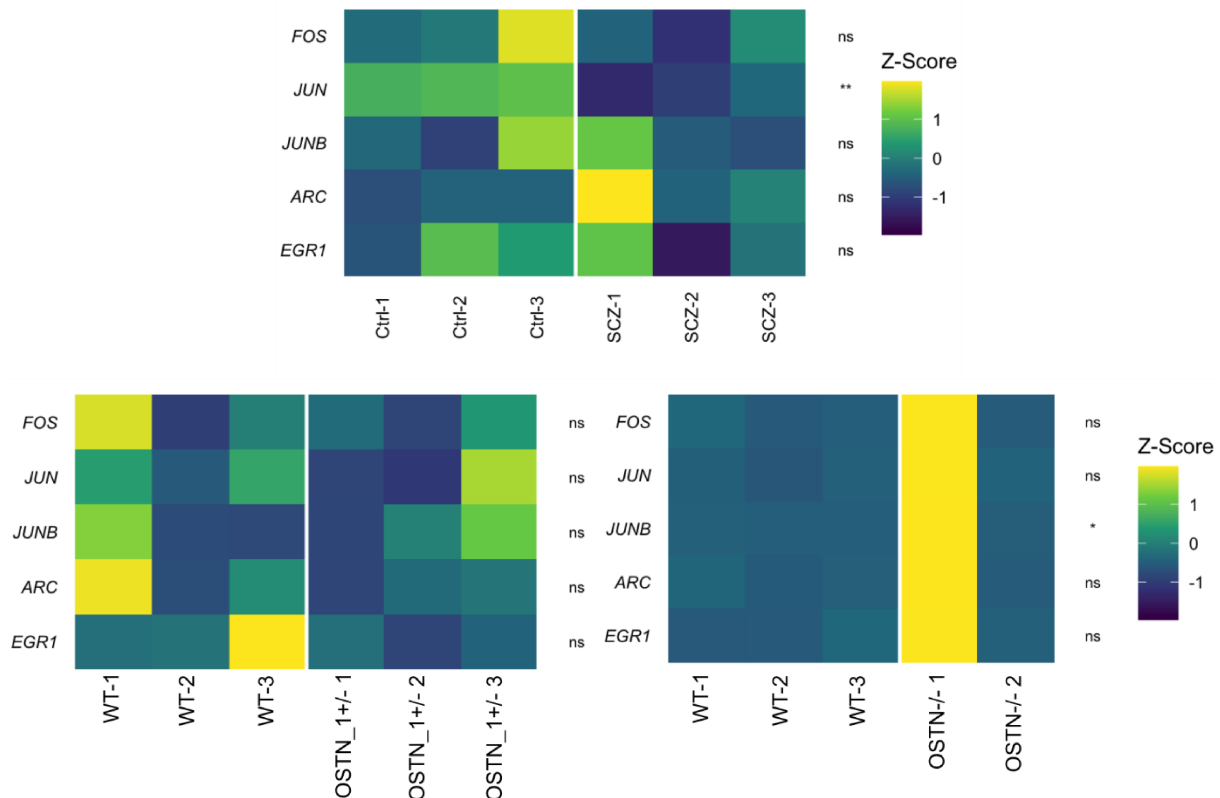


Figure 37: Expression patterns of activity related genes in d42 neuronal cultures

RNAseq data analysis for activity related genes. Heatmaps (z-scaled) show expression patterns for Ctrl, SCZ, WT, OSTN_1+/- and OSTN-/- neurons. N = 2-3, Benjamini-Hochberg adjusted p-values calculated with Wald test, * $p < 0.05$, ** $p < 0.01$, ns = not significant, Heatmaps and statistics by Dr. Anne Hoffrichter.

To investigate synaptically more mature neurons, I attempted to cultivate neurons for Ca^{2+} imaging longer up to d70 and performed Ca^{2+} imaging. There were no significant differences in the analyzed parameters except for the relative number of active cells which was significantly lower in SCZ neuronal cultures than in Ctrl neuronal cultures (Figure 38A) under baseline conditions (Ctrl 49.79 ± 4.7 %; SCZ 30.85 ± 3 %). This lack of significant differences was reflected as well in the cross-correlation matrixes (Figure 38B) and raster plots (Figure 38C).

Results

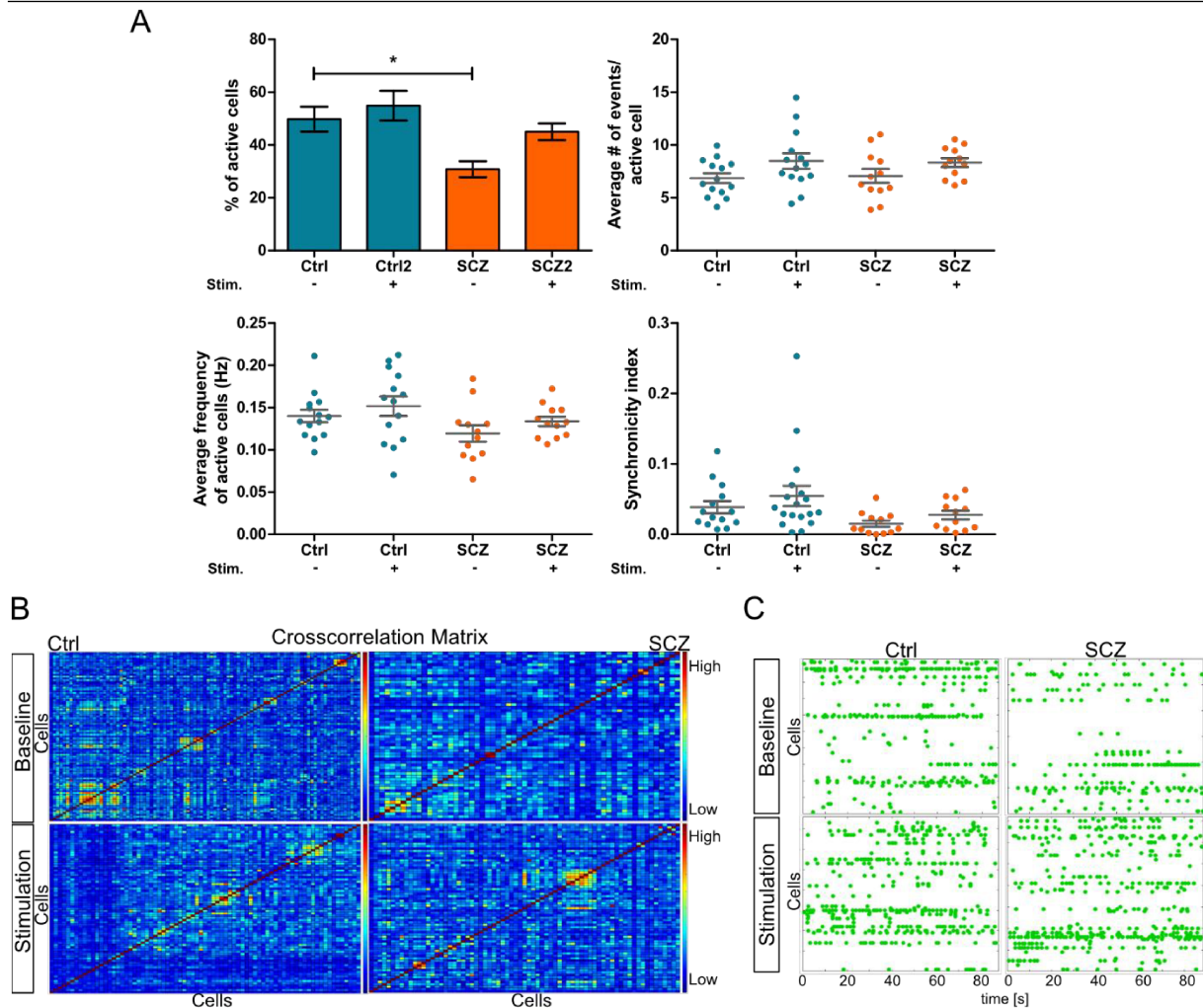


Figure 38: Ca²⁺ imaging of d70 Ctrl and SCZ neuronal cultures

To investigate functionality of more mature Ctrl and SCZ neuronal cultures, d70 neuronal cultures were loaded with calcium indicator Fluo4-AM and imaged under baseline and stimulating conditions. **A)** Quantification of the relative number of active cells, number of events per active cell, average frequency of active cell and synchronicity index of Ctrl and SCZ neuronal cultures baseline vs. stimulation. **B)** Representative cross-correlation matrix and **C)** representative raster plot of cells with imaging and stimulation buffer. N= 1-2 n = 2-3 positions/well, data presented as mean \pm SEM, Kruskal-Wallis test with Dunn's multiple comparison test, * $p < 0.05$

7.6.2 Electrophysiological measurements reveal changes in sEPSC frequencies

Another approach to tackle the study of neuronal functionality were electrophysiological measurements. All measurements were performed and analyzed by Dr. Mahnaz Davoudi. For the electrophysiology experiments, neurons were co-cultured with mouse astrocytes until around d56/57 of the terminal differentiation. Whole-cell patch clamp recordings on Ctrl and SCZ neurons uncovered several significant differences between these two cell lines. For one, the peak K⁺ currents were significantly increased in SCZ neurons whereas peak Na⁺ currents were not significantly different (Figure 39A). Furthermore, evoked action potentials (eAPs)

Results

were measured and analyzed for their amplitude and total number of eAPs. The amplitude of eAPs in SCZ neurons was significantly smaller while in line with that the total number of eAPs was higher in SCZ neurons (Figure 39B). Rise and decay times of spontaneous excitatory postsynaptic currents (sEPSCs) and amplitude and frequency of sEPSCs were additional parameters that were investigated. No difference was observed for the rise time, but decay time was significantly reduced in SCZ neurons (Figure 39C). There was no difference in sEPSCs amplitudes although a significantly lower frequency was observed in SCZ neurons (Figure 39D).

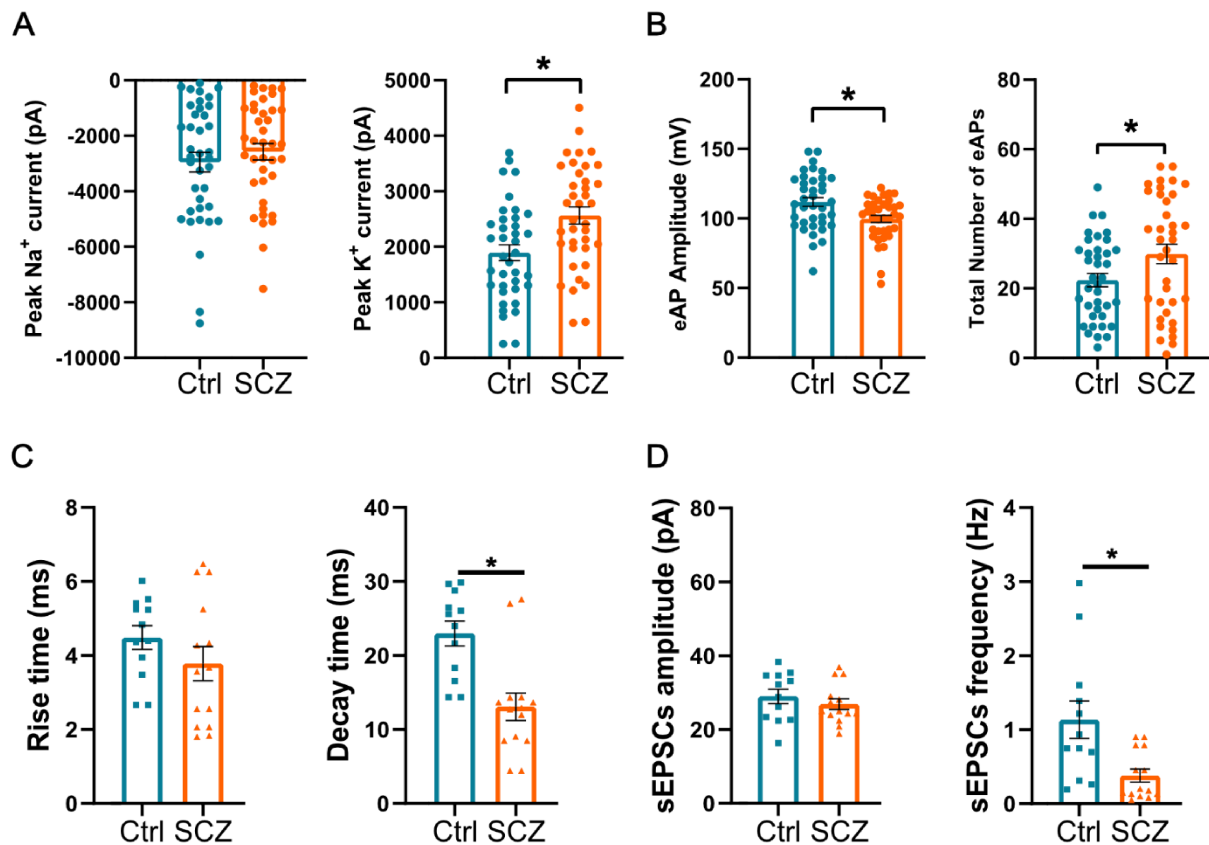


Figure 39: D56/57 SCZ neurons co-cultured on astrocytes display reduced sEPSC frequency
A) Peak Na²⁺ and K⁺ currents of Ctrl and SCZ neurons. **B)** Amplitude (mV) and total number of evoked action potentials of Ctrl and SCZ neurons. **C)** Rise and decay times (ms) of sEPSCs of Ctrl and SCZ neurons. **D)** Amplitude (pA) and frequency (Hz) of sEPSCs of Ctrl and SCZ neurons. N = 4, n = 38 cells total, data presented as mean ± SEM, Mann-Whitney U test, * *p* < 0.05, Electrophysiological measurements, analysis, graphs and statistics were done by Dr. Mahnaz Davoudi.

To further investigate a potential OSTN specific effect on neuronal functionality, whole-cell patch clamp recordings were conducted on WT, OSTN_{2+/-} and OSTN^{-/-} neurons at around d56/57 as well. Neurons were again co-cultured with mouse astrocytes. The measured peak Na⁺ currents were not significantly different between the neuronal cultures. However, peak K⁺ currents were significantly higher in OSTN_{2+/-} and OSTN^{-/-} than in the WT cultures (Figure 40A).

Results

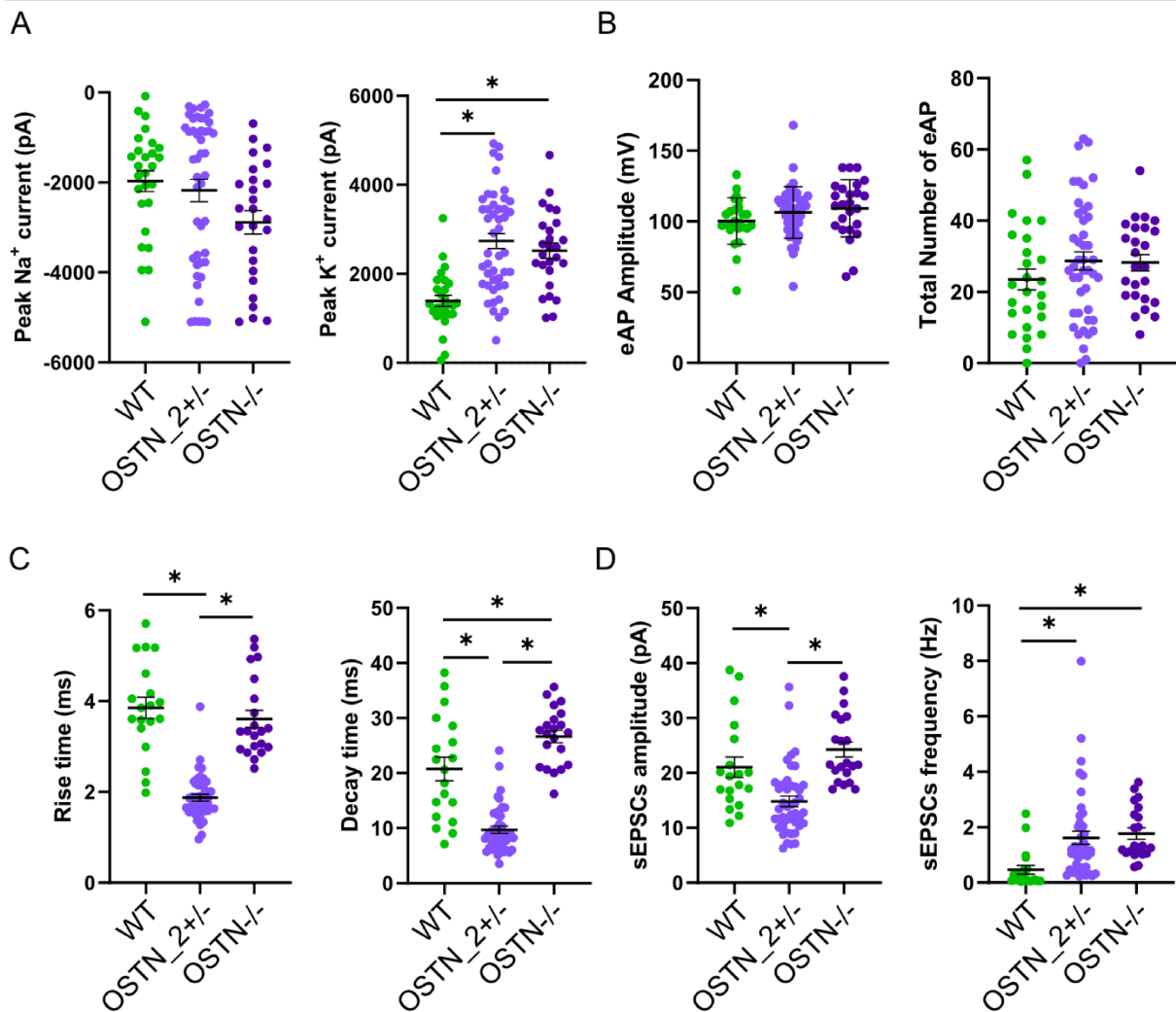


Figure 40: D56/57 OSTN mutant neurons co-cultured on astrocytes display increased sEPSC frequency

A) Peak Na²⁺ and K⁺ currents of WT, OSTN_{2+/-} and OSTN_{-/-} neurons. **B)** Amplitude (mV) and total number of evoked action potentials of WT, OSTN_{2+/-} and OSTN_{-/-} neurons. **C)** Rise and decay times (ms) of sEPSCs of WT, OSTN_{2+/-} and OSTN_{-/-} neurons. **D)** Amplitude (pA) and frequency (Hz) of sEPSCs of WT, OSTN_{2+/-} and OSTN_{-/-} neurons. N = 2 batches, n= 52-54 cells total, data presented as mean ± SEM, Kruskal-Wallis test with Dunn's multiple comparison test, * *p* < 0.05, Electrophysiological measurements, analysis, graphs and statistics were done by Dr. Mahnaz Davoudi.

Contrary to what was observed in Ctrl vs. SCZ neurons, there were no significant distinctions between WT, OSTN_{2+/-} and OSTN_{-/-} neuronal cultures regarding eAP amplitudes or total number of eAPs (Figure 40B). Next, the rise and decay times were analyzed, and it was revealed that OSTN_{2+/-} neurons had a significantly shorter rise time than WT and OSTN_{-/-}. The same was true for the decay time which was again significantly shorter in OSTN_{2+/-} neurons than in WT and OSTN_{-/-} neurons. When comparing WT and OSTN_{-/-} however, it was shown that OSTN_{-/-} neurons' longer decay time was significantly different from WT (Figure 40C). Lastly, the analysis of sEPSCs revealed significant variations between these neuronal cultures. The amplitude of OSTN_{2+/-} neurons was significantly smaller than in WT and OSTN_{-/-} neuronal cultures while OSTN_{-/-} neurons' sEPSC amplitudes were slightly but not

significantly bigger than in WT neurons. On the other hand, sEPSC frequencies were significantly elevated in both OSTN₂^{+/-} and OSTN^{-/-} neuronal cultures compared to WT neuronal cultures (Figure 40D).

7.7 Organoids as a measure to investigate more complex systems

Two-dimensional cell culture, especially pure monocultures are sure to have limitations. In a 2D cell culture model one dimension is effectively missing thus the concept of a more complex 3D environment may deepen insights into morphological and neurodevelopmental anomalies. Therefore, organoids were generated from Ctrl and SCZ hiPSCs with the support of Dr. Andrea C. Rossetti which were cultivated and then fixed in 4 % PFA at specific time points, embedded, cryo-sectioned and subsequently stained for various markers. IFs were performed for SOX2 and HUC/D, a progenitor and general neuronal marker respectively, and phospho-vimentin (pVIM) which marks mitotic cells (Figure 41). Three individual batches were prepared, and IFs were performed at d37, however no quantification was conducted. Nonetheless, a qualitative analysis suggested an increase of neuronal differentiation in SCZ organoids, as supported by the wider area positive for the neuronal marker HUC/D. The hypothesis that patient-derived organoids have a more pronounced neurogenesis/neuronal differentiation, was supported by preliminary indications of a reduction of pVIM⁺ cells at the ventricular lining. Ctrl and SCZ cells were also employed to generate an additional 3D model, as a proof of principle that these cells could be a valid starting point to generate more complex cellular models. Following a protocol established in our laboratory, I generated, in collaboration with Dr. Rossetti, neural spheroids and I tested the possibility to transduce such 3D structures with the previously used AAV. After the transduction, I performed an IF on whole spheroids followed by optical clearing (308). Afterwards spheroids were imaged, and it was proven that the transduction, staining and clearing was successful, thus offering a valuable tool to investigate neuronal morphology in a 3D context in the future (spheroid data not shown).

Results

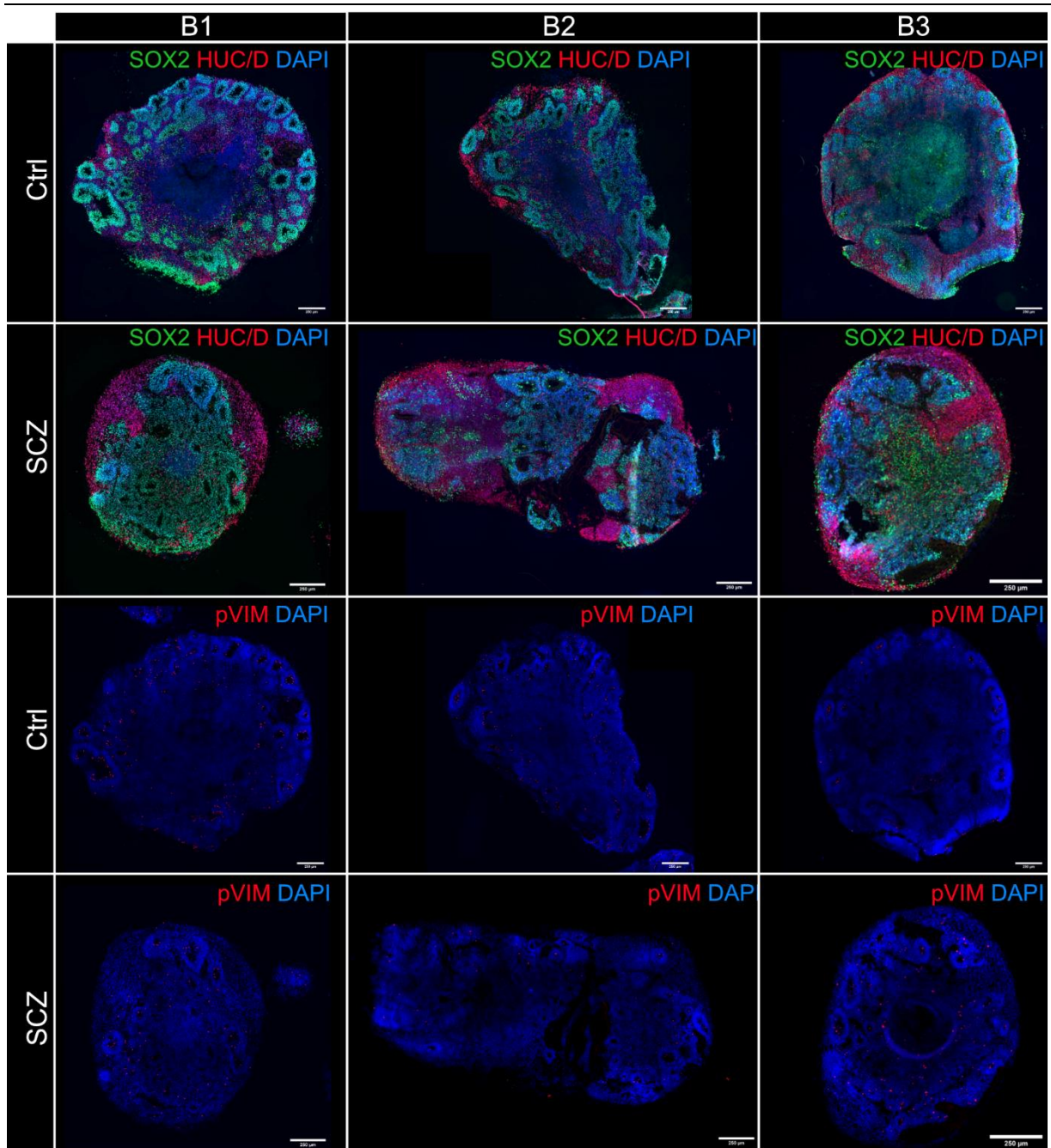


Figure 41: IF on cryosections of d37 Ctrl and SCZ organoids

Three batches of Ctrl and SCZ organoids. IF for progenitor marker SOX2, general neuronal marker HUC/D and mitotic marker phospho-vimentin (pVIM). N = 3 batches, scale bars = 250 μ m. Organoids were generated in collaboration with Dr. Andrea C. Rossetti, cryosections and IFs in collaboration with Helene Schamber.

8. Discussion

Mental disorders increasingly get into the limelight of society, getting increasing interest in basic and translational research. Next to anxiety disorders, depression, bipolar disorder and post-traumatic stress disorder, SCZ is among the most prevalent psychiatric disorders (309). Nonetheless, there is little understanding of its underlying causes, besides the knowledge that SCZ is a multifactorial disorder involving the interplay between genetic and environmental factors. To complicate the landscape of this disorder, there are plentiful genetic variations that differ between affected individuals. Further, if from one side the limited therapeutic options and the side effects of the available treatments make the compliance of the patients difficult, the limited number of appropriate models to find new pharmacological targets and the hurdles in the transferability of results to clinical research are slowing down research progress. Therefore, it is essential to explore new biological models to investigate psychiatric disorders in a more physiological system and lessen the gap between animal and clinical research. In this context, human iPSCs represent an ideal tool, thanks to its human origin, its easy accessibility, its expansion, differentiation potential and thus scalability. One of the most important advantages of this approach is that hiPSCs reflect the exact genetic background of the donor, thus allowing to study the genetic basis of a disease and test new compounds on human cells from a specific individual, paving the way for personalized medicine. However, as for every model system, there are certain drawbacks. For instance, during the reprogramming process the epigenetic information is lost (250) and cultures (2D or 3D) derived from hiPSCs reflect rather early development phases as they lack the maturity of cells grown in an organism. Further, all *in vitro* models must be regarded critically for their lack of complexity, even though it can be increased by co-cultures, 3D or fusion models. Moreover, to properly investigate disorders in such reductionist approach, it is necessary to identify phenotypes first and establish reliable readouts. In spite of any drawbacks, hiPSC greatly qualify for modeling SCZ *in vitro* to unravel cellular phenotypes and explore stable and scalable analyses which was the overall base of this thesis.

8.1 Generation of hiPSC-derived cortical neurons as a model for schizophrenia

The first challenge of this project was the identification of suitable cell lines to establish an analysis pipeline applicable to various sets of experimental outlines. To establish such a workflow, it is helpful to investigate cells where a phenotype is expected. In our laboratory I had the opportunity to run my experiments on a small cohort of available SCZ patient-derived and first-degree relative-derived hiPSCs. The available background information about this

cohort was limited to the age at cell donation, sex of the donor and the categorization of a F20 diagnosis, based on the international statistical classification of diseases and related health problems (ICD-10). The limited information unfortunately also limits the attribution of cellular phenotypes to possible symptoms.

The investigation, performed prior to this project, of rare copy number variations in these different genetic backgrounds failed to reveal commonalities between the SCZ cell lines. Once again this demonstrates the genetic heterogeneity of these patients and the difficulty to associate any symptoms to a genetic cause. However, one of the patient-derived cell lines displayed a heterozygous 3q28 deletion which has not been associated with SCZ so far. This deletion was priorly validated in the original somatic donor cells which confirmed this patient-specific genetic anomaly that was absent in the corresponding first-degree relative. Due to this large heterozygous deletion, these cells were chosen for this project. An analysis of the 3q28 locus with the available data on the human genome, revealed about 40 genes (Supplementary Table S1). After consideration of the known functions and expression patterns I chose two genes for further investigation: *OSTN* and *IL1RAP*. This choice was based on previous association with SCZ and their functions and effects on neurons. On the one hand, *IL1RAP* is an essential component of the IL-1 β signaling pathway which was previously associated with SCZ (98,160). Furthermore, IL-1 β signaling is known to impact neurons on synaptic (147) and morphological levels (163,165). *OSTN* on the other hand, has not been associated with SCZ so far, but was discovered to be repurposed exclusively in the human and anthropoid primate brain (172). Being involved in muscle endurance and bone growth in the periphery (174,191), *OSTN* in the brain was shown to reduce neuronal ramification in cortical neurons in an activity-dependent manner. *OSTN* expression in the brain seems to be induced by MEF2C, by its binding to several MREs that are altered in other species (e.g. mouse and rat) which likely is the reason for this species exclusivity (172).

To better evaluate the influence of the genetic alterations, present in the SCZ cell line, it was decided to generate an isogenic hiPSC system by targeting the *OSTN* gene with CRISPR/Cas9. *OSTN* was chosen, due to its novelty and exclusivity to humans and anthropoid primates and its dependence on MEF2C which has previously been associated with SCZ (310). Therefore, two CRISPR/Cas9 systems were used, as described previously. Both systems were used in parallel to increase success probability and were introduced into a healthy control cell line by nucleofection. The commercial system yielded one heterozygous clone which was confirmed by PCR and Sanger sequencing which was used in this thesis (*OSTN_1+/-*). The PX459 system yielded many clones, heterozygous and homozygous, which were too validated by Sanger sequencing. The accuracy of the introduced mutation varied between the different clones, meaning that in many cases a deletion of a couple of base pairs

(bp) occurred but the number of bp and the exact position varied slightly between the clones. I chose two clones for this thesis, a heterozygous clone (OTN_2+/-) which reflects the situation in the SCZ line, and a homozygous clone (OSTN-/-) for a more complete picture. Slight differences of the mutations were neglected, since they still amounted to a frameshift mutation with a premature stop codon. Since the template (SCZ line) displayed no specific mutation but the heterozygous deletion of an entire cytogenic band, any disruption of the *OSTN* gene which likely renders the protein not fully functional was acceptable. The main difference of OSTN_1+/- towards the other clones was the targeted positions, which were on opposite ends of the coding sequence of *OSTN* (Figure 11A). Further validation of OSTN levels in SCZ or *OSTN* mutant cell lines proved to be challenging, since neither in Ctrl nor in WT neurons OSTN was detectable by SDS-PAGE and western blot. The antibody was validated for western blot by applying recombinant human OSTN, which was detected without any trouble (Figure 14C). *OSTN* expression was confirmed in IF and on RNA level by RT-PCR and qPCR. While IF and qPCR revealed that expression levels were very low, judged by the Ct values, KCl stimulation induced a slight increase in *OSTN* expression which was achieved in a proof of principle approach evaluated by qPCR. Nonetheless, *OSTN* levels were still minimal. The information on OSTN in the brain is very limited, but based on Ataman et al. *OSTN* is expressed by SATB2⁺, VGLUT1⁺ and CTIP2⁻ neurons (172), hence expression levels may be on lower side in neurons of cortical layer V/VI. Despite the challenges I faced in the quantification of OSTN, the goal to generate an isogenic system with a mutation of *OSTN* was reached successfully and could be validated by Sanger sequencing. Further, expression and inducibility of OSTN could be confirmed.

Another part of this project was the establishment of an efficient differentiation protocol with a high yield of glutamatergic cortical neurons since the PFC is among the affected brain regions that have been identified in SCZ (311,312). The initial progenitor differentiation phase by classic dual SMAD inhibition (214) that resulted in very homogenous cortical progenitor cultures (Figure 13A), was followed by a protocol for terminal differentiation of cortical neurons which was adjusted from protocols by Kemp et al. and Telezhkin et al. (261,262). The protocol amounted to a combination of small molecules that supported cell cycle exit, neuronal differentiation and synapse formation. After six weeks of terminal differentiation, neuronal cultures showed a high yield of cortical neurons expressing pan-neuronal markers (MAP2, TAU, NEUN), cortical layer V/VI markers (TBR1, CTIP2) and glutamatergic marker VGLUT1. The obtained cultures were very pure, containing very low levels of astroglia (markers S100B, GFAP) and low contamination by GABAergic neurons (Figure 13C). The protocol also ensured robust synaptogenesis, albeit that process required a longer maturation phase of the neurons which is a common issue in hiPSC derived models. This prompted my choices when to measure neuronal function and the analysis of synapses to ensure the presence of functional

synapses. Since long cultivation periods to achieve maturity are costly and have a high risk of failure due to technical issues (i.e. detachment of the cells) there are now approaches to speed up neuronal maturation by supplying a compound cocktail to the cells that enables a shift of immature gene expression to mature gene expression by inducing chromatin remodeling (313). This could be tested and applied to this model in the future to further increase efficiency of the model and working pipeline.

In summary, based on the genetic evaluation of the 3q28 locus, an isogenic hiPSC system for *OSTN* mutation was successfully established, as well as a differentiation protocol that reliably generates cortical neuronal cultures of high purity. These cultures express characteristic markers for neuronal identity and over time reach synaptic maturity which makes these cultures and the differentiation protocol eligible for the investigation of SCZ.

8.2 Impacts of *OSTN* and *IL-1 β* pathways on neuronal morphology

After the successful generation of the *OSTN* mutant cells and the establishment of an efficient differentiation protocol, I aimed to identify SCZ relevant phenotypes in hiPSC-derived cortical neurons. As previously described both, *OSTN* and *IL1RAP* expression are supposed to influence neuronal morphology (Figure 4 and 7). Hence, due to the heterozygous 3q28 deletion two limiting factors of neuronal ramification were impacted, which is why I hypothesized that SCZ neurons should display higher ramification levels.

Initially, an early outgrowth assay (d3 and 5) was performed for Ctrl and SCZ neurons to gain a first impression on morphological behavior of the neurons. Already in this early, immature state, SCZ neurons proved to be bigger, although not yet more complex than Ctrl. This phenotype could hint to faster outgrowth abilities (Figure 18).

These initial results were in line with the hypothesis, however, to further corroborate this, subsequent morphological analyses were performed on neuronal cultures around day 55-60 by transduction with an AAV introducing a mCherry expression under the CaMKIIa promoter. I could prove that also in the more mature neurons, in a culture of higher density, SCZ neurons surpassed Ctrl neurons in size and overall branching, only the number of primary neurites was lower in SCZ neurons (Figure 19). This is in line with results by Ataman and colleagues who demonstrated that a loss of function of *OSTN* induces a significant increase in neuronal ramification (172). However, the heterozygous deletion in SCZ cells encompasses a variety of genes including *IL1RAP* which should have a similar morphological effect on neurons like *OSTN* and may amplify this difference in neuron size. Therefore, to elucidate the effect of *OSTN* by itself, WT and the *OSTN* mutant neurons were analyzed in the same way. For the

Sholl analysis of the heterozygous clone *OSTN_2+/-* a slight increase in ramification could be observed, however overall size and intersections were similar to the WT, only the primary neurites showed the same result as in the Ctrl vs. SCZ comparison. The results for *OSTN_1+/-* and *OSTN-/-* however were more ambiguous. Surprisingly, *OSTN_1+/-* and *OSTN-/-* displayed overall smaller, less ramified neurons (Figure 20) which is not in line with the previously stated hypothesis. This deviation from the hypothesis needs to be carefully evaluated since there are some aspects that need to be considered. The heterozygous clone *OSTN_1+/-* was generated with a commercial CRISPR/Cas9 system, that has the potential to target three positions in the gene to maximize knockout probability. However, here, only one site was successfully targeted and resulted in a heterozygous clone. The targeted site is positioned towards the end of the coding sequence (Figure 11), which could result in an insufficiently perturbed protein that might still be able to exert part of its function. This needs to be further investigated, since the information gained from the analyses in this thesis are not sufficient to properly evaluate the situation. Since there is little information about *OSTN* in the brain, it is hard to predict what a homozygous *OSTN* mutation will lead to. Ataman and colleagues investigated the loss of function of *OSTN* by siRNA application and achieved an *OSTN* knockdown (high efficiency 84-94 %) and subsequently observed an increase in ramification (172). Nonetheless, the comparability of a (nearly complete) knockdown by siRNA which occurs for some days in the neuronal culture to a homozygous mutation which is continuously present throughout all differentiation stages is limited. From the present results of the homozygous clone, where the ramification is massively reduced compared to the WT, it is not deducible whether any over-compensatory mechanisms are active. For the abovementioned reasons, I laid the focus in this project mainly on *OSTN_2+/-* as a heterozygous clone with a mutation at the beginning of the coding sequence.

Another issue that needs to be discussed for this analysis, but also in general for hiPSC-derived models, is the batch variability, which was quite high in case of the WT Sholl analysis (supplementary Figure S1). Three individual batches were analyzed for the WT and a moderate batch variability was to be expected (like between batch 1 and batch 2), however a difference of the size of WT batch 3 to the other two batches is uncommon and must be taken into account. This problem could be addressed with different approaches, first in any case it is recommendable to increase the number of analyzed batches to get a better picture of the morphology. Afterwards, depending on the results it can be considered to perform a statistical correction by e.g. an outlier analysis. Since batch 3 displayed neurons of almost twice the size of the other two batches, its inclusion had a significant impact on the outcome of the results regarding *OSTN_2+/-*. This was demonstrated in the appendix of this thesis (supplementary Figure S2). WT batches 1 and 2, before inclusion of WT batch 3, resulted in a phenotype of WT vs. *OSTN_2+/-* that reproduces the situation in Ctrl and SCZ. It is likely that with increased

N numbers, results will become clearer, while probably leveling out between WT batch 1+2 and batch 3.

In sum, I proved that SCZ neurons tend to grow faster and to be overall bigger than Ctrl neurons in an early stage, and SCZ neurons were significantly bigger and more ramified in a mature neuronal culture being in line with previously published data (163,165,172). Previous works in context of SCZ research in hiPSC-derived neurons, could also report changes in neurite length and number, albeit mostly towards a decrease of those parameters (273,276,279,283,285). The results of WT vs *OSTN* mutants are inconclusive, due to high batch variability of WT neurons, but suggest a tendency to partially reflect the phenotype uncovered for SCZ neurons.

RNAseq data of Ctrl vs. SCZ and WT vs. *OSTN*_{1+/-} and *OSTN*_{-/-} neurons on d42 strongly suggested influences on neuronal morphology as well. Especially, but not exclusively, in the heterozygous 3q28 deletion context many GO terms related to neuronal morphology and growth were enriched. Upon closer inspection it became clear that several genes such as *SLIT1*, *ROBO1* and 2, *SEMA3A* and 5B, *EPHB1*, *COBL*, *UNC5A* and *SSTR2* were significantly differentially expressed (Figure 17). These genes are all involved in axon guidance or neurite branching and growth. For example *UNC5A* may be involved in branching morphogenesis during differentiation (314), and *COBL* is important for neurite branching (315). Furthermore, the other mentioned genes such as *SLIT1*, *ROBO1* and *ROBO2* (316–318), *EPHB1* (319), *SEMA3A* (320) and *SSTR2* (321) are important for axon guidance, branching, neurite outgrowth and elongation, while *SEMA5B*, additionally to its role in axon guidance is involved in synapse elimination (322). *COBL*, *ROBO2* and *SEMA3A* for instance, are higher expressed in the presented SCZ neurons, which could provide a base for the observed stronger ramification of neurons. It was shown, that more of these genes are differentially expressed in the SCZ context than in the isogenic context where only *SSTR2* (in *OSTN*_{1+/-}) and *ROBO2* (*OSTN*_{-/-}) were significantly different, which provides a clue about the smaller effect of the *OSTN* mutations on ramification. This suggests, that the heterozygous 3q28 has a stronger impact on gene expression than a mutation of *OSTN* alone which is to be expected, since many genes are affected by this heterozygous deletion and synergistic effects (e.g. potentially by *OSTN* and *IL1RAP*) are likely. Additionally, some of these genes (e.g. *SLIT1*, *ROBO2*, *SEMA3A*) have previously been suggested to be associated with SCZ (323–325).

All in all, the presented RNAseq data confirms a great influence of heterozygous 3q28 deletion and, albeit significantly less prominent, *OSTN* mutation on morphology related genes, uncovering starting points for future mechanistic investigations. But it also stresses the very high level of complexity of a SCZ genetic background vs a single gene approach. Furthermore,

future RNAseq experiments with a higher sequencing depth may be able to provide a more detailed insight into the impacts of *OSTN* mutation on neuronal processes.

The final step in the morphological analysis was to test, by modulation of OSTN and IL-1 β pathways, if the occurring phenotypes can be altered. Overall, the most prominent change was observed with IL-1 β treatment in Ctrl and OSTN_2+/- where both lines showed a significant reduction in Sholl intersections (Figure 22 and 23), an effect which is consistent with the literature (163,165). In SCZ neurons a slight reduction was observed albeit not significant, which is not too surprising considering that *IL1RAP*, that encodes an essential co-receptor of the IL-1 β signaling pathway (77,122,157), is affected by the heterozygous deletion. The OSTN treatment in Ctrl and, starting at 60 μ m from the soma, also in OSTN_2+/- showed a trend, although non-significant, towards less ramified neurons which is in line with the (limited) literature on the topic (172). Also, in SCZ neurons a reduction (non-significant) of ramification upon OSTN treatment was observed which was slightly stronger than in the IL-1 β treatment, likely since the potential receptor of OSTN is not affected by the heterozygous deletion. A double treatment with OSTN and IL-1 β led to a reduction in ramification in Ctrl and OSTN_2+/-, however compared to the untreated neurons it was not significant, which contradicts an amplifying effect of OSTN and IL-1 β pathway. OSTN in the periphery has been shown to exert anti-inflammatory effects likely by NP accumulation or PKG activation, which is involved in axon guidance (192,194,196,326). Therefore, a compensatory process that prevents cumulative effects may take place in the double treatment, but the current data are not sufficient to draw a conclusion. These results in Ctrl and SCZ for OSTN and IL-1 β are statistically sound since several batches could be analyzed, data on OSTN_2+/- for OSTN treatment included two batches as well while all other treatments are just preliminary results and must be considered with reservation. Moreover, the results of the remaining treatments were rather inconclusive and to properly evaluate them an increase of N is pivotal. A first impression when looking at the results of Ctrl and OSTN_2+/- was, that AP-811 treatment led to reduced ramification. In case the NPRC is the receptor for OSTN in the brain as well, this could imply that OSTN effects in the brain are also mediated by NP accumulation, since AP-811, same as OSTN, is an NPRC antagonist. Interestingly, in Ctrl, and more moderately in SCZ, a double treatment of AP-811+OSTN led to increased ramification which may suggest that another receptor for OSTN exists in neurons that is maybe bound with less affinity but could have an opposing effect on ramification when activated.

In sum, the results could confirm effects of IL-1 β and OSTN on neuronal morphology. While a cumulative effect of OSTN+IL-1 β treatment could not be confirmed, my data points to a potential interaction. Moreover, here I present a proof of principle that iPSC-derived neuronal cultures are responsive to small molecules associated to SCZ pathology and are inducing

disease-like phenotypes. This is not only showing that the model used in this thesis could be relevant, but also that the signaling pathways I chose might be interesting for additional investigations.

8.3 Influence of OSTN and IL-1 β pathways on synapses

Synapses are the sites of communication and contact between neurons and SCZ can be regarded as a synaptopathy, since several processes involving synapses have been described to be involved in its pathogenesis. This includes neurodevelopmental processes such as excessive synaptic pruning by microglia (46) or alterations in synapses, receptor landscape and impairment of vesicle release (56,276,327). Thus, the second major investigation category in this project was the analysis of synapses. This was mainly done by the analysis of the RNAseq data and quantification of synaptic particles.

The analysis of synapses at early time points was mainly done on RNAseq data (d42), since it became clear during the project, that the cultured neurons require quite some time to form mature synapses. The expression of genes related to synapses, vesicle release (SNARE complex), synaptic receptors and adhesion molecules was investigated in Ctrl, SCZ, WT, OSTN_{1+/-} and OSTN_{-/-} neuronal cultures (Figures 25-27). First, most of the significant differences occurred again in the context of Ctrl vs. SCZ neurons and the isogenic context displayed rather tendencies and barely any significant differences. In the isogenic system, the only significant difference that was present in both OSTN_{1+/-} and OSTN_{-/-} neurons was *PRSS12*, which was significantly lower expressed than in WT neurons. *PRSS12* is known to be involved in excitatory synapse formation and maintenance (328,329). Therefore, a reduced expression could hint towards reduced synaptic stability and consequently increased synapse loss over time. However, to date, there is no direct connection known between *OSTN* and *PRSS12*. Due to the more complex genetic background, the SCZ neurons, on the other hand, displayed a variety of significantly differentially expressed genes. Especially RNA levels of postsynaptic markers were impacted by the heterozygous 3q28 deletion such as *SHANK2*, *SYNPO*, *SHISA6*, *GRM3* and *LZTS3*. But also, presynaptic markers like *SYN3* and *BSN* (not significant), receptor (subunits) like *GRIN2C*, *GLRA2* and several GABAR subunits (*GABRA1*, *GABRA4* etc.), SNARE complex members *SNAP25*, *SYT13* and *17* and various adhesion molecules for instance cadherins and protocadherins (*CDH2*, *PCDH17*, *PCDHGB1*), *NRG1*, *CNTNAP2*, *DSCAM*, *DSCAML1*, and *PTPRD*, an interaction partner of IL-1RAP and IL-1RAPL1 for synapse differentiation and stabilization (162,330), were significantly differentially expressed in SCZ neurons. All these genes and their corresponding proteins are important for proper synapse formation, maintenance and function (like signal transmission). The differential

expression suggests that synapse numbers and probably stability differ between Ctrl and SCZ neurons, also, regarding neuronal functionality and activity differences between the cultures were likely. Furthermore, some of these genes have been already associated with SCZ (e.g. *CDH2*, *CNTNAP2*, *PCDH17*, *NRG1*)(281,331–333). Overall, this expression data suggests a strong impact of the heterozygous 3q28 deletion on synapse related genes, although it cannot be excluded that there are further genetic features of the SCZ line that also take an influence.

When I analyzed synapses in a mature state (around d105) it was evident that SCZ neurons had more functional synapses than Ctrl neurons (measured by colocalization of SYN/PSD95, Figure 24). This indicates a temporal component that has to be considered in this *in vitro* model, since in western blot analysis at d42 SCZ neurons showed slightly reduced SYN1 levels. It means that SCZ neurons at some point surpass Ctrl neurons regarding synapse density, which additionally further emphasizes the capacity of this model to recapitulate developmental phases. In the SCZ line, due to its genetics, IL-1 β signaling is likely dysfunctional, thus I expected more synapses in SCZ compared to Ctrl neurons. Since IL-1 β signaling has been shown to reduce synapses and dendritic spines (138,147) conversely reduced signaling could lead to more synapses.

As expected, *OSTN* mutation did not have a strong effect on a transcriptomic level at d42, however I analyzed WT and mutant neurons around d105 as well (Figure 28). Surprisingly, all mutant clones displayed significantly reduced SYN particles and partially significantly reduced PSD95 particles and colocalization. As mentioned previously, in the RNAseq data there was only *PRSS12* (among the analyzed genes) that could be connected to this phenomenon. *PRSS12* was downregulated in the mutant clones. Hence, its role in synapse formation and maintenance (329) and its downregulation in *OSTN_1*^{+/-} and *OSTN*^{-/-} could be part of an explanation for reduced synapse density. Unfortunately, the expression levels of *PRSS12* in *OSTN_2*^{+/-} remain to be elucidated, but it would be interesting to see if *PRSS12* is downregulated in this clone as well. Nonetheless, it would remain to be elucidated how *OSTN* and *PRSS12* would be connected, which is why there are likely additional underlying causes that need to be uncovered.

Overall, both, heterozygous 3q28 deletion and *OSTN* mutation on its own, have an impact on the number of synapses, albeit an opposing effect. This opposing effect may be attributed to the impact of altered IL-1 β signaling in SCZ neurons due to the heterozygous 3q28 deletion, however the current data cannot exclude the involvement of other genes and pathways which led to these results. Current literature often showed reductions in synapses in SCZ (56,276) opposing the results presented here for the SCZ neurons, however assumably a significant increase as well as a significant decrease in synapses would lead to an imbalance that could negatively affect brain functions.

I did two initial attempts to further decipher influences of OSTN and IL-1 β pathway on synapses by applying the previously mentioned treatment combinations on neurons around d55-60 (AAV transduced) and d105. First of all, SYN levels of mCherry⁺ SCZ neurons around d55-60 were already higher than in Ctrl neurons, indicating that SCZ neurons surpass Ctrl neurons in synapse numbers between d42 and d55-60. Most treatments had no significant effect on SCZ neurons, except IL-1Ra+IL-1 β led to a significant decrease in SYN particles/100 μm^2 neurite, while in Ctrl neurons a significant increase was observed in OSTN+IL-1 β , AP-811, AP-811+OSTN, IL-1Ra+IL-1 β and AP-811+IL-1Ra, while the remaining treatments did not show significant differences (Figure 29). These results are surprising, since the only known effect predicted for IL-1 β treatment would be a reduction in synapses, which is not reflected in the current data. The data obtained from WT and OSTN₂^{+/-} are similarly inconclusive, all treatments trended towards less SYN particles/100 μm^2 , however the one condition (IL-1 β) - where this was to be expected- the results were not significant (Figure 30). On day 105 neurons the results were more consistent, since for Ctrl and WT there were almost no differences between treatments. SCZ neurons, if a significant difference occurred, displayed an increase in all parameters (Figure 31+S3). Interestingly, I observed that the treatments exerted a different effect depending on the time point of maturation in both Ctrl and SCZ line. Specifically, it seems more mature Ctrl neurons (d105) cope better with the applied stimuli compared to SCZ neurons. Indeed, all the synaptic parameters analyzed are modulated only in the SCZ cells. Since our lab already demonstrated, that more mature neurons are less susceptible to stressful stimuli (334), this data might suggest that at these late stages of differentiation, SCZ neurons may be more complex morphologically but lack maturity compared to Ctrl.

To summarize, here I demonstrate that the patient derived neurons and the recombinant systems are susceptible to the pharmacological modulation. The complexity of the genetic background of the patient and -on the other side- the potential low impact of *OSTN* specific mutations alone on the synaptic compartment, gave a rather complicate picture to unravel. Further mechanistic experiments focused on dissecting the involvement and the interaction between the molecular pathways analyzed should be considered. However, here I indicate that the maturation state could be involved in the response to the treatments.

8.4 Consequences of heterozygous 3q28 deletion on neuronal function

Substantial changes in morphology in combination with differences in synapse density strongly suggest an impact on neuronal connectivity. IL-1 β signaling could have an impact not only in neuronal morphology, but also on neuronal function. For instance, IL-1 β can increase sEPSC

frequency and thereby induce neurotoxicity (144–146). In line with the previously presented results of this project and the information from the literature, the last major investigation category was the functional analysis of the neuronal cultures.

First the data on the AIS for Ctrl and SCZ neurons showed on average a significantly shorter AIS which was located significantly closer to the soma (Figure 32). According to the general hypothesis, the AIS can regulate neuronal excitability by shifting length and location, if activity levels are low and the neuron needs to increase excitability, the AIS would become longer and would shift closer to the soma. If activity levels were high and neurons need to become less excitable the opposite should happen, the AIS would shorten and increase the distance to the soma (307). Thus, the results for the SCZ neurons could suggest a compensatory behavior of the AIS to maintain a specific level of excitability. However, the measurement of the AIS was a too indirect parameter to test neuronal functionality in comparison to the live cell experiments, which is why further AIS analyses were omitted.

In Ca^{2+} imaging, under baseline conditions no differences were observed in any of the parameters. Upon stimulation, SCZ cultures displayed more active cells than Ctrl and the synchronicity index, albeit being very low in general, was higher in stimulated SCZ cultures, indicating a slightly stronger network activity (Figure 34). The average number of events and frequency increased in both cell lines with stimulation, but did not differ significantly between cell lines, which could hint towards an overall similar neuronal excitability, which would be in line with the previously suspected AIS compensatory behavior. Analysis of d70 Ctrl and SCZ neurons painted a similar picture, albeit neurons were more mature at that time, the only significant difference was the relative number of active cells which was reduced in SCZ neurons under baseline conditions (Figure 38). Upon stimulation all parameters increased but not significantly which more or less reflected the situation at d45.

In general, synchronicity indices are very low which indicates a weak network activity. According to the results I presented this far, SCZ neurons are more complex with an increased number of synapses. Hence, a higher inter-neuronal connectivity could be expected, however this is not reflected by the synchronicity indices. In that light, it is important to note that the increased ramification occurs in the distal parts of the SCZ neurons. In a physiological environment, neurons receive inputs from many other neurons of many types and have to process and distinguish every input, which is essential for i.e. sequence memory. That means that an activation of distal synapses does not necessarily lead to AP generation unless for example a large number of synapses receives input simultaneously, while inputs towards few proximal synapses could directly result in AP generation (335). Furthermore, subcellular spatial resolution of inputs might be neuron type-dependent, for example in mice, corticocortical and thalamocortical excitatory neurons seem to preferentially target different cellular compartments

on interneurons than i.e. parvalbumin-positive inhibitory neurons (336). These physiological mechanisms to integrate incoming signals may play a role in the SCZ neurons as well. Additionally, in a SCZ study on hiPSC-derived neurons a similar phenomenon has been observed: neurons in this case displayed reduced neurites and PSD levels but nonetheless displayed normal Ca^{2+} transients and electrophysiological activity (276). This demonstrates the complexity of the integration and interpretation of the presented data and to gain a deeper understanding further experiments such as determination of subcellular synapse distribution and investigation of neuronal in- and outputs in a more complex system will be necessary. For instance, a co-culture with e.g. GABAergic neurons with or without astrocytes or a 3D system, such as brain organoids, could facilitate the study of these more complex functional interactions. Both systems could provide a more holistic view and more detailed information on potential functional differences.

The same Ca^{2+} imaging analysis was performed for WT and *OSTN* mutant neurons on d45 (Figure 35) and similar to Ctrl and SCZ, no major differences occurred. Furthermore, modulation of *OSTN* and *IL-1 β* pathways on Ctrl and SCZ neurons, for the most part did not show any noteworthy differences. In consideration of results of the *OSTN* mutant cells and also the insights of SCZ neurons, the influence of *OSTN* and *IL-1 β* directly on neuronal functionality seems marginal.

In sum, the Ca^{2+} imaging data revealed overall no major differences in neuronal activity and network activity in any of the investigated cell lines. Hence, neither the heterozygous 3q28 deletion nor the *OSTN* mutation could be attributed to altered neuronal function by Ca^{2+} imaging. Nevertheless, it has to be kept in mind that Ca^{2+} imaging and analysis had its technical shortcomings in this project. For instance, the use of Fluo-4 AM is accompanied by dye diffusion and photobleaching which was a reason to image new positions for the stimulation, which could also explain the occasional reduction of active cells (%) upon stimulation. Another consideration to be made is the purity and maturity of the culture, since there are barely any astroglia, synaptic connectivity and stability may not be as good which could be a clue as to why the network activity (synchronicity index) is so low, even at d70. Further, there is still potential to optimize the Ca^{2+} imaging analysis further to obtain more robust results.

In line with the Ca^{2+} imaging results, RNAseq data on d42 neurons (all cell lines) showed almost no significant differences in activity related gene expression.

In parallel to Ca^{2+} imaging analysis, electrophysiological measurements were performed around d56/57 in co-culture with mouse-derived astrocytes (Figure 39+40). These measurements enable the analysis of neuronal functionality in greater depth and a better evaluation of potential underlying synaptic processes. SCZ and *OSTN* mutant neurons showed

altered spontaneous activity while SCZ neurons additionally displayed changes in excitability compared to Ctrl. These results slightly differ from the Ca^{2+} data in terms of activity levels, but it has to be taken into account that the neurons for the electrophysiology were co-cultured with (mouse-derived) astrocytes. This could indicate the necessity to use more complex systems to support neuronal functionality and boost the emergence of pathological phenotypes.

Moreover, multi-electrode array measurements could likely give a better understanding of network activity than Ca^{2+} imaging. The literature on neuronal activity in SCZ neurons is also divided reporting on one hand no differences in functional parameters (276), or on the other hand reduced active neurons with decreased spontaneous firing rate and reduced excitability (280). In addition, decreased EPSC amplitude and frequency in cortical (56) and hippocampal neurons (277) were reported as well as reduced Ca^{2+} transients in cortical neurons (278). Thus, more in-depth research is needed to further decipher underlying mechanisms in SCZ whereby it is pivotal to investigate various systems (e.g. glutamatergic and GABAergic) to put results into perspective since likely imbalances of these systems play a central role in the pathogenesis of SCZ.

9. Summary and outlook

In the presented thesis, a hiPSC-based model system was used to investigate the role of a heterozygous 3q28 deletion in the pathogenesis of SCZ. Further, isogenic hiPSCs were generated for *OSTN*, a gene affected by the heterozygous 3q28 deletion. This project proved hiPSCs as an invaluable tool to bridge the gap between animal models and clinical research, since *OSTN* expression in the brain is exclusive for humans and primates. With these models, it was possible to start to decipher the effects of these genetic alterations on cortical neurons.

In summary, the here presented thesis could uncover the following major findings:

1. Heterozygous 3q28 deletion and *OSTN* mutation strongly affect neuronal morphology.
2. Modulation of the *OSTN* and IL-1 β pathway respectively, influences neuronal morphology.
3. Heterozygous 3q28 deletion strongly affects gene expression related to neuronal growth, synaptic markers and adhesion molecules.
4. Heterozygous 3q28 deletion increases mature synapses while *OSTN* mutation alone has a decreasing effect.
5. Electrophysiological intrinsic and synaptic properties are altered by heterozygous 3q28 deletion and *OSTN* mutation.

This project is the first to recapitulate the effect of *OSTN* on neuronal morphology since the first statement of *OSTN* repurposing by Ataman et al. (172). Albeit this specific deletion has not been associated with SCZ so far, *IL1RAP* located on 3q28 was previously shown to be involved in SCZ as well as the IL-1 β pathway in general (98,160). Moreover, further SCZ associated genes were shown to be differentially expressed due to the heterozygous 3q28 deletion.

In this study I could establish a workflow, starting with the identification of candidate genes out of a complex genetic background, followed by the generation of an isogenic system to better understand functions of the candidate gene. By the means of transcriptomic tools to in-depth morphological analysis to functional readouts, I was able to characterize the iPSC models and identify potential cellular phenotypes. Of note, this approach can be applied to other patient-derived lines diagnosed with complex disorders to pinpoint underlying molecular mechanisms. In sum, my work provides indications for possible mechanisms involved in SCZ and some solid investigation tools, which, due to their potential for automatization and scalability, can be useful to the approach of personalized medicine and compound testing in the future. However, due

Summary and outlook

to the challenging aspects of this topic, there is still some work to be done, for one, to increase the N numbers in the respective experiments and then, incorporation of further experiments to deepen the understanding of underlying mechanisms. This would increase the comprehension of SCZ pathology. It would be also beneficial to consider 3D models to investigate neuronal morphology etc. in a more complex context in order to take another step on the long road to identify commonalities and causalities for SCZ.

10. References

1. Barbato A. World Health Organization Schizophrenia and public health: An Action Programme on Mental Health for Underserved Populations. *Nations Ment Heal.* 1996;
2. Gejman P V, Sanders AR, Duan J. The role of genetics in the etiology of schizophrenia. *Psychiatr Clin North Am.* 2010 Mar;33(1):35–66.
3. Picchioni MM, Murray RM. Schizophrenia. *BMJ.* 2007;335(July):91–5.
4. Cannon TD, Van Erp TGM, Bearden CE, Loewy R, Thompson P, Toga AW, et al. Early and Late Neurodevelopmental Influences in the Prodrome to Schizophrenia: Contributions of Genes, Environment, and Their Interactions. *Schizophr Bull.* 2003;29(4):653–69.
5. Spauwen J, Krabbendam L, Lieb R, Wittchen HU, van Os J. Impact of psychological trauma on the development of psychotic symptoms: relationship with psychosis proneness. *Br J Psychiatry.* 2006;188(6):527–33.
6. Whitfield CL, Dube SR, Felitti VJ, Anda RF. Adverse childhood experiences and hallucinations. *Child Abus Negl.* 2005;29:797–810.
7. Bebbington PE, Bhugra D, Brugha T, Singleton N, Farrell M, Jenkins R, et al. Psychosis, victimisation and childhood disadvantage: evidence from the second British National Survey of Psychiatric Morbidity. *Br J Psychiatry.* 2004 Sep;185(SEPT.):220–6.
8. Spataro J, Mullen PE, Burgess PM, Wells DL, Moss SA. Impact of child sexual abuse on mental health. 2004;416–21.
9. Dean K, Murray RM. Environmental risk factors for psychosis. *Dialogues Clin Neurosci.* 2005;7(1):69–80.
10. Morgan C, Fisher H. Environment and schizophrenia: Environmental factors in schizophrenia: Childhood trauma - A critical review. *Schizophr Bull.* 2007;33(1):3–10.
11. Millan MJ, Andrieux A, Bartzokis G, Cadenhead K, Dazzan P, Fusar-Poli P, et al. Altering the course of schizophrenia: Progress and perspectives. *Nat Rev Drug Discov.* 2016;15(7):485–515.
12. Heilbronner U, Samara M, Leucht S, Falkai P, Schulze TG. The Longitudinal Course of Schizophrenia Across the Lifespan: Clinical, Cognitive, and Neurobiological Aspects. *Harv Rev Psychiatry.* 2016;24(2):118–28.
13. Emsley R, Nuamah I, Gopal S, Hough D, Fleischhacker WW. Relapse After Antipsychotic Discontinuation in Schizophrenia as a Withdrawal Phenomenon vs Illness Recurrence: A Post Hoc Analysis of a Randomized Placebo-Controlled Study. *J Clin Psychiatry.* 2018;79(4):e1–7.
14. Emsley R, Oosthuizen PP, Koen L, Niehaus DJH, Martinez G. Symptom recurrence following intermittent treatment in first-episode schizophrenia successfully treated for 2 years: A 3-year open-label clinical study. *J Clin Psychiatry.* 2012;73(4):541–7.
15. Howes OD, McDonald C, Cannon M, Arseneault L, Boydell J, Murray RM. Pathways to schizophrenia: The impact of environmental factors. *Int J Neuropsychopharmacol.* 2004;7(SUPPL. 1).
16. Zhu J, Zhuo C, Liu F, Qin W, Xu L, Yu C. Distinct disruptions of resting-state functional brain networks in familial and sporadic schizophrenia. *Sci Rep.* 2016;6(March):6–15.
17. Karlsgodt KH, Sun D, Cannon TD. Structural and Functional Brain Abnormalities in Schizophrenia. *Curr Dir Psychol Sci.* 2010 Aug;19(4):226–31.

References

18. Zhao C, Zhu J, Liu X, Pu C, Lai Y, Chen L, et al. Structural and functional brain abnormalities in schizophrenia: A cross-sectional study at different stages of the disease. *Prog Neuro-Psychopharmacology Biol Psychiatry*. 2018;83(11):27–32.
19. Glantz LA, Lewis DA. Decreased dendritic spine density on prefrontal cortical pyramidal neurons in schizophrenia. *Arch Gen Psychiatry*. 2000 Jan;57(1):65–73.
20. Howes OD, Kapur S. The dopamine hypothesis of schizophrenia: Version III - The final common pathway. *Schizophr Bull*. 2009;35(3):549–62.
21. Hu W, MacDonald ML, Elswick DE, Sweet RA. The glutamate hypothesis of schizophrenia: evidence from human brain tissue studies. *Ann N Y Acad Sci*. 2015;1338(1):38–57.
22. Harvey CD, Svoboda K. Locally dynamic synaptic learning rules in pyramidal neuron dendrites. *Nature*. 2007;450(7173):1195–200.
23. Eastwood SL, Burnet PWJ, Harrison PJ. GluR2 glutamate receptor subunit flip and flop isoforms are decreased in the hippocampal formation in schizophrenia: A reverse transcriptase-polymerase chain reaction (RT-PCR) study. *Mol Brain Res*. 1997;44(1):92–8.
24. Gao XM, Sakai K, Roberts RC, Conley RR, Dean B, Tamminga CA. Ionotropic glutamate receptors and expression of N-methyl-D-aspartate receptor subunits in subregions of human hippocampus: Effects of schizophrenia. *Am J Psychiatry*. 2000;157(7):1141–9.
25. Clinton SM, Haroutunian V, Davis KL, Meador-Woodruff JH. Altered transcript expression of NMDA receptor-associated postsynaptic proteins in the thalamus of subjects with schizophrenia. *Am J Psychiatry*. 2003;160(6):1100–9.
26. Eastwood SL, McDonald B, Burnet PWJ, Beckwith JP, Kerwin RW, Harrison PJ. Decreased expression of mRNAs encoding non-NMDA glutamate receptors GluR1 and GluR2 in medial temporal lobe neurons in schizophrenia. *Mol Brain Res*. 1995;29(2):211–23.
27. Mueller HT, Meador-Woodruff JH. NR3A NMDA receptor subunit mRNA expression in schizophrenia, depression and bipolar disorder. *Schizophr Res*. 2004;71(2–3):361–70.
28. Akbarian S, Sucher NJ, Bradley D, Tafazzoli A, Trinh D, Hetrick WP, et al. Selective alterations in gene expression for NMDA receptor subunits in prefrontal cortex of schizophrenics. *J Neurosci*. 1996;16(1):19–30.
29. Bauer D, Gupta D, Haroutunian V, Meador-Woodruff JH, McCullumsmith RE. Abnormal expression of glutamate transporter and transporter interacting molecules in prefrontal cortex in elderly patients with schizophrenia. *Schizophr Res*. 2008;104(1–3):108–20.
30. Bauer D, Haroutunian V, Meador-Woodruff JH, McCullumsmith RE. Abnormal glycosylation of EAAT1 and EAAT2 in prefrontal cortex of elderly patients with schizophrenia. *Schizophr Res*. 2010;117(1):92–8.
31. Verrall L, Walker M, Rawlings N, Benzel I, Kew JNC, Harrison PJ, et al. d-Amino acid oxidase and serine racemase in human brain: normal distribution and altered expression in schizophrenia. *Eur J n*. 2007;26(6):1657–69.
32. Kristiansen L V., Beneyto M, Haroutunian V, Meador-Woodruff JH. Changes in NMDA receptor subunits and interacting PSD proteins in dorsolateral prefrontal and anterior cingulate cortex indicate abnormal regional expression in schizophrenia. *Mol Psychiatry*. 2006;11(8):737–47.
33. Oni-Orisan A, Kristiansen L V., Haroutunian V, Meador-Woodruff JH, McCullumsmith RE. Altered Vesicular Glutamate Transporter Expression in the Anterior Cingulate Cortex in Schizophrenia. *Biol Psychiatry*. 2008;63(8):766–75.
34. Steffek AE, McCullumsmith RE, Haroutunian V, Meador-Woodruff JH. Cortical expression of glial fibrillary acidic protein and glutamine synthetase is decreased in schizophrenia. *Schizophr*

References

- Res. 2008;103(1–3):71–82.
35. Katsel P, Byne W, Roussos P, Tan W, Siever L, Haroutunian V. Astrocyte and glutamate markers in the superficial, deep, and white matter layers of the anterior cingulate gyrus in schizophrenia. *Neuropsychopharmacology*. 2011;36(6):1171–7.
 36. Eggers AE. A serotonin hypothesis of schizophrenia. *Med Hypotheses*. 2013;80(6):791–4.
 37. Kuroki T, Nagao N, Nakahara T. Neuropharmacology of second-generation antipsychotic drugs: a validity of the serotonin–dopamine hypothesis. In: Di Giovanni G, Di Matteo V, Esposito E, editors. *Serotonin–Dopamine Interaction: Experimental Evidence and Therapeutic Relevance*. Elsevier; 2008. p. 199–212. (Progress in Brain Research; vol. 172).
 38. Marques TR, Ashok AH, Angelescu I, Borgan F, Myers J, Lingford-Hughes A, et al. GABA-A receptor differences in schizophrenia: a positron emission tomography study using [¹¹C]Ro154513. *Mol Psychiatry*. 2021;26(6):2616–25.
 39. de Jonge JC, Vinkers CH, Hulshoff Pol HE, Marsman A. GABAergic mechanisms in schizophrenia: Linking postmortem and In vivo studies. *Front Psychiatry*. 2017;8(AUG):118.
 40. Shi Y, Zhang Y, Lou J. The influence of cell membrane and SNAP25 linker loop on the dynamics and unzipping of SNARE complex. *PLoS One*. 2017;12(4):1–15.
 41. Thompson PM, Egbufoama S, Vawter MP. SNAP-25 reduction in the hippocampus of patients with schizophrenia. *Prog Neuro-Psychopharmacology Biol Psychiatry*. 2003;27(3):411–7.
 42. Dulubova I, Khvotchev M, Liu S, Huryeva I, Sudhof TC, Rizo J. Munc18-1 binds directly to the neuronal SNARE complex. *Proc Natl Acad Sci*. 2007;104(8):2697–702.
 43. Urigüen L, Gil-Pisa I, Munarriz-Cuezva E, Berrocoso E, Pascau J, Soto-Montenegro ML, et al. Behavioral, neurochemical and morphological changes induced by the overexpression of munc18-1a in brain of mice: relevance to schizophrenia. *Transl Psychiatry*. 2013;3:1–10.
 44. Wang M, Zhang L, Gage FH. Microglia, complement and schizophrenia. *Nat Neurosci*. 2019;22(3):333–4.
 45. Sekar A, Bialas AR, De Rivera H, Davis A, Hammond TR, Kamitaki N, et al. Schizophrenia risk from complex variation of complement component 4 Schizophrenia Working Group of the Psychiatric Genomics Consortium HHS Public Access. *Nature* Febr. 2016;11(5307589):177–83.
 46. Sellgren CM, Gracias J, Watmuff B, Biag JD, Thanos JM, Whittredge PB, et al. Increased synapse elimination by microglia in schizophrenia patient-derived models of synaptic pruning. *Nat Neurosci*. 2019;22(3):374–85.
 47. Feinberg I. Schizophrenia: Caused by a fault in programmed synaptic elimination during adolescence? *J Psychiatr Res*. 1982;17(4):319–34.
 48. Keshavan MS, Anderson S, Pettegrew JW. Is schizophrenia due to excessive synaptic pruning in the prefrontal cortex? The Feinberg hypothesis revisited. *J Psychiatr Res*. 1994;28(3):239–65.
 49. Keshavan M, Lizano P, Prasad K. The synaptic pruning hypothesis of schizophrenia: promises and challenges. *World Psychiatry*. 2020;19(1):110–1.
 50. Najjar S, Pearlman DM, Alper K, Najjar A, Devinsky O. Neuroinflammation and psychiatric illness. *J Neuroinflammation*. 2013;10.
 51. Fan X, Goff DC, Henderson DC. Inflammation and schizophrenia. *Expert Rev Neurother*. 2007;7(7):789–96.

References

52. J Muir W, M Gosden C, J Brookes A, Fantès J, Evans K, Anderson S, et al. Direct microdissection and microcloning of a translocation breakpoint region, t(1;11)(q42.2;q21), associated with schizophrenia. *Cytogenet Cell Genet.* 1995;70:35–40.
53. Blackwood DHR, Fordyce A, Walker MT, St. Clair DM, Porteous DJ, Muir WJ. Schizophrenia and Affective Disorders—Cosegregation with a Translocation at Chromosome 1q42 That Directly Disrupts Brain-Expressed Genes: Clinical and P300 Findings in a Family. *Am J Hum Genet.* 2001;69(2):428–33.
54. StClair D, Blackwood D, Muir W, Carothers A, Walker M, Spowart G, et al. Association within a family of a balanced autosomal translocation with major mental illness. *Lancet.* 1990;336:13–6.
55. Tomoda T, Hikida T, Sakurai T. Role of DISC1 in Neuronal Trafficking and its Implication in Neuropsychiatric Manifestation and Neurotherapeutics. *Neurotherapeutics.* 2017;14(3):623–9.
56. Wen Z, Nguyen HN, Guo Z, Lalli MA, Wang X, Su Y, et al. Synaptic dysregulation in a human iPSC cell model of mental disorders. *Nature.* 2014;515(7527):414–8.
57. Guo X, Zhang Y, Du J, Yang H, Ma Y, Li J, et al. Association analysis of ANK3 gene variants with schizophrenia in a northern Chinese Han population. *Oncotarget.* 2016;7(52):85888–94.
58. Jenkins SM, Bennett V. Ankyrin-G coordinates assembly of the spectrin-based membrane skeleton, voltage-gated sodium channels, and L1 CAMs at Purkinje neuron initial segments. *J Cell Biol.* 2001;155(5):739–45.
59. Hsu WCJ, Nilsson CL, Laezza F. Role of the axonal initial segment in psychiatric disorders: Function, dysfunction, and intervention. *Front Psychiatry.* 2014;5(AUG):1–11.
60. Kirov G, Ivanov D, Williams NM, Preece A, Nikolov I, Milev R, et al. Strong evidence for association between the dystrobrevin binding protein 1 gene (DTNBP1) and schizophrenia in 488 parent-offspring trios from Bulgaria. *Biol Psychiatry.* 2004;55(10):971–5.
61. Schwab SG, Knapp M, Mondabon S, Hallmayer J, Borrmann-Hassenbach M, Albus M, et al. Support for Association of Schizophrenia with Genetic Variation in the 6p22.3 Gene, Dysbindin, in Sib-Pair Families with Linkage and in an Additional Sample of Triad Families. *Am J Hum Genet.* 2003;72(1):185–90.
62. Straub RE, Jiang Y, Maclean CJ, Ma Y, Webb BT, Kadambi B, et al. Genetic Variation in the 6p22.3 Gene DTNBP1, the Human Ortholog of the Mouse Dysbindin Gene, Is Associated with Schizophrenia. *Am J Hum Genet.* 2002;71:337–48.
63. Corvin AP, Morris DW, McGhee K, Schwaiger S, Scully P, Quinn J, et al. Confirmation and refinement of an “at-risk” haplotype for schizophrenia suggests the EST cluster, Hs.97362, as a potential susceptibility gene at the Neuregulin-1 locus. *Mol Psychiatry.* 2004;9(2):208–12.
64. Liu H, Heath SC, Sobin C, Roos JL, Galke BL, Blundell ML, et al. Genetic variation at the 22q11 *PRODH2/DGCR6* locus presents an unusual pattern and increases susceptibility to schizophrenia. *Proc Natl Acad Sci.* 2002;99(6):3717–22.
65. Amaral P, Carbonell-Sala S, De La Vega FM, Faial T, Frankish A, Gingeras T, et al. The status of the human gene catalogue. *ArXiv.* 2023 Mar;
66. Morimoto K, Nakajima K. Role of the Immune System in the Development of the Central Nervous System. *Front Neurosci.* 2019;13(September).
67. Daneman R, Prat A. The Blood-Brain Barrier. *Cold Spring Harb Perspect Biol.* 2015 Jan;7(1):a020412.
68. Louveau A, Smirnov I, Keyes TJ, Eccles JD, Rouhani SJ, Peske JD, et al. Structural and functional features of central nervous system lymphatic vessels. *Nature.* 2015;523(7560):337–41.

References

69. Aspelund A, Antila S, Proulx ST, Karlsten TV, Karaman S, Detmar M, et al. A dural lymphatic vascular system that drains brain interstitial fluid and macromolecules. *J Exp Med*. 2015;212(7):991–9.
70. Ma T, Wang F, Xu S, Huang JH. Meningeal immunity: Structure, function and a potential therapeutic target of neurodegenerative diseases. *Brain Behav Immun*. 2021;93(July 2020):264–76.
71. Mazzitelli JA, Smyth LCD, Cross KA, Dykstra T, Sun J, Du S, et al. Cerebrospinal fluid regulates skull bone marrow niches via direct access through dural channels. *Nat Neurosci*. 2022;25(5):555–60.
72. Pulous FE, Cruz-Hernández JC, Yang C, Kaya Z, Paccalet A, Wojtkiewicz G, et al. Cerebrospinal fluid can exit into the skull bone marrow and instruct cranial hematopoiesis in mice with bacterial meningitis. *Nat Neurosci*. 2022;25(5):567–76.
73. Paré A, Mailhot B, Lévesque SA, Juzwik C, Doss PMIA, Lécuyer MA, et al. IL-1 β enables CNS access to CCR2hi monocytes and the generation of pathogenic cells through GM-CSF released by CNS endothelial cells. *Proc Natl Acad Sci U S A*. 2018;115(6):E1194–203.
74. Yarlagadda A, Alfson E, Clayton AH. The blood brain barrier and the role of cytokines in neuropsychiatry. *Psychiatry*. 2009;6(11):18–22.
75. Ousman SS, Kuberski P. Immune surveillance in the central nervous system. *Nat Neurosci*. 2012;15(8):1096–101.
76. Kitazawa M, Cheng D, Tsukamoto MR, Koike MA, Wes PD, Vasilevko V, et al. Blocking IL-1 Signaling Rescues Cognition, Attenuates Tau Pathology, and Restores Neuronal β -Catenin Pathway Function in an Alzheimer's Disease Model. *J Immunol*. 2011;187(12):6539–49.
77. Pinteaux E, Abdulaal WH, Mufazalov IA, Humphreys NE, Simonsen-Jackson M, Francis S, et al. Cell-specific conditional deletion of interleukin-1 (IL-1) ligands and its receptors: a new toolbox to study the role of IL-1 in health and disease. *J Mol Med*. 2020;98(7):923–30.
78. Tsakiri N, Kimber I, Rothwell NJ, Pinteaux E. Differential effects of interleukin-1 alpha and beta on interleukin-6 and chemokine synthesis in neurones. *Mol Cell Neurosci*. 2008;38(2):259–65.
79. Parish CL, Finkelstein DI, Tripanichkul W, Satoskar AR, Drago J, Horne MK. The role of interleukin-1, interleukin-6, and glia in inducing growth of neuronal terminal arbors in mice. *J Neurosci*. 2002;22(18):8034–41.
80. Wolf SA, Steiner B, Akpinarli A, Kammertoens T, Nassenstein C, Braun A, et al. CD4-Positive T Lymphocytes Provide a Neuroimmunological Link in the Control of Adult Hippocampal Neurogenesis. *J Immunol*. 2009;182(7):3979–84.
81. Ziv Y, Ron N, Butovsky O, Landa G, Sudai E, Greenberg N, et al. Immune cells contribute to the maintenance of neurogenesis and spatial learning abilities in adulthood. *Nat Neurosci*. 2006;9(2):268–75.
82. Kipnis J, Cohen H, Cardon M, Ziv Y, Schwartz M. T cell deficiency leads to cognitive dysfunction: Implications for therapeutic vaccination for schizophrenia and other psychiatric conditions. *Proc Natl Acad Sci U S A*. 2004;101(21):8180–5.
83. Rattazzi L, Piras G, Ono M, Deacon R, Pariante CM, D'Acquisto F. CD4+ but not CD8+ T cells revert the impaired emotional behavior of immunocompromised RAG-1-deficient mice. *Transl Psychiatry*. 2013;3(April):1–16.
84. Kipnis J, Gadani S, Derecki NC. Pro-cognitive properties of T cells. *Nat Rev Immunol*. 2012;12(9):663–9.
85. Alves de Lima K, Rustenhoven J, Da Mesquita S, Wall M, Salvador AF, Smirnov I, et al.

References

- Meningeal $\gamma\delta$ T cells regulate anxiety-like behavior via IL-17a signaling in neurons. Vol. 21, Nature Immunology. 2020. p. 1421–9.
86. Ribeiro M, Brigas HC, Temido-Ferreira M, Pousinha PA, Regen T, Santa C, et al. Meningeal $\gamma\delta$ T cell-derived IL-17 controls synaptic plasticity and short-term memory. Vol. 4, Science Immunology. 2019.
87. Li AJ, Katafuchi T, Oda S, Hori T, Oomura Y. Interleukin-6 inhibits long-term potentiation in rat hippocampus slices. Brain Res. 1997;748(1–2):30–8.
88. März P, Herget T, Lang E, Otten U, Rose-John S. Activation of gp130 by IL-6/soluble IL-6 receptor induces neuronal differentiation. Eur J Neurosci. 1997 Dec;9(12):2765–73.
89. Roberts AJ, Khom S, Bajo M, Vlkolinsky R, Polis I, Cates-Gatto C, et al. Increased IL-6 expression in astrocytes is associated with emotionality, alterations in central amygdala GABAergic transmission, and excitability during alcohol withdrawal. Brain Behav Immun. 2019;82(August):188–202.
90. Oyanedel CN, Kelemen E, Scheller J, Born J, Rose-John S. Peripheral and central blockade of interleukin-6 trans-signaling differentially affects sleep architecture. Brain Behav Immun. 2015;50:178–85.
91. Kummer KK, Zeidler M, Kalpachidou T, Kress M. Role of IL-6 in the regulation of neuronal development, survival and function. Cytokine. 2021;144(April):155582.
92. Filiano AJ, Xu Y, Tustison NJ, Marsh RL, Baker W, Smirnov I, et al. Unexpected role of interferon- γ in regulating neuronal connectivity and social behaviour. Nature. 2016;535(7612):425–9.
93. Brombacher TM, Nono JK, De Gouveia KS, Makena N, Darby M, Womersley J, et al. IL-13–Mediated Regulation of Learning and Memory. J Immunol. 2017;198(7):2681–8.
94. Fenn AM, Hall JCE, Gensel JC, Popovich PG, Godbout JP. IL-4 signaling drives a unique arginase+/IL-1 β + microglia phenotype and recruits macrophages to the inflammatory CNS: Consequences of age-related deficits in IL-4R α after traumatic spinal cord injury. Vol. 34, Journal of Neuroscience. 2014. p. 8904–17.
95. Zhao X, Wang H, Sun G, Zhang J, Edwards NJ, Aronowski J. Neuronal interleukin-4 as a modulator of microglial pathways and ischemic brain damage. J Neurosci. 2015;35(32):11281–91.
96. Ron-Harel N, Cardon M, Schwartz M. Brain homeostasis is maintained by “danger” signals stimulating a supportive immune response within the brain’s borders. Brain Behav Immun. 2011;25(5):1036–43.
97. Oitzl MS, van Oers H, Schöbitz B, Ron de Kloet E. Interleukin-1 β , but not interleukin-6, impairs spatial navigation learning. Brain Res. 1993;613(1):160–3.
98. Söderlund J, Schröder J, Nordin C, Samuelsson M, Walther-Jallow L, Karlsson H, et al. Activation of brain interleukin-1B in schizophrenia. Mol Psychiatry. 2009;14(12):1069–71.
99. Murray CA, Lynch MA. Dietary supplementation with vitamin E reverses the age-related deficit in long term potentiation in dentate gyrus. J Biol Chem. 1998;273(20):12161–8.
100. Pырillou K, Burzynski LC, Clarke MCH. Alternative Pathways of IL-1 Activation, and Its Role in Health and Disease. Front Immunol. 2020;11(December):1–19.
101. Zhu H, Hu S, Li Y, Sun Y, Xiong X, Hu X, et al. Interleukins and Ischemic Stroke. Front Immunol. 2022;13(January):1–18.
102. Moraes CA, Santos G, Spohr TCLS, D’Avila JC, Lima FRS, Benjamim CF, et al. Activated

References

- Microglia-Induced Deficits in Excitatory Synapses Through IL-1 β : Implications for Cognitive Impairment in Sepsis. *Mol Neurobiol.* 2015;52(1):653–63.
103. Lin CC, Edelson BT. New Insights into the Role of IL-1 β in Experimental Autoimmune Encephalomyelitis and Multiple Sclerosis. *J Immunol.* 2017;198(12):4553–60.
104. Dunn E, Sims JE, Nicklin MJH, O'Neill LAJ. Annotating genes with potential roles in the immune system: Six new members of the IL-1 family. *Trends Immunol.* 2001;22(10):533–6.
105. Pizarro TT, Cominelli F. Cloning IL-1 and the Birth of a New Era in Cytokine Biology. *J Immunol.* 2007;178(9):5411–2.
106. Sims JE, Pan Y, Smith DE, Nicklin MJH, Barton JL, Bazan JF, et al. A new nomenclature for IL-1-family genes. *Trends Immunol.* 2001;22(10):536–7.
107. Afonina IS, Tynan GA, Logue SE, Cullen SP, Bots M, Lüthi AU, et al. Granzyme B-dependent proteolysis acts as a switch to enhance the proinflammatory activity of IL-1 α . *Mol Cell.* 2011;44(2):265–78.
108. Kobayashi Y, Yamamoto K, Saido T, Kawasaki H, Oppenheim JJ, Matsushima K. Identification of calcium-activated neutral protease as a processing enzyme of human interleukin 1 α . *Proc Natl Acad Sci U S A.* 1990;87(14):5548–52.
109. Kostura MJ, Tocci MJ, Limjuco G, Chin J, Cameron P, Hillman AG, et al. Identification of a monocyte specific pre-interleukin 1 β convertase activity. *Proc Natl Acad Sci U S A.* 1989;86(14):5227–31.
110. Ruddiman R, Thornberry NA, Bull HG, Calaycay JR, Chapman KT, Howard AD, et al. A novel heterodimeric cysteine protease is required for interleukin-1 β processing in monocytes. *Nature.* 1992;355(6372):242–4.
111. Alnemri ES, Livingston DJ, Nicholson DW, Salvesen G, Thornberry NA, Wong WW, et al. Human ICE/CED-3 protease nomenclature. *Cell.* 1996;87(2):171.
112. Tapia VS, Daniels MJD, Palazón-Riquelme P, Dewhurst M, Luheshi NM, Rivers-Auty J, et al. The three cytokines IL-1 β , IL-18, and IL-1 α share related but distinct secretory routes. *J Biol Chem.* 2019;294(21):8325–35.
113. Keller M, Rüegg A, Werner S, Beer HD. Active Caspase-1 Is a Regulator of Unconventional Protein Secretion. *Cell.* 2008;132(5):818–31.
114. Weber A, Wasiliew P, Kracht M. Interleukin-1 (IL-1) Pathway. *Sci Signal.* 2010 Jan 19;3(105):1–7.
115. Acuner Ozbabacan SE, Gursoy A, Nussinov R, Keskin O. The Structural Pathway of Interleukin 1 (IL-1) Initiated Signaling Reveals Mechanisms of Oncogenic Mutations and SNPs in Inflammation and Cancer. *PLoS Comput Biol.* 2014;10(2).
116. Srikanth N, Deliz-Aguirre R, Gola DK, Bilay M, Ziska E, Taylor MJ. IRAK4 autophosphorylation controls inflammatory signaling by activating IRAK oligomerization. *bioRxiv.* 2023 Jan 1;2023.12.21.572799.
117. Xu Y, Tao X, Shen B, Horng T, Medzhitov R, Manley JL, et al. Structural basis for signal transduction by the Toll/interleukin-1 receptor domains. *Nature.* 2000;408(6808):111–5.
118. Re F, Muzio M, De Rossi M, Polentarutti N, Giri JG, Mantovani A, et al. The type II “receptor” as a decoy target for interleukin 1 in polymorphonuclear leukocytes: characterization of induction by dexamethasone and ligand binding properties of the released decoy receptor. *J Exp Med.* 1994 Feb;179(2):739–43.
119. Colotta F, Re F, Muzio M, Bertini R, Polentarutti N, Sironi M, et al. Interleukin-1 type II receptor:

References

- a decoy target for IL-1 that is regulated by IL-4. *Science*. 1993 Jul;261(5120):472–5.
120. Colotta F, Dower SK, Sims JE, Mantovani A. The type II “decoy” receptor: A novel regulatory pathway for interleukin 1. *Immunol Today*. 1994;15(12):562–6.
121. McMahan CJ, Slack JL, Mosley B, Cosman D, Lupton SD, Brunton LL, et al. A novel IL-1 receptor, cloned from B cells by mammalian expression, is expressed in many cell types. *EMBO J*. 1991;10(10):2821–32.
122. Greenfeder SA, Nunes P, Kwee L, Labow M, Chizzonite RA, Ju G. Molecular cloning and characterization of a second subunit of the interleukin 1 receptor complex. *J Biol Chem*. 1995;270(23):13757–65.
123. Vambutas A, DeVoti J, Goldofsky E, Gordon M, Lesser M, Bonagura V. Alternate splicing of interleukin-1 receptor type II (IL1R2) in vitro correlates with clinical glucocorticoid responsiveness in patients with AIED. *PLoS One*. 2009;4(4).
124. Symons JA, Young PR, Duff GW. Soluble type II interleukin 1 (IL-1) receptor binds and blocks processing of IL-1 β precursor and loses affinity for IL-1 receptor antagonist. *Proc Natl Acad Sci U S A*. 1995;92(5):1714–8.
125. Peters VA, Joesting JJ, Freund GG. IL-1 receptor 2 (IL-1R2) and its role in immune regulation. *Brain Behav Immun*. 2013;32:1–8.
126. Smith DE, Hanna R, Friend D, Moore H, Chen H, Farese AM, et al. The Soluble Form of IL-1 Receptor Accessory Protein Enhances the Ability of Soluble Type II IL-1 Receptor to Inhibit IL-1 Action. *Immunity*. 2003;18(1):87–96.
127. Pereira M, Gazzinelli RT. Regulation of innate immune signaling by IRAK proteins. *Front Immunol*. 2023;14(February):1–14.
128. Tunalı G, Bedós MR, Nagarajan D, Fridh P, Papakyriacou I, Mao Y. IL-1 receptor-associated kinase-3 acts as an immune checkpoint in myeloid cells to limit cancer immunotherapy. *J Clin Invest*. 2023;133(7):1–17.
129. Rhyasen GW, Starczynowski DT. IRAK signalling in cancer. *Br J Cancer*. 2015;112(2):232–7.
130. Jain A, Kaczanowska S, Davila E. IL-1 receptor-associated kinase signaling and its role in inflammation, cancer progression, and therapy resistance. *Front Immunol*. 2014;5(NOV):1–8.
131. Brissoni B, Agostini L, Kropf M, Martinon F, Swoboda V, Lippens S, et al. Intracellular Trafficking of Interleukin-1 Receptor I Requires Tollip. *Curr Biol*. 2006;16(22):2265–70.
132. Didierlaurent A, Brissoni B, Velin D, Aebi N, Tardivel A, Käslin E, et al. Tollip Regulates Proinflammatory Responses to Interleukin-1 and Lipopolysaccharide. *Mol Cell Biol*. 2006;26(3):735–42.
133. Burns K, Clatworthy J, Martin L, Martinon F, Plumpton C, Maschera B, et al. Tollip, a new component of the IL-1RI pathway, links IRAK to the IL-1 receptor. *Nat Cell Biol*. 2000;2(6):346–51.
134. Burns K, Janssens S, Brissoni B, Olivos N, Beyaert R, Tschopp J. Inhibition of interleukin 1 receptor/toll-like receptor signaling through the alternatively spliced, short form of MyD88 is due to its failure to recruit IRAK-4. *J Exp Med*. 2003;197(2):263–8.
135. Li L, Fothergill T, Hutchins BI, Dent EW, Kalil K. Wnt5a evokes cortical axon outgrowth and repulsive guidance by tau mediated reorganization of dynamic microtubules. *Dev Neurobiol*. 2014;74(8):797–817.
136. Park SY, Kang MJ, Han JS. Interleukin-1 beta promotes neuronal differentiation through the Wnt5a/RhoA/JNK pathway in cortical neural precursor cells. *Mol Brain*. 2018;11(1):1–12.

References

137. Corradini I, Focchi E, Rasile M, Morini R, Desiato G, Tomasoni R, et al. Maternal Immune Activation Delays Excitatory-to-Inhibitory Gamma-Aminobutyric Acid Switch in Offspring. *Biol Psychiatry*. 2018;83(8):680–91.
138. Pozzi D, Menna E, Canzi A, Desiato G, Mantovani C, Matteoli M. The communication between the immune and nervous systems: The role of IL-1 β in synaptopathies. *Front Mol Neurosci*. 2018;11(April):1–11.
139. Goshen I, Kreisel T, Ounallah-Saad H, Renbaum P, Zalstein Y, Ben-Hur T, et al. A dual role for interleukin-1 in hippocampal-dependent memory processes. *Psychoneuroendocrinology*. 2007;32(8–10):1106–15.
140. Akaneya Y, Takahashi M, Hatanaka H. Interleukin-1 β enhances survival and interleukin-6 protects against MPP⁺ neurotoxicity in cultures of fetal rat dopaminergic neurons. Vol. 136, *Experimental Neurology*. 1995. p. 44–52.
141. Galic MA, Riazi K, Pittman QJ. Cytokines and brain excitability. *Front Neuroendocrinol*. 2012;33(1):116–25.
142. Bellinger FP, Madamba S, Siggins R. Interleukin 1beta inhibits synaptic strength and LTP in the rat CA1 hippocampus. *Brain Res*. 1993;628:227–34.
143. Gardoni F, Boraso M, Zianni E, Corsini E, Galli CL, Cattabeni F, et al. Distribution of interleukin-1 receptor complex at the synaptic membrane driven by interleukin-1 β and NMDA stimulation. *J Neuroinflammation*. 2011;8:1–6.
144. Rossi S, Furlan R, De Chiara V, Motta C, Studer V, Mori F, et al. Interleukin-1 β causes synaptic hyperexcitability in multiple sclerosis. *Ann Neurol*. 2012 Jan;71(1):76–83.
145. Mandolesi G, Musella A, Gentile A, Grasselli G, Haji N, Sepman H, et al. Interleukin-1 β alters glutamate transmission at Purkinje cell synapses in a mouse model of multiple sclerosis. *J Neurosci*. 2013;33(29):12105–21.
146. Rossi S, Motta C, Studer V, Macchiarulo G, Volpe E, Barbieri F, et al. Interleukin-1 β causes excitotoxic neurodegeneration and multiple sclerosis disease progression by activating the apoptotic protein p53. *Mol Neurodegener*. 2014;9:56.
147. Tomasoni R, Morini R, Lopez-Atalaya JP, Corradini I, Canzi A, Rasile M, et al. Lack of IL-1r8 in neurons causes hyperactivation of IL-1 receptor pathway and induces MECP2-dependent synaptic defects. *Elife*. 2017;6:1–26.
148. Han Q, Lin Q, Huang P, Chen M, Hu X, Fu H, et al. Microglia-derived IL-1 β contributes to axon development disorders and synaptic deficit through p38-MAPK signal pathway in septic neonatal rats. *J Neuroinflammation*. 2017;14(1):1–18.
149. Jurgens HA, Amancherla K, Johnson RW. Influenza Infection Induces Neuroinflammation, Alters Hippocampal Neuron Morphology, and Impairs Cognition in Adult Mice. *J Neurosci*. 2012;32(12):3958–68.
150. Hein AM, Stasko MR, Matousek SB, Scott-McKean JJ, Maier SF, Olschowka JA, et al. Sustained hippocampal IL-1beta overexpression impairs contextual and spatial memory in transgenic mice. *Brain Behav Immun*. 2010 Feb;24(2):243–53.
151. Barrientos RM, Higgins EA, Biedenkapp JC, Sprunger DB, Wright-Hardesty KJ, Watkins LR, et al. Peripheral infection and aging interact to impair hippocampal memory consolidation. *Neurobiol Aging*. 2006;27(5):723–32.
152. Barrientos RM, Frank MG, Hein AM, Higgins EA, Watkins LR, Rudy JW, et al. Time course of hippocampal IL-1 β and memory consolidation impairments in aging rats following peripheral infection. *Brain Behav Immun*. 2009;23(1):46–54.

References

153. Katsuki H, Nakai S, Hirai Y, Akaji K ichi, Kiso Y, Satoh M. Interleukin-1 β inhibits long-term potentiation in the CA3 region of mouse hippocampal slices. *Eur J Pharmacol.* 1990;181(3):323–6.
154. Chen J, Buchanan JB, Sparkman NL, Godbout JP, Freund GG, Johnson RW. Neuroinflammation and disruption in working memory in aged mice after acute stimulation of the peripheral innate immune system. *Brain Behav Immun.* 2008;22(3):301–11.
155. Gadad BS, Vargas-Medrano J, Ramos EI, Najera K, Fagan M, Forero A, et al. Altered levels of interleukins and neurotrophic growth factors in mood disorders and suicidality: an analysis from periphery to central nervous system. *Transl Psychiatry.* 2021;11(1):1–11.
156. Katila H, Appelberg B, Hurme M, Rimón R. Plasma levels of interleukin-1 β and interleukin-6 in schizophrenia, other psychoses, and affective disorders. *Schizophr Res.* 1994;12(1):29–34.
157. Wesche H, Korherr C, Kracht M, Falk W, Resch K, Martin MU. The interleukin-1 receptor accessory protein (IL-1RAcP) is essential for IL-1-induced activation of interleukin-1 receptor-associated kinase (IRAK) and stress-activated protein kinases (SAP kinases). *J Biol Chem.* 1997;272(12):7727–31.
158. Jensen LE, Whitehead AS. Expression of alternatively spliced interleukin-1 receptor accessory protein mRNAs is differentially regulated during inflammation and apoptosis. *Cell Signal.* 2003;15(8):793–802.
159. Smith DE, Lipsky BP, Russell C, Ketchum RR, Kirchner J, Hensley K, et al. A central nervous system-restricted isoform of the interleukin-1 receptor accessory protein modulates neuronal responses to interleukin-1. *Immunity.* 2009 Jun;30(6):817–31.
160. Cheng P, Zhang R, Shan S, Yuan B, Chen J, Qiu Z, et al. Novel IL1RAP mutation associated with schizophrenia interferes with neuronal growth and related NF- κ B signal pathways. *Neurosci Lett.* 2022;775(October 2021):136533.
161. Prieto GA, Snigdha S, Baglietto-Vargas D, Smith ED, Berchtold NC, Tong L, et al. Synapse-specific IL-1 receptor subunit reconfiguration augments vulnerability to IL-1 β in the aged hippocampus. *Proc Natl Acad Sci U S A.* 2015;112(36):E5078–87.
162. Yoshida T, Shiroshima T, Lee SJ, Yasumura M, Uemura T, Chen X, et al. Interleukin-1 receptor accessory protein organizes neuronal synaptogenesis as a cell adhesion molecule. *J Neurosci.* 2012;32(8):2588–600.
163. Montani C, Ramos-Brossier M, Ponzoni L, Gritti L, Cwetsch AW, Braida D, et al. The X-linked intellectual disability protein IL1RAPL1 regulates dendrite complexity. *J Neurosci.* 2017;37(28):6606–27.
164. Ramos-Brossier M, Montani C, Lebrun N, Gritti L, Martin C, Seminatore-nole C, et al. Novel IL1RAPL1 mutations associated with intellectual disability impair synaptogenesis. *Hum Mol Genet.* 2015;24(4):1106–18.
165. Pavlowsky A, Gianfelice A, Pallotto M, Zanchi A, Vara H, Khelfaoui M, et al. A Postsynaptic Signaling Pathway that May Account for the Cognitive Defect Due to IL1RAPL1 Mutation. *Curr Biol.* 2010;20(2):103–15.
166. Yasumura M, Yoshida T, Yamazaki M, Abe M, Natsume R, Kanno K, et al. IL1RAPL1 knockout mice show spine density decrease, learning deficiency, hyperactivity and reduced anxiety-like behaviours. *Sci Rep.* 2014;4:1–12.
167. Gambino F, Kneib M, Pavlowsky A, Skala H, Heitz S, Vitale N, et al. IL1RAPL1 controls inhibitory networks during cerebellar development in mice. *Eur J Neurosci.* 2009;30(8):1476–86.
168. Thomas G, Moffatt P, Salois P, Gaumond MH, Gingras R, Godin É, et al. Osteocrin, a Novel

References

- Bone-specific Secreted Protein That Modulates the Osteoblast Phenotype. *J Biol Chem.* 2003;278(50):50563–71.
169. Nishizawa H, Matsuda M, Yamada Y, Kawai K, Suzuki E, Makishima M, et al. Musclin, a Novel Skeletal Muscle-derived Secretory Factor. *J Biol Chem.* 2004;279(19):19391–5.
170. Moffatt P, Thomas G, Sellin K, Bessette MC, Lafrenière F, Akhouayri O, et al. Osteocrin is a specific ligand of the natriuretic peptide clearance receptor that modulates bone growth. *J Biol Chem.* 2007;282(50):36454–62.
171. Bord S, Ireland DC, Moffatt P, Thomas GP, Compston JE. Characterization of osteocrin expression in human bone. *J Histochem Cytochem.* 2005;53(10):1181–7.
172. Ataman B, Boulting GL, Harmin DA, Yang MG, Baker-Salisbury M, Yap EL, et al. Evolution of Osteocrin as an activity-regulated factor in the primate brain. *Nature.* 2016;539(7628):242–7.
173. Watanabe-Takano H, Ochi H, Chiba A, Matsuo A, Kanai Y, Fukuhara S, et al. Mechanical load regulates bone growth via periosteal Osteocrin. *Cell Rep.* 2021;36(2):109380.
174. Subbotina E, Sierra A, Zhu Z, Gao Z, Koganti SRK, Reyes S, et al. Musclin is an activity-stimulated myokine that enhances physical endurance. *Proc Natl Acad Sci U S A.* 2015;112(52):16042–7.
175. Yasui A, Nishizawa H, Okuno Y, Morita K, Kobayashi H, Kawai K, et al. Foxo1 represses expression of musclin, a skeletal muscle-derived secretory factor. *Biochem Biophys Res Commun.* 2007;364(2):358–65.
176. Lee YJ, Park SY, Lee SJ, Boo YC, Choi JY, Kim JE. Ucma, a direct transcriptional target of Runx2 and Osterix, promotes osteoblast differentiation and nodule formation. *Osteoarthr Cartil.* 2015;23(8):1421–31.
177. Kanai Y, Yasoda A, Mori KP, Watanabe-Takano H, Nagai-Okatani C, Yamashita Y, et al. Circulating osteocrin stimulates bone growth by limiting C-type natriuretic peptide clearance. *J Clin Invest.* 2017;127(11):4136–47.
178. Maack T, Suzuki M, Almeida FA, Nussenzveig D, Scarborough RM, McEnroe GA, et al. Physiological Role of Silent Receptors of Atrial Natriuretic Factor. *Science (80-).* 1987 Oct 30;238(4827):675–8.
179. Nussenzveig DR, Lewicki JA, Maack T. Cellular mechanisms of the clearance function of type C receptors of atrial natriuretic factor. *J Biol Chem.* 1990;265(34):20952–8.
180. Murthy KS, Makhoul GM. Identification of the G protein-activating domain of the natriuretic peptide clearance receptor (NPR-C). *J Biol Chem.* 1999;274(25):17587–92.
181. Anand-Srivastava MB, Sehl PD, Lowe DG. Cytoplasmic domain of natriuretic peptide receptor-C inhibits adenylyl cyclase. Involvement of a pertussis toxin-sensitive G protein. *J Biol Chem.* 1996;271(32):19324–9.
182. Zhou H, Murthy KS. Identification of the G protein-activating sequence of the single-transmembrane natriuretic peptide receptor C (NPR-C). *Am J Physiol - Cell Physiol.* 2003;284(5 53-5):1255–61.
183. Egom EEA. Natriuretic Peptide Clearance Receptor (NPR-C) Pathway as a Novel Therapeutic Target in Obesity-Related Heart Failure With Preserved Ejection Fraction (HFpEF). *Front Physiol.* 2021;12(May):1–12.
184. Katada T, Ui M. Direct modification of the membrane adenylyl cyclase system by islet-activating protein due to ADP-ribosylation of a membrane protein. *Proc Natl Acad Sci U S A.* 1982;79(10):3129–33.

References

185. Palaparti A, Anand-Srivastava MB. Angiotensin II modulates ANP-R2/ANP-C receptor-mediated inhibition of adenylyl cyclase in vascular smooth muscle cells: Role of protein kinase C. *J Mol Cell Cardiol.* 1998;30(8):1471–82.
186. Chinkers M, Garbers DL, Chang MS, Lowe DG, Chin H, Goeddel D V., et al. A membrane form of guanylate cyclase is an atrial natriuretic peptide receptor. *Nature.* 1989;338(6210):78–83.
187. Khurana ML, Pandey KN. Receptor-mediated stimulatory effect of atrial natriuretic factor, brain natriuretic peptide, and C-type natriuretic peptide on testosterone production in purified mouse Leydig cells: activation of cholesterol side-chain cleavage enzyme. *Endocrinology.* 1993 Nov;133(5):2141–9.
188. Schulz S, Singh S, Bellet RA, Singh G, Tubb DJ, Chin H, et al. The primary structure of a plasma membrane guanylate cyclase demonstrates diversity within this new receptor family. *Cell.* 1989;58(6):1155–62.
189. Francis SH, Corbin JD. Cyclic nucleotide-dependent protein kinases: Intracellular receptors for cAMP and cGMP action. *Crit Rev Clin Lab Sci.* 1999;36(4):275–328.
190. Chiba A, Watanabe-Takano H, Terai K, Fukui H, Miyazaki T, Uemura M, et al. Osteocrin, a peptide secreted from the heart and other tissues, contributes to cranial osteogenesis and chondrogenesis in zebrafish. *Dev.* 2017;144(2):334–44.
191. Watanabe-Takano H, Ochi H, Chiba A, Matsuo A, Kanai Y, Fukuhara S, et al. Periosteum-derived Osteocrin regulates bone growth through both endochondral ossification and intramembranous ossification. *Development.* 2019;1–43.
192. Nishiguchi Y, Hata Y, Date R, Fujimoto D, Umemoto S, Kanki T, et al. Osteocrin, a bone-derived humoral factor, exerts a renoprotective role in ischemia-reperfusion injury in mice. *Nephrol Dial Transplant.* 2022;37(3):444–53.
193. Ji M, Zuo Z, Zhang M, Xu Z, Hu G. Osteocrin alleviates cardiac hypertrophy via attenuating oxidative stress. *Peptides.* 2022;152(February):170773.
194. Hu C, Zhang X, Zhang N, Wei W, Li L, Ma Z, et al. Osteocrin attenuates inflammation, oxidative stress, apoptosis, and cardiac dysfunction in doxorubicin-induced cardiotoxicity. *Clin Transl Med.* 2020;10(3):1–19.
195. Zhang X, Hu C, Yuan XP, Yuan YP, Song P, Kong CY, et al. Osteocrin, a novel myokine, prevents diabetic cardiomyopathy via restoring proteasomal activity. *Cell Death Dis.* 2021;12(7):1–12.
196. Miyazaki T, Otani K, Chiba A, Nishimura H, Tokudome T, Takano-Watanabe H, et al. A new secretory peptide of natriuretic peptide family, osteocrin, suppresses the progression of congestive heart failure after myocardial infarction. *Circ Res.* 2018;122(5):742–51.
197. de Bold AJ, Borenstein HB, Veress AT, Sonnenberg H. A rapid and potent natriuretic response to intravenous injection of atrial myocardial extract in rats. *Life Sci.* 1981;28(1):89–94.
198. Flynn TG, Davies PL. The biochemistry and molecular biology of atrial natriuretic factor. *Biochem J.* 1985;232(2):313–21.
199. Andrade FA, Restini CBA, Grando MD, Ramalho LN, Bendhack LM. Vascular relaxation induced by C-type natriuretic peptide involves the Ca²⁺/NO-synthase/NO pathway. *PLoS One.* 2014;9(5):1–9.
200. Potter LR, Yoder AR, Flora DR, Antos LK, Dickey DM. Natriuretic Peptides: Their Structures, Receptors, Physiologic Functions and Therapeutic Applications BT - cGMP: Generators, Effectors and Therapeutic Implications. In: Schmidt HHHW, Hofmann F, Stasch JP, editors. *Handbook of Experimental Pharmacology.* Berlin, Heidelberg, Germany: Springer Berlin Heidelberg; 2009. p. 341–66.

References

201. Mahinrad S, Bulk M, Van Der Velpen I, Mahfouz A, Van Roon-Mom W, Fedarko N, et al. Natriuretic peptides in post-mortem brain tissue and cerebrospinal fluid of non-demented humans and Alzheimer's disease patients. *Front Neurosci.* 2018;12(NOV):1–12.
202. Decker JM, Wójtowicz AM, Bartsch JC, Liotta A, Braunewell KH, Heinemann U, et al. C-type natriuretic peptide modulates bidirectional plasticity in hippocampal area CA1 in Vitro. *Neuroscience.* 2010;169(1):8–22.
203. Wiggins AK, Shen PJ, Gundlach AL. Atrial natriuretic peptide expression is increased in rat cerebral cortex following spreading depression: Possible contribution to SD-induced neuroprotection. *Neuroscience.* 2003;118(3):715–26.
204. Fernández-Susavila H, Rodríguez-Yáñez M, Dopico-López A, Arias S, Santamaría M, Ávila-Gómez P, et al. Heads and tails of natriuretic peptides: Neuroprotective role of brain natriuretic peptide. *J Am Heart Assoc.* 2017;6(12).
205. Kuribayashi K, Kitaoka Y, Kumai T, Munemasa Y, Kitaoka Y, Isenoumi K, et al. Neuroprotective effect of atrial natriuretic peptide against NMDA-induced neurotoxicity in the rat retina. *Brain Res.* 2006;1071(1):34–41.
206. Takahashi K, Yamanaka S. Induction of Pluripotent Stem Cells from Mouse Embryonic and Adult Fibroblast Cultures by Defined Factors. *Cell.* 2006;126(4):663–76.
207. Takahashi K, Tanabe K, Ohnuki M, Narita M, Ichisaka T, Tomoda K, et al. Induction of Pluripotent Stem Cells from Adult Human Fibroblasts by Defined Factors. *Cell.* 2007;131(5):861–72.
208. Chen IP, Fukuda K, Fusaki N, Iida A, Hasegawa M, Lichtler A, et al. Induced pluripotent stem cell reprogramming by integration-free sendai virus vectors from peripheral blood of patients with craniometaphyseal dysplasia. *Cell Reprogram.* 2013;15(6):503–13.
209. Mallanna SK, Duncan SA. Differentiation of hepatocytes from pluripotent stem cells. *Curr Protoc Stem Cell Biol.* 2013;1(SUPPL.26):1–13.
210. Ogaki S, Morooka M, Otera K, Kume S. A cost-effective system for differentiation of intestinal epithelium from human induced pluripotent stem cells. *Sci Rep.* 2015;5(October):1–11.
211. Chal J, Oginuma M, Al Tanoury Z, Gobert B, Sumara O, Hick A, et al. Differentiation of pluripotent stem cells to muscle fiber to model Duchenne muscular dystrophy. *Nat Biotechnol.* 2015;33(9):962–9.
212. Pawlowski M, Ortmann D, Bertero A, Tavares JM, Pedersen RA, Vallier L, et al. Inducible and Deterministic Forward Programming of Human Pluripotent Stem Cells into Neurons, Skeletal Myocytes, and Oligodendrocytes. *Stem Cell Reports.* 2017;8(4):803–12.
213. Barretto N, Zhang H, Powell SK, Fernando MB, Zhang S, Flaherty EK, et al. ASCL1- and DLX2-induced GABAergic neurons from hiPSC-derived NPCs. *J Neurosci Methods.* 2020;334(February):108548.
214. Chambers SM, Fasano CA, Papapetrou EP, Tomishima M, Sadelain M, Studer L. Highly efficient neural conversion of human ES and iPS cells by dual inhibition of SMAD signaling. *Nat Biotechnol.* 2009;27(3):275–80.
215. Rojas S V., Kensah G, Rotaermel A, Baraki H, Kutschka I, Zweigerdt R, et al. Transplantation of purified iPSC-derived cardiomyocytes in myocardial infarction. *PLoS One.* 2017;12(5):1–14.
216. Lyra-Leite DM, Gutiérrez-Gutiérrez Ó, Wang M, Zhou Y, Cyganek L, BurrIDGE PW. A review of protocols for human iPSC culture, cardiac differentiation, subtype-specification, maturation, and direct reprogramming. *STAR Protoc.* 2022;3(3):1–23.
217. Xie Y, Schutte RJ, Ng NN, Ess KC, Schwartz PH, O'Dowd DK. Reproducible and efficient

References

- generation of functionally active neurons from human hiPSCs for preclinical disease modeling. *Stem Cell Res.* 2018;26:84–94.
218. Pak CH, Danko T, Zhang Y, Aoto J, Anderson G, Maxeiner S, et al. Human Neuropsychiatric Disease Modeling using Conditional Deletion Reveals Synaptic Transmission Defects Caused by Heterozygous Mutations in NRXN1. *Cell Stem Cell.* 2015;17(3):316–28.
219. Vandana JJ, Manrique C, Lacko LA, Chen S. Human pluripotent-stem-cell-derived organoids for drug discovery and evaluation. *Cell Stem Cell.* 2023;30(5):571–91.
220. Rossetti AC, Koch P, Ladewig J. Drug discovery in psychopharmacology: From 2D models to cerebral organoids. *Dialogues Clin Neurosci.* 2019;21(2):203–10.
221. Fu CL, Dong BC, Jiang X, Li D, Yao J. A cell therapy approach based on iPSC-derived midbrain organoids for the restoration of motor function in a Parkinson's disease mouse model. *Heliyon.* 2024;10(2):e24234.
222. Gotoh S, Ito I, Nagasaki T, Yamamoto Y, Konishi S, Korogi Y, et al. Generation of alveolar epithelial spheroids via isolated progenitor cells from human pluripotent stem cells. *Stem Cell Reports.* 2014;3(3):394–403.
223. Krencik R, Weick JP, Liu Y, Zhang ZJ, Zhang SC. Specification of transplantable astroglial subtypes from human pluripotent stem cells. *Nat Biotechnol.* 2011;29(6):528–34.
224. Miura Y, Sato M, Kuwahara T, Ebata T, Tabata Y, Sakurai H. Transplantation of human iPSC-derived muscle stem cells in the diaphragm of Duchenne muscular dystrophy model mice. *PLoS One.* 2022;17(4 April):1–15.
225. Shahjalal HM, Abdal Dayem A, Lim KM, Jeon T II, Cho SG. Generation of pancreatic β cells for treatment of diabetes: Advances and challenges. Vol. 9, *Stem Cell Research and Therapy.* 2018.
226. Sun AX, Yuan Q, Tan S, Xiao Y, Wang D, Khoo ATT, et al. Direct Induction and Functional Maturation of Forebrain GABAergic Neurons from Human Pluripotent Stem Cells. *Cell Rep.* 2016;16(7):1942–53.
227. Tsuchida T, Murata S, Hasegawa S, Mikami S, Enosawa S, Hsu HC, et al. Investigation of Clinical Safety of Human iPS Cell-Derived Liver Organoid Transplantation to Infantile Patients in Porcine Model. *Cell Transplant.* 2020;29:1–13.
228. Turhan AG, Hwang JW, Chaker D, Tasteyre A, Latsis T, Griscelli F, et al. iPSC-Derived Organoids as Therapeutic Models in Regenerative Medicine and Oncology. *Front Med.* 2021;8(October):1–7.
229. Denayer T, Stöhrn T, Van Roy M. Animal models in translational medicine: Validation and prediction. *New Horizons Transl Med.* 2014;2(1):5–11.
230. Doncheva NT, Palasca O, Yarani R, Litman T, Anthon C, Groenen MAM, et al. Human pathways in animal models: Possibilities and limitations. *Nucleic Acids Res.* 2021;49(4):1859–71.
231. Bitar M, Kuiper S, O'Brien EA, Barry G. Genes with human-specific features are primarily involved with brain, immune and metabolic evolution. *BMC Bioinformatics.* 2019;20(Suppl 9):1–12.
232. Jinek M, Chylinski K, Fonfara I, Hauer M, Doudna JA, Charpentier E. A programmable dual-RNA-guided DNA endonuclease in adaptive bacterial immunity. *Science.* 2012 Aug;337(6096):816–21.
233. Dana H, Mahmoodi Chalbatani G, Mahmoodzadeh H, Karimloo R, Rezaiean O, Moradzadeh A, et al. Molecular Mechanisms and Biological Functions of siRNA. *Int J Biomed Sci.*

References

- 2017;13(2):48–57.
234. Martinez-Curiel R, Jansson L, Tsupykov O, Avaliani N, Aretio-Medina C, Hidalgo I, et al. Oligodendrocytes in human induced pluripotent stem cell-derived cortical grafts remyelinate adult rat and human cortical neurons. *Stem Cell Reports*. 2023;18(8):1643–56.
235. Cao SY, Hu Y, Chen C, Yuan F, Xu M, Li Q, et al. Enhanced derivation of human pluripotent stem cell-derived cortical glutamatergic neurons by a small molecule. *Sci Rep*. 2017;7(1):1–11.
236. TCW J, Wang M, Pimenova AA, Bowles KR, Hartley BJ, Lacin E, et al. An Efficient Platform for Astrocyte Differentiation from Human Induced Pluripotent Stem Cells. *Stem Cell Reports*. 2017;9(2):600–14.
237. Douvaras P, Sun B, Wang M, Kruglikov I, Lалlos G, Zimmer M, et al. Directed Differentiation of Human Pluripotent Stem Cells to Microglia. *Stem Cell Reports*. 2017;8(6):1516–24.
238. Du ZW, Chen H, Liu H, Lu J, Qian K, Huang CTL, et al. Generation and expansion of highly pure motor neuron progenitors from human pluripotent stem cells. *Nat Commun*. 2015;6:1–9.
239. Yang N, Chanda S, Marro S, Ng YH, Janas JA, Haag D, et al. Generation of pure GABAergic neurons by transcription factor programming. *Nat Methods*. 2017;14(6):621–8.
240. Grigor'eva E V., Malankhanova TB, Surumbayeva A, Pavlova S V., Minina JM, Kizilova EA, et al. Generation of GABAergic striatal neurons by a novel iPSC differentiation protocol enabling scalability and cryopreservation of progenitor cells. *Cytotechnology*. 2020;72(5):649–63.
241. Chanda S, Ang CE, Lee QY, Ghebrial M, Haag D, Shibuya Y, et al. Direct Reprogramming of Human Neurons Identifies MARCKSL1 as a Pathogenic Mediator of Valproic Acid-Induced Teratogenicity. *Cell Stem Cell*. 2019;25(1):103-119.e6.
242. Jansch C, Ziegler GC, Forero A, Gredy S, Wäldchen S, Vitale MR, et al. Serotonin-specific neurons differentiated from human iPSCs form distinct subtypes with synaptic protein assembly. *J Neural Transm*. 2021;128(2):225–41.
243. Mahajani S, Raina A, Fokken C, Kügler S, Bähr M. Homogenous generation of dopaminergic neurons from multiple hiPSC lines by transient expression of transcription factors. *Cell Death Dis*. 2019;10(12).
244. Dooves S, Nadadhur AG, Gasparotto L, Heine VM. Co-culture of Human Stem Cell Derived Neurons and Oligodendrocyte Progenitor Cells. *Bio-protocol*. 2019;9(17):1–17.
245. Vahsen BF, Gray E, Candalija A, Cramb KML, Scaber J, Dafinca R, et al. Human iPSC co-culture model to investigate the interaction between microglia and motor neurons. *Sci Rep*. 2022;12(1):1–17.
246. Lancaster MA, Knoblich JA. Generation of cerebral organoids from human pluripotent stem cells. *Nat Protoc*. 2014 Oct;9(10):2329–40.
247. McCracken KW, Howell JC, Wells JM, Spence JR. Generating human intestinal tissue from pluripotent stem cells in vitro. *Nat Protoc*. 2011 Nov;6(12):1920–8.
248. Lewis-Israeli YR, Wasserman AH, Gabalski MA, Volmert BD, Ming Y, Ball KA, et al. Self-assembling human heart organoids for the modeling of cardiac development and congenital heart disease. *Nat Commun*. 2021;12(1).
249. Li X, Tao Y, Bradley R, Du Z, Tao Y, Kong L, et al. Fast Generation of Functional Subtype Astrocytes from Human Pluripotent Stem Cells. *Stem Cell Reports*. 2018;11(4):998–1008.
250. Kim K, Doi A, Wen B, Ng K, Zhao R, Cahan P, et al. Epigenetic memory in induced pluripotent stem cells. *Nature*. 2010 Sep;467(7313):285–90.

References

251. Erharter A, Rizzi S, Mertens J, Edenhofer F. Take the shortcut – direct conversion of somatic cells into induced neural stem cells and their biomedical applications. *FEBS Lett.* 2019;593(23):3353–69.
252. Mertens J, Paquola ACM, Ku M, Hatch E, Böhnke L, Ladjevardi S, et al. Directly Reprogrammed Human Neurons Retain Aging-Associated Transcriptomic Signatures and Reveal Age-Related Nucleocytoplasmic Defects. *Cell Stem Cell.* 2015;17(6):705–18.
253. Chen G, Gulbranson DR, Hou Z, Bolin JM, Ruotti V, Probasco MD, et al. Chemically defined conditions for human iPSC derivation and culture. *Nat Methods.* 2011;8(5):424–9.
254. Lee H, Shamy G AI, Elkabetz Y, Schofield CM, Harrision NL, Panagiotakos G, et al. Directed Differentiation and Transplantation of Human Embryonic Stem Cell-Derived Motoneurons. *Stem Cells.* 2007;25(8):1931–9.
255. Perrier AL, Tabar V, Barberi T, Rubio ME, Bruses J, Topf N, et al. Derivation of midbrain dopamine neurons from human embryonic stem cells. *Proc Natl Acad Sci U S A.* 2004;101(34):12543–8.
256. Stanton BZ, Peng LF. Small-molecule modulators of the Sonic Hedgehog signaling pathway. *Mol Biosyst.* 2009;6(1):44–54.
257. Dorey K, Amaya E. FGF signalling: diverse roles during early vertebrate embryogenesis. *Development.* 2010 Nov;137(22):3731–42.
258. Kirkeby A, Grealish S, Wolf DA, Nelander J, Wood J, Lundblad M, et al. Generation of Regionally Specified Neural Progenitors and Functional Neurons from Human Embryonic Stem Cells under Defined Conditions. *Cell Rep.* 2012;1(6):703–14.
259. Huang SMA, Mishina YM, Liu S, Cheung A, Stegmeier F, Michaud GA, et al. Tankyrase inhibition stabilizes axin and antagonizes Wnt signalling. *Nature.* 2009;461(7264):614–20.
260. Neaverson A, Andersson MHL, Arshad OA, Foulser L, Goodwin-Trotman M, Hunter A, et al. Differentiation of human induced pluripotent stem cells into cortical neural stem cells. *Front Cell Dev Biol.* 2023;10(January):1–24.
261. Telezhkin V, Schnell C, Yarova P, Yung S, Cope E, Hughes A, et al. Forced cell cycle exit and modulation of GABAA, CREB, and GSK3 β signaling promote functional maturation of induced pluripotent stem cell-derived neurons. *Am J Physiol - Cell Physiol.* 2016;310(7):C520–41.
262. Kemp PJ, Rushton DJ, Yarova PL, Schnell C, Geater C, Hancock JM, et al. Improving and accelerating the differentiation and functional maturation of human stem cell-derived neurons: role of extracellular calcium and GABA. *J Physiol.* 2016;594(22):6583–94.
263. Bell S, Hettige NC, Silveira H, Peng H, Wu H, Jefri M, et al. Differentiation of Human Induced Pluripotent Stem Cells (iPSCs) into an Effective Model of Forebrain Neural Progenitor Cells and Mature Neurons. *Bio-protocol.* 2019;9(5):1–18.
264. Hikida T, Jaaro-Peled H, Seshadri S, Oishi K, Hookway C, Kong S, et al. Dominant-negative DISC1 transgenic mice display schizophrenia-associated phenotypes detected by measures translatable to humans. *Proc Natl Acad Sci.* 2007;104(36):14501–6.
265. Krueger DD, Howell JL, Hebert BF, Olausson P, Taylor JR, Nairn AC. Assessment of cognitive function in the heterozygous reeler mouse. *Psychopharmacology (Berl).* 2006;189(1):95–104.
266. Gassmann M, Casagrande F, Orioli D, Simon H, Lai C, Klein R, et al. Aberrant neural and cardiac development in mice lacking the ErbB4 neuregulin receptor. *Lett to Nat.* 1995;378:390–4.
267. Erickson SL, O'Shea KS, Ghaboosi N, Loverro L, Frantz G, Bauer M, et al. ErbB3 is required for normal cerebellar and cardiac development: a comparison with ErbB2-and heregulin-

References

- deficient mice. *Development*. 1997;124:4999–5011.
268. Harrison PJ, Law AJ. Neuregulin 1 and Schizophrenia: Genetics, Gene Expression, and Neurobiology. *Biol Psychiatry*. 2006;60(2):132–40.
269. Mei L, Xiong WC. Neuregulin 1 in neural development, synaptic plasticity and schizophrenia. *Nat Rev Neurosci*. 2008;9(6):437–52.
270. Hathy E, Szabó E, Varga N, Erdei Z, Tordai C, Czehlár B, et al. Investigation of de novo mutations in a schizophrenia case-parent trio by induced pluripotent stem cell-based in vitro disease modeling: convergence of schizophrenia- and autism-related cellular phenotypes. *Stem Cell Res Ther*. 2020;11(1):1–15.
271. Paulsen B da S, Maciel R de M, Galina A, da Silveira MS, Souza C dos S, Drummond H, et al. Altered oxygen metabolism associated to neurogenesis of induced pluripotent stem cells derived from a schizophrenic patient. *Cell Transplant*. 2012;21(7):1547–59.
272. Zuccoli GS, Nascimento JM, Moraes-Vieira PM, Rehen SK, Martins-de-Souza D. Mitochondrial, cell cycle control and neuritogenesis alterations in an iPSC-based neurodevelopmental model for schizophrenia. *Eur Arch Psychiatry Clin Neurosci*. 2023;273(8):1649–64.
273. Brennand K, Savas JN, Kim Y, Tran N, Simone A, Hashimoto-Torii K, et al. Phenotypic differences in hiPSC NPCs derived from patients with schizophrenia. *Mol Psychiatry*. 2015;20(3):361–8.
274. Hashimoto-Torii K, Torii M, Fujimoto M, Nakai A, ElFatimy R, Mezger V, et al. Roles of Heat Shock Factor 1 in Neuronal Response to Fetal Environmental Risks and Its Relevance to Brain Disorders. *Neuron*. 2014;82(3):560–72.
275. Yoon KJ, Nguyen HN, Ursini G, Zhang F, Kim NS, Wen Z, et al. Modeling a genetic risk for schizophrenia in iPSCs and Mice reveals neural stem cell deficits associated with adherens junctions and polarity. *Cell Stem Cell*. 2014;15(1):79–91.
276. Brennand KJ, Simone A, Jou J, Gelboin-Burkhart C, Tran N, Sangar S, et al. Modelling schizophrenia using human induced pluripotent stem cells. *Nature*. 2011;473(7346):221–5.
277. Yu DX, Di Giorgio FP, Yao J, Marchetto MC, Brennand K, Wright R, et al. Modeling hippocampal neurogenesis using human pluripotent stem cells. *Stem Cell Reports*. 2014;2(3):295–310.
278. Grunwald LM, Stock R, Haag K, Buckenmaier S, Eberle MC, Wildgruber D, et al. Comparative characterization of human induced pluripotent stem cells (hiPSC) derived from patients with schizophrenia and autism. *Transl Psychiatry*. 2019;9(1).
279. Ishii T, Ishikawa M, Fujimori K, Maeda T, Kushima I, Arioka Y, et al. In vitro modeling of the bipolar disorder and schizophrenia using patient-derived induced pluripotent stem cells with copy number variations of PCDH15 and RELN. *eNeuro*. 2019;6(5).
280. Naujock M, Speidel A, Fischer S, Kizner V, Dorner-Ciossek C, Gillardon F. Neuronal Differentiation of Induced Pluripotent Stem Cells from Schizophrenia Patients in Two-Dimensional and in Three-Dimensional Cultures Reveals Increased Expression of the Kv4.2 Subunit DPP6 That Contributes to Decreased Neuronal Activity. *Stem Cells Dev*. 2020 Dec;29(24):1577–87.
281. Flaherty E, Deranieh RM, Artimovich E, Lee IS, Siegel AJ, Levy DL, et al. Patient-derived hiPSC neurons with heterozygous CNTNAP2 deletions display altered neuronal gene expression and network activity. *npj Schizophr*. 2017;3(1).
282. Page SC, Sripathy SR, Farinelli F, Ye Z, Wang Y, Hiler DJ, et al. Electrophysiological measures from human iPSC-derived neurons are associated with schizophrenia clinical status

References

- and predict individual cognitive performance. *Proc Natl Acad Sci U S A*. 2022;119(3):1–12.
283. Robicsek O, Karry R, Petit I, Salman-Kesner N, Müller FJ, Klein E, et al. Abnormal neuronal differentiation and mitochondrial dysfunction in hair follicle-derived induced pluripotent stem cells of schizophrenia patients. *Mol Psychiatry*. 2013;18(10):1067–76.
284. Zhao D, Lin M, Chen J, Pedrosa E, Hrabovsky A, Fourcade HM, et al. MicroRNA profiling of neurons generated using induced pluripotent stem cells derived from patients with schizophrenia and schizoaffective disorder, and 22q11.2 del. *PLoS One*. 2015;10(7):1–24.
285. Toyoshima M, Akamatsu W, Okada Y, Ohnishi T, Balan S, Hisano Y, et al. Analysis of induced pluripotent stem cells carrying 22q11.2 deletion. *Transl Psychiatry*. 2016;6(11).
286. Topol A, Zhu S, Hartley BJ, English J, Hauberg ME, Tran N, et al. Dysregulation of miRNA-9 in a Subset of Schizophrenia Patient-Derived Neural Progenitor Cells. *Cell Rep*. 2016 May;15(5):1024–36.
287. Han J, Kim HJ, Schafer ST, Paquola A, Clemenson GD, Toda T, et al. Functional Implications of miR-19 in the Migration of Newborn Neurons in the Adult Brain. *Neuron*. 2016;91(1):79–89.
288. Sawada T, Chater TE, Sasagawa Y, Yoshimura M, Fujimori-Tonou N, Tanaka K, et al. Developmental excitation-inhibition imbalance underlying psychoses revealed by single-cell analyses of discordant twins-derived cerebral organoids. *Mol Psychiatry*. 2020;25(11):2695–711.
289. Stachowiak EK, Benson CA, Narla ST, Dimitri A, Chuye LEB, Dhiman S, et al. Cerebral organoids reveal early cortical maldevelopment in schizophrenia—computational anatomy and genomics, role of FGFR1. *Transl Psychiatry*. 2017;7(11).
290. Srikanth P, Lagomarsino VN, Muratore CR, Ryu SC, He A, Taylor WM, et al. Shared effects of DISC1 disruption and elevated WNT signaling in human cerebral organoids. *Transl Psychiatry*. 2018;8(1).
291. Notaras M, Lodhi A, Dündar F, Collier P, Sayles NM, Tilgner H, et al. Schizophrenia is defined by cell-specific neuropathology and multiple neurodevelopmental mechanisms in patient-derived cerebral organoids. *Mol Psychiatry*. 2022;27(3):1416–34.
292. Qian X, Su Y, Adam CD, Deutschmann AU, Pather SR, Goldberg EM, et al. Sliced Human Cortical Organoids for Modeling Distinct Cortical Layer Formation. *Cell Stem Cell*. 2020;26(5):766-781.e9.
293. Dubonyte U, Asenjo-Martinez A, Werge T, Lage K, Kirkeby A. Current advancements of modelling schizophrenia using patient-derived induced pluripotent stem cells. *Acta Neuropathol Commun*. 2022;10(1):1–20.
294. Lee D, Seo J, Jeong H chan, Lee H, Lee SB. The Perspectives of Early Diagnosis of Schizophrenia Through the Detection of Epigenomics-Based Biomarkers in iPSC-Derived Neurons. *Front Mol Neurosci*. 2021;14(November).
295. Liu YN, Lu SY, Yao J. Application of induced pluripotent stem cells to understand neurobiological basis of bipolar disorder and schizophrenia. *Psychiatry Clin Neurosci*. 2017;71(9):579–99.
296. Prytkova I, Brennand KJ. Prospects for modeling abnormal neuronal function in schizophrenia using human induced pluripotent stem cells. *Front Cell Neurosci*. 2017;11(November):1–8.
297. Räsänen N, Tiihonen J, Koskuvi M, Lehtonen Š, Koistinaho J. The iPSC perspective on schizophrenia. *Trends Neurosci*. 2022;45(1):8–26.
298. Iefremova V, Manikakis G, Krefft O, Jabali A, Weynans K, Wilkens R, et al. An Organoid-Based Model of Cortical Development Identifies Non-Cell-Autonomous Defects in Wnt Signaling

References

- Contributing to Miller-Dieker Syndrome. *Cell Rep.* 2017;19(1):50–9.
299. Jabali A, Hoffrichter A, Uzquiano A, Marsoner F, Wilkens R, Siekmann M, et al. Human cerebral organoids reveal progenitor pathology in EML1-linked cortical malformation. *EMBO Rep.* 2022;23(5):1–17.
300. Ran FA, Hsu PD, Wright J, Agarwala V, Scott DA, Zhang F. Genome engineering using the CRISPR-Cas9 system. *Nat Protoc.* 2013;8(11):2281–308.
301. Sun Z, Südhof TC. A simple Ca²⁺-imaging approach to neural network analyses in cultured neurons. *J Neurosci Methods.* 2021;349(December 2020):109041.
302. Artimovich E, Jackson RK, Kilander MBC, Lin YC, Nestor MW. PeakCaller: An automated graphical interface for the quantification of intracellular calcium obtained by high-content screening. *BMC Neurosci.* 2017;18(1):1–15.
303. Livak KJ, Schmittgen TD. Analysis of relative gene expression data using real-time quantitative PCR and the 2- $\Delta\Delta$ CT method. *Methods.* 2001;25(4):402–8.
304. Love MI, Huber W, Anders S. Moderated estimation of fold change and dispersion for RNA-seq data with DESeq2. *Genome Biol.* 2014;15(12):1–21.
305. Yu G, Wang LG, Han Y, He QY. ClusterProfiler: An R package for comparing biological themes among gene clusters. *Omi A J Integr Biol.* 2012;16(5):284–7.
306. Ferreira TA, Blackman A V, Oyrer J, Jayabal S, Chung AJ, Watt AJ, et al. Neuronal morphometry directly from bitmap images. *Nat Methods.* 2014;11(10):982–4.
307. Huang CYM, Rasband MN. Axon initial segments: structure, function, and disease. *Ann N Y Acad Sci.* 2018;1420(1):46–61.
308. Renner H, Otto M, Grabos M, Schöler HR, Bruder JM. Fluorescence-based single-cell analysis of whole-mount-stained and cleared microtissues and organoids for high throughput screening. *Bio-protocol.* 2021;11(12):1–14.
309. Osborn TL, Wasanga CM, Ndeti DM. Transforming mental health for all. *The BMJ.* 2022.
310. Mitchell AC, Javidfar B, Pothula V, Ibi D, Shen EY, Peter CJ, et al. MEF2C transcription factor is associated with the genetic and epigenetic risk architecture of schizophrenia and improves cognition in mice. *Mol Psychiatry.* 2018;23(1):123–32.
311. Volk DW, Lewis DA. Impaired prefrontal inhibition in schizophrenia: Relevance for cognitive dysfunction. *Physiol Behav.* 2002;77(4–5):501–5.
312. Gao X, Grendel J, Muhia M, Castro-Gomez S, Susens U, Isbrandt D, et al. Disturbed prefrontal cortex activity in the absence of schizophrenia-like behavioral dysfunction in arc/arg3.1 deficient mice. *J Neurosci.* 2019;39(41):8149–63.
313. Hergenreder E, Minotti AP, Zorina Y, Oberst P, Zhao Z, Munguba H, et al. Combined small-molecule treatment accelerates maturation of human pluripotent stem cell-derived neurons. *Nat Biotechnol.* 2024;
314. Huang FF, Ben Aissa M, Lévesque G, Carreau M. FANCC localizes with UNC5A at neurite outgrowth and promotes neuritogenesis. *BMC Res Notes.* 2018;11(1):1–7.
315. Izadi M, Seemann E, Schlobinski D, Schwintzer L, Qualmann B, Kessels MM. Functional interdependence of the actin nucleator cobl and cobl-like in dendritic arbor development. *Elife.* 2021;10:1–38.
316. López-Bendito G, Flames N, Ma L, Fouquet C, Di Meglio T, Chedotal A, et al. Robo1 and Robo2 cooperate to control the guidance of major axonal tracts in the mammalian forebrain. *J*

References

- Neurosci. 2007;27(13):3395–407.
317. Round JE, Sun H. The adaptor protein Nck2 mediates Slit1-induced changes in cortical neuron morphology. *Mol Cell Neurosci*. 2011;47(4):265–73.
318. Zhang HY, Zheng LF, Yi XN, Chen Z Bin, He ZP, Zhao D, et al. Slit1 promotes regenerative neurite outgrowth of adult dorsal root ganglion neurons in vitro via binding to the Robo receptor. *J Chem Neuroanat*. 2010;39(4):256–61.
319. Bush JO, Soriano P. Ephrin-B1 regulates axon guidance by reverse signaling through a PDZ-dependent mechanism. *Genes Dev*. 2009;23(13):1586–99.
320. Shelly M, Cancedda L, Lim BK, Popescu AT, Cheng P lin, Gao H, et al. Semaphorin3A regulates neuronal polarization by suppressing axon formation and promoting dendrite growth. *Neuron*. 2011;71(3):433–46.
321. Le Verche V, Kaindl AM, Verney C, Csaba Z, Peineau S, Olivier P, et al. The somatostatin 2A receptor is enriched in migrating neurons during rat and human brain development and stimulates migration and axonal outgrowth. *PLoS One*. 2009;4(5).
322. O'Connor TP, Cockburn K, Wang W, Tapia L, Currie E, Bamji SX. Semaphorin 5B mediates synapse elimination in hippocampal neurons. *Neural Dev*. 2009;4(1):1–19.
323. Yang Y, Guan W, Sheng XM, Gu HJ. Role of Semaphorin 3A in common psychiatric illnesses such as schizophrenia, depression, and anxiety. *Biochem Pharmacol*. 2024;226(April):116358.
324. Wang Z, Li P, Wu T, Zhu S, Deng L, Cui G. Axon guidance pathway genes are associated with schizophrenia risk. *Exp Ther Med*. 2018;16(6):4519–26.
325. Yu S, Wang Z, Nan J, Li A, Yang X, Tang X. Potential Schizophrenia Disease-Related Genes Prediction Using Metagraph Representations Based on a Protein-Protein Interaction Keyword Network: Framework Development and Validation. *JMIR Form Res*. 2023;7(1):1–17.
326. Piper M, van Horck F, Holt C. The role of cyclic nucleotides in axon guidance. *Adv Exp Med Biol*. 2007;621:134–43.
327. Malavasi ELV, Economides KD, Grünewald E, Makedonopoulou P, Gautier P, Mackie S, et al. DISC1 regulates N-methyl-D-aspartate receptor dynamics: abnormalities induced by a Disc1 mutation modelling a translocation linked to major mental illness. *Transl Psychiatry*. 2018;8(1):1–16.
328. Ksiazek I, Burkhardt C, Lin S, Seddik R, Maj M, Bezakova G, et al. Synapse loss in cortex of agrin-deficient mice after genetic rescue of perinatal death. *J Neurosci*. 2007;27(27):7183–95.
329. Stephan A, Mateos JM, Kozlov S V., Cinelli P, Kistler AD, Hettwer S, et al. Neurotrophin cleaves agrin locally at the synapse. *FASEB J*. 2008;22(6):1861–73.
330. Yoshida T, Yasumura M, Uemura T, Lee SJ, Ra M, Taguchi R, et al. IL-1 receptor accessory protein-like 1 associated with mental retardation and autism mediates synapse formation by trans-synaptic interaction with protein tyrosine phosphatase δ . *J Neurosci*. 2011;31(38):13485–99.
331. Dean B, Keriakous D, Scarr E, Thomas EA. Gene Expression Profiling in Brodmann's Area 46 from Subjects with Schizophrenia. *Aust New Zeal J Psychiatry*. 2007 Apr 1;41(4):308–20.
332. Ivarsson O, Chou TT, Hjaltason O, Birgisdottir B, Jonsson H. Neuregulin 1 and Susceptibility to Schizophrenia. *Am J Hum Genet*. 2002;71:877–92.
333. Karagyaur M, Primak A, Bozov K, Sheleg D, Arbatsky M, Dzhauari S, et al. Novel missense variants in brain morphogenic genes associated with depression and schizophrenia. *Front Psychiatry*. 2024;15(April).

References

334. Wilkens R, Hoffrichter A, Kleinsimlinghaus K, Bohl B, Haag C, Lehmann N, et al. Diverse maturity-dependent and complementary anti-apoptotic brakes safeguard human iPSC-derived neurons from cell death. *Cell Death Dis.* 2022;13(10).
335. Hawkins J, Ahmad S. Why Neurons Have Thousands of Synapses, a Theory of Sequence Memory in Neocortex. *Front Neural Circuits.* 2016;10(March):1–13.
336. Sohn J, Okamoto S, Kataoka N, Kaneko T, Nakamura K, Hioki H. Differential inputs to the perisomatic and distal-dendritic compartments of VIP-positive neurons in layer 2/3 of the mouse barrel cortex. *Front Neuroanat.* 2016;10(DEC):1–18.
337. Gene [Internet]. Bethesda (MD): National Library of Medicine (US), National Center for Biotechnology Information; 2004 – [cited 2024 Jun 17]. Available from: <https://www.ncbi.nlm.nih.gov/gene/>

11. Appendix

Appendix I for introduction section 3.2

Table S1: List of genes located on 3q28

List of 40 described genes obtained from NCBI gene data base (337), 13 more uncharacterized loci on 3q28 (not listed in this table)

Gene ID	Genetic locus	Description
CCDC50	3q28	Coiled-coil domain containing 50
CCT6P4	3q28	Chaperonin Containing TCP1, Subunit 6 (Zeta) Pseudogene 4
CELIAC11	3q28	Celiac disease, susceptibility to, 11
CLDN1	3q28	Claudin 1
CLDN16	3q28	Claudin 16
ENAHP1	3q28	Enabled homolog pseudogene
ENOPH1P1	3q28	Enolase-phosphatase 1 pseudogene
FGF12	3q28-q29	Fibroblast growth factor 12
FGF12-AS1	3q28	FGF12 antisense RNA1
FGF12-AS2	3q28	FGF12 antisense RNA2
FGF12-AS3	3q28	FGF12 antisense RNA3
GCNT1P3	3q28	Glucosaminyl (N-Acetyl) transferase 1 pseudogene 3
GMNC	3q28	Geminin coiled-coil domain containing
IL1RAP	3q28	Interleukin-1 receptor accessory protein
LINC02013	3q28	Long intergenic non-protein coding RNA 2013
LNCR5	3q28	Lung cancer susceptibility 5
LOC100129725	3q28	PERP, TP53 apoptosis effector pseudogene
LPP	3q27.3-q28	LIM domain containing preferred translocation partner in lipoma
LPP-AS1	3q28	LPP-antisense RNA1
MIR28	3q28	microRNA28
MIR944	3q28	microRNA944
MTAPP2	3q28	Methylthioadenosine phosphorylase pseudogene 2
NMNAT1P3	3q28	Nicotinamide nucleotide adenylyltransferase 1 pseudogene 3
OSTN	3q28	Osteocrin/Musclin
OSTN-AS1	3q28	OSTN antisense RNA1
P3H2	3q28	Prolyl 3-hydroylase 2
P3H2-AS1	3q28	P3H2 antisense RNA1
PERPP1	3q28	PERP pseudogene 1
PYDC2	3q28	Pyrin domain containing 2
PYDC2-AS1	3q28	PYDC2 antisense RNA 1
RN7SKP222	3q28	RN7SK pseudogene 222
RN7SKP296	3q28	RN7SK pseudogene 296
RNU6-1109P	3q28	RNA, U6 small nuclear 1109, pseudogene
SNAR-I	3q28	Small NF90 (ILF3) associated RNA I
TMEM207	3q28	Transmembrane protein 207

Appendix

TP63	3q28	Tumor protein p63
TPRG1	3q28	Tumor protein p63 regulated 1
TPRG1-AS1	3q28	TPRG1 antisense RNA1
TPRG1-AS2	3q28	TPRG1 antisense RNA2
UTS2B	3q28	Urotensin 2B

Appendix II for results section 7.4.4 and 7.4.7

The batch variation in WT neuron morphology was very big, with batch 3 being significantly different from the other two batches. WT batch 3 had neurons about double the size (on average) of the other two batches which must be considered for the analysis. Nevertheless, in this project batch 3 was included in the analyses (Figure S1).

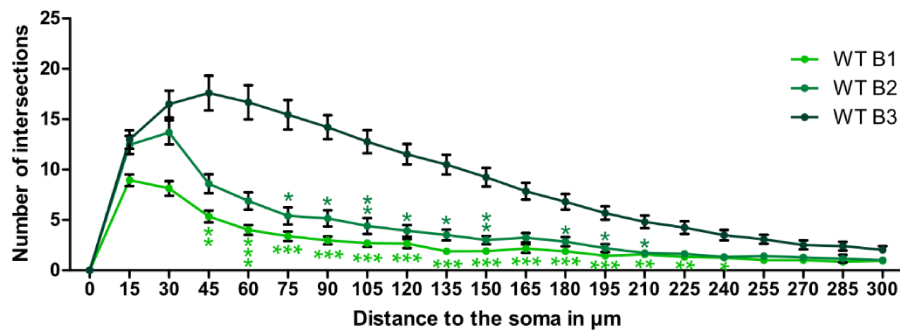


Figure S1: Sholl graphs of single WT neuron batches demonstrate large batch variance

Results of Sholl analysis of single WT neuron batches, plotted are the number of intersections and the distance to the soma. Sholl radius step size = 15 µm. N = 3 batches, n = 25-32 neurons, data presented as mean ± SEM, Kruskal-Wallis test with Dunn's multiple comparison test, * p < 0.05, ** p < 0.01, *** p < 0.001

Before the seemingly atypical (compared to the other batches) WT neuron batch 3 emerged, the phenotypes of the *OSTN* mutant clones were more like the phenotype of Ctrl vs. SCZ neurons which is shown in Figure S2 (for illustration of batch impact). In particular, *OSTN*₂^{+/-} neurons had significantly more intersections 45-150 µm from the soma compared to the WT whereas *OSTN*₁^{+/-} neurons did not show significant differences. *OSTN*^{-/-} neurons still displayed fewer intersections at every Sholl radius than the WT neurons but only at 30 µm and 90-120 µm distance to the soma the difference was significant (Figure S2A). The number of primary neurites did not show significant differences before atypical WT batch 3 (WT 10.47 ± 0.56; *OSTN*₁^{+/-} 11.9 ± 0.696; *OSTN*₂^{+/-} 8.68 ± 0.279; *OSTN*^{-/-} 9.125 ± 0.735). However, in addition to the significantly fewer intersections (sum) and smaller neurons of the *OSTN*^{-/-} clone (sum of intersections 40.25 ± 2.741; total length 603.8 ± 41.12), before WT batch 3 inclusion *OSTN*₂^{+/-} neurons (sum of intersections 95.36 ± 4.196; total length 1430 ± 62.94) had significantly more intersections (sum) and bigger neurons compared to the WT (sum of intersections 68.21 ± 3.96; total length 1023 ± 59.4; Figure S2B). This demonstrates how much

of an impact the high batch variability can have on the results, which should be addressed by increasing Ns and statistical means.

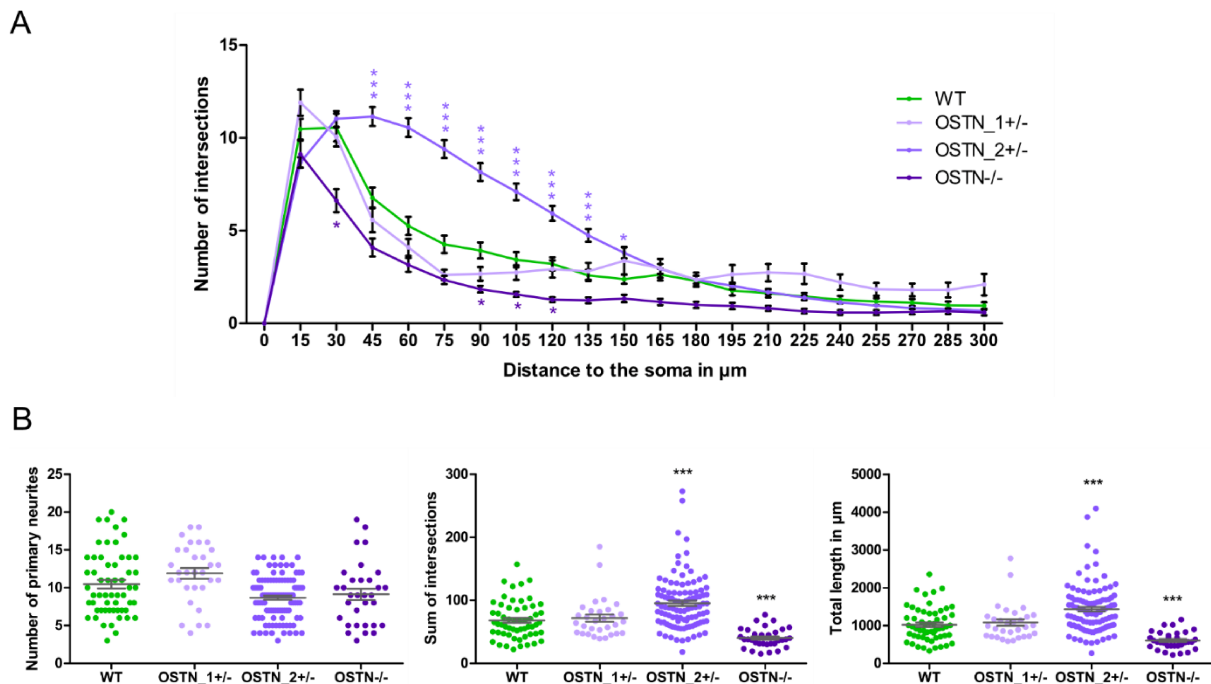


Figure S2: Sholl analysis of WT and *OSTN* mutant neurons (d55-60), before WT batch 3 inclusion
 Neuronal cultures were transduced with an AAV that enables mCherry expression under the CaMKII α promoter and subsequently analyzed. Results before inclusion of WT batch 3. **A)** Results of Sholl analysis, WT vs. *OSTN*_{1+/-}, *OSTN*_{2+/-} and *OSTN*^{-/-} neurons, plotted are the number of intersections and the distance to the soma. Sholl radius step size = 15 μ m. **B)** Results of further morphology parameters: number of primary neurites, sum of intersections and the total length of neurons. WT N= 2 batches, n = 57 neurons, *OSTN*_{1+/-} N = 1 batch, n = 31 neurons, *OSTN*_{2+/-} N = 3 batches, n = 103 neurons, *OSTN*^{-/-} N = 1 batch, n = 32 neurons, data presented as mean \pm SEM, Kruskal-Wallis test with Dunn's multiple comparison test, * $p < 0.05$, ** $p < 0.01$, *** $p < 0.001$

Due to technical issues (cell detachment during staining process), most treatment conditions of *OSTN*_{2+/-} neurons could not be analyzed (only available data: untreated, AP-811+*OSTN* and AP-811+IL-1Ra). SYN particles/100 μ m did not show significant differences for *OSTN*_{2+/-} and mostly not for WT neurons except for IL-1 β (48.66 ± 1.098) and AP-811+*OSTN* (40.62 ± 1.289) treatments which displayed increased and reduced SYN particles/100 μ m respectively (WT untreated 46.04 ± 1.391 ; Figure S3A).

Appendix

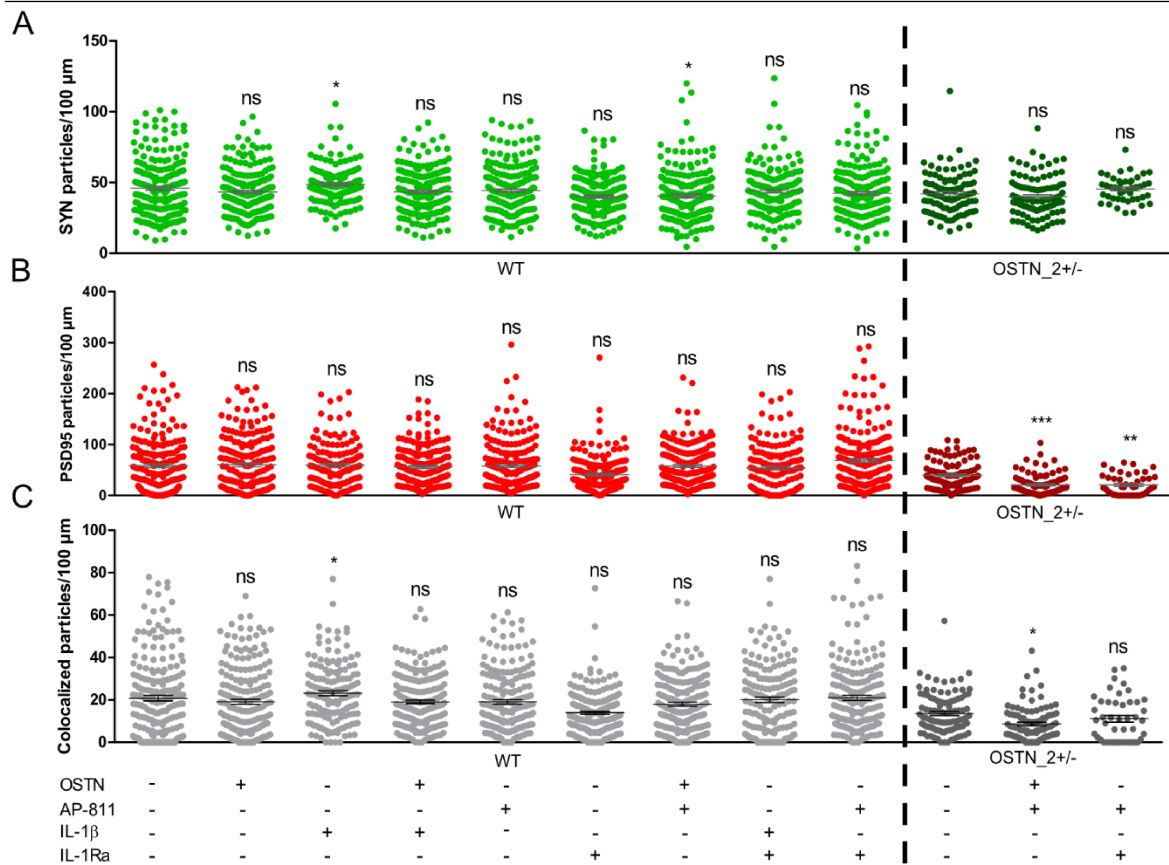


Figure S3: Modulation of OSTN and IL-1 β pathways barely impacts synaptic particle density in d105 WT neurons

SYN and PSD95 and their colocalization particle density was analyzed in d105 WT and OSTN_2+/- neurons with and without combinations of OSTN and IL-1 β pathway activation and inhibition. **A)** Quantitative analysis of SYN particles per 100 μ m. **B)** Quantitative analysis of PSD95 particles per 100 μ m. **C)** Quantitative analysis of SYN and PSD95 particle colocalization per 100 μ m. Treatments for this analysis: 8d 200 nM AP-811, 7d 100 nM OSTN, 5d 100 ng/ml IL-1Ra, 5d 50 ng/ml IL-1 β , duration and concentrations for combined treatments were the same. WT N = 2 batches, n = 147-208 neurites per condition, OSTN_2+/- N = 1 batch, n = 45-100, data presented as mean \pm SEM, Kruskal-Wallis test with Dunn's multiple comparison test, * $p < 0.05$, ** $p < 0.01$, *** $p < 0.001$, ns = not significant.

The PSD95 particle density was not altered by any treatment in WT neurons, but significantly reduced by AP-811+OSTN (20.99 ± 1.926) and AP-811+IL-1Ra (21.05 ± 2.997) treatment in OSTN_2+/- neurons (untreated 39.75 ± 2.65 ; Figure S3B). Colocalization of SYN and PSD95 particles was significantly increased in WT neurons treated with IL-1 β (WT untreated 20.78 ± 1.316 ; IL-1 β 23.21 ± 1.205) and significantly lower in OSTN_2+/- neurons treated with AP-811+OSTN (OSTN_2+/- untreated 13.65 ± 0.951 ; AP-811+OSTN 8.711 ± 0.804). All other treatment conditions in WT and OSTN_2+/- neurons did not have significant effects on SYN/PSD95 colocalization (Figure S3C). Due to the lack of the proper controls for OSTN_2+/- it is not possible to evaluate this data properly.

12. Contributions

The reprogramming of the control and patient cell lines (Ctrl, WT, SCZ) was performed before the start of this project by Dr. Sandra Horschitz (Hector Institute for Translational Brain Research, Central Institute of Mental Health, Mannheim, Germany) and Gina Tillmann (Hector Institute for Translational Brain Research, Central Institute of Mental Health, Mannheim, Germany) and the hiPSC were kindly provided to me for this project.

The electrophysiological measurements and the analysis were performed by Dr. Mahnaz Davoudi (Hector Institute for Translational Brain Research, Central Institute of Mental Health, Mannheim, Germany) in cooperation with PD Dr. Georg Köhr (Department of Neurophysiology, Mannheim Center for Translational Neuroscience, University of Heidelberg/Medical Faculty Mannheim, Germany).

The analysis for the RNA sequencing data was done in close collaboration with Dr. Anne Hoffrichter (Hector Institute for Translational Brain Research, Central Institute of Mental Health, Mannheim, Germany) who wrote all the apps for the quality control and further analysis and generated the graphs for the figures.

The AAV used in this project was kindly provided by the group of Prof. Dr. Valery Grinevich (Central Institute of Mental Health, Mannheim, Germany).

3D cell culture, cryo-sectioning and staining of the slices were performed in close collaboration with Dr. Andrea C. Rossetti and Helene Schamber (Hector Institute for Translational Brain Research, Central Institute of Mental Health, Mannheim, Germany).

13. Acknowledgements

First, I would like to thank Prof. Dr. Philipp Koch for giving me the opportunity to do research in his lab on such an interesting topic and for giving me the freedom to develop this project on my own, giving me guidance when needed.

Then, I would like to thank Prof. Dr. Valery Grinevich for being my first examiner of this thesis, for the guidance and providing the AAV used in this thesis. I am very grateful to Prof. Dr. Christoph Schuster and Prof. Dr. Ana Oliveira for agreeing to complete my thesis defense committee. I also thank Prof. Dr. Peter Kirsch for his guidance as a member of my thesis advisory committee. I am grateful that I could join the graduate school of the IZN Heidelberg for the duration of my PhD research.

Thanks to Dr. Mahnaz Davoudi and PD Dr. Georg Köhr for the help with the electrophysiology experiments.

A big thank you to Anne for your invaluable help with the analysis and visualization of the RNAseq data and being always ready to help.

Many thanks to Isa, Gina and Helene who always helped with any issues and made sure the lab was always running smoothly. Special thanks to Isa for all the late-night emergency solutions or joint cell culture sessions especially with new protocols, we had a good time.

Thanks to all my great (former) colleagues: Bettina, Ruven, Ammar, Fabio, Karen, Andrea, Anne, Marco, Raquel, Annasara, Sandra, Isabel and Isa and all the new colleagues. It was a real pleasure to share so much time with everyone, you made these years worthwhile with inspiring research and private conversations and making the lab a better place.

I am deeply grateful to Andrea for your help with initial 3D experiments, your expertise that you were always willing to share, your enthusiasm about the project, inspiring discussions and in general your help and time. I always enjoyed our occasionally shared bike rides to or from work which was always a time for good conversations.

Thanks to Anne, Julia, Karen, Fabio, Raquel and Annasara for my occasional boulder sessions with you guys, even though I was not super consistent I always enjoyed this time.

Lots of thanks to Karen for all the times you were "bored at home" or you had "too much chocolate" which is why you made a cake and unfortunately had to bring it to the office... Then there were the entertaining and musically extraordinary microscope sessions, I missed that! Thanks to you and also Fabio for staying in touch even after leaving the lab.

Acknowledgements

A huge thank you to Elina and Sarah for our joint online analyzing and writing sessions, the emotional support and constant motivation. You really helped me pulling through and finally we all saw it through to the end!

I also want to thank my best and longest friend Tabi for keeping me motivated, reminding me to also take breaks and understanding the struggle, because also in other sciences this is a tough cookie. But stay motivated, you will make it as well and it will be a great work, I know it! Thank you for always being my friend and being there no matter what!

I am enormously grateful to Malin, Elena and Julia, we started together, we went through frustration and successes together, we shared our cell cultures, were "exiled" together and could always count on help and scientific advice from each other, no matter how busy we were. I could always rely on you guys be it workwise or in private matters. We were a literal dream team, and I am going to miss you in my work life! I am very thankful for your support, for all the girls' evenings, sports sessions and all the good times we had, let's keep our regular meetings up! You helped me to keep going, thank you for being really good friends it wouldn't have been the same without you!

I am very thankful to my family, my parents and grandmas, you made this way I chose possible, you always supported, encouraged and believed in me. Thank you, Anna, for being the best sister one can ask for, your emotional support, the encouragement (the snacks and the talks), all the surprises you organized for me that always made me smile and always having an open ear for your little sister. Thank you!

Thanks to all friends who were rooting for me, believed in me and morally supported me throughout my PhD journey. Thanks to Molly and Charlie for being great emotional support animals – always lending a paw, closely supervising my progress, from behind the keyboard, or my lap...while sleeping. Your cuteness is illegal!

A T. rex-sized thank you to my partner Philipp Blei, you have been supporting me for many years now, keeping up with my ventures: first the long-distance times, my stressful final weeks of my Master's, then my idea to do a PhD and also to adopt those two kittens. Thank you for keeping me going in stressful times, always being there for me, always being understanding and encouraging, having my back with everyday stuff when I was too stressed to help you out. Thank you for your incredible patience, being an amazing person and always a calm anchor for me, always recognizing and solving me being hangry and slowing me down when needed!

Thank you everyone! I am really happy I got to know so many great people and I hope we can stay in touch! All the best to everyone!